frontiers | Research Topics

Chemical physics and physical chemistry editor's pick 2024

Edited by
Malgorzata Biczysko

Published in
Frontiers in Chemistry

ISSN 1664-8714
ISBN 978-2-8325-5864-5
DOI 10.3389/978-2-8325-5864-5

About Frontiers

Frontiers is more than just an open access publisher of scholarly articles: it is a pioneering approach to the world of academia, radically improving the way scholarly research is managed. The grand vision of Frontiers is a world where all people have an equal opportunity to seek, share and generate knowledge. Frontiers provides immediate and permanent online open access to all its publications, but this alone is not enough to realize our grand goals.

Frontiers journal series

The Frontiers journal series is a multi-tier and interdisciplinary set of open-access, online journals, promising a paradigm shift from the current review, selection and dissemination processes in academic publishing. All Frontiers journals are driven by researchers for researchers; therefore, they constitute a service to the scholarly community. At the same time, the *Frontiers journal series* operates on a revolutionary invention, the tiered publishing system, initially addressing specific communities of scholars, and gradually climbing up to broader public understanding, thus serving the interests of the lay society, too.

Dedication to quality

Each Frontiers article is a landmark of the highest quality, thanks to genuinely collaborative interactions between authors and review editors, who include some of the world's best academicians. Research must be certified by peers before entering a stream of knowledge that may eventually reach the public - and shape society; therefore, Frontiers only applies the most rigorous and unbiased reviews. Frontiers revolutionizes research publishing by freely delivering the most outstanding research, evaluated with no bias from both the academic and social point of view. By applying the most advanced information technologies, Frontiers is catapulting scholarly publishing into a new generation.

What are Frontiers Research Topics?

Frontiers Research Topics are very popular trademarks of the *Frontiers journals series*: they are collections of at least ten articles, all centered on a particular subject. With their unique mix of varied contributions from Original Research to Review Articles, Frontiers Research Topics unify the most influential researchers, the latest key findings and historical advances in a hot research area.

Find out more on how to host your own Frontiers Research Topic or contribute to one as an author by contacting the Frontiers editorial office: frontiersin.org/about/contact

Chemical physics and physical chemistry editor's pick 2024

Topic editor
Malgorzata Biczysko — University of Wrocław, Poland

Citation
Biczysko, M., ed. (2025). *Chemical physics and physical chemistry editor's pick 2024*. Lausanne: Frontiers Media SA. doi: 10.3389/978-2-8325-5864-5

Table of contents

frontiers | Frontiers in Chemistry

TYPE Original Research
PUBLISHED 05 July 2023
DOI 10.3389/fchem.2023.1229586

OPEN ACCESS

EDITED BY
Takamasa Momose,
University of British Columbia, Canada

REVIEWED BY
Kazuyuki Takeda,
Kyoto University, Japan
Kirill Sheberstov,
École Normale Supérieure, France
Pedro Miguel Aguiar,
Montreal University, Canada
Paul Vasos,
University of Bucharest, Romania

*CORRESPONDENCE
Giuseppe Pileio,
g.pileio@soton.ac.uk

RECEIVED 26 May 2023
ACCEPTED 22 June 2023
PUBLISHED 05 July 2023

CITATION
Robertson TBR, Bannister RC, Cartlidge TAA, Hugger T, Breham S, Zick K, Engelke F, Thompson S and Pileio G (2023), A dual-core NMR system for field-cycling singlet assisted diffusion NMR.
Front. Chem. 11:1229586.
doi: 10.3389/fchem.2023.1229586

A dual-core NMR system for field-cycling singlet assisted diffusion NMR

Thomas B. R. Robertson[1], Rose C. Bannister[1], Topaz A. A. Cartlidge[1], Thimo Hugger[2], Sebastien Breham[2], Klaus Zick[2], Frank Engelke[2], Sam Thompson[1] and Giuseppe Pileio[1]*

[1]School of Chemistry, University of Southampton, Southampton, United Kingdom, [2]Bruker Biospin GmbH, Silberstreifen, Rheinstetten, Germany

Long-lived singlet spin order offers the possibility to extend the spin memory by more than an order of magnitude. This enhancement can be used, among other applications, to *assist* NMR diffusion experiments in porous media where the extended lifetime of singlet spin order can be used to gain information about structural features of the medium as well as the dynamics of the imbibed phase. Other than offering the possibility to explore longer diffusion times of the order of many minutes that, for example, gives unprecedented access to tortuosity in structures with interconnected pores, singlet order has the important advantage to be immune to the internal field gradients generated by magnetic susceptibility inhomogeneities. These inhomogeneities, however, are responsible for very short T_2 decay constants in high magnetic field and this precludes access to the singlet order in the first instance. To overcome this difficulty and take advantage of singlet order in diffusion experiments in porous media, we have here developed a dual-core system with radiofrequency and 3-axis pulsed field gradients facilities in low magnetic field, for preparation and manipulation of singlet order and a probe, in high magnetic field, for polarisation and detection. The system operates in field-cycling and can be used for a variety of NMR experiments including diffusion tensor imaging (both singlet assisted and not). In this paper we present and discuss the new hardware and its calibration, and demonstrate its capabilities through a variety of examples.

KEYWORDS

singlet assisted diffusion NMR, long-lived spin order, diffusion NMR, NMR equipment, field cycling NMR

Introduction

Molecular diffusion is encoded in a variety of magnetic resonance methods to extract structural and chemical-physical information on the diffusing molecule, the liquid it is dissolved in and the structure within which molecular diffusion occurs. Widely used examples of diffusion NMR experiments include: diffusion ordered spectroscopy (DOSY) where the signals belongings to the same molecular species in a mixture are separated and resolved according to their different diffusion coefficient (Morris, 2009); diffusion weighted MRI (DW-MRI) where contrast between tissues in the living matter is achieved through changes in the apparent diffusion coefficient of water confined within the different compartments characterising the micro-structure of specific tissues (Merboldt et al.,

1985); diffusion tensor imaging (DTI) where the size, shape and orientation of compartments in a porous structure is mapped through the measurement of the whole diffusion tensor (Basser et al., 1994).

When molecules diffuse within a porous structure, measurements of the diffusion tensor provide structural information such as porosity, pore size distribution, tortuosity, etc., to characterise the porous medium itself. Such information is of fundamental importance to understand the property of the medium and/or guide the design of improved media (Callaghan, 2011). The anisotropic confinement of molecular diffusion, imposed by the structural characteristics of the medium, imparts a particular *shape* to the diffusion tensor and this can be measured through the DTI technique. DTI provides a form of indirect imaging of structures with pores that are too small for real-space magnetic resonance imaging (this latter has a typical spatial resolution of ~0.1–1 mm^3). In structures with relatively big pores (say above 100 μm^3), for which structural imaging via MRI can already provide good quality 2D and 3D images, diffusion-NMR techniques would still play an important role in its ability to catch the dynamics inside the medium, an important information that is fundamental to many applications. For example, the connectivity between distant pores, as rendered by the tortuosity parameter, is of crucial importance in battery electrodes and fuel-cells gas diffusion layers. Similarly, tortuosity is relatable to the availability of nutrients and the removal of waste in the various parts of scaffoldings used in tissue engineering. Generally, if the pores of a medium are too big with respect to the maximum distance traveled by molecules during the experiment, then the anisotropic confinement is not correctly captured and the structure within which molecules diffuse appears to be (incorrectly) isotropic, making DTI-derived information unreliable. This becomes relevant considering that, in conventional diffusion NMR experiments, the molecular diffusion time is limited by the lifetime of either transverse or longitudinal nuclear spin order. Most typically, the lifetime of longitudinal order is bigger or equal than the lifetime of transverse spin order, ranging between a few milliseconds and a few seconds. The relatively short persistence of diffusion-encoded NMR signals translates in a limitation to the size of pores and pore-pore distances that can be reliably probed via conventional diffusion-NMR techniques. However, in some circumstances, like, for example, when dealing with low-gamma nuclei such as ^{13}C or ^{15}N to cite a few commonly-encountered species, the lifetime of longitudinal and transverse spin order can be of the order of many tens of seconds or even a few minutes. Systems possessing such long spin order lifetimes can be therefore used as spies to probe anysotropic confinement, pore interconnectivity and so on.

Working on the same logic but using a different approach, our group has recently proposed to extended the scope of diffusion-NMR through the use of long-lived singlet spin order (Dumez et al., 2014; Pileio et al., 2015; Pileio and Ostrowska, 2017; Tourell et al., 2018). In two-spin-1/2 systems and under well-understood circumstances, singlet order persists for many minutes (sometimes many tens of) against the few-seconds-long persistence of longitudinal or transverse order prepared in the same systems (Pileio, 2020). Long-lived singlet order can be generated through a variety of pulse sequence schemes (Pileio, 2017) and, by combining singlet order preparation/readout schemes with diffusion encoding pulsed field gradient techniques it was possible to measure small diffusion coefficients (Cavadini et al., 2005; Cavadini and Vasos, 2008), slow dynamic processes, (Sarkar et al., 2007a; Sarkar et al., 2007b), slow flows, (Pileio et al., 2015), cavity sizes of the order of millimetres through singlet enhanced q-space imaging (Yadav et al., 2010; Torres et al., 2012; Pileio and Ostrowska, 2017), track molecules over minute-long time intervals (Dumez et al., 2014), and measure shape and orientation of millimetre-sized channels in porous media via singlet assisted DTI (paper in preparation). We have dubbed the generic class encompassing all these techniques as singlet-assisted diffusion NMR (SAD-NMR).

However, the analysis of diffusion NMR data in porous structures is often complicated by phenomena related to the magnetic susceptibility mismatch between the porous matrix and the imbibing liquid (or gas). These susceptibility differences, despite often just of the order of a few ppm's, create two sorts of deleterious problems, they: (i) generate internal field gradients whose intensity is often larger than the field gradient pulses used to encode molecular diffusion in NMR; (ii) produce a strong relaxation mechanism for transverse magnetisation (Callaghan, 1991; Callaghan, 2011). With regard to the first problem, SAD-NMR is very advantageous since singlet order is immune to magnetic field gradients. However, the strong transverse magnetization decay in porous media impedes the preparation of singlet order because this typically requires transverse magnetisation to survive for tens (sometimes hundreds) of milliseconds. In order to understand this phenomenon, some of us have recently developed analytical equations and a simulation code to predict the relaxation of transverse order due to susceptibility inhomogeneities in a porous structure of arbitrary complexity (Cartlidge et al., 2022). The severity of these effects depends upon the value of the static magnetic field the sample is immersed in, and become negligible at magnetic field strengths of the order of 100 mT or below, depending on the actual size of the inhomogeneities. Unfortunately, magnetic resonance detection at such low field is very poor and only time-domain NMR experiments are then feasible. In time-domain however, chemical shift resolution is lost, with all related consequences.

The use of low magnetic field, required to reduce susceptibility-related issues, is here combined with the high-resolution and high-sensitivity features of high-field NMR by working in a field-cycling fashion. Field-cycling NMR has become an active area of magnetic resonance with application that spans from gathering dispersion curves (measurement of relaxation at different magnetic fields) for studying food, proteins and MRI contrast agents, to gaining contrast in low-field MRI experiments (Anoardo et al., 2001; Kimmich and Anoardo, 2004; Broche et al., 2019). Field-cycling can be implemented in two complementary ways: (i) by ramping the magnetic field with the use of an electromagnet or, (ii) by shuttling the sample between two (or more) regions of space with different magnetic field values. The first method provides a very rapid field-switching time (a Tesla in a few milliseconds), but the maximum field achievable is limited to a relatively low value of around 2 Tesla. The sample shuttling method is somewhat slower (although some shuttle systems can cover many Tesla within tens of milliseconds) but can be implemented around virtually any available

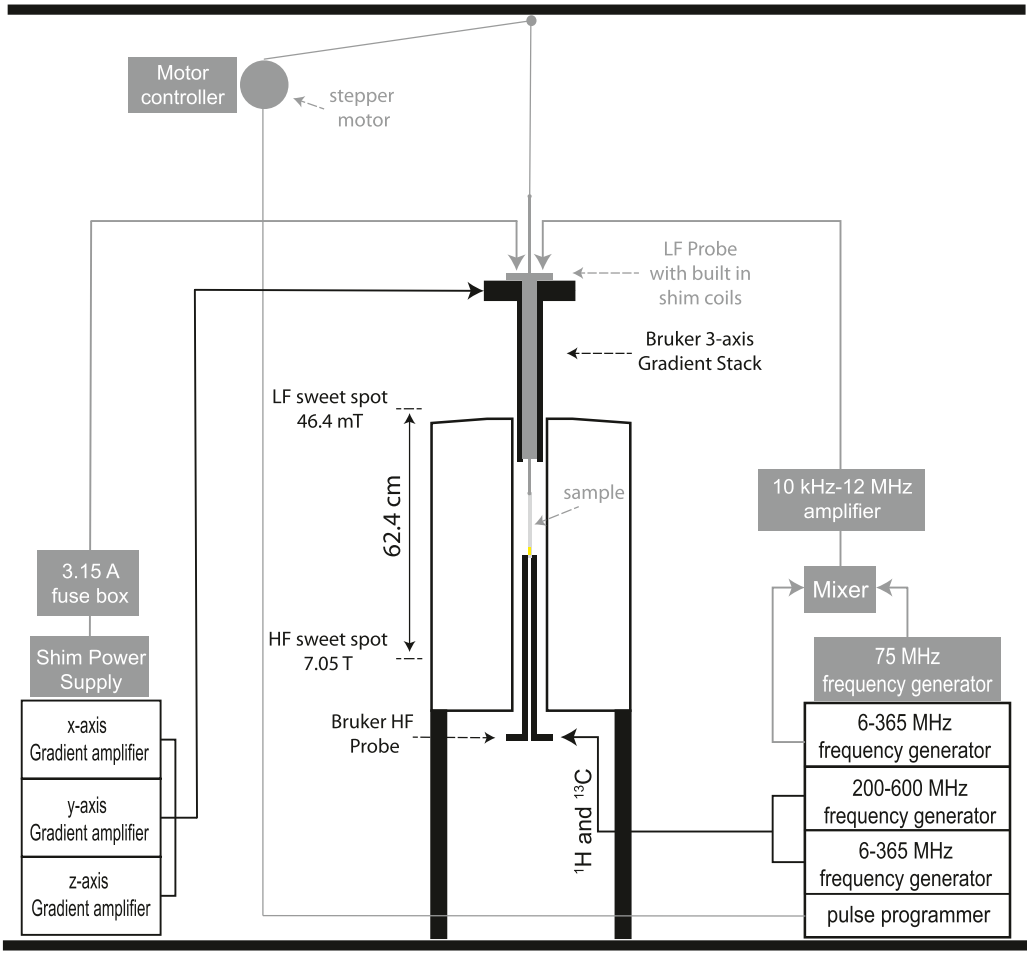

FIGURE 1
A schematic view of the dual-core magnetic resonance setup developed in this work. All parts in grey are customised add-ons to existing hardware.

static magnetic field value. Several groups have built sample shuttles to run magnetic resonance experiments at two or more fields (Swanson and Kennedy, 1993; Redfield, 2003; Chou et al., 2012; Charlier et al., 2013; Cousin et al., 2016; Zhukov et al., 2018; TomHon et al., 2020). Our laboratory has a custom-built sample shuttle to measure relaxation of longitudinal (T_1), transverse (T_2) and singlet order (T_S) and a temperature-controlled sample shuttle where the sample temperature is maintained constant through the sample within 0.05°C as the sample travels across magnetic field spanning from 7 T to 50 mT (Hall et al., 2020).

In this paper, we report about the construction of a dual-core NMR system with radiofrequency facilities at both 7 T and 46.4 mT (500 kHz ^{13}C Larmor frequency) plus 3-axis gradient facilities at 46.4 mT to allow singlet-assisted diffusion tensor imaging in porous media (and several other experiments, including SAD-NMR schemes) at a field where the negative effects of magnetic susceptibility inhomogeneities become negligible. The system is complemented by a shuttle with 3-axis accurate sample positioning that moves the sample from the high-field probe, where the sample is firstly polarised and later detected, to the low field probe where diffusion is encoded into singlet order via a combination of pulsed field gradients and radiofrequency pulses. The paper aims to discuss the details of the equipment and demonstrates its uses by measuring T_1, T_2, T_S, diffusion coefficients, tortuosity and diffusion tensors in isotropic liquid samples as well as in porous media with large magnetic susceptibility inhomogeneities.

Hardware development

Hardware design

The customised equipment here presented is built and assembled around a 7.05 T Oxford Instruments unshielded magnet coupled to a Bruker Avance III 300 MHz console and equipped with a 10 mm MICWB40 Bruker probe with a ^{1}H/^{13}C resonator that sits in the 7.05 T sweet spot (Figure 2E). A schematic view of the setup is reported in Figure 1 with the actual parts rendered in 3D in Figure 2. More details about the construction are reported in the Supplementary Material to this paper. The regions labelled as high (HF) and low field (LF) correspond to 7.05 T and

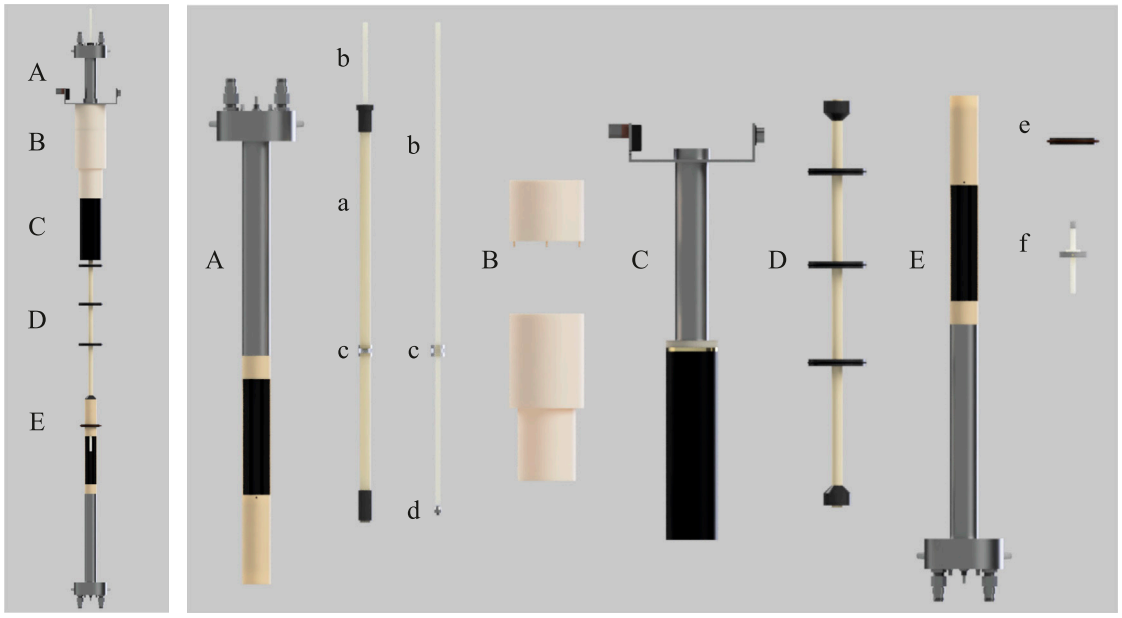

FIGURE 2
A rendered view of the setup developed in this work. **(A)** custom-made 500 kHz probe, **(B)** POM mounting for probe/gradients onto top of magnet bore, **(C)** Bruker Micro 2.5 WB 3-axis gradients, **(D)** Sample guide tube connecting low and high field probes, **(E)** Bruker MICWB40 probe with custom centering guide and sample depth gauge (e, f). Internal components are: (a) GRP sample rod guide tube with xy rod guide (labelled as c); (b) ASA 7 mm square sample guide rod; (c) Perspex rod guide cylinder with 7.1 mm square hole to ensure sample remains coaxial with both probes and is consistently positioned within the xy plane; (d) Acrylic attachment with external M5 screw thread for NMR tube mounting; (e) Centering guide for high field probe mounting; (f) PTFE sample positioning stopper for shuttle.

46.4 mT, respectively. These are located in the magnet sweet spot (HF) and 62.4 cm above the sweet spot along the magnet stray field (LF). At 46.4 mT the Larmor frequency of ^{13}C is 500 kHz which is the frequency at which the LF probe is tuned. The next few sections contain details of the hardware setup.

Low field probe

The LF probe (Figure 2A) was designed and manufactured in collaboration with Bruker BioSpin GmbH. The circuitry is built inside a modified MICWB40 Bruker probe case which is bore-through to facilitate the sample shuttling stage. The probe radiofrequency coil is tuned to 500 kHz and accommodates a 10 mm NMR tube. It is a saddle coil with 10 mm inner diameter and 30 mm length. The B_1 field has been calculated to be 0.12 mT A^{-1} with a quite flat profile over 20 mm. The coil center is placed in a region of the stray field where the maximum field spread over 20 mm has been measured to be 4.7 mT, corresponding to about 50 kHz for ^{13}C. Therefore, the probe is also equipped with a Z-shim coil to correct for these inhomogeneities. The shim coil geometry is optimized for linearity in a cylindrical volume with 10 mm diameter and 25 mm length and was wound with copper wire with a diameter of 1 mm.

Special care had to be taken regarding the RF coil performance. A design goal of a conventional NMR coils is usually to maximize the Q-factor for maximum transmit and receive efficiency, but due to the very low working frequency of 500 kHz, a high Q-factor would result in a very long rise time of the current in the resonant circuit, which would limit the achievable width of the excitation profile, due to the required short pulse lengths of the experiments. On the other hand, reducing the Q-factor too much would result in mean and peak power values that are just not feasible due to the non-availability of amplifiers and of course electronic failure of the probe due to arcing and heating. Therefore, a compromise between a fast rise time and low reference power had to be found. We therefore used both Electromagnetic and spin dynamics simulations to found out that a saddle coil with 4 windings and an added resistance would constitute a good compromise with a calculated Q-factor value of about 5 (see Supplementary Material).

3-axis field gradients

The low field probe fits within the 40 mm internal diameter of a Bruker Micro2.5 WB 3-axis gradient system (Figure 2C). Gradients are driven by a Bruker GREAT 60 A amplifier rack generating a maximum gradient strength of 1.5 T m^{-1}. The gradient system is held inverted and centred in the LF spot by a custom built plastic support detailed in Supplementary Figure S5.

Sample shuttle

Sample transport between the HF and LF sweet spots is achieved using a Trinamic TMCL-1160 stepper motor operated

by the customised software as previously reported by our group (Hall et al., 2020). The motor is positioned outside the magnet stray field at ceiling height. Unfortunately, due to limited ceiling clearance and the need for the sample guide rod described below, it was not feasible to mount the stepper motor directly above the magnet as would be ideal. A 25 cm circumference spindle wheel 3D-printed from ABS plastic winds a high tensile strength Dyneema cord with a low stretch ratio. The cord pulls up and down an acrylonitrile styrene acrylate (ASA) 70 cm long sample guide rod with a 7 mm × 7 mm square section profile and 1 mm wall thickness (part b in Figure 2). The rod slides through a square hole of 7.1 mm size (Figure 2C), placed within the LF probe body in order to maintain micrometric sample alignment at all time as necessary for DTI structural studies. The top of the square rod engages via a brass hook to the pulling cord. The bottom of the square rod has an acrylic attachment (part d in Figure 2) with an external (M5) screw thread to allow attachment to a standard 5 or 10 mm Wilmad-Labglass Pressure Vacuum Valve NMR Tubes for rapid sample exchange between experiments. The shuttle's speed and its acceleration profile can be adjusted and specified in the spectrometer's user interface (Bruker Topspin's interface in our case). We have also implemented the modality in which the user specifies the shuttling time and the velocity is adjusted accordingly. Our intended use of this shuttle gravitates around long-lived spin order in doubly-labelled ^{13}C molecules. Typically, these molecules have many-second long T_1 and thus fast shuttling times are not needed. In a typical experiment we use a shuttling time of 3 s to cover the HF-LF distance of 62.4 cm, corresponding to about 0.2 m s^{-1}.

Electronics

The 500 kHz radiofrequency is generated by mixing the signal generated by one channel of the Bruker console, set at 75.5 MHz, with the one generated by an external frequency synthesizer (PTS 250SHO2EYX-8/X-26), set at a fixed frequency of 75.0 MHz and synchronised on the same clock of the Bruker console. Frequency mixing is done using a Mini-circuits ZP-3-S+ frequency mixer. The output signal is filtered via a Mini-circuits BLP-70 low pass filter to eliminate the higher frequency. The so-generated signal is amplified by a 40 W RF Amplifier working in the range 10kHz-12 MHz at 50 dB (purchased from Electronics and Innovation, model 2100L).

The Z-shim coil within the LF probe is powered by a Rohde and Schwarz NGA101 power supply. The current reaching the Z-shim coil is limited to 5 A with the use of a fuse box placed along the transmission line.

A custom-printed circuit board is used to supply power to the motor driver and to amplify the trigger outputs from the spectrometer console (working at 5 V) to the motor controller (working at 10 V). Position and timing of the shuttle is controlled by the spectrometer computer using custom-made Python scripts integrated within the acquisition software. Prior to acquisition, the values for the speed, acceleration and target field strength are set by the user within the acquisition tab, read by the Python scripts and stored in the motor memory. During acquisition, TTL signals from the spectrometer console triggers the motor to move up or down at times specified in the pulse program.

Hardware calibration

This section describes the experiments and procedures done to optimise the magnetic field homogeneity in the LF region and to calibrate the pulse length for ^{13}C in the LF probe.

Field shimming

To find the sweet spot for the LF probe, we measured the stray field above the sweet spot of the 7.05 T magnet and along the *z*-axis for over 1 m, and with a 1 cm spatial resolution, using a Hall device (Lakeshore 460 3 channel gaussmeter with MMZ-2518-UH probe). A 500 kHz Larmor frequency for the ^{13}C would correspond to a field of 46.4 mT and this was found to be 62.4 cm above the HF sweet spot. The magnetic field within 10 mm above and below this point (the LF sweet spot) has been sampled with a 5 ± 1 mm spatial resolution (see column 2, Supplementary Table S1 in Supplementary Material) and was found to vary, almost linearly, by about 4.8 mT across the 20 mm region.

To obtain a ballpark value for the current to be supplied to the Z-shim coil placed within the LF probe to correct for the B_0 inhomogeneity, we have measured the magnetic field around the LF sweet spot as a function of the current supplied. The results of these measurements are reported in columns 3-14 of Supplementary Table S1 in Supplementary Material. From these data, which suffer from imperfection in the manual positioning of the field probe (estimated to be of the order of 1 mm), the field results almost flat within 0.1 mT and over 20 mm when the Z-shim is driven by a 3.2 A current.

Ahead of these field measurements we have checked that the inner surface of the LF probe does not heat too much when the Z-shim coil is turned on. This has been done with the use of a PT100 temperature probe placed in the centre of the coil region while airflow through the coil was restricted. These measurements (Supplementary Figures S17, 18 in Supplementary Material) show that a 3.5 A current leads to an increase in temperature from 20.8 to a maximum of 39.5°C in 80 min.

Clearly, these shim adjustments ignore the sample and all the shuttle mobile parts. To obtain an actual value for the field homogeneity correction required for the complete system, we have measured the decay of transverse magnetization for sample **S1** as a function of the variable echo time using the field-cycling version of a spin-echo pulse sequence shown in Figure 3A applied for different values of the current supplied to the Z-shim coil.

Diffusion in a field gradient is, in fact, a well studied phenomenon and analytical equations are readily available (Callaghan, 2011; Cartlidge et al., 2022). These equations basically say that the better the field homogeneity the slower NMR signals will decay. This is shown in Supplementary Figure S29 of Supplementary Material, which reports about a simulation of the phenomenon using recently published methods (Cartlidge et al., 2022). Hence, for the sake of optimising the shim current, one can qualitatively observe which current produces the slower signal decay curve in a single echo experiment with variable echo times. The results of these calibration experiments, run on sample **S1** (see **Materials and Methods** section), for a set of Z-shim coil currents around 3 A, are reported in Figure 3B and show that the best

10.3389/fchem.2023.1229586

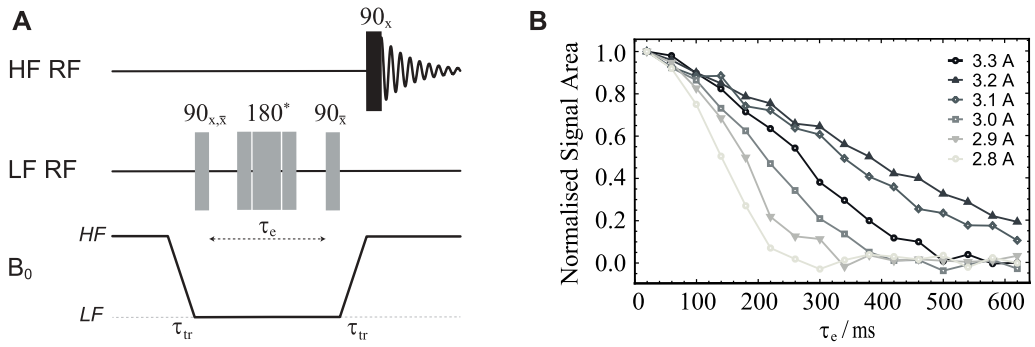

FIGURE 3
(A) Pulse sequence used to optimise the magnetic field homogeneity around the LF sweet spot. The central 180° pulse marked with an asterisk is a composite pulse implemented as $90_x180_y90_x$. The duration of the 90° pulse length was 21.5 μs (obtained as explained below). **(B)** Normalised signal area plotted against the echo time τ_e obtained using the pulse sequence in **(A)** and sample **S1** (see Table 1). The different curves refer to experiments run with different values of electric current in the Z-shim coil (as shown).

TABLE 1 Labeling and composition of samples used in this work.

name	Molecular spy	Solvent	Beads
S1	$^{13}C_1$ sodium pyruvate	D_2O	-
S2	1,2-diphenyl-$^{13}C_2$-acetylene	CD_3CN	-
S3	1,2-diphenyl-$^{13}C_2$-acetylene	CD_3CN	PE (500–600 μm)

shimming is achieved by supplying 3.2 A, as previously measured without the presence of the sample.

Finally, we have checked the sample internal temperature using a sample of ethylene glycol to find that the internal temperature of the sample while in LF is (30.5 ± 0.5) °C, in an experiment involving multiple scans with the longest time spent in low field (2 min, see Figure 11) and a 3 min wait in HF (see Supplementary Material). Note that the sample sits at 25°C while in the HF probe. The heating in LF is due to the heat produced by the shim coil. This can be drastically minimized if the shim corrections are turned *on* during the pulse sequence only and turned *off* while the sample is in HF or during the diffusion time in diffusion experiments.

Pulse calibration

To optimise the pulse length for ^{13}C at 500 kHz Larmor frequency, we used a sample of $^{13}C_1$ sodium pyruvate in D_2O (sample **S1** in Table 1) and the pulse sequence shown in Figure 4A. In these experiments, two transients where collected at each value of the low field pulse duration (β) in order to compensate for magnetization build-up during transport between the low and the high fields. The first HF pulse is absent ($\theta = 0^{\circ}$) during the first transient whereas it becomes a 180° pulse for the second transient. Concomitantly, the receiver's phase is cycled between 0° and 180° between the two transients, effectively subtracting the signal acquired in the two transients. Prior to pulse optimisation, and in order to find the correlation between the nominal and the effective power output of the amplifier, the peak-to-peak voltage produced by the low field amplifier was measured as a function of the spectrometer's power level settings for the channel. Knowing the coil characteristics, we have decided to supply an effective power of 61.6 W, corresponding to a voltage of 55.5 V. According to simulation of the actual coil, this should provide a pulse length of around 20 μs for a 90° pulse.

The results of a pulse calibration obtained using the pulse sequence in Figure 4A and with B_0 inhomogeneities compensation obtained by supplying a 3.2 A current to the Z-shim coil is reported in Figure 4B. Note that the signal is null when the low field pulse is an exact 90° pulse because of the high field 90° pulse placed before acquisition. In this experiment, the transport time τ_{tr} was set to 4 s (much shorter than the sample T_1^{HF} (**S1**) = 65 ±4 s). The resulting value of the 90° pulse length is 21.5 μs and is used for all experiments discussed below.

Note also that, because our setup uses radiofrequency pulses in quite a low field, it is important to estimate the size of the Bloch-Siegert shift (Bloch and Siegert, 1940). This shift results from the counter rotating component of the radiofrequency field and it is generally negligible in most high-field NMR conditions. Essentially, the Bloch-Siegert effect contributes with a term proportional to $\hat{I}_z$ in the spin Hamiltonian. Such term generates an off-resonance effect for the radiofrequency pulse itself, meaning that the pulse rotates the magnetization about an effective axis that is tilted by:

$$\theta_e = ArcTan\left(\frac{\omega_1}{\omega_{BS}}\right) \tag{1}$$

with respect to the direction of static magnetic field. In the previous equation, the term ω_{BS} represents the magnitude of the Bloch-Siegert shift and is calculated as:

$$\omega_{BS} = \frac{\omega_1^2}{4\omega_{rf}} \tag{2}$$

with ω_1 being the angular nutation frequency of the applied radiofrequency field and ω_{rf} its oscillation frequency. In our apparatus, the application of a pulse along the x-axis generates a Bloch-Siegert shift which is calculated to be ω_{BS} = 490.8 Hz. This

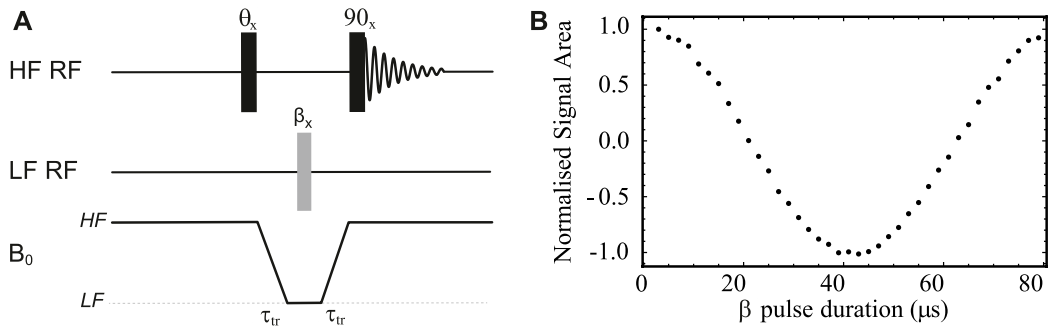

FIGURE 4
(A) Pulse sequence used to calibrate ^{13}C pulse length in the LF probe. **(B)** Low field pulse calibration curves obtained using the pulse sequence in **(A)** and sample **S1** (see Table 1). The optimisation was obtained with a 3.2 A electric current supplied to the Z-shim coil.

TABLE 2 Summary of relaxation decay constant measured in this work. * not supported because not a spin pair, † not measurable because of short T_2. - not measured.

Sample	T_1^{HF} (s)	T_1^{LF} (s)	T_2^{HF} (s)	T_2^{LF} (s)	T_S^{HF} (s)	T_S^{LF} (s)
S1	64 ± 4	70 ± 2	9.5 ± 0.4	16.8 ± 0.6	*	*
S2	16 ± 2	13 ± 1	7.0 ± 0.5	-	325 ± 18	261 ± 38
S3	21 ± 1	20.5 ± 0.3	0.31 ± 0.04	3.9 ± 0.9	†	268 ± 8

corresponds to an effective tilt angle of $\theta_e = 89.6^\circ$ which is negligibly different from the nominal 90° expected for an *x*-axis pulse.

Materials and methods

Sample preparation

Three different samples were used in this paper with the intent to calibrate the new hardware and demonstrate its capabilities.

Sample **S1** was prepared by dissolving 40 mg of $^{13}C_1$ sodium pyruvate in 500 μL of D_2O inside a 5 mm OD Wilmad-Labglass pressure/vacuum valve NMR tube. The molecule was chosen because it gives a single peak and has a long T_1 of 65 ± 4 s at 7.05 T which minimises signal losses during sample transport time. **S1** is used below to calibrate the low field pulse length and to demonstrate measurements of T_1, T_2 and isotropic diffusion in low magnetic field using the new hardware setup operated in field-cycling mode.

For demonstrations involving long-lived spin order, such as the measurement of singlet decay constants, T_S, or singlet-assisted diffusion NMR experiments, we used the singlet-bearing molecule 1,2-diphenyl-$^{13}C_2$-acetylene, first introduced by Feng et al. (2013) and synthesised in house according to the novel procedure described below.

Sample **S2** was prepared by dissolving 21.6 mg of 1,2-diphenyl-$^{13}C_2$-acetylene in 500 μL of acetonitrile-d_3 inside a 5 mm OD Wilmad-Labglass pressure/vacuum valve NMR tube.

Sample **S3** was prepared by dissolving 90 mg of 1,2-diphenyl-$^{13}C_2$-acetylene in 500 μL of acetonitrile-d_3. The solution was poured over polyethylene beads with a diameter distribution of 500–600 μm (purchased from Cospheric CMPS), randomly packed at the bottom of a 10 mm OD Norell High vacuum/pressure tube. The total packing height was 2 cm in order to fully encompass the probe coil region with sufficient excess to ensure that the packing was as uniform as possible across the region of interest. The packing was done by weighing out ca. 0.4 g of the polyethylene beads and adding this to the NMR tube in 2 aliquots. Between each aliquot gentle manual tapping was undertaken and after the addition of all aliquots the sample was manually tapped for 1 min to aid packing. **S3** was intended to serve as a model porous system and is used below to demonstrate the ability of the new hardware to measure the diffusion tensor and other NMR parameters in low magnetic field where the negative effects of susceptibility inhomogeneities, that usually impair those experiments in high field, become negligible. All tubes were modified so that their top valve screws directly into the sample guide rod of the shuttling system. The 10 mm tubes also required modification of the valve to reduce the maximum outer diameter at any point to 9.8 mm as this must pass through the low field probe during shuttling. None of the 3 samples was degassed to remove dissolved oxygen; this is because paramagnetic oxygen dissolved in solution under standard conditions, causes only minor effects on the relaxation times of longitudinal and singlet order in ^{13}C-spin pairs. Table 1 resumes all samples used in this work whereas Table 2 resumes the various decay constants measured on these three sample as explained below.

NMR methods

Measurements of T_1, T_2 and T_S at high field have been done using the following standard methods: inversion recovery (IR),

(Hahn, 1949), carr-purcell-meiboom-gill (CPMG) (Meiboom and Gill, 1958) and magnetisation-to-singlet based methods (M2SS2M), (Pileio et al., 2010), respectively. For measurements in field-cycling mode, ad-hoc pulse sequences were introduced as detailed below. Errors displayed alongside each quantity measured in the experimental section refer to the statistical error from the non-linear regression of the experimental data (the area under the NMR signal acquired in each particular experiments) and are calculated using standard routines in Wolfram Mathematica.

Chemical synthesis

1,2-diphenyl-$^{13}C_2$-acetylene (**III** in Figure 5) was synthesised via Sonogashira reaction of iodobenzene (**I**) with commercially available trimethyl (phenylethynyl-1,2–$^{13}C_2$)silane (99 atom % ^{13}C, Sigma Aldrich) to give trimethyl (phenylethynyl-1,2–$^{13}C_2$) silane (**II**), which was subjected to a one-pot desilylation/ Sonogashira reaction with idodobenzene, resulting in an overall 49% yield. See Supplementary Material for full procedures, characterisation, and spectral data.

Results and discussion

Relaxation of longitudinal order in low magnetic field

Low-field measurements of the decay constant of longitudinal order in low field (T_1^{LF}) were done using the field-cycling version of the inversion recovery pulse sequence shown in Figure 6A. The flip angle of the initial high-field pulse, θ, is cycled between 0° and 180° in two successive transients while the receiver phase alternates between 0° and 180° to compensate for magnetization build up during sample transport. The longitudinal magnetization prepared in the HF probe, inverted or not by the initial θ pulse, is then transferred to LF where a 180° radiofrequency pulse is applied. After a variable time τ_v, the sample is shuttled back to HF where a 90° pulse generates transverse magnetization that is detected in the HF probe. The experiment is repeated for incremental values of the variable time interval τ_v and T_1^{LF} is retrieved by fitting the normalised signal area plotted *versus* τ_v to the function: $s_{T_1^{LF}} = A + Be^{-\tau_v/T_1^{LF}}$, as in conventional IR experiments.

The procedure is demonstrated with the use of sample **S1** and results are plotted in Figure 6B. In these experiments, the sample is polarised in the HF probe for 180 s and shuttled between HF and LF probes in 4 s. The variable time τ_v is incremented between 1 and 512 s in 8 steps. The normalised signal area of the sample's ^{13}C-NMR spectrum acquired in HF is plotted against τ_v in Figure 6B. The experimental points are fitted to $s_{T_1^{LF}}(\tau_v)$ and yielded T_1^{LF} (**S1**) = 70 ± 2 s, which is quite close to the value of T_1^{HF} (**S1**) measured at 7.05 T on the same sample.

Relaxation of transverse order in low magnetic field

The low-field value of the decay constant of transverse order (T_2^{LF}) is measured using the field-cycling version of the carr-

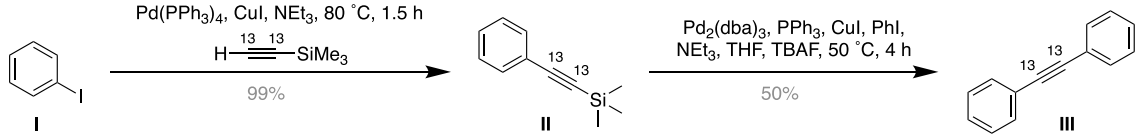

FIGURE 5
Synthetic route used to prepare 1,2-diphenyl-$^{13}C_2$-acetylene.

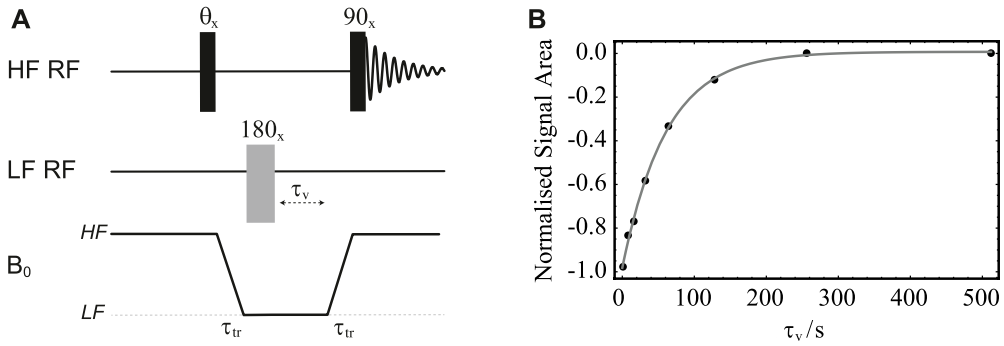

FIGURE 6
(A) Pulse sequence in field-cycling mode used to measure T_1 in LF. **(B)** Normalised signal area under the peak in the ^{13}C-NMR spectrum of sample **S1** acquired in HF plotted against the variable time τ_v. Solid circles are experimental measurements whereas the grey line is the best fit to $s_{T_1^{LF}}$.

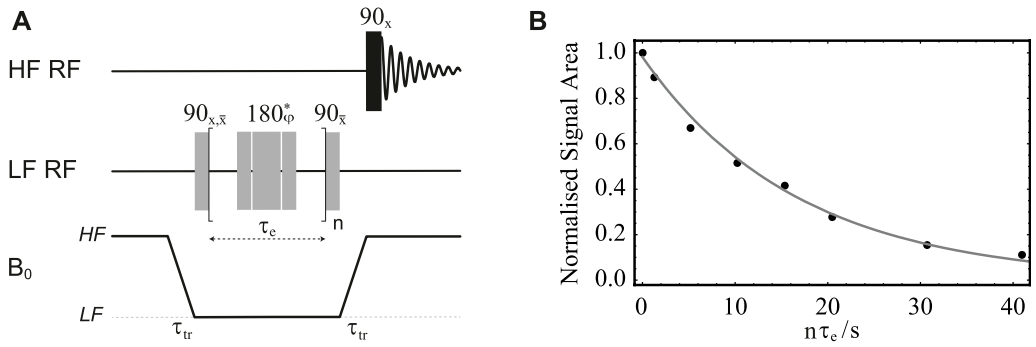

FIGURE 7
(A) Pulse sequence in field-cycling mode used for measurement of T_2 in LF. The central 180° pulse marked with an asterisk is a composite pulse implemented as $90_x180_y90_x$; its overall phase is cycled as $\varphi = \{x, x, \bar{x}, \bar{x}, \bar{x}, \bar{x}, x, x, \bar{x}, \bar{x}, \bar{x}, \bar{x}, x, x, \bar{x}, \bar{x}, x\}$ through the n repetitions. **(B)** Normalised signal area under the peak in the ^{13}C-NMR spectrum of sample **S1** acquired in HF plotted against $n\tau_e$. Solid circles are experimental measurements whereas the grey line is the best fit to $s_{T_2^{LF}}$.

purcell-meiboom-gill pulse sequence shown in Figure 7A. The phase of the initial low field pulse is cycled between 0° and 180° while the receiver phase is alternated between 0° and 180° in two successive transients to compensate for magnetization build up during sample transport. The central 180° pulse is a composite pulse implemented as $90_x180_y90_x$ with its overall phase cycled as $\varphi = \{x, x, \bar{x}, \bar{x}, \bar{x}, x, x, \bar{x}, \bar{x}, \bar{x}, x, x, \bar{x}, \bar{x}, x\}$ through the n echo repetitions. To measure T_2^{LF}, the echo time τ_e is fixed to a small value (10 ms in our case) so to minimise diffusion-induced signal attenuation and the echo block is repeated for a variable number of times, n. After the echo train, transverse magnetization is stored along the field z-direction via a 90° pulse applied in LF. The sample is shuttled back to HF where a signal is detected after the application of a 90° pulse in the HF probe. The normalised signal area of the signal acquired in HF is plotted against $n \times \tau_e$ and the curve is fitted to the exponential decay: $s_{T_2^{LF}}(n\tau_e) = Ae^{-n\tau_e/T_2^{LF}}$, as in conventional CPMG experiments.

The procedure is demonstrated with the use of sample **S1** and results are reported in Figure 7B. In these experiments, the sample is firstly polarised in the HF probe for 180 s. The echo time, τ_e, is fixed to 20 ms and the echo block repeated n times, with n incremented between 1 and 2048 in 8 steps. The sample transport time is set to 4 s. The plot of the normalised signal area acquired in HF *versus* $n\tau_e$ is reported in Figure 7B. The experimental points are fitted to $s_{T_2^{LF}}$ and yielded a value of T_2^{LF} (**S1**) = 16.8 ± 0.6 s. Incidentally, the transverse relaxation decay constant for the same sample in high field was found to be T_2^{HF} (**S1**) = 9.6 ± 0.4 s.

Isotropic diffusion in low magnetic field

To measure molecular diffusion in low field, we have introduced the field-cycling version of the stimulated-echo pulse sequence shown in Figure 8A. The phase of the initial low field pulse is cycled between 0° and 180° while the receiver's phase is alternated between 0° and 180° in two successive transients to compensate for magnetization build up during sample transport. To measure the isotropic diffusion coefficient D_0, one would typically fix the value of the diffusion time Δ and vary the strength of the bipolar gradient g, usually expressed as a percentage of the maximum gradient available. The gradient duration δ is set to be much shorter than Δ and the actual values of Δ and δ are chosen such that the signal decays nicely while g is varied within a suitable interval of the available maximum gradient strength. The gradient g_1 is a spoiler gradient to clean up the signal from unwanted byproducts. The normalised signal area plotted *versus* g is then fitted to the diffusion curve: $s_{D_0} = Ae^{-D_0(\gamma\delta g)^2(\Delta-\delta/3)}$, as in conventional diffusion experiments (Stejskal and Tanner, 1965). If the whole diffusion tensor is required, as in diffusion tensor imaging (DTI) experiments, then the procedure above is repeated for a minimum of 6 times, each time choosing a different direction along which the pulsed field gradient is applied. This is because the diffusion tensor is a symmetric rank-2 tensor with six independent values. The choice of these six directions can be optimised once for all and several optimized set of directions are available in literature. We have chosen to work with the 6 directions obtained via a repulsion algorithm (Jones et al., 1999). The results of the 6 experiments, each containing a number of experimental points resulting from the increment of the value of g along each chosen direction, are then processed together to yield the six independent values of the diffusion tensor following standard procedures (Mori and Toumier, 2013).

Diffusion NMR experiments in low magnetic field are complicated by the effects of concomitant (a.k.a. Maxwell) gradients (Baron et al., 2012). Basically, in order to satisfy Maxwell's laws, magnetic field gradients must have null divergence and curl. Gradient system used in NMR and MRI generally have cylindrical symmetry with coils built to generate a magnetic field pulse (here assumed uniform) along the static magnetic field direction, and whose strength varies along some direction in space. However, according to Maxwell equations, those coils generate the following field vectors (Bernstein et al., 1998; Meier et al., 2008):

$$\begin{aligned}\vec{B}_{G_x} &= \{G_x z,\ 0,\ G_x x\}\\ \vec{B}_{G_y} &= \{0,\ G_y z,\ G_y y\}\\ \vec{B}_{G_z} &= \left\{-\frac{G_z}{2}x,\ -\frac{G_z}{2}y,\ G_z z\right\}\end{aligned} \tag{3}$$

with

$$G_x = \frac{\partial B_z}{\partial x};\quad G_y = \frac{\partial B_z}{\partial y};\quad G_z = \frac{\partial B_z}{\partial z}; \tag{4}$$

This means that by turning on a gradient along x with the intention of producing a magnetic field component that points along z but whose strength varies along the *x*-axis, one necessarily produces magnetic field components pointing along the *x* and *y* directions as well. These unwanted components are known as concomitant or Maxwell gradients. Taking into account the underlying static magnetic field $\vec{B}_S = \{0, 0, B_0\}$, the magnitude of the total field when in presence of a gradient pulse with these characteristics, expanded in a Taylor series truncated to the second order in the gradient strength, is:

$$\begin{aligned}\|\vec{B}_{G_x}\| &= \sqrt{\left(\vec{B}_S + \vec{B}_{G_x}\right)\cdot\left(\vec{B}_S + \vec{B}_{G_x}\right)} \approx B_0 + G_x x + \frac{G_x^2 z^2}{2B_0}\\ \|\vec{B}_{G_y}\| &= \sqrt{\left(\vec{B}_S + \vec{B}_{G_y}\right)\cdot\left(\vec{B}_S + \vec{B}_{G_y}\right)} \approx B_0 + G_y y + \frac{G_y^2 z^2}{2B_0}\\ \|\vec{B}_{G_z}\| &= \sqrt{\left(\vec{B}_S + \vec{B}_{G_z}\right)\cdot\left(\vec{B}_S + \vec{B}_{G_z}\right)} \approx B_0 + G_z z + \frac{G_z^2\left(x^2 + y^2\right)}{8B_0}\end{aligned} \tag{5}$$

Hence, in the presence of a field gradient applied along the *z* direction, the actual magnetic field experienced by a certain molecule in a given position within the sample (to the second order) points slightly off the *z*-axis as dictated by the third line of Eq. 3. Moreover, its magnitude will also contain the undesired terms proportional to x^2 and y^2 as dictated by the third line of Eq. 5. Similar unwanted tilting of the local magnetic field direction and extra terms in its magnitude are present in case of gradients applied along the *x* and *y* directions. The extent of the undesired term is proportional to the ratio between the gradient strength and the static magnetic field. In conventional high field experiments, where the static magnetic field is of the order of a few Tesla and the maximum available gradient strengths are of the order of a Tesla per meter, the effect of Maxwell gradients are negligible. In our current setup, instead, the field gradients are applied in a magnetic field of 46.4 mT and the maximum gradient strength available is 1.5 T m^{-1}. Assuming the NMR sample is 20 mm long and centred in the LF sweet spot, the field experienced by spins located 10 mm above the LF sweet spot is calculated to be 62.4 mT when the gradient is applied at full strength. In those circumstances, the total magnetic field is tilted by about 10° away from the *z*-axis. To mitigate these phenomena the maximum gradient strength used in LF must be limited. The same calculations above redone for a maximum gradient strength of 75 mT m^{-1} (5% of the maximum available in our hardware) would result in a field intensity of 47.1 mT for spins located 10 mm above the LF sweet spot and the tilt angle away from the *z*-axis would only be 0.6°. In order to perform NMR diffusion experiments with gradients ranging from 0 to a maximum of 75 mT m^{-1} one has to increase either (or both) the diffusion time (Δ in Figure 8A) or the gradient pulse duration (*δ* in Figure 8A). The relaxation time of longitudinal spin order, T_1, sets a limit to the maximum useable value of Δ while the value of *δ* must be kept much smaller than Δ to fulfill the approximations which underpins the theoretical description of diffusion-NMR experiments (Callaghan, 2011).

Fortunately, in singlet assisted diffusion NMR, Δ can be of the order of many tens of seconds while *δ* can remain in the milliseconds regime. Hence, gradient strengths of a few mT m^{-1} can provide meaningful diffusion information despite the presence of concomitant gradients. This is yet another important feature of long-lived spin order and singlet-assisted diffusion NMR.

Before introducing singlet-assisted diffusion NMR experiments, though, we demonstrate how the new hardware can be used to measure the diffusion tensor with the use of the pulse sequence in Figure 8A and sample **S1**. For this experiment, the sample was polarised in HF for 180 s and then transported in LF with a transport time of 4 s. The diffusion time Δ was set to 300 ms and the duration of the diffusion gradient, *δ* was set to 20 ms. The gradient g_1 had a duration of 2 ms and a strength of 0.26 T m^{-1} and was applied along the negative *z* direction. The diffusion gradient *g* was varied from 15 to 150 mT m^{-1} (1%–10% of the available maximum) in 8 linearly

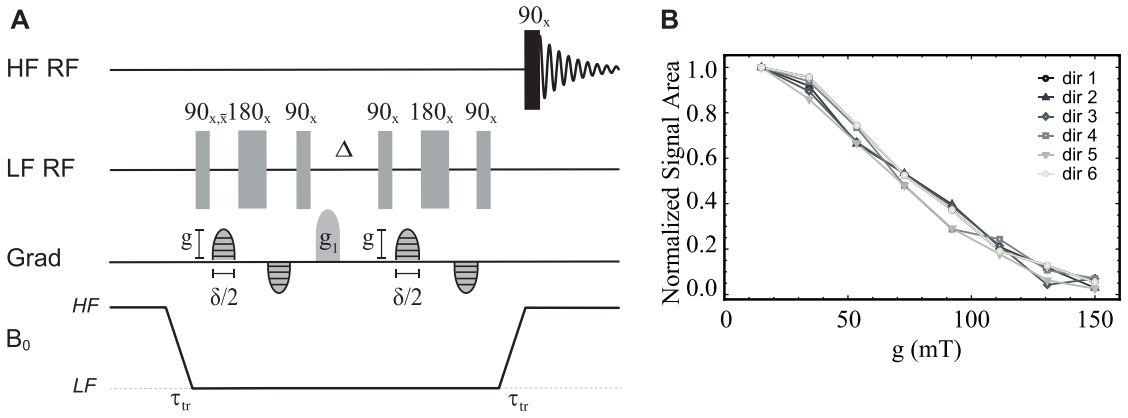

FIGURE 8
(A) Pulse sequence in field-cycling mode used for measurement of diffusion in LF. **(B)** Normalised signal area under the peak in the ^{13}C-NMR spectrum of sample **S1** acquired in HF plotted against the gradient strength *g*. Solid lines are added as a guide for the eyes.

TABLE 3 The x, y and z component (d_x, d_y, d_z) of the unitary vectors pointing along the six direction of space optimised according to a repulsion algorithm in Jones et al., (1999) and used for diffusion tensor imaging experiments in this paper.

	dir 1	dir 2	dir 3	dir 4	dir 5	dir 6
d_x	1.000	0.447	0.447	0.447	0.447	−0.447
d_y	0.000	0.895	0.277	−0.724	−0.724	−0.277
d_z	0.000	0.000	0.850	−0.525	0.525	0.850

spaced values. The whole experiment was repeated 6 times with the gradient g each time applied along a different direction (see Table 3), optimised using a repulsion algorithm in Jones et al., (1999).

The normalised signal area of sample **S1**'s ^{13}C-NMR spectrum acquired in HF is plotted against g for all six directions in Figure 8B.

As expected in the case of isotropic diffusion, all six directions give curves that are identical within error. This is because in isotropic solutions unrestricted molecular diffusion is the same in any direction of space. Furthermore, the 48 experimental points, 8 per direction, were fitted together to yield a nearly spherical diffusion tensor with a fractional anisotropy FA(**S1**) = 0.07 ± 0.02 and an isotropic diffusion coefficient D_0(**S1**) = (6.4 ± 0.2) × 10^{-10} m s^{-2}. The small but not exactly zero value of fractional anisotropy is likely due to small differences in the gradient performances along the different directions, which is typically observed in DTI experiments and can be calibrated for. The measured value of the diffusion coefficient falls in the expected range for a small molecule in deuterated water solutions. When the same experiment is repeated using Δ = 150 ms, δ = 2 ms and g varied from 15 to 1,500 mT m^{-1} (1%–100% of the available maximum) the resulting diffusion curves cannot be fitted to the diffusion curve because of the effect of concomitant gradients (not shown).

Relaxation of singlet order in porous systems

As briefly explained in the introduction, measuring the lifetime of singlet spin order in a sample containing a porous matrix in high magnetic fields is complicated, and often made impossible, by the mismatch between the magnetic susceptibility of the material constituting the porous structure and the one of the imbibed liquid. These susceptibility inhomogeneities, even if just of the order of a few part-per-millions, generates a T_2-like mechanism that relaxes transverse magnetisation in milliseconds (Cartlidge et al., 2022) and leaves no time to generate singlet spin order because this typically requires hundreds' of milliseconds (Carravetta et al., 2004; Carravetta and Levitt, 2004; DeVience et al., 2013; Kiryutin et al., 2013; Theis et al., 2014; Pileio, 2020). Our group is particularly interested in exploiting the extended lifetime of singlet order to measure the diffusion tensors and tortuosity in porous media. For this, access to the long-lived singlet states of a "spy" molecule imbibed within the pores of the medium is fundamental. Fortunately, the relaxation phenomena due to spin diffusing in porous media are field dependent and become negligible in low magnetic field. This very fact is what has driven the development of the dual-core equipment described in this paper.

As a first demonstration of the new opportunities offered by our hardware, we measured the low field value of the decay constant of singlet spin order (T_S^{LF}) in a sample where singlet-bearing molecules diffuse between the pores of a random packing of spherical beads (sample **S3**). Long-lived singlet order can be created in virtually any two-spin-1/2 system where the two spins are inequivalent. However, it is much more convenient to work with nearly-equivalent spin pairs because in such a case the singlet order is almost an eigenstate of the spin Hamiltonian and therefore its does not need to be sustained by transport in low-field (Carravetta et al., 2004) or radiofrequency irradiation (Carravetta and Levitt, 2004). Spin inequivalence can be of chemical or magnetic nature. In chemically inequivalent spin pairs, we have a difference in chemical shift between the two spins; to have a nearly-chemically-equivalent spin pair we need the difference in chemical shift frequency between the two nuclei ($|\omega_1 - \omega_2|$) to be much smaller than their mutual scalar coupling (J_{12}), i.e., $|\omega_1 - \omega_2| \ll J_{12}$. In magnetically inequivalent pairs, we have a different scalar coupling between the two spins and a remote third spin in the molecule; to have a nearly-magnetically-equivalent spin pair, we need the difference in the scalar coupling between each spin in the pair and the third nucleus ($|J_{13}$-$J_{23}|$) to be much smaller than their mutual scalar coupling (J_{12}), i.e., $|J_{13} - J_{23}| \ll J_{12}$. In the context of this work, it is more convenient to work with nearly-magnetically-equivalent spin pair. This is because the parameters to access the singlet order will not change between HF and LF. Conversely, nearly-chemical-equivalence is field dependent because this relies on the chemical shift frequency. The two ^{13}C labels introduced in compound **III** (see Figure 5) constitute a nearly-magnetically-equivalent spin pair through their small scalar coupling to the protons in ortho on the ring. The scalar coupling between the two ^{13}C nuclei is $J_{C_1C_2}$ = 182 Hz, whereas the scalar coupling between the ^{13}C nuclei and the protons in ortho are $J_{C_1H_o}$ = 5.5 Hz and $J_{C_2H_o}$ = −0.6 Hz. (Feng et al., 2013). The scalar couplings with the protons in meta and para are very small and can be effectively neglected.

To calibrate the parameters to access singlet order and to have a reference value for the singlet order decay constant in a non-porous system, we have first conducted experiments using sample **S2**. For the actual measurement of T_S^{LF} we have produced a version of the M2SS2M pulse sequence adapted to work in field-cycling mode on our equipment. A sketch of the pulse sequence is reported in Figure 9A. The sample is first polarised in HF and then shuttled to LF where a first 90° pulse creates transverse polarization. The phase of this pulse in cycled between 90° and 270° while the receiver phase is also cycled between 90° and 270° across two successive transients so to compensate for polarization buildup during both τ_v and transport. The M2S block has been described in detail elsewhere (Pileio et al., 2010). It converts transverse magnetisation into singlet order through a train of spin echoes synchronised with the spin system's parameters. To maximise efficiency, theory predicts that the echo time must be set to $\tau_e = 1/(4(J_{12}^2 + (J_{13} - J_{23})^2)^{1/2})$ and the number of echoes to $n_1 = \pi/(2\ ArcTan(J_{13} - J_{23}/J_{12}))$ with $n_2 = n_1/2$ (Feng et al., 2013). The central 180° pulse in the M2S block is a composite pulse implemented as $90_x180_y90_x$ with its overall phase cycled as $\varphi = \{x, x, \bar{x}, \bar{x}, \bar{x}, \bar{x}, x, x, \bar{x}, \bar{x}, \bar{x}, \bar{x}, x, x, \bar{x}, \bar{x}, x, x\}$ through the n_1 and n_2 repetitions. After a variable time, τ_v (incremented in a series of experiments to measure the singlet order decay constant), a

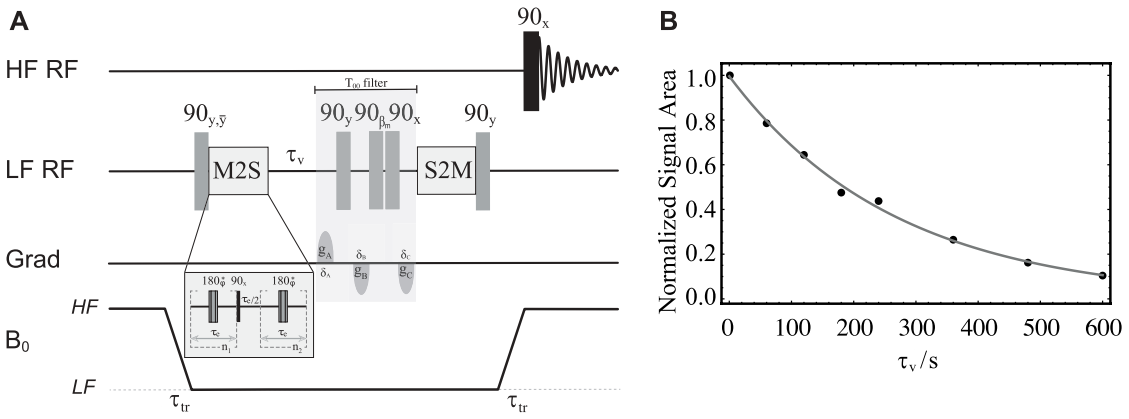

FIGURE 9
(A) Pulse sequence in field-cycling mode used for measurement of T_S in LF. **(B)** Solid circles are experimental normalised signal areas acquired in HF and plotted against the variable time τ_v. The solid gray line is the best fit to s_{T_S}.

T_{00} filter is used to filter out unwanted byproducts (Pileio, 2020). The S2M block that follows is the time reverse of the M2S and converts singlet order back to transverse magnetization. This latter is stored along the static magnetic field direction by the last 90° pulse in LF. The sample is then transported back to HF for a 90° pulse and successive signal detection.

To calibrate the value of τ_e and n_1 required by the pulse sequence in Figure 9A, we run a train of synchronised spin echoes where we varied τ_e and n_1, in turn, and around the theoretical values obtained using the equations above and the experimental values of the scalar couplings involved therein. Note that since the magnetic inequivalence does not depends on the value of the static magnetic field, these optimisations can be done either in HF or in LF. This calibration, run on sample **S2** in HF, returned the following values: τ_e = 2.75 ms, n_1 = 48 (and $n_2 = n_1/2 = 24$). These values were then used to measure a T_S^{LF} (**S2**) = 261 ± 38 s. In these experiments, the transport time was fixed to 3 s and the variable time τ_v was incremented from 1 to 600 s in 8 steps. The value of T_S^{LF} we found is consistent with the one reported by Feng et al. (2013) for the same molecule (there measured at a different field and in a different solvent). Incidentally, we measured a value of T_1^{LF}(**S2**) = 13 ± 1 s for the same sample and using the pulse sequence in Figure 6A. The longitudinal order decay constant for the same sample but measured in high field was T_1^{HF}(**S2**) = 16 ± 2 s. The singlet order dacay constant in high field was T_S^{HF} (**S2**) = 325 ± 18 s.

Successively, using the same pulse sequence in Figure 9A and the values of τ_e and n_1 taken from the optimization above, the value of T_S^{LF} was measured for sample **S3** as a model for porous media applications. For this experiment, the transport time was fixed to 3 s and the variable time τ_v was incremented from 1 to 600 s in 8 steps. The resulting experimental normalised signal areas are shown as solid circles in Figure 9B. These were fitted to the exponential decay curve $s_{T_S^{LF}} = Ae^{-\tau_v/T_S^{LF}}$ to yield a singlet decay time constant of T_S^{LF}(**S3**) = 268 ± 8 s, which is consistent, within errors, with the value earlier found for sample **S2**, thus confirming that the singlet order decay constant is unaffected by the presence of the beads. Note that the smaller error in the measurement of T_S^{LF} for **S3** (compared to what obtained for **S2**) may be due to the presence, in **S3**, of the beads that stop thermal convection. Also note that such an experiment cannot be performed in HF since the susceptibility difference of 2.8 ppm, between the PE beads and the acetonitrile solution, is responsible for a very short T_2 in HF, T_2^{HF}(**S3**) = 0.31 ± 0.04 s. Incidentally, we measured a value of T_1^{LF}(**S3**) = 20.5 ± 0.3 s for the same sample.

Singlet-assisted diffusion NMR in porous media

As a final example, we have addressed the problem of measuring diffusion in porous media and in the long-time regime, i.e., when the diffusion time is long enough so that molecules can travel, on average, for much longer distances than the average pore size. These experiments provide important information such as structural anisotropy, shape and orientation of cavities and channels, as well as tortuosity, i.e., a measure of how difficult is for a diffusing molecule to cover a certain distance as it moves across the pores of a porous structure.

The pulse sequence introduced to measure the diffusion of singlet-bearing molecules imbibed in porous media is shown in Figure 10. It is a version of the singlet-assisted-diffusion NMR sequence presented in Tourell et al. (2018), here adapted to work in field-cycling mode. Recalling the discussion above regarding the pulse sequence in Figure 9A, and in analogy with the more conventional stimulated echo sequence (STE), the pulse sequence in Figure 10 marks molecular positions with a bipolar gradient placed during the last echo of the n_1 train of the M2S block (now labelled as PFG-M2S to outline the presence of the pulsed field gradient). After storage of the magnetisation as long-lived spin order, molecular positions are decoded through the use of an additional bipolar pulsed field gradient placed during the first echo of the n_1 train of the S2M block. The distance between the two bipolar gradients is the diffusion time, Δ. Because molecular position is stored as long-lived singlet order, the diffusion time is amenable to be minutes long rather than the few seconds allowed by longitudinal order exploited in STE experiments.

As for all other pulse sequences introduced in this paper, magnetization is stored along the static magnetic field direction

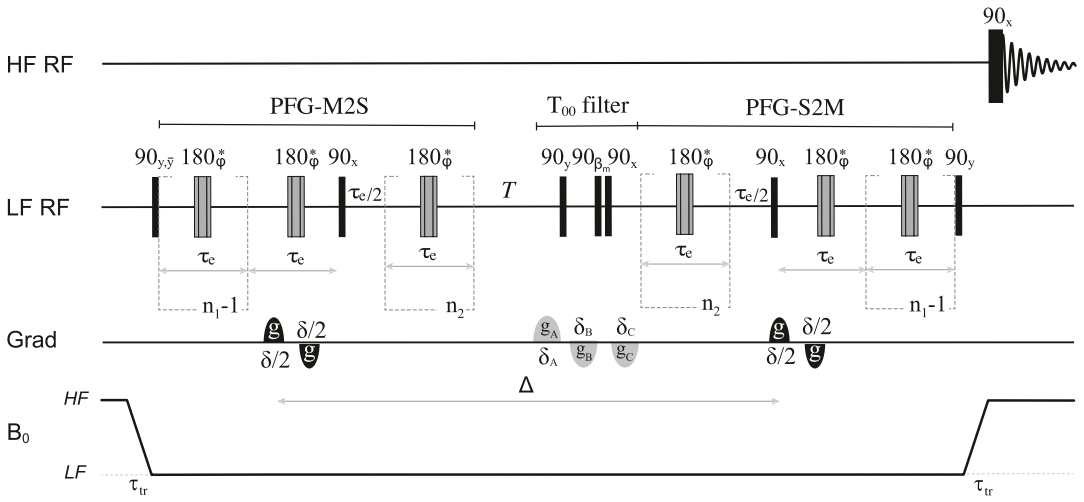

FIGURE 10
Pulse sequence used for singlet-assisted diffusion experiments in a field-cycling mode.

before transport to HF, and detection is achieved following a 90° pulse in the HF probe. To measure diffusion along a given direction, the bipolar pulses are applied along the chosen direction. To retrieve the whole diffusion tensor, the same experiment is repeated with bipolar pulsed field gradients applied along a minimum of 6 independent directions. Finally, to measure tortuosity along a certain direction of space, the diffusion coefficient is measured as a function of the diffusion time Δ to obtain $D(\Delta)$. The ratio $D(\Delta)/D_0$ tends to the tortuosity value as Δ tends to infinity (Latour et al., 1993). In practice, an asymptotic value of $D(\Delta)/D_0$ is reached once the diffusion time is long enough for molecules to travel across many pores and probe a representative part of the structure.

In Figure 11 we report the result of a set of low-field measurements of the ratio $D(\Delta)/D_0$ for sample **S3** and for several values of the diffusion time. In these experiments, we set τ_e = 2.75 ms and n_1 = 48 from the optimization above. The transport time was fixed to 3 s. The duration of the bipolar gradient, δ, was set to 2 ms while Δ was varied from 2.5 to 120 s as shown in Figure 11. For each value of Δ, the gradient strength of the bipolar gradients, g, was varied in 4 steps and within a range that is different for different values of Δ, and chosen so to have a good sampling of the diffusion equation while keeping the maximum strength low enough to avoid the above discussed complications due to concomitant gradients. Namely, g was ranging within the interval 1%–15% for Δ = 2.5 s and within the interval 1%–3% for Δ = 120 s, with the percentage figure referring to the percentage of the maximum available gradient (1.5 T m^{-1}). The bipolar gradients were applied along the z-direction. As expected, the ratio $D_{zz}(\Delta)/D_0$, plotted in Figure 11, reaches an asymptotic value as Δ is increased. Such limiting value corresponds to the tortuosity of the system. Depending on the porosity and the looseness of the packing, tortuosity varies in randomly-packed-bead systems; simulations done on systems with porosity between 0.36 and 0.46 and for various methods of packings, give a tortuosity value that varies within 0.71–0.76 (Khirevich et al., 2011). Our experimental value of 0.71 (dotted line in Figure 11) falls in the right interval, although we have not properly characterised our packing because this is beyond the scope of this paper.

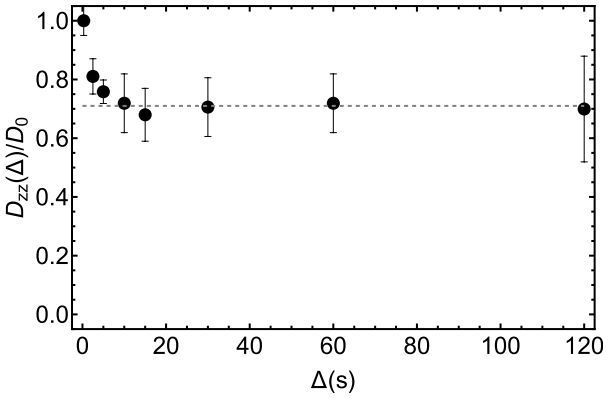

FIGURE 11
Experimental measurements of the diffusion coefficient along the z-direction in the LF probe obtained by using the pulse sequence in Figure 10 and for different values of the diffusion time, Δ. The dashed gray line has been added to guide the eyes towards the asymptotic value of the experimental tortuosity.

Finally, we have used the pulse sequence in Figure 10 to measure the full diffusion tensor in LF and for two different values of Δ, namely, 2 s and 30 s. For these experiments we have used the parameters: τ_e = 2.75 ms, n_1 = 48, n_2 = 24, τ_{tr} = 3 s, δ = 2 ms. The gradient strength, g was varied in 4 steps between 1% and 15% of the maximum for Δ = 2 s and between 1% and 6% for Δ = 30 s. For each value of Δ, the bipolar gradients were applied, in successive experiments, along the six different directions of space reported in Table 3. The 24 (six times four) points were fitted together to reconstruct the whole diffusion tensor according to established procedures (Basser et al., 1994; Mori and Toumier, 2013). The tensor was then diagonalised to obtain the diffusion coefficient along the three principal direction of diffusion. The diagonalised experimental diffusion tensors so derived are:

$$\mathbf{D}'(\mathbf{S3}, 2\,\mathrm{s}) = \begin{pmatrix} 1.1 \pm 0.3 & 0 & 0 \\ 0 & 1.2 \pm 0.1 & 0 \\ 0 & 0 & 1.5 \pm 0.2 \end{pmatrix} \times 10^{-9}\mathrm{m}^2\ \mathrm{s}^{-1} \quad (6)$$

with an associated fractional anisotropy FA(**S3**) = 0.14 and:

$$\mathbf{D}'(\mathbf{S3}, 30\,\mathrm{s}) = \begin{pmatrix} 0.70 \pm 0.08 & 0 & 0 \\ 0 & 0.96 \pm 0.01 & 0 \\ 0 & 0 & 1.3 \pm 0.2 \end{pmatrix} \times 10^{-9}\mathrm{m}^2\ \mathrm{s}^{-1} \quad (7)$$

with an associated fractional anisotropy FA(**S3**) = 0.30. As expected, the value of FA for the structure becomes more apparent when the experiment is done at larger Δ. By taking the ratios between the diffusion coefficients along the same principal direction but for different value of Δ, namely, $D'_{\alpha\alpha}(30\,\mathrm{s})/D'_{\alpha\alpha}(2\,\mathrm{s})$, one gets 0.64, 0.80 and 0.87 for the principal x-, y- and z-directions, respectively. This highlights how tortuosity is different along different directions of space and how this information can be retrieved by measuring the full diffusion tensor as a function of the diffusion time.

Conclusion

In this paper, we have presented a new hardware development consisting in a dual-core NMR spectrometer with high-resolution detection facility in high field (7.05 T) and both radiofrequency and 3-axis gradient facilities in low field (46.4 mT). The hardware is complemented by a sample shuttle with precision 3-axis positioning to work in field cycling mode. The equipment is fully controlled by the spectrometer console through the pulse programs and it has been mainly developed to perform diffusion experiments in porous materials. These kind of experiments in porous media are usually impaired (and often invalidated) by the short decay time of the transverse spin magnetization resulting from magnetic susceptibility inhomogeneities between the medium and the imbibed solution. Because such effect is field dependent, the ability to use RF and field pulse gradients in low field, while retaining the high field facility for sample polarisation and detection, makes those experiments now doable in our apparatus. After presenting the hardware, we have discussed a series of calibration procedures and examples of experiments that can be performed on it, namely, measurement of T_1 and T_2 relaxation decay constants, as well as diffusion in one or multiple directions. Moreover, we showed how this new hardware gives access to manipulations of long-lived spin order in porous media (previously impossible where susceptibility inhomogeneities are larger than a few ppm's) by measuring the relaxation decay constant of singlet spin order in a test sample where molecules are diffusing within randomly-packed plastic beads. Additionally, we demonstrated how the new hardware gives unprecedented access to tortuosity and whole diffusion tensors in porous media. This information is of relevance in several disciplines such as material science and biology. For example, we plan to use this new hardware to measure diffusion and tortuosity within the gas-diffusion-layer of fuel cells. Such experimental data are relevant, for example, for simulations of fuel cells functionalities. We are also working on using this new hardware to measure diffusion and tortuosity in biological tissues obtained by growing cells on 3D-printed scaffoldings. Information on those systems are relevant to the field of tissue engineering either in tissue regeneration applications or for the characterisation of 3D models of cancer.

Data availability statement

The original contributions presented in the study are included in the article/Supplementary Material, further inquiries can be directed to the corresponding author.

Author contributions

TR: Build and Design of Equipment, Conceptualisation, Experiments, Data analysis, Writing—Review and Editing; RB, ST: Chemical synthesis, Writing—Review and Editing; TC: Numerical simulations and Data Analysis; TH, SB, KZ, and FE: Design and Manufacturing of low-field probe, Conceptualisation. GP: Conceptualization, Methodology, Experiments, Supervision, Validation, Funding Acquisition, Writing—original draft, Writing—Review and Editing. All authors contributed to the article and approved the submitted version.

Funding

The Leverhulme Trust supported this project through the Research Project Grant RPG-2019-298; The EPSRC United Kingdom supported this project through the grant EP/N033558/1.

Acknowledgments

We are very grateful to The Leverhulme Trust and EPSRC United Kingdom for supporting this project through the Research Project Grants RPG-2019-298 (LT) and EP/N033558/1 (EPSRC). We thank Alan Glass, Haydn Glass, Dr. Andrew Hall and Dr. Weidong Gong for technical support.

Conflict of interest

TH, SB, KZ, and FE were employed by Bruker Biospin GmbH.

The remaining authors declare that the research was conducted in the absence of any commercial or financial relationships that could be construed as a potential conflict of interest.

Publisher's note

Supplementary material

The Supplementary Material for this article can be found online at: https://www.frontiersin.org/articles/10.3389/fchem.2023.1229586/full#supplementary-material

References

Anoardo, E., Galli, G., and Ferrante, G. (2001). Fast-field-cycling NMR: Applications and instrumentation. *Appl. Magn. Reson.* 20, 365–404. doi:10.1007/bf03162287

Baron, C. A., Lebel, R. M., Wilman, A. H., and Beaulieu, C. (2012). The effect of concomitant gradient fields on diffusion tensor imaging. *Magn. Reson. Med.* 68, 1190–1201. doi:10.1002/mrm.24120

Basser, P., Mattiello, J., and Lebihan, D. (1994). Estimation of the effective self-diffusion tensor from the NMR spin echo. *J. Magn Reson. Ser. B* 103, 247–254. doi:10.1006/jmrb.1994.1037

Bernstein, M. A., Zhou, X. J., Polzin, J. A., King, K. F., Ganin, A., Pelc, N. J., et al. (1998). Concomitant gradient terms in phase contrast MR: Analysis and correction. *Magn. Reson. Med.* 39, 300–308. doi:10.1002/mrm.1910390218

Bloch, F., and Siegert, A. (1940). Magnetic resonance for nonrotating fields. *Phys. Rev.* 57, 522–527. doi:10.1103/physrev.57.522

Broche, L. M., Ross, P. J., Davies, G. R., MacLeod, M.-J., and Lurie, D. J. (2019). A whole-body Fast Field-Cycling scanner for clinical molecular imaging studies. *Sci. Rep.* 9, 10402. doi:10.1038/s41598-019-46648-0

Callaghan, P. T. (1991). *Principles of nuclear magnetic resonance microscopy*. Oxford: Clarendon Press.

Callaghan, P. T. (2011). *Translational dynamics and magnetic resonance: Principles of pulsed gradient spin echo NMR*. Oxford University Press.

Carravetta, M., and Levitt, M. H. (2004). Long-lived nuclear spin states in high-field solution NMR. *J. Am. Chem. Soc.* 126, 6228–6229. doi:10.1021/ja0490931

Carravetta, M., Johannessen, O. G., and Levitt, M. H. (2004). Beyond the T1 limit: Singlet nuclear spin states in low magnetic fields. *Phys. Rev. Lett.* 92, 153003. doi:10.1103/physrevlett.92.153003

Cartlidge, T. A. A., Robertson, T. B. R., Utz, M., and Pileio, G. (2022). Theory and simulation framework for the relaxation of nuclear spin order in porous media. *J. Phys. Chem. B* 126, 6536–6546. doi:10.1021/acs.jpcb.2c03575

Cavadini, S., and Vasos, P. R. (2008). Singlet states open the way to longer time-scales in the measurement of diffusion by NMR spectroscopy. *Concepts Magn. Reson. Part A* 32A, 68–78. doi:10.1002/cmr.a.20100

Cavadini, S., Dittmer, J., Antonijevic, S., and Bodenhausen, G. (2005). Slow diffusion by singlet state NMR spectroscopy. *J. Am. Chem. Soc.* 127, 15744–15748. doi:10.1021/ja052897b

Charlier, C., Khan, S. N., Marquardsen, T., Pelupessy, P., Reiss, V., Sakellariou, D., et al. (2013). Nanosecond time scale motions in proteins revealed by high-resolution NMR relaxometry. *J. Am. Chem. Soc.* 135, 18665–18672. doi:10.1021/ja409820g

Chou, C.-Y., Chu, M., Chang, C.-F., and Huang, T.-H. (2012). A compact high-speed mechanical sample shuttle for field-dependent high-resolution solution NMR. *J. Magn. Reson.* 214, 302–308. doi:10.1016/j.jmr.2011.12.001

Cousin, S. F., Charlier, C., Kadeřávek, P., Marquardsen, T., Tyburn, J.-M., Bovier, P.-A., et al. (2016). High-resolution two-field nuclear magnetic resonance spectroscopy. *Phys. Chem. Chem. Phys.* 18, 33187–33194. doi:10.1039/c6cp05422f

DeVience, S. J., Walsworth, R. L., and Rosen, M. S. (2013). Preparation of nuclear spin singlet states using spin-lock induced crossing. *Phys. Rev. Lett.* 111, 173002. doi:10.1103/physrevlett.111.173002

Dumez, J.-N., Hill-Cousins, J. T., Brown, R. C. D., and Pileio, G. (2014). Long-lived localization in magnetic resonance imaging. *J. Magn. Reson.* 246, 27–30. doi:10.1016/j.jmr.2014.06.008

Feng, Y., Theis, T., Liang, X., Wang, Q., Zhou, P., and Warren, W. S. (2013). Storage of hydrogen spin polarization in long-lived 13C2 singlet order and implications for hyperpolarized magnetic resonance imaging. *J. Am. Chem. Soc.* 135, 9632–9635. doi:10.1021/ja404936p

Hahn, E. L. (1949). An accurate nuclear magnetic resonance method for measuring spin-lattice relaxation times. *Phys. Rev.* 76, 145–146. doi:10.1103/physrev.76.145

Hall, A. M., Cartlidge, T. A., and Pileio, G. (2020). A temperature-controlled sample shuttle for field-cycling NMR. *J. Magnetic Reson.* 317, 106778. doi:10.1016/j.jmr.2020.106778

Jones, D. K., Horsfield, M. A., and Simmons, A. (1999). Optimal strategies for measuring diffusion in anisotropic systems by magnetic resonance imaging. *Magn. Reson. Med.* 42, 515–525. doi:10.1002/(sici)1522-2594(199909)42:3<515::aid-mrm14>3.0.co;2-q

Khirevich, S., Holtzel, A., Daneyko, A., Seidel-Morgenstern, A., and Tallarek, U. (2011). Structure-transport correlation for the diffusive tortuosity of bulk, monodisperse, random sphere packings. *J. Chromatogr. A* 1218 (37), 6489–6497. doi:10.1016/j.chroma.2011.07.066

Kimmich, R., and Anoardo, E. (2004). Field-cycling NMR relaxometry. *Prog. Nucl. Magn. Reson. Spectrosc.* 44, 257–320. doi:10.1016/j.pnmrs.2004.03.002

Kiryutin, A. S., Ivanov, K. L., Yurkovskaya, A. V., Vieth, H.-M., and Lukzen, N. N. (2013). Manipulating spin hyper-polarization by means of adiabatic switching of a spin-locking RF-field. *Phys. Chem. Chem. Phys.* 15, 14248–14255. doi:10.1039/c3cp52061g

Latour, L. L., Mitra, P. P., Kleinberg, R. L., and Sotak, C. H. (1993). Time-dependent diffusion-coefficient of fluids in porous- media as a probe of surface-to-volume ratio. *J. Magn. Reson. A* 101, 342–346. doi:10.1006/jmra.1993.1056

Meiboom, S., and Gill, D. (1958). Modified spin-echo method for measuring nuclear relaxation times. *Rev. Sci. Instrum.* 29, 688–691. doi:10.1063/1.1716296

Meier, C., Zwanger, M., Feiweier, T., and Porter, D. (2008). Concomitant field terms for asymmetric gradient coils: Consequences for diffusion, flow, and echo-planar imaging. *Magn. Reson. Med.* 60, 128–134. doi:10.1002/mrm.21615

Merboldt, K.-D., Hanicke, W., and Frahm, J. (1985). Self-diffusion NMR imaging using stimulated echoes. *J. Magnetic Reson.* 64, 479–486. doi:10.1016/0022-2364(85)90111-8

Mori, S., and Toumier, J. D. (2013). *Introduction to diffusion tensor imaging: And higher order models*. Second edition. Amsterdam: Elsevier Inc.

Morris, G. A. (2009). *eMagRes*. John Wiley and Sons, Ltd.

Pileio, G., and Ostrowska, S. (2017). Accessing the long-time limit in diffusion NMR: The case of singlet assisted diffusive diffraction q-space. *J. Magn. Reson.* 285, 1–7. doi:10.1016/j.jmr.2017.10.003

Pileio, G., Carravetta, M., and Levitt, M. H. (2010). Storage of nuclear magnetization as long-lived singlet order in low magnetic field. *Proc. Natl. Acad. Sci.* 107, 17135–17139. doi:10.1073/pnas.1010570107

Pileio, G., Dumez, J.-N., Pop, I.-A., Hill-Cousins, J. T., and Brown, R. C. D. (2015). Real-space imaging of macroscopic diffusion and slow flow by singlet tagging MRI. *J. Magn. Reson.* 252, 130–134. doi:10.1016/j.jmr.2015.01.016

Pileio, G. (2017). Singlet NMR methodology in two-spin-1/2 systems. *Prog. Nucl. Magn. Reson. Spectrosc.* 98-99, 1–19. doi:10.1016/j.pnmrs.2016.11.002

Pileio G. (Editor) (2020). *Long-lived nuclear spin order: Theory and applications* (London, UK: Royal Society of Chemistry).

Redfield, A. G. (2003). Shuttling device for high-resolution measurements of relaxation and related phenomena in solution at low field, using a shared commercial 500 MHz NMR instrument. *Magn. Reson. Chem.* 41, 753–768. doi:10.1002/mrc.1264

Sarkar, R., Vasos, P. R., and Bodenhausen, G. (2007a). Singlet-state exchange NMR spectroscopy for the study of very slow dynamic processes. *J. Am. Chem. Soc.* 129, 328–334. doi:10.1021/ja0647396

Sarkar, R., Ahuja, P., Moskau, D., Vasos, P. R., and Bodenhausen, G. (2007b). Extending the scope of singlet-state spectroscopy. *ChemPhysChem* 8, 2652–2656. doi:10.1002/cphc.200700545

Stejskal, E. O., and Tanner, J. E. (1965). Spin diffusion measurements: Spin echoes in the presence of a time-dependent field gradient. *J. Chem. Phys.* 42, 288–292. doi:10.1063/1.1695690

Swanson, S., and Kennedy, S. (1993). A sample-shuttle nuclear-magnetic-relaxation-dispersion spectrometer. *J. Magn. Reson. Ser. A* 102, 375–377. doi:10.1006/jmra.1993.1121

Theis, T., Feng, Y., Wu, T., and Warren, W. S. (2014). Composite and shaped pulses for efficient and robust pumping of disconnected eigenstates in magnetic resonance. *J. Chem. Phys.* 140, 014201. doi:10.1063/1.4851337

TomHon, P., Akeroyd, E., Lehmkuhl, S., Chekmenev, E. Y., and Theis, T. (2020). Automated pneumatic shuttle for magnetic field cycling and parahydrogen hyperpolarized multidimensional NMR. *J. Magn. Reson.* 312, 106700. doi:10.1016/j.jmr.2020.106700

Torres, A. M., Ghadirian, B., and Price, W. S. (2012). Diffusion–diffraction using singlet spin states and various NMR coherences in a J-coupled AX spin system. *RSC Adv.* 2, 3352–3360. doi:10.1039/c2ra20063e

Tourell, M. C., Pop, I.-A., Brown, L. J., Brown, C. D. T., and Pileio, G. (2018). Singlet-assisted diffusion-NMR (SAD-NMR): Redefining the limits when measuring tortuosity in porous media. *Phys. Chem. Chem. Phys.* 20, 13705–13713. doi:10.1039/c8cp00145f

Yadav, N. N., Torres, A. M., and Price, W. S. (2010). NMR q-space imaging of macroscopic pores using singlet spin states. *J. Magn. Reson.* 204, 346–348. doi:10.1016/j.jmr.2010.03.010

Zhukov, I. V., Kiryutin, A. S., Yurkovskaya, A. V., Grishin, Y. A., Vieth, H.-M., and Ivanov, K. L. (2018). Field-cycling NMR experiments in an ultra-wide magnetic field range: Relaxation and coherent polarization transfer. *Phys. Chem. Chem. Phys.* 20, 12396–12405. doi:10.1039/c7cp08529j

frontiers | Frontiers in Chemistry

TYPE Original Research
PUBLISHED 13 July 2023
DOI 10.3389/fchem.2023.1217260

OPEN ACCESS

EDITED BY
Stanislav Baluschev,
Max Planck Institute for Polymer Research, Germany

REVIEWED BY
Andrea Lapini,
University of Parma, Italy
Renren Deng,
Zhejiang University, China

*CORRESPONDENCE
Yoichi Murakami,
murakami.y.af@m.titech.ac.jp

RECEIVED 05 May 2023
ACCEPTED 06 July 2023
PUBLISHED 13 July 2023

CITATION
Murakami Y and Enomoto R (2023), Stable and low-threshold photon upconversion in nondegassed water by organic crystals.
Front. Chem. 11:1217260.
doi: 10.3389/fchem.2023.1217260

Stable and low-threshold photon upconversion in nondegassed water by organic crystals

Yoichi Murakami* and Riku Enomoto

Laboratory for Zero-Carbon Energy, Institute of Innovative Research, Tokyo Institute of Technology, Meguro, Tokyo, Japan

Photon upconversion (UC) is a technology that converts lower-energy photons (longer wavelength light) into higher-energy photons (shorter wavelength light), the opposite of fluorescence. Thus, UC is expected to open a vast domain of photonic applications that are not otherwise possible. Recently, UC by triplet–triplet annihilation (TTA) between organic molecules has been studied because of its applicability to low-intensity light, although the majority of such studies have focused on liquid samples in the form of organic solvent solutions. To broaden the range of applications, solid-state UC materials have been an active area of research. We recently developed air-stable, high-performance molecular UC crystals that utilize a stable solid-solution phase of bicomponent organic crystals. This article begins with a brief overview of previous challenges in developing and improving solid-state TTA–UC materials. Then, we briefly review and explain the concept as well as advantages of our molecular solid-solution UC crystals. We applied these organic crystals for the first time to a water environment. We observed blue UC emission upon photoexcitation at 542 nm (green–yellow light) and then measured the excitation intensity dependence as well as the temporal stability of the UC emission in air-saturated water. In nondegassed water, these organic crystals were stable, functioned with a low excitation threshold intensity of a few milliwatts per square centimeter, and exhibited high photo-irradiation durability at least over 40 h; indicating that the developed organic crystals are also viable for aqueous conditions. Therefore, the organic crystals presented in this report are expected to extend the domain of UC-based photonic applications in practical water systems including *in vivo* diagnostic, clinical, and therapeutic applications.

KEYWORDS

triplet-triplet annihilation, upconversion, organic crystal, solid solution, *in vivo* application

1 Introduction

The research area of photon upconversion (UC) by triplet–triplet annihilation (TTA), termed TTA–UC, has been progressing since some initial works in early 2000s (Keivanidis et al., 2003; Kozlov and Castellano, 2004) until the present date; many review papers have been published (for example, Singh-Rachford and Castellano, 2010; Simon and Weder, 2012; Schulze and Schmidt, 2015; Gray et al., 2018; Seo et al., 2022; Alves et al., 2022). The applicability to low-intensity light sources, including noncoherent sunlight (Baluschev et al., 2006; Schulze and Schmidt, 2015), differentiates TTA–UC technology from previous UC technology consisting of rare-earth-doped inorganic materials that require high-intensity lasers (Auzel, 2004). However, excited triplet states of organic molecules or chromophores

used in TTA–UC are quenched when they are contacted by an oxygen molecule (O_2) (Turro et al., 2009), which further generates highly reactive singlet oxygen that could irreversibly degrade organic molecules. Furthermore, because intermolecular energy transfer in TTA–UC is based on the Dexter mechanism, which only occurs over a short distance (typically less than 1 nm; Turro et al., 2009), TTA–UC is inherently easier to implement in liquid systems in which the chromophores' Brownian motion facilitates mutual collisions and hence triplet energy transfer (TET) as well as TTA. Therefore, studies of TTA–UC have mostly been conducted by using degassed organic solvents, in which O_2 molecules have been removed either by freeze–pump–thaw cycles or inert gas bubbling.

Thus, it has been challenging to develop efficient and durable solid-state TTA–UC materials—'durable' refers to stability against continuous photo-irradiation and photo-irradiation in the presence of O_2—compared with conventional degassed and tightly sealed organic-solvent-solution samples. Initial trials aimed at forming solid-state TTA–UC materials did not result in high efficiency and low excitation thresholds, mainly because of the lack of fluidic solvents and hence the Brownian motion of the triplet-energy-carrying species. A typical case among the initial works developed solid samples by embedding palladium octaethylporphyrin (triplet sensitizer) and 9,10-diphenylanthracene (DPA, triplet annihilator) into polyurethane (Singh-Rachford et al., 2009); UC emission was evident only above the glass transition temperature of the polymer matrix, upon which the chromophores started to undergo translational thermal motions necessary for intermolecular TET. Another initial study (Merkel and Dinnocenzo, 2009) doped platinum octaethylporphyrin (PtOEP, triplet sensitizer) and DPA into a poly (methylmethacrylate) film, but the resulting UC efficiency was much less than 1% because of substantial hindrance of intermolecular TET in such rigid materials.

As will be outlined in a subsequent paragraph, much effort has focused on developing high-performance solid-state TTA–UC materials, which are expected to have broad applications. Furthermore, imparting solid-state TTA–UC materials with aqueous functionalities would facilitate innovative *in vivo* photonic applications encompassing vast domains of diagnostic, clinical, and therapeutic applications. Although several *in vivo* compatible TTA–UC materials have been reported (Liu et al., 2013; Park et al., 2018; Seo et al., 2022; Vepris et al., 2022), the corresponding performance (e.g., UC efficiency and excitation threshold intensity) has been limited or low. In particular, durability under continuous photo-irradiation in nondegassed water has not yet been demonstrated unequivocally to our best knowledge.

In Section 2, we briefly review some representative efforts to develop solid-state TTA–UC materials in the context of the present study. In Section 3, we explain our recently developed strategy of utilizing a thermodynamically stable phase of a bicomponent solid-solution that affords molecularly uniform (i.e., aggregation-free), durable, and efficient TTA–UC solids; which are organic crystals formed by van der Waals forces. In Section 4, we present original results that demonstrate the ability of such organic crystals to carry out stable and durable UC under continuous photo-irradiation in nondegassed water.

2 Brief overview of previous solidification strategy

Research on high-performance solid-state TTA–UC materials started in the early 2010s, as documented by several review papers (for example, Simon and Weder, 2012; Joarder et al., 2018; Gray et al., 2018; Seo et al., 2022; Alves et al., 2022). Here we briefly overview some of the history in order to clarify the context of this report.

Figure 1A indicates the principles of TTA–UC in solid systems. Here, S and A denote the sensitizer and annihilator, respectively; both are usually organic molecules (chromophores). First, S is photo-excited by absorbing a photon of energy of $h\nu_1$, which converts S into an excited singlet state (^{1}S*). If there is strong intersystem crossing, ^{1}S* immediately converts into the excited triplet state (^{3}S*), which has much longer lifetime than that of ^{1}S*. Furthermore, if there is sufficient orbital overlap between the S and A chromophores, a state of ^{3}A* can be created as a result of TET from ^{3}S* with a quantum efficiency of Φ_{TET}; generally, a low Φ_{TET} might be caused by thermodynamic mismatch between the energy levels of ^{3}S* and ^{3}A*, too short a lifetime of ^{3}S*, or insufficient orbital overlap between the S and A chromophores. Subsequently, the state of ^{3}A* might diffuse as a triplet exciton among many A units, until ^{3}A* either decays back into the ground state or causes TTA when it encounters another triplet exciton. The latter might cause emission of an upconverted photon of energy $h\nu_2$ ($>h\nu_1$) from the singlet state of ^{1}A* (Figure 1A).

To our knowledge, Monguzzi et al. (2012) is the first explicit study of TTA–UC that used a crystalline organic solid. They tried to dope a PtOEP sensitizer into a crystal of DPA via co-crystallization in the organic solvent, aiming to achieve triplet exciton diffusion through the crystal of DPA. However, because of the substantial aggregation of PtOEP, which formed on the surface of the DPA crystal as a separate phase, TET from PtOEP to DPA was substantially hindered (Figure 1B). As the result, they reported only weak UC emission relative to strong phosphorescence from PtOEP (Monguzzi et al., 2012), an indication of inefficient TET toward DPA. Subsequently, other researchers studied the effect of PtOEP aggregates on the properties of UC emission from a polycrystalline film of DPA (Goudarzi and Keivanidis, 2017).

To overcome this aggregation problem, many researchers have used kinetically controlled strategies, as some of the representative ones are graphically classified in Figure 1C. The first kind (<i> in Figure 1C) is by rapidly cooling a thermal melt of a sensitizer–annihilator mixture to quench it into a homogeneous glassy solid. This method mitigated formation of a sensitizer aggregate but the highly disordered annihilator solid led to low UC performance, such as high excitation threshold intensity (Vadrucci et al., 2014). The second kind (<ii> in Figure 1C) is by rapid precipitation of microcrystals by rapidly mixing the organic solvent solution of chromophores with a poor solvent (Ogawa et al., 2017). Although this method enhanced the dispersibility of the sensitizer in the polycrystalline micropowders of the annihilator, very small (less than 1 μm, by the scanning electron microscope images) crystalline domains in such precipitated powders hindered efficient transport of the triplet excitons in the materials and led to low UC performance. The third kind (<iii> in Figure 1C) used casting of a solution of the sensitizer and annihilator in a low boiling

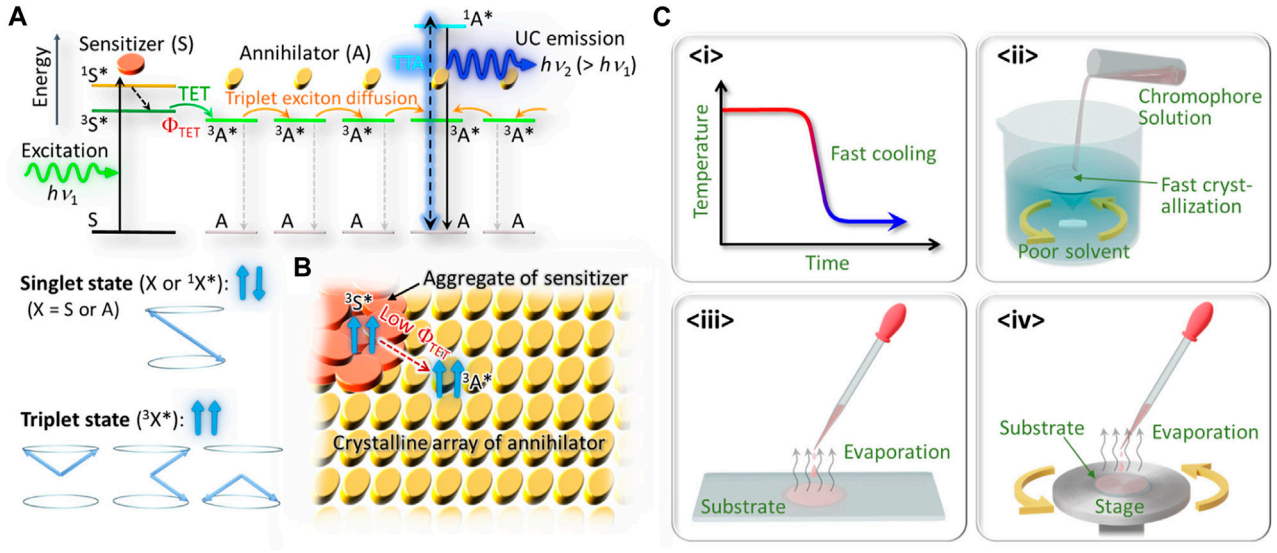

FIGURE 1
(A) Schematic of TTA–UC in solid materials in which lower-energy photons ($h\nu_1$) are up-converted into higher-energy photons ($h\nu_2$) as a result of triplet energy transfer (TET) and triplet–triplet annihilation (TTA). **(B)** Schematic of sensitizer aggregation on/in a crystal of an annihilator. **(C)** Classification of some typical kinetically controlled approaches taken to date, <i > to <iv>; see main text for details.

point organic solvent onto a substrate, such that rapid evaporation of the solvent formed a polycrystalline thin film before the sensitizer started to form the aggregate (Hosoyamada et al., 2016; Kamada et al., 2017; Abulikemu et al., 2019). The fourth kind (<iv> in Figure 1C) is similar to <iii> but researchers used spin-coating of an organic solvent solution to form a thin solid film over the entire substrate (Goudarzi and Keivanidis, 2014; Karpicz et al., 2014; Goudarzi and Keivanidis, 2017; Ogawa et al., 2018).

All of these methods mitigated the sensitizer aggregation problem to some extent. However, some researchers have pointed out that "amorphous and polycrystalline thin films of organic semiconductor are characterized by a significant degree of disorder, in particular when they are cast from solution" (Mikhnenko et al., 2015). This statement seems to explain the limited performance of the aforementioned examples, in which the sample fabrication methods relied on fast solidification, which inherently resulted in a substantial thermodynamic nonequilibrium in the samples as well as a high density defects or grain boundaries in such microcrystals. Therefore, mitigating the sensitizer aggregation problem often led to a new problem—limited UC performance—that resulted from the short lifetime and diffusion distance of the triplet excitons in solid materials.

3 Organic solid-solution strategy we propose

Recently, we proposed a novel concept in the field of TTA–UC: generating thermodynamically stable bicomponent molecular crystals; we have demonstrated its effectiveness (Enomoto et al., 2021). This concept does not use fast solidification and hence does not result in low crystallinity and small crystalline domains. In particular, we conceived of a solid-solution phase that is generally represented by the α-phase of a bicomponent crystal system, the phase diagram of which is schematically illustrated by Figure 2A. The horizontal position in this diagram represents molar fraction of the sensitizer (x; $0 \le x \le 1$). By this definition, in the α-phase ($x \approx 0$), a small quantity of sensitizer is doped into a crystal of the annihilator; this is driven by the increase of the mixing entropy, which is a thermodynamic force that lowers the Gibbs free energy of bicomponent systems (Schroeder, 2000). In the β-phase ($x \approx 1$), on the contrary, a small quantity of the annihilator is doped into a crystal of the sensitizer; this is the sensitizer aggregate, formation of which should be avoided (Figure 2A). The region between the α- and β-phases is the physical mixture (eutectic mixture) of these phases. Because this eutectic phase contains microaggregates of the sensitizer, formation of this eutectic phase should also be avoided. Therefore, one should opt for the α-phase to achieve the purpose. Accordingly, we searched for optimal conditions that can selectively generate the intended crystals of α-phase by experimentally testing various conditions; including the sensitizer–annihilator combination, type of organic solvent for recrystallization, recrystallization method, temperature, as well as starting concentrations of the sensitizer and annihilator in the solvent.

Eventually, we discovered that the annihilator 9-(2-naphthyl)-10-[4-(1-naphthyl)phenyl]anthracene (ANNP, Figure 2B) can realize our concept. ANNP has two side moieties attached to anthracene, which is a blue-emitting chromophore. These side moieties enable stable accommodation of a small quantity of PtOEP (Enomoto et al., 2021); PtOEP is a common green-absorbing sensitizer in the field of TTA–UC. Such solid-solution-based UC crystals—formed by van der Waals forces—exhibited unprecedented UC performance in air; including a UC quantum efficiency of up to 16% (out of a maximum of 50%), ultralow excitation threshold intensity of ca. 0.2× natural sunlight

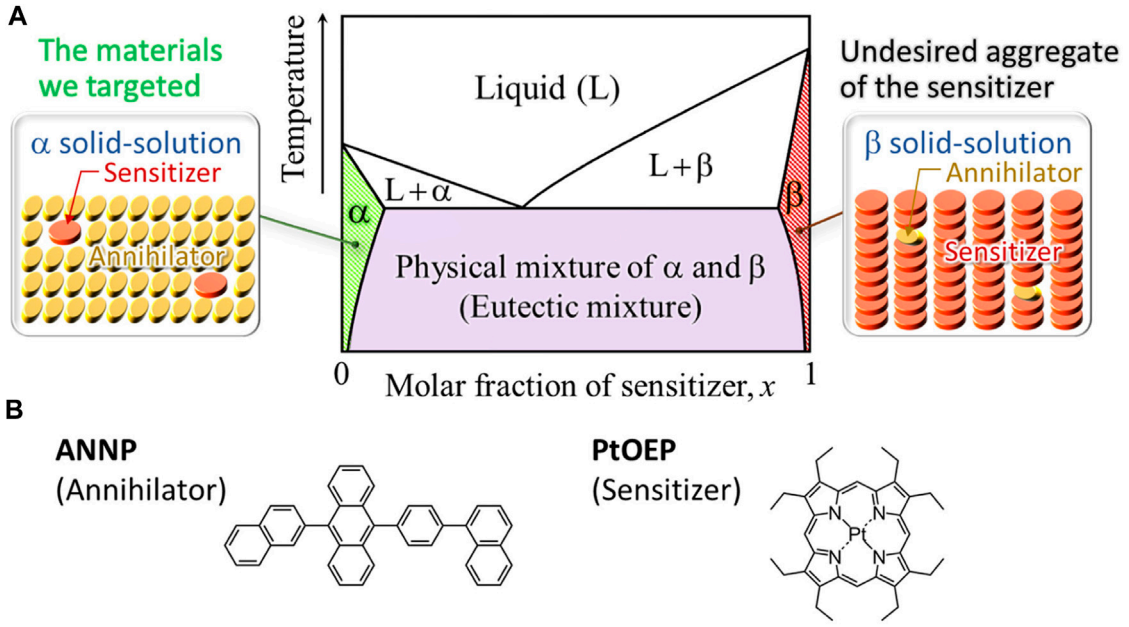

FIGURE 2
(A) Schematic phase diagram representing a bicomponent eutectic system comprised of two solid-solution phases α and β. In present case, an α phase corresponds to an annihilator crystal into which a small quantity of the sensitizer is entropically doped and a β phase is the sensitizer aggregate. The region between the α and β phases represents the eutectic mixture of these phases. **(B)** The annihilator and sensitizer chromophores used in this study.

intensity, and endurance against continuous photoirradiation over tens of hours without photodegradation (Enomoto et al., 2021). However, we did not test whether the van der Waals solid-solution UC crystals were compatible with aqueous environments, despite recent active extension of the application target of TTA–UC into the area of water-compatible (or aqueous) applications (Turshatov et al., 2011; Wohnhaas et al., 2011; Kim et al., 2016; Seo et al., 2022). This is the motivation of the study reported here; we present our experimental results next.

4 Results: efficient and durable UC in nondegassed water

We prepared UC crystals from ANNP and PtOEP (Enomoto et al., 2021). Figure 3A (left panel) shows a photograph of the UC crystals actually used in this report. These crystals were transparent, were pinkish (uniformly colored; because of the PtOEP), and exhibited a thin flat-plate geometry. The volumetric concentration of the doped PtOEP in the crystal of ANNP was ca. 5.0×10^{-5} M, corresponding to a mole ratio of PtOEP to ANNP of approximately 1:50,000. The container in the photograph was a cylindrical quartz dish with an outer diameter and height of 17 and 5 mm, respectively.

Subsequently, we poured nondegassed pure water into the quartz dish and covered the dish with a quartz lid. For all experiments in this report, we used water from a commercial water purification system (Direct-Q UV 3, Merck Millipore). Because this water was purified at room temperature from tap water and had been stored under air in a tank until use, we assume that air was dissolved in it at almost the saturation concentration. We found that the crystals did not dissolve in water, which is reasonable considering the aromatic and thus hydrophobic nature of ANNP. Upon horizontal irradiation of continuous-wave laser light (wavelength: 542 nm, green–yellow) at the crystals immersed in water, we observed blue emission (Figure 3A, right panel).

In the following measurements (for Figures 3B–D), we characterized the UC emission properties of the crystals in nondegassed water held in a glass tube with a square cross section. This tube had inner and outer dimensions of 1 mm × 1 mm and 2 mm × 2 mm, respectively. To prevent evaporation of the water during the measurements, the open end of the glass tube was closed with a low melting point solder. Upon 542-nm laser light irradiation, we observed UC emission ranging from 425 to 500 nm (Figure 3B), coinciding with the fluorescence spectrum of ANNP (Enomoto et al., 2021). Notably, in the emission spectrum, we found no phosphorescence from PtOEP at ca. 650 nm, which would indicate solid aggregates of PtOEP (Goudarzi and Keivanidis, 2014; Karpicz et al., 2014; Vadrucci et al., 2014; Goudarzi and Keivanidis, 2017). Thus, the present material has resolved the long standing problem of sensitizer aggregation as we have discussed in detail (Enomoto et al., 2021).

Figure 3C shows the excitation intensity dependence of the sample crystals in nondegassed water. We first increased the intensity of the excitation at 542 nm (open marks) and then decreased it (filled marks) to check the reproducibility of the UC emission intensity. We fitted these data points to a theoretical curve [Eq. (36) of Murakami and Kamada, 2021]. From this fitting, we determined the excitation threshold intensity (I_{th}) to be ca. 2.9 mW cm^{-2}; which is sufficiently low for most *in vivo* photonic applications, considering that typical handheld laser pointers generate 1-mW optical power with a typical spot radius of 2–3 mm (i.e., 14–32 mW cm^{-2}).

Figure 3D shows the results of our long-term stability tests of a sample under continuous photo-irradiation for >41 h in nondegassed

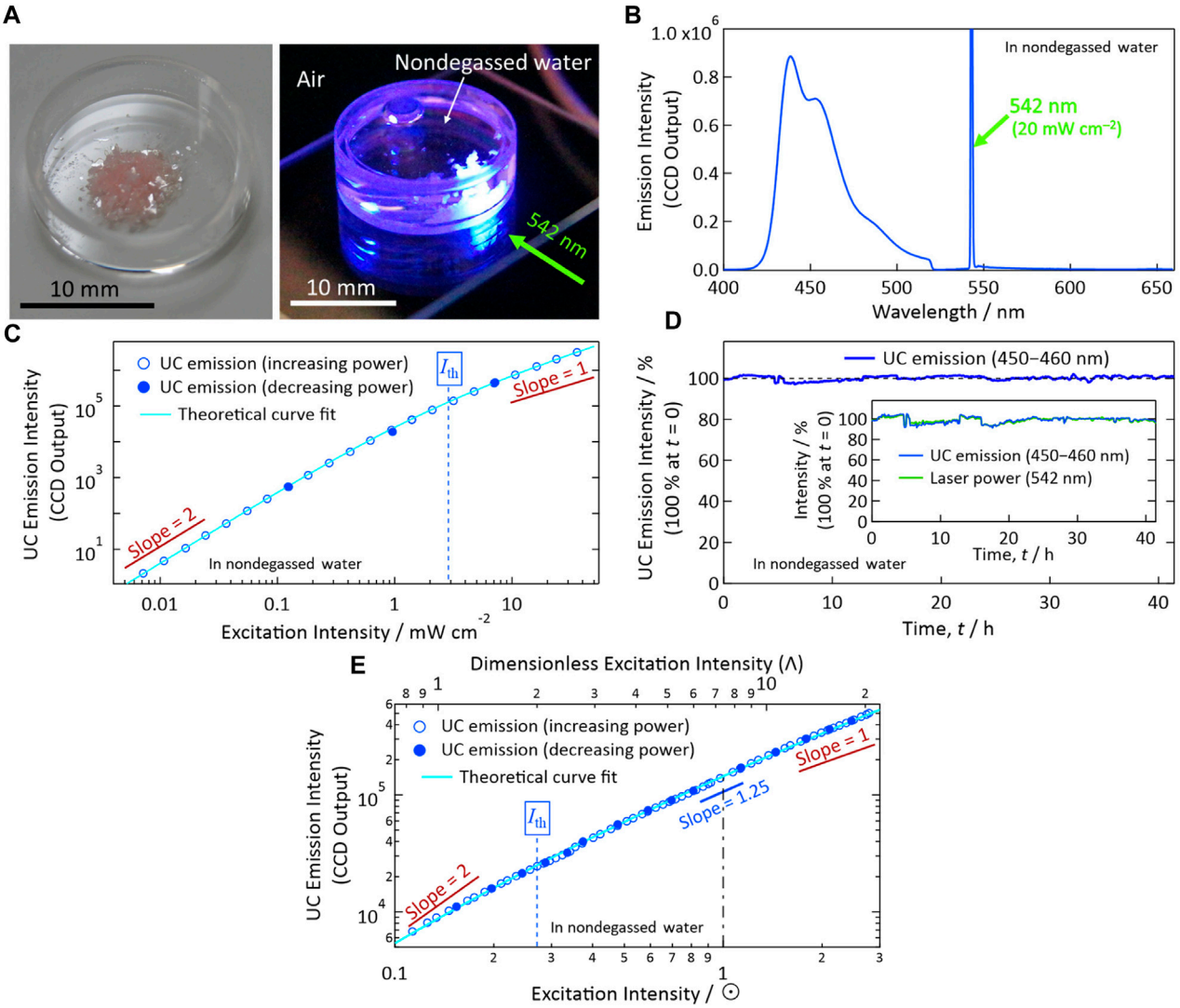

FIGURE 3
Photoemission properties in nondegassed water. **(A)** Left: Photograph of the solid-solution UC crystals (PtOEP-doped ANNP crystals) used in this report. Note the transparent and slightly pinkish color of the crystals with planer shape. Right: Photograph of the crystals in nondegassed water up-converting an incident laser light at 542 nm (green–yellow) into blue emission. We acquired this photograph through a notch filter to eliminate the incident laser light. **(B)** Photoemission spectrum upon excitation with a 542-nm laser at 20 mW cm^{-2}. **(C)** Excitation intensity dependence of the UC emission intensity measured using a 542-nm laser. I_{th} indicates the excitation threshold intensity. **(D)** Temporal stability of the UC emission intensity (100% at t = 0, spectrally integrated between 450 and 460 nm) under continuous photoexcitation with a 542-nm laser at an intensity of ca. 20 mW cm^{-2}. We corrected the emission intensity by the temporal fluctuation of the laser power shown in the inset. **(E)** Dependence of the UC emission intensity on the simulated sunlight irradiance represented in units of sun (⊙). The simulated sunlight comprised only wavelengths longer than 510 nm; see Enomoto et al., 2021 for details. In panels (C, E), we acquired the data represented by open marks by increasing the excitation power, and then we acquired the data represented by filled marks by decreasing the excitation power to check the quantitative reproducibility.

water, measured at an excitation intensity of ca. 20 mW cm^{-2}, ca. one order of magnitude greater than I_{th}. We corrected the emission intensity by the fluctuation of the laser power as indicated in the inset. The stability of the UC emission, or that of the present material under continuous photo-irradiation, was excellent, even in the presence of oxygen in the water. This outstanding stability is attributable to the molecularly close-packed crystalline arrangement of ANNP as implied by the results of our previous single-crystal X-ray analysis (Enomoto et al., 2021). Because these UC properties are similar to those measured previously in air and the preparation procedure of the sample crystals (Figure 3A) was identical to that used beforehand, we hypothesize that the UC quantum efficiency here is similar to that determined previously in air (Enomoto et al., 2021). Such high photoirradiation stability in oxygen-dissolved water is highly advantageous for achieving broad types of aqueous photonic applications that can be rendered possible by utilizing UC.

Figure 3E shows dependence of the UC emission intensity on the simulated sunlight irradiance represented in units of Sun (⊙), measured in nondegassed water; such a situation would be a typology for enhancing sunlight-driven photocatalysis in aqueous system with an assistance of UC. The simulated sunlight was passed through a 510 nm long-pass filter and thus comprised only wavelengths longer than

510 nm; see Enomoto et al., 2021 for experimental details. As shown by Figure 3E, the UC crystals exhibited low I_{th} of ca. 0.27☉, which is similar to I_{th} we reported previously in air (ca. 0.2☉; Enomoto et al., 2021). Therefore, the use of the present UC crystals in nondegassed water does not affect their superior I_{th}.

We make some notes on our solid-solution crystals. So far, we have been able to make similar solid-solution crystals combining other sensitizers and ANNP, aiming to achieve a larger anti-Stokes shift. One representative case is a combination of ZnOEP and ANNP, which yielded light-yellowish crystals. ZnOEP in organic solvents typically exhibits Q-band absorption peaked at around 570 nm (which is longer wavelength than that of PtOEP). However, as indicated by Supplementary Figure S1A, the UC emission from the ZnOEP-ANNP solid-solution crystal is significantly weaker than that from the present PtOEP-ANNP solid-solution crystals. Our quantum-chemical simulations reveal that TET from ZnOEP to ANNP is highly unfavored (Supplementary Figure S1B). Thus, to achieve a large anti-Stokes shift, we have to find better annihilator that has a lower triplet energy level.

For some applications, i) solid-solution crystals formed on a flat surface or ii) solid-solution microcrystals may be useful. As for i), we recently reported a new method of forming a solid-solution polycrystalline film on a flat substrate (Enomoto and Murakami, 2023). However, this technique requires relatively low melting temperature for the annihilator (preferably lower than 150 °C). Thus, the high melting temperature of ANNP (254 °C) and resultant partial decomposition of ANNP have hindered the use of this new method for the present ANNP system, as shown by Supplementary Figure S2. As for ii), one of the easiest methods to form microcrystals is to use the rapid precipitation technique (*cf.* Figure 1C <ii>). However, the resulted PtOEP-doped-ANNP microcrystals exhibited rather poor performances (Section 3 of *Supplementary Material*; Supplementary Figure S3). This fact not only supports our discussion in Section 2 above but also corroborates the superiority of the near-equilibrium crystal growth to generate high quality solid-solution UC crystals. Therefore, to realize high-performance solid-solution UC microcrystals, a new way of nucleation density control under near-equilibrium crystal growth would be necessary.

5 Conclusion

This article has outlined the longstanding sensitizer aggregation problem and reviewed representative methods used to date for circumventing this problem via kinetic control. Whereas such kinetic approaches have progressed from initial works, the low crystallinity and small size of the crystalline domain that result from such fast solidification methods is also problematic. To fundamentally resolve this dilemma, we conceived and demonstrated the effectiveness of a solid-solution phase consisting of an α-phase in a bicomponent phase diagram (Figure 2A). In such van der Waals organic crystals prepared at much slower (*i.e.*, near-equilibrium) speeds, the driving force of the inclusion of a small quantity of one species (sensitizer) into a crystal of the other species (annihilator) is a thermodynamic force that results from the increased mixing entropy of two components (Schroeder, 2000).

Whereas such TTA–UC organic crystals have not been applied to aqueous systems beforehand, for the first time we have demonstrated that crystalline UC materials can function in a stable manner in water without degassing. The low excitation threshold and excellent photostability against continuous laser irradiation indicates that this material is promising for expanding the potential range of photo-related applications in aqueous environments; including *in vivo* diagnostic, clinical, and therapeutic applications.

Data availability statement

The raw data supporting the conclusion of this article will be made available by the authors, without undue reservation.

Author contributions

YM conceived the idea of the study. YM and RE discussed the experimental plan. RE conducted the experiments and analyzed the data. RE and YM prepared the figures. YM wrote the manuscript. All authors contributed to the article and approved the submitted version.

Funding

This research was conducted with funding from JSPS KAKENHI Grant Numbers JP17H03183 and JP20H02082 (YM).

Acknowledgments

We cordially thank people at Idemitsu Kosan Co., Ltd. who developed ANNP and provided it to us. We thank Dr. Michael Scott Long for checking and improving English of a draft of this manuscript.

Conflict of interest

The authors declare that the research was conducted in the absence of any commercial or financial relationships that could be construed as a potential conflict of interest.

Publisher's note

Supplementary material

The Supplementary Material for this article can be found online at: https://www.frontiersin.org/articles/10.3389/fchem.2023.1217260/full#supplementary-material

References

Abulikemu, A., Sakagami, Y., Heck, C., Kamada, K., Sotome, H., Miyasaka, H., et al. (2019). Solid-state, near-infrared to visible photon upconversion *via* triplet–triplet annihilation of a binary system fabricated by solution casting. *ACS Appl. Mater. Interfaces* 11, 20812–20819. doi:10.1021/acsami.9b04148

Alves, J., Feng, J., Nienhaus, L., and Schmidt, T. W. (2022). Challenges, progress and prospects in solid state triplet fusion upconversion. *J. Mater. Chem. C* 10, 7783–7798. doi:10.1039/d1tc05659j

Auzel, F. (2004). Upconversion and anti-Stokes processes with f and d ions in solids. *Chem. Rev.* 104, 139–174. doi:10.1021/cr020357g

Baluschev, S., Miteva, T., Yakutkin, V., Nelles, G., Yasuda, A., and Wegner, G. (2006). Up-conversion fluorescence: Noncoherent excitation by sunlight. *Phys. Rev. Lett.* 97, 143903. doi:10.1103/PhysRevLett.97.143903

Enomoto, R., Hoshi, M., Oyama, H., Agata, H., Kurokawa, S., Kuma, H., et al. (2021). van der Waals solid solution crystals for highly efficient in-air photon upconversion under subsolar irradiance. *Mater. Horiz.* 8, 3449–3456. doi:10.1039/d1mh01542g

Enomoto, R., and Murakami, Y. (2023). Solvent-free temperature gradient melt formation of efficient visible-to-UV photon upconversion organic films with subsolar threshold and over 100 h photostability in air. *J. Mater. Chem. C* 11, 1678–1683. doi:10.1039/D2TC04578H

Goudarzi, H., and Keivanidis, P. E. (2017). All-solution-based aggregation control in solid-state photon upconverting organic model composites. *ACS Appl. Mater. Interfaces* 9, 845–857. doi:10.1021/acsami.6b12704

Goudarzi, H., and Keivanidis, P. E. (2014). Triplet–triplet annihilation-induced up-converted delayed luminescence in solid-state organic composites: Monitoring low-energy photon up-conversion at low temperatures. *J. Phys. Chem. C* 118, 14256–14265. doi:10.1021/jp5052936

Gray, V., Moth-Poulsen, K., Albinsson, B., and Abrahamsson, M. (2018). Towards efficient solid-state triplet–triplet annihilation based photon upconversion: Supramolecular, macromolecular and self-assembled systems. *Coord. Chem. Rev.* 362, 54–71. doi:10.1016/j.ccr.2018.02.011

Hosoyamada, M., Yanai, N., Ogawa, T., and Kimizuka, N. (2016). Molecularly dispersed donors in acceptor molecular crystals for photon upconversion under low excitation intensity. *Chem. Eur. J.* 22, 2060–2067. doi:10.1002/chem.201503318

Joarder, B., Yanai, N., and Kimizuka, N. (2018). Solid-state photon upconversion materials: Structural integrity and triplet–singlet dual energy migration. *J. Phys. Chem. Lett.* 9, 4613–4624. doi:10.1021/acs.jpclett.8b02172

Kamada, K., Sakagami, Y., Mizokuro, T., Fujiwara, Y., Kobayashi, K., Narushima, K., et al. (2017). Efficient triplet–triplet annihilation upconversion in binary crystalline solids fabricated *via* solution casting and operated in air. *Mater. Horiz.* 4, 83–87. doi:10.1039/c6mh00413j

Karpicz, R., Puzinas, S., Gulbinas, V., Vakhnin, A., Kadashchuk, A., and Rand, B. P. (2014). Exciton dynamics in an energy up-converting solid state system based on diphenylanthracene doped with platinum octaethylporphyrin. *Chem. Phys.* 429, 57–62. doi:10.1016/j.chemphys.2013.12.004

Keivanidis, P. E., Baluschev, S., Miteva, T., Nelles, G., Scherf, U., Yasuda, A., et al. (2003). Up-conversion photoluminescence in polyfluorene doped with metal(II)–octaethyl porphyrins. *Adv. Mater.* 15, 2095–2098. doi:10.1002/adma.200305717

Kim, H., Kwon, O. S., Kim, S., Choi, W., and Kim, J. H. (2016). Harnessing low energy photons (635 nm) for the production of H_2O_2 using upconversion nanohybrid photocatalysts. *Energy Environ. Sci.* 9, 1063–1073. doi:10.1039/C5EE03115J

Kozlov, D. V., and Castellano, F. N. (2004). Anti-Stokes delayed fluorescence from metal–organic bichromophores. *Chem. Commun.* 24, 2860–2861. doi:10.1039/B412681E

Liu, Q., Yin, B., Yang, T., Yang, Y., Shen, Z., Yao, P., et al. (2013). A general strategy for biocompatible, high-effective upconversion nanocapsules based on triplet–triplet annihilation. *J. Am. Chem. Soc.* 135, 5029–5037. doi:10.1021/ja3104268

Merkel, P. B., and Dinnocenzo, J. P. (2009). Low-power green-to-blue and blue-to-UV upconversion in rigid polymer films. *J. Lumin.* 129, 303–306. doi:10.1016/j.jlumin.2008.10.013

Mikhnenko, O. V., Blom, P. W. M., and Nguyen, T. Q. (2015). Exciton diffusion in organic semiconductors. *Energy Environ. Sci.* 8, 1867–1888. doi:10.1039/c5ee00925a

Monguzzi, A., Tubino, R., Hoseinkhani, S., Campione, M., and Meinardi, F. (2012). Low power, non-coherent sensitized photon up-conversion: Modelling and perspectives. *Phys. Chem. Chem. Phys.* 14, 4322–4332. doi:10.1039/c2cp23900k

Murakami, Y., and Kamada, K. (2021). Kinetics of photon upconversion by triplet–triplet annihilation: A comprehensive tutorial. *Phys. Chem. Chem. Phys.* 23, 18268–18282. doi:10.1039/d1cp02654b

Ogawa, T., Hosoyamada, M., Yurash, B., Nguyen, T. Q., Yanai, N., and Kimizuka, N. (2018). Donor–acceptor–collector ternary crystalline films for efficient solid-state photon upconversion. *J. Am. Chem. Soc.* 140, 8788–8796. doi:10.1021/jacs.8b04542

Ogawa, T., Yanai, N., Kouno, H., and Kimizuka, N. (2017). Kinetically controlled crystal growth approach to enhance triplet energy migration-based photon upconversion. *J. Photonics Energy* 8, 1. doi:10.1117/1.JPE.8.022003

Park, J., Xu, M., Li, F., and Zhou, H. C. (2018). 3D long-range triplet migration in a water-stable metal–organic framework for upconversion-based ultralow-power *in vivo* imaging. *J. Am. Chem. Soc.* 140, 5493–5499. doi:10.1021/jacs.8b01613

Schroeder, D. V. (2000). *An introduction to thermal physics*. Boston, United States: Addison Wesley.

Schulze, T. F., and Schmidt, T. W. (2015). Photochemical upconversion: Present status and prospects for its application to solar energy conversion. *Energy Environ. Sci.* 8, 103–125. doi:10.1039/c4ee02481h

Seo, S. E., Choe, H. S., Cho, H., Kim, H., Kim, J. H., and Kwon, O. S. (2022). Recent advances in materials for and applications of triplet–triplet annihilation-based upconversion. *J. Mater. Chem. C* 10, 4483–4496. doi:10.1039/d1tc03551g

Simon, Y. C., and Weder, C. (2012). Low-power photon upconversion through triplet–triplet annihilation in polymers. *J. Mater. Chem.* 22, 20817–20830. doi:10.1039/c2jm33654e

Singh-Rachford, T. N., and Castellano, F. N. (2010). Photon upconversion based on sensitized triplet–triplet annihilation. *Coord. Chem. Rev.* 254, 2560–2573. doi:10.1016/j.ccr.2010.01.003

Singh-Rachford, T. N., Lott, J., Weder, C., and Castellano, F. N. (2009). Influence of temperature on low-power upconversion in rubbery polymer blends. *J. Am. Chem. Soc.* 131, 12007–12014. doi:10.1021/ja904696n

Turro, N. J., Ramamurthy, V., and Scaiano, J. C. (2009). *Principles of molecular photochemistry an introduction*. Herndon, VA, USA: University Science Books.

Turshatov, A., Busko, B., Baluschev, S., Miteva, T., and Landfester, K. (2011). Micellar carrier for triplet–triplet annihilation-assisted photon energy upconversion in a water environment. *New J. Phys.* 13, 083035. doi:10.1088/1367-2630/13/8/083035

Vadrucci, R., Weder, C., and Simon, Y. C. (2014). Low-power photon upconversion in organic glasses. *J. Mater. Chem. C* 2, 2837–2841. doi:10.1039/c3tc32473g

Vepris, O., Eich, Y., Feng, Y., Fuentes, G., Zhang, H., Kaijzel, E. L., et al. (2022). Optically coupled PtOEP and DPA molecules encapsulated into PLGA-nanoparticles for cancer bioimaging. *biomedicines* 10, 1070. doi:10.3390/biomedicines10051070

Wohnhaas, C., Turshatov, A., Mailänder, V., Lorenz, S., Baluschev, S., Miteva, T., et al. (2011). Annihilation upconversion in cells by embedding the dye system in polymeric nanocapsules. *Macromol. Biosci.* 11, 772–778. doi:10.1002/mabi.201000451

frontiers | Frontiers in Chemistry

TYPE Original Research
PUBLISHED 04 August 2023
DOI 10.3389/fchem.2023.1224336

OPEN ACCESS

EDITED BY
Daniel Abergel,
École Normale Supérieure, France

REVIEWED BY
Flavio Kock,
University of Toronto Scarborough, Canada
William S. Price,
Western Sydney University, Australia

*CORRESPONDENCE
Giuseppe Pileio,
g.pileio@soton.ac.uk

RECEIVED 17 May 2023
ACCEPTED 03 July 2023
PUBLISHED 04 August 2023

CITATION
Melchiorre G, Giustiniano F, Rathore S and Pileio G (2023), Singlet-assisted diffusion-NMR (SAD-NMR): extending the scope of diffusion tensor imaging via singlet NMR.
Front. Chem. 11:1224336.
doi: 10.3389/fchem.2023.1224336

Singlet-assisted diffusion-NMR (SAD-NMR): extending the scope of diffusion tensor imaging via singlet NMR

Giulia Melchiorre, Francesco Giustiniano, Sundeep Rathore and Giuseppe Pileio*

School of Chemistry, University of Southampton, Southampton, United Kingdom

In this study, long-lived nuclear singlet order methods are combined with diffusion tensor imaging with the purpose of characterizing the full diffusion tensor of molecules diffusing freely in large pores of up to a millimeter in size. Such sizes are out of reach in conventional diffusion tensor imaging because of the limitations imposed by the relaxation decay constant of the longitudinal magnetization. A singlet-assisted diffusion tensor imaging methodology able to circumvent such limitations is discussed, and the new possibilities that it offers are demonstrated through simulation and experiments on plastic phantoms containing cylindrical channels of 1 mm in diameter.

KEYWORDS

diffusion NMR, diffusion tensor imaging, long-lived spin order, singlet spin order, nuclear magnetic resonance

1 Introduction

Brownian diffusion is a form of molecular translational motion in which molecules travel through space in a random way as dictated by intermolecular collisions, thermal energy, and the structural boundaries of the space they travel within. Measurements of such motion can be used to make important deductions concerning both the diffusing species itself and its surroundings (Price, 2009; Callaghan, 2011). The most basic value that can be measured to characterize this form of motion is the molecular self-diffusion coefficient, a quantity that measures the extent of molecular translation through Brownian motion in an isotropic space. Molecular diffusion (the prefix "self-" is dropped hereafter, but is implied in all instances in which we refer to diffusion in this paper), however, is not always isotropic; this is the case, for example, when the size and shape of a container impose confinement on molecules that move within it, or when molecules retain some sort of positional order, as in a liquid crystalline phase. To characterize those situations, two quantities, namely, the structural length l_S and the diffusion length l_D, are commonly introduced. l_s reflects the average dimension of confinement (for example, the average diameter of spherical pores or the average length of channels in a structure), whereas l_D represents the average distance traveled by the molecules during the diffusion time Δ, also known as the root mean square displacement, $l_D = \sqrt{2D\Delta}$, with D representing the diffusion coefficient. These quantities are of particular importance in the study of porous media, which are heterogeneous materials characterized by a matrix hosting a network of voids referred to as pores. The size and shape of such pores can restrict molecular diffusion so that the diffusive motion itself becomes anisotropic, i.e., so that it differs when measured along different directions in space. In these

systems (and many others), it is generally more correct to discuss diffusion in terms of a diffusion tensor and to refer to the isotropic diffusion coefficient as the trace of the diffusion tensor. As discussed below, the diffusion tensor can also be diagonalized to reveal the principal directions of diffusion (the tensor eigenvectors) and the diffusion coefficients along those principal directions (the tensor eigenvalues).

Molecular diffusion can be encoded in nuclear magnetic resonance (NMR) experiments (Callaghan, 2011), and NMR measurements of diffusion have already been used to obtain a plethora of molecular and structural information on a variety of systems, spanning from the domain of material sciences (rocks, bones, etc.) to medicine (blood cells, intercellular space, and brain fibers) (Hurlimann et al., 1994; Kuchel et al., 1997; Price et al., 1997; Price et al., 1999; Bullitt et al., 2003; Thorat et al., 2009; Park et al., 2012; Gobel et al., 2017). In particular, and with relevance to this paper, the full diffusion tensor can be measured using the magnetic resonance technique known as diffusion tensor imaging (DTI) (Mori and Tournier, 2013). In DTI, the full diffusion tensor is reconstructed after measurement of molecular diffusion along a minimum of six directions, chosen so as to evenly probe the space around the molecule (Basser et al., 1994; Momot et al., 2011; Mori and Tournier, 2013). There are many spectacular applications of the DTI technique *in vivo* in the medical field, and the most striking of these is perhaps brain tractography (Basser et al., 1994; Pierpaoli et al., 1996; Basser and Jones, 2002).

All magnetic resonance-based diffusion methods (the most famous of which are based on the pulsed-gradient spin echo (PGSE) or pulsed-gradient stimulated spin echo (PGSTE) pulse sequences) have a common approach: a pulsed magnetic field gradient (PFG) imposes a difference in the Larmor frequency of spins along a given direction, thus marking the positions of molecules along that dimension of space; subsequently, molecules (and the spins they carry) undergo Brownian motion for a given time interval, referred to as the diffusion time; finally, a further PFG "reads out" the new molecular positions, revealing the extent of diffusive motion they have undertaken, reflected by a change in signal intensity. It is, therefore, evident that the positional information encoded by the first PFG must survive throughout the diffusion time in order to be decoded by the second PFG. Most typically, NMR-encoded information persists for a maximum time that is of the order of T_1, the relaxation decay constant of longitudinal spin order. Therefore, T_1 sets a limit on the diffusion timescale and, hence, on the diffusion space-scale. Important structural information remains hidden, or incorrect conclusions can be drawn, if molecules are not allowed to properly explore the surrounding space. In DTI, for example, diffusion would still appear isotropic (having the same diffusion coefficient in all directions) even when molecules diffused in a highly anisotropic structure made by long and narrow channels if T_1 only allowed for molecules to move an average distance that is much smaller than the smallest spatial dimension of the space they were filling. With a typical T_1 value of seconds and a diffusion coefficient of the order of 10^{-9} m^2 s^{-1}, molecules usually travel an average of 10–200 μm during a conventional NMR diffusion experiment. This distance specifies the maximum dimension of the structures that can be accurately studied with conventional NMR diffusion techniques.

In systems consisting of two coupled spin-1/2 nuclei, spin order can be prepared in the form of singlet order, which is a form of nuclear spin order that survives longer than T_1, most typically by an order of magnitude or more (Pileio, 2020). Molecules containing such a spin system can therefore be used as probes of molecular diffusion in systems where motions occur on a long timescale or over large distances. Indeed, singlet order has already been combined with NMR diffusion experiments to measure very slow flow (Pileio et al., 2015), to image diffusion over a macroscopic scale or probe millimeter-sized confinements with q-space diffraction techniques (Pileio and Ostrowska, 2017), and to measure tortuosity in porous media (Tourell et al., 2018). We group all these methods, in which long-lived spin order is exploited in diffusion experiments, under the acronym SAD-NMR, which stands for singlet-assisted diffusion nuclear magnetic resonance.

In this paper, we discuss a further application of SAD-NMR, with the aim of extending the scope of conventional DTI techniques to allow measurements of the diffusion tensor in porous structures containing pores and channels with sizes on the order of millimeters.

With the intention of discussing the technique and assessing its novel limitations, we present experimental results obtained on 3D-printed model structures containing channels of 1-mm ID.

2 Methodology

2.1 Basics of DTI

In diffusion tensor imaging studies, molecular diffusion in anisotropic environments is described by a diffusion tensor $\boldsymbol{D}$, which is a rank-2 tensor of the form:

$$\boldsymbol{D} = \begin{pmatrix} D_{xx} & D_{xy} & D_{xz} \\ D_{yx} & D_{yy} & D_{yz} \\ D_{zx} & D_{zy} & D_{zz} \end{pmatrix}. \tag{1}$$

The diffusion tensor is symmetric ($D_{ij} = D_{ji}$) and therefore contains only six independent values: $D_{xx}, D_{xy}, D_{xz}, D_{yy}, D_{yz}, D_{zz}$. These values can be measured, and the full tensor characterized, if molecular diffusion is measured along at least six independent directions in space.

Diffusion coefficients along any given direction are routinely measured in NMR using one of the many pulse sequences developed over the years, the most basic of these being the pulsed-gradient spin echo cited above. Modifications of this experiment introduced in order to prolong the diffusion time (PGSTE), correct for eddy currents (PGSTEbp), and compensate for thermal convection (PGdSTE and PGdSTEbp) have been available for some years and are widely used by the NMR community (Callaghan, 2011). The results obtained in this work should be compared with those obtained using the PGSTEbp pulse sequence (see Figure 1A), which provides access to the longest diffusion time among all conventional (i.e., non-singlet-based) DTI techniques. As derived by Stejskal and Tanner (1965), PGSTEbp experiments produce an NMR signal whose intensity follows the equation:

$$S = S_0\, e^{-\gamma^2 g_\alpha^2 \delta^2 D_\alpha \left(\Delta - \frac{\delta}{3} - \frac{\tau}{2}\right)}. \tag{2}$$

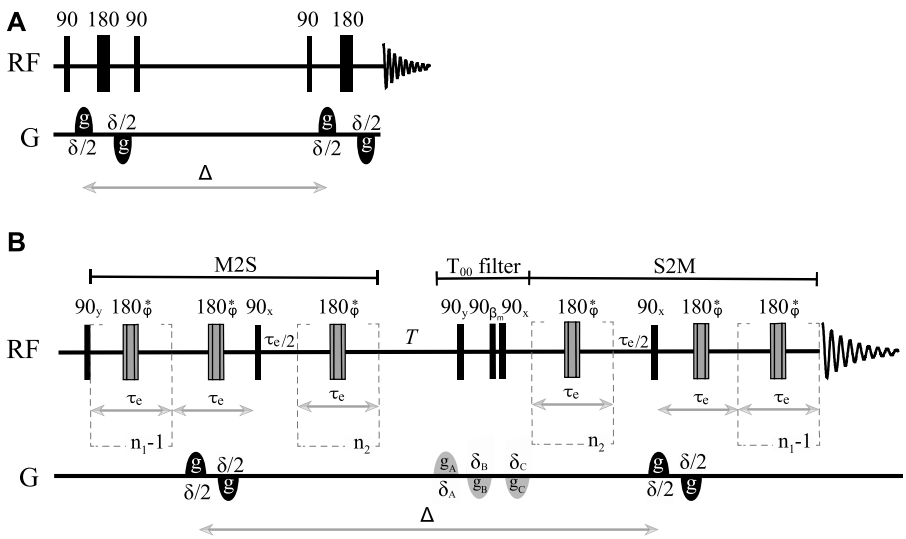

FIGURE 1
Sketch of **(A)** the pulsed field gradient stimulated echo pulse sequence with bipolar gradients (PFG-STEbp) and **(B)** the singlet-assisted diffusion pulse sequence with bipolar gradients and singlet order filter. $n_1 = \pi J/(2\Delta\nu)$ and $n_2 = n_1/2$. $\tau_e = 1/(2\sqrt{J^2 + \Delta\nu^2})$. β_m represents the magic angle, and * indicates a composite 180° pulse built as $90_x180_y90_x$ and with an overall phase ϕ cycled within each echo train as $[x,x,\bar{x},\bar{x},\bar{x},x,x,\bar{x},\bar{x},\bar{x},x,x,x,\bar{x},\bar{x},x]$.

The signal is a function of the direction (α), total duration (δ), and strength (g_α) of the gradient; the diffusion time (Δ); and the diffusion coefficient along that direction (D_α). S_0 is the signal when $g_\alpha = 0$ and τ is the duration of the echo. Most commonly, once a direction is chosen, the diffusion time is fixed and a series of experiments is performed by varying the gradient strength while keeping its duration fixed within the limit $\delta \ll \Delta$ (the condition under which Eq. 2 was derived). Alternatively, it is possible to fix the strength and vary the duration, or to fix both the strength and the duration and vary the diffusion time. In order to derive the diffusion coefficient along the $\alpha - th$ direction, Eq. 2 is fitted to the areas of the acquired NMR peaks.

To reconstruct the whole diffusion tensor, the PGSTEbp experiment (or any alternative) is run along (at least) $n_d = 6$ independent directions. To interpret the entire dataset when multiple directions are chosen, the equation for the NMR signal is rewritten as follows:

$$S_{g_\alpha} = S_0\, e^{-\gamma^2\delta^2 g_\alpha^2 \left(\Delta - \frac{\delta}{3} - \frac{\tau}{2}\right)\alpha^T \mathbf{D}\alpha}, \tag{3}$$

where $\alpha = \{\alpha_x, \alpha_y, \alpha_z\}$ now represents a unit vector that specifies the direction of space along which the pulsed field gradient is applied, and the superscript ^{T} indicates its transpose.

Note that the choice of the six directions along which diffusion is measured and from which the diffusion tensor is reconstructed is arbitrary so long as they are independent of each other. However, it is best if these directions are chosen to sample the 3D space as uniformly as possible (Jones et al., 1999). The number of directions can also be increased to more than six; this improves accuracy at the expense of experimental time. If the gradient strength is incremented in n_g steps per direction, a total of $n_d{}^*n_g$ areas of experimental signal will be available. The linearized version of Eq. 3 results in a linear system of $n_d{}^*n_g$ equations that can be matched to the experimental signal areas and solved simultaneously to yield the six unknown components of the diffusion tensor. The diffusion tensor thus reconstructed is

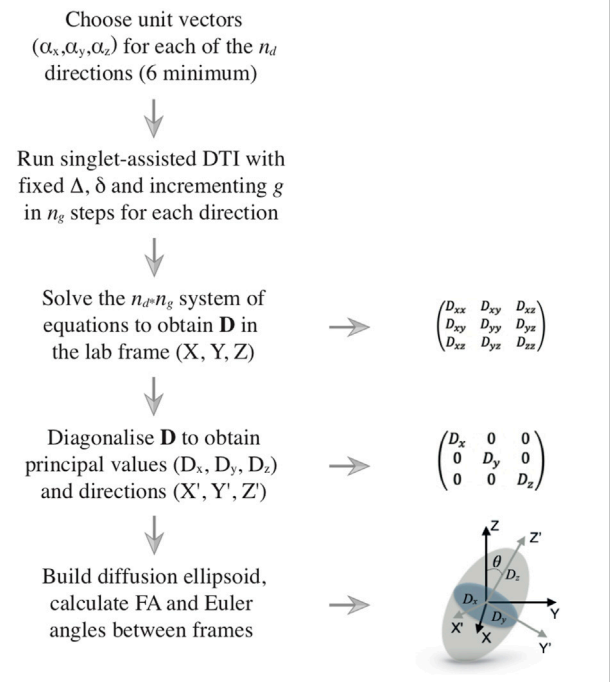

FIGURE 2
Flow diagram illustrating the DTI procedure. The left column shows the logical flow of operations, starting from the choice of the directions along which the diffusion is measured and ending with the processing of the results, which are typically rendered in terms of a diffusion ellipsoid and its fractional anisotropy. The right column shows several details of the various steps.

expressed in the laboratory frame since the gradient pulses are applied along the laboratory frame directions.

The diffusion tensor is diagonalized to obtain its principal values (D_x, D_y, D_z) and principal axes (X', Y', Z') as the eigenvalues and eigenvectors of the tensor, respectively. The principal values represent the extent of diffusion along the principal directions. The orientation of the principal frame with respect to the laboratory frame (always expressible in terms of 3 Euler angles) can provide insight into the existence, orientation, and geometry of compartments where diffusion is facilitated in some directions rather than others. This is conveniently captured by drawing the ellipsoid that describes the principal diffusion tensor. The three main axes of this ellipsoid point along the three principal directions (eigenvectors), whilst the elliptic radius along those principal directions is equal (or proportional) to the corresponding eigenvalue. The full procedure is summarized in Figure 2.

If diffusion is identical in all directions of the space, the diagonal diffusion tensor has three identical eigenvalues and its associated ellipsoid is, in fact, a sphere. If diffusion is equal in two directions and faster in the third, the ellipsoid is prolate, with its main axis pointing along the direction of faster diffusion. Similar reasoning can be used for other cases. A crucial point to take into consideration is that the shape of the ellipsoid is connected to the shape of the container inside which diffusion is happening (the pores or channels inside a porous medium, for example). However, for the confinement to become influential and its structural features to be correctly reflected by the diffusion ellipsoid, molecules need to diffuse far enough to feel the restrictions of the container. Recalling the structural and diffusion length previously introduced, the diffusion ellipsoid would appear spherical whenever $l_D \ll l_S$. Since for a given molecule diffusing in a structure both D and l_S are fixed, the parameter that must be adjusted in order to correctly probe the structure is the diffusion time Δ. The longer the diffusion time is, the bigger the characteristic structural lengths that can be probed with meaningful results. In this paper, we propose an alternative to the PGSTEbp experiment that granted access to much longer diffusion times.

Finally, information about the shape of the diffusion tensor is often conveyed in the form of a single index known as fractional anisotropy (FA), calculated as follows (Basser and Pierpaoli, 1996):

$$\mathrm{FA} = \sqrt{1 - \frac{D_x D_y + D_x D_z + D_y D_z}{{D_x}^2 + {D_y}^2 + {D_z}^2}}. \tag{4}$$

The fractional anisotropy value ranges from 0 to 1, with 0 obtained in the case of isotropic diffusion and 1 in a fully anisotropic structure such as a long, thin channel.

2.2 Singlet-assisted DTI

As briefly introduced above, long-lived spin order can provide access to very long diffusion times. This form of order has already been exploited in this respect to measure small diffusion coefficients (Sarkar et al., 2008; Ahuja et al., 2009) or slow flow (Pileio et al., 2015). Here, we aim to combine the latest methodologies for the manipulation of this form of spin order with the more conventional DTI technique discussed earlier. Our proposed methodology is based on the pulse sequence illustrated in Figure 1B (pulse sequence code, in the Bruker TopSpin language, is available upon request) and has been labeled as SAD-TI (singlet-assisted diffusion tensor imaging). In our approach, as in PGSE and PGSTE, the well-studied (Pileio, 2017) singlet preparation (M2S) and reading (S2M) pulse sequence blocks have been sensitized to molecular diffusion with the introduction of a bipolar pulsed field gradient. Specifically, two opposite-in-sign field gradients are placed before and after the 180° radiofrequency pulse within the first echo train of the M2S block. From that time point onwards, molecular position is encoded until a second identical bipolar gradient is applied after the diffusion time Δ, as shown in Figure 1B. At the end of the M2S block, diffusion-sensitized magnetization has been converted to diffusion-sensitized long-lived order, which provides access to much longer diffusion times than those available with spin-echo or stimulated-echo experiments, where diffusion encoding is performed on transverse and longitudinal order, respectively. This is because the decay time constant of singlet order, T_S, is often more than an order of magnitude longer than the decay time constant of transverse order (T_2, exploited in PGSE) and longitudinal order (T_1, exploited in PGSTE). The values of n_1, n_2, and τ_e occurring in the M2S/S2M blocks are indicated in the caption of Figure 1.

It is worth noting that the minimum Δ accessible with this method is limited by the cumulative duration of the part of the M2S after the bipolar gradient, the duration of the singlet filter, and the initial duration of the S2M until the gradient. This minimum time is of the order of several hundreds of milliseconds. Moreover, the maximum amount of initial polarization that is detectable after the sequence M2S–filter–S2M is theoretically limited to 2/3 (Pileio, 2017) (and in practice generally found to be ~1/2 because of pulse imperfections and T_2-driven losses during the echo trains), and this signal loss must be weighed against the benefits of accessing a much longer timescale. In order to obtain the six independent components of the diffusion tensor in the laboratory frame in the SAD-TI experiment, Eq. 3 is fitted to the signal areas recorded in a series of experiments run at different values of gradient strength, one set of gradient strengths for each of the (minimum) six directions, as detailed above.

2.3 Errors on diffusion tensors and related quantities

In order to estimate the errors on the principal values and direction of the diffusion tensor, as well as on fractional anisotropy and all other quantities, we used a Monte Carlo approach implemented in a custom-made Mathematica notebook. Note that an analytic approach is also available (Poonawalla and Zhou, 2004) but here not used because unfamiliar to us. Our procedure runs as follows:

1. The standard deviation of each of the six independent diffusion coefficients is extracted from the fitting routine (we use the *NonlinearModelFit* routine in Mathematica).
2. A new diffusion tensor is built by randomly choosing a value for each of its six components using a normal distribution centered

10.3389/fchem.2023.1224336

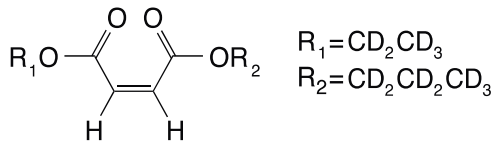

FIGURE 3
Molecular scheme of 1-(ethyl-d_5) 4-(propyl-d_7) (Z)-but-2-enedioate, used in this study as a singlet-bearing molecular probe for singlet-assisted DTI experiments.

at the parameter's best-fit value; its standard deviation is derived in step 1.

3. The new diffusion tensor is diagonalized, and eigenvalues and eigenvectors are stored in separate arrays.
4. The fractional anisotropy value and the angle between the eigenvector corresponding to the larger eigenvalue and the z-laboratory axis are calculated and stored in separate arrays (any other quantity of interest can be derived in the same way).
5. Steps 1–4 are repeated N times (50,000 in this paper).
6. The average and the standard deviation of the arrays derived via steps 3–5 (containing N sets of eigenvalues, eigenvectors, fractional anisotropies, and Euler angles) are computed and reported.

3 Materials and methods

3.1 The molecular probe

The SAD-TI method requires a molecular probe that supports long-lived spin states so that it can travel for long durations and long distances within the large channels and pores of the structure to probe its anisotropy. In our laboratory, we have custom-designed a variety of probes that suit this purpose, and for the current investigations, we used the molecule of 1-(ethyl-d_5),4-(propyl-d_7)(*Z*)-but-2-enedioate (EPM) sketched in Figure 3.

The two protons on the double bond constitute the singlet pair, whereas all the other protons have been substituted by deuterons to minimize out-of-pair dipolar relaxation contributions and prolong the singlet lifetime. The difference in chemical shift frequency between the two protons is 3.1 ppb (0.93 Hz in our 7.04 T magnet), and their mutual scalar coupling constant is 11.9 Hz. These values qualify the magnetic properties of the molecular probe as a nearly equivalent spin system. In such systems, singlet order is a good eigenvalue of the high-field spin Hamiltonian and remains long-lived without the need for singlet-locking irradiation, which would not be compatible with diffusion experiments because it can generate heat and related convective flow. The isotropic diffusion coefficient for this molecule, measured in an isotropic liquid sample prepared as a 0.25 M solution of EPM in acetone-d_6 in a 10-mm OD NMR tube, is $D_0 = 1.6 \times 10^{-9}$ $m^2\,s^{-1}$ (obtained using a standard convection-compensated PGdSTEbp pulse sequence).

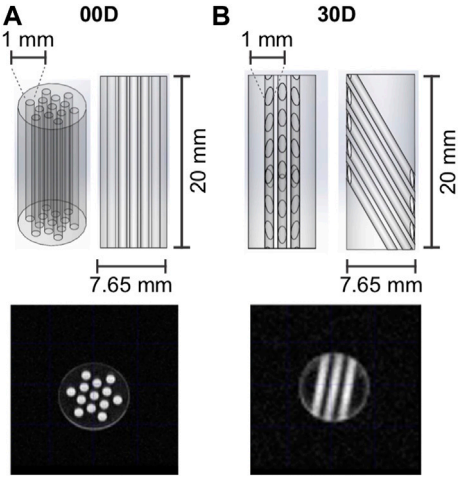

FIGURE 4
Geometry and dimensions of channel structures **(A)** 00D and **(B)** 30D, which were used in the experiments reported in this paper. The MRI images were generated with a multi-slice multi-echo (MSME) sequence (FOV 2 × 2 cm^2, 128 × 128 matrix, slice thickness 1 cm, TE = 5.08 ms). Sagittal slices (not shown) were taken to confirm that all channels were fully filled with the EPM solution.

3.2 Structures under investigation

To demonstrate the potential of the SAD-TI methodology, we measured the diffusion tensor of our probe molecule dissolved in a low-viscosity liquid and contained in the long, narrow cylindrical channels cut into the plastic structures shown in Figure 4. Both structures were machined in-house from a rod of polyoxymethylene (POM; this was chosen because it has good resistance to many common organic solvents and is easy to machine). The outer diameter of each structure was 7.65 mm, and the length was 20 mm. Structure 00D (Figure 4A) contained 13 cylindrical channels of 1 mm diameter. The total volume of the 13 channels was 204 mm^3. The long axis of the channels was oriented along the long axis of the rod, a fact that we indicate as $\theta = 0^\circ$. The angle θ is intended to represent the angle between the long axis of the channels and that of the rod. However, the manufactured structures were additionally aligned with their long axis parallel to the direction of the static magnetic field. Hence, θ also represents the angle between the long axis of the channels and the static magnetic field. Structure 30D (Figure 4B) had 15 cylindrical channels of 1 mm diameter oriented such that their long axis formed an angle $\theta = 30^\circ$ with respect to the long axis of the rod. The total volume of the empty channels in structure 30D was 127 mm^3. Both plastic structures were held within a 10-mm OD (7.8 mm ID) medium-wall LPV NMR tube. The volume of the annular cylinder arising between the tube ID and the plastic OD was 36 mm^3, and molecules trapped in this region of space experienced a different form of constriction to those trapped in the cylindrical channels.

Structures 00D and 30D were imbibed in 350 μL of a 0.25 M solution of EPM in acetone-d_6. The NMR tubes were then degassed through 10 cycles of freeze–pump–thaw to minimize the O_2 content and hence prolong relaxation times. MRI images of the tubes were

taken to confirm that all channels were properly filled with the EPM solution (see Figure 4).

3.3 Instrumentation

All experiments were run on an Oxford Inst. 7.04 T Magnet coupled to an Avance III Bruker NMR console. This instrument is equipped with a Bruker MIC5 microimaging probe carrying a 10-mm $^{1}H/^{13}C$ resonator and a 3-axis gradient system able to deliver pulsed field gradients of up to 1.5 T m^{-1}. The samples were maintained at room temperature (21°C), and the probe's temperature controller was turned off in order to achieve a more uniform sample temperature and minimize convection flow, although thermal convection is here negligible given the relatively small diameter of the channels.

3.4 Numerical simulations

In this paper, we present numerical simulations for comparison with experimental data. The routines developed to calculate the diffusion tensor in the structures discussed in Section 3.1 were written in Mathematica (simulation code available upon request). Simulations were based on a simple random-walk approach comprising the following steps (for each structure and each value of diffusion time):

1. The actual sample shape and geometry are reconstructed using the concept of *Region* in Mathematica.
2. The experimentally measured isotropic diffusion coefficient D_0 and the diffusion time Δ used in the experiment are entered.
3. The total number of molecules is set to N_M = 10,000.
4. The total number of random steps is set to N_J = 10,000. This represents the number of steps that each molecule takes during the diffusion time Δ; hence, the time step (how long a step lasts) is derived as $t_s = \Delta/N_J$.
5. An array of N_M initial molecular positions $r_i = (x_i, y_i, z_i)$ is randomly generated such that all molecules lie within the voids of the structure (i.e., within the channels or the annular cylinder formed between the inner wall of the tube and the outer wall of the plastic rod).
6. Starting from r_i, the molecular position of each of the N_M molecules is propagated for N_J steps, each step taking a length $l_s = (6\ D_0\ t_s)^{1/2}$. At each step, the new molecular positions are checked to verify that they fall within the voids of the structure, and if not, a new random step is taken. This process results in an array containing all final positions $r_f = (x_f, y_f, z_f)$ for each of the N_M molecules.
7. The $\alpha\beta$ component of the diffusion tensor ($D_{\alpha\beta}$) is derived as follows:

$$D_{\alpha\beta} = \frac{1}{2\,\Delta\,N_M}\sum_{k=1}^{N_M}\left(\alpha_{f,k} - \alpha_{i,k}\right)\left(\beta_{f,k} - \beta_{i,k}\right),$$

with $\alpha, \beta \in [x, y, z]$, k being an index that runs on the number of molecules, and the subscripts i and f indicating the initial and final positions, respectively.

TABLE 1 Longitudinal and singlet order decay constants measured in the sample investigated in this study.

Sample	T_1 (s)	T_S (s)
EPM in acetone-d_6 in 00D	22 ± 1	230 ± 10
EPM in acetone-d_6 in 30D	23 ± 1	260 ± 30

TABLE 2 Minimum and maximum values of gradient strength for the pulse sequence in Figure 1B, expressed as a percentage of the maximum gradient strength available (1.5 T m^{-1}). The last column indicates the number of transients acquired and summed upon acquisition.

Δ (S)	g_{min} (% of max)	g_{max} (% of max)	Transients
1.5	1	60	2
30	1	14	4
120	1	6.5	8
240	1	4.7	16

TABLE 3 Unit vectors for each of the six directions used in all experiments.

	d_1	d_2	d_3	d_4	d_5	d_6
α_x	1	0.447	0.447	0.447	0.447	−0.447
α_y	0	0.895	0.277	−0.724	−0.724	−0.277
α_z	0	0	0.850	−0.525	0.525	0.850

8. Once the six independent $D_{\alpha\beta}$'s are calculated, the full diffusion tensor is constructed and diagonalized, and parameters such as the apparent isotropic diffusion coefficient and the fractional anisotropy value are calculated.

4 Results and discussion

Before proceeding with the measurement of the diffusion tensor, we measured the decay constant of the longitudinal and singlet orders, T_1 and T_S, respectively, for the two structures investigated here. T_1 was measured with a standard saturation recovery technique, and T_S was measured with the M2S/S2M pulse sequence (Pileio et al., 2010; Tayler and Levitt, 2011). The results are summarized in Table 1. The small differences in these parameters across the two structures were within errors and are most likely due to differences in the quality of the degassing procedure.

The lifetime of singlet order is, therefore, approximately 13 times longer than that of longitudinal order, in this particular case. Lifetime enhancement factors of up to 140-fold have been observed (Stevanato et al., 2015).

To demonstrate the advantages of the SAD-TI procedure and define its limits, we ran the pulse sequence shown in Figure 1B on both 00D and 30D structures. For each structure, experiments were repeated at four different values of diffusion time Δ (namely, 1.5, 30, 120, and 240 s), with the purpose of highlighting the limits of conventional DTI against the benefits of SAD-TI. For each value of Δ, the gradient strength g was incremented in eight steps, linearly spaced within the limits indicated in

TABLE 4 Experimental and simulated results of the SAD-TI procedure on 00D and 30D at different values of diffusion time. The diffusion length l_D is calculated using the measured isotropic diffusion coefficient and the actual value of Δ. Differences are calculated as experimental minus simulated values divided by experimental values.

		Experiments			Simulations			Difference		
Δ (s)	l_D (μm)	D_0^a (10^{-9} m s^{-2})	FA	θ (°)	D_0^a (10^{-9} m s^{-2})	FA	θ (°)	D_0^a	*FA*	θ
00D										
1.5	70	1.66 ± 0.04	0*	65 ± 28	1.45	0.08	2.5	13%	—	—
30	310	1.25 ± 0.05	0.27 ± 0.04	0.9 ± 3	1.17	0.27	0.8	6%	0%	11%
120	620	0.92 ± 0.02	0.59 ± 0.01	0.3 ± 0.1	0.88	0.59	0.3	4%	0%	0%
240	875	0.83 ± 0.02	0.86 ± 0.02	1 ± 0.1	0.72	0.74	0.5	13%	14%	50%
30D										
1.5	70	1.65 ± 0.03	0*	64 ± 26	1.45	0.07	13.4	12%	—	—
30	310	1.27 ± 0.03	0.27 ± 0.02	29.3 ± 2	1.17	0.27	24.7	8%	0%	16%
120	620	0.87 ± 0.06	0.62 ± 0.02	29.3 ± 1	0.85	0.57	27.1	2%	8%	8%
240	875	0.72 ± 0.02	0.84 ± 0.02	32.0 ± 0.4	0.72	0.69	27.0	0%	18%	16%

Table 2. The duration of the diffusion-sensitizing gradients was kept fixed at $\delta = 320\ \mu$s. The strengths and durations of the gradients in the T_{00} filter were $g_A = -g_B = -g_C = 45$ mT m^{-1} (3% of maximum), $\delta_A = 1.0$ ms, $\delta_B = 1.2$ ms, and $\delta_C = 2.2$ ms.

The unit vectors for the six directions were chosen from those suggested by Jones et al. (1999) and are summarized in Table 3.

The values of the parameters in the M2S/S2M blocks in the pulse sequence were experimentally optimized around the theoretical values and found to be $n_1 = 20$, $n_2 = 10$, and $\tau_e = 41.8$ ms.

The results of the SAD-TI procedure are reported in Table 4. Instrumental differences in the gradient performances along different directions were corrected by independently calibrating the gradients along each direction, such that the SAD-TI experiment with $\Delta = 1.5$ s resulted in an exactly spherical (i.e., isotropic) tensor. This was effectively achieved by multiplying each of the unit vectors in Table 3 by a correction factor calculated as follows:

$$c_i = \frac{D_i}{\Sigma_{i=1}^{n_d} D_i}, \tag{5}$$

where c_i is the correction factor for the ith-direction, D_i is the diffusion coefficient measured along the ith-direction in our SAD-TI experiment with $\Delta = 1.5$ s, and the term in the denominator is effectively the average diffusion coefficient along the n_d directions (six in our case). The success of this calibration procedure results in a perfectly null FA value for the $\Delta = 1.5$ s case.

As expected, at very short diffusion times (of the order of a few seconds), it was not possible to measure either the correct fractional anisotropy or the orientation of the channels with respect to the magnetic field. At modestly long diffusion times (of the order of ~3T_1), the channel orientation was correctly obtained, although the measured fractional anisotropy was quite far from the expected value of ~0.95 for a cylinder of 1 mm radius and 20 mm length. Our numerical simulations of the diffusion tensor in the actual geometries were in good agreement with the experimental values, despite the low level of sophistication of the model used to simulate the random walks and the relatively low number of random steps and molecules employed. To obtain a correct value for FA, a diffusion time of several minutes was required. This can be explained as follows: in order to track the channel orientation, it is sufficient merely to identify the direction associated with the largest eigenvalue of the diffusion tensor, no matter the exact value of the diffusion coefficients along each principal direction. For this reason, the channel orientation was correctly measured even at relatively short diffusion times (note that this still required diffusion times of tens of seconds). To properly characterize the FA, the limiting value of the diffusion coefficient along each principal direction must be correctly measured, and for this to happen, a diffusion time that allows for a diffusion length of the order of the characteristic length of the structure must be used. To further highlight the importance of the technique, we plotted the diffusion constant measured for structure 00D along each principal direction at different values of diffusion time, normalized to the isotropic diffusion constant (Figure 5). The plot shows that diffusion is essentially free along the *z*-direction (coinciding with the long axis of the channels) and restricted, to an equivalent extent, along the two perpendicular directions. In a structure with connected pores, the value of $D_{\alpha\beta}(\Delta)/D_0$ tends to be $1/\alpha$ for sufficiently long diffusion time Δ, with α representing the tortuosity (Latour et al., 1993), i.e., the ratio of the effective path length to the shortest path length in a porous medium. Tortuosity is, therefore, an indicator of pore connectivity and, as such, a fundamental quantity in understanding fluid transport through the material.

Although tortuosity is not explicitly addressed in this paper, Figure 5 demonstrates how the singlet-assisted DTI technique presented here can provide easy access to the value of tortuosity along the three principal directions of a porous medium with large pores.

To make a fair comparison with other techniques, this same information can be accessed through conventional DTI (PGSTE-based) if a molecule with very long T_1 or a larger diffusion constant is available. Assuming that relaxation is dominated by a dipole–dipole interaction, as is often the case for small molecules in non-viscous liquids, minutes-long T_1 values are rare and usually linked to nuclei with a low gyromagnetic ratio, whose NMR sensitivity is often the limiting factor in diffusion studies within porous media. The use of gases, whose self-diffusion coefficients are 4–5 orders of magnitude greater than those of liquids, is a good alternative, since the molecules can move much further, even within a short diffusion time. The use of hyperpolarized-Xe has indeed been proposed for diffusion studies of

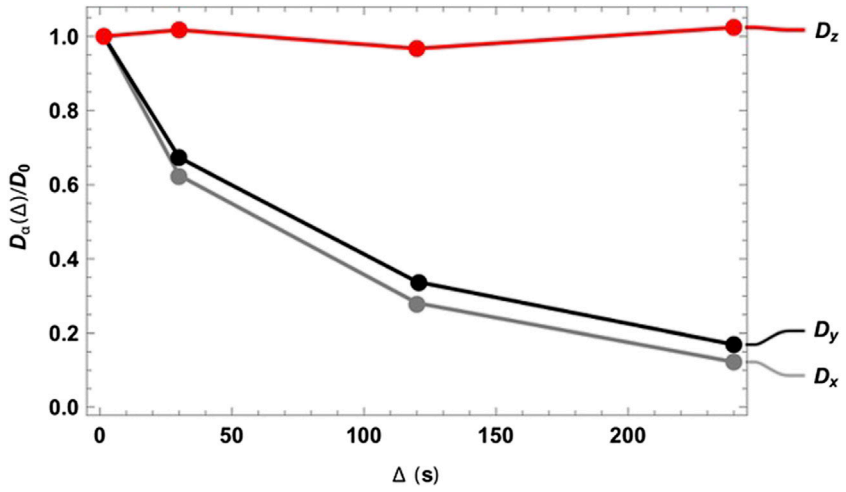

FIGURE 5
Diffusion constant measured for structure 00D along the three principal directions normalized to the isotropic diffusion constant and plotted against the diffusion time Δ. The rapid drop observed in the *x* and *y* principal directions reflects restricted motion in that plane. No restriction is observed in the *z* principal direction, since this coincides with the long axis of the channel.

a similar nature (Mair et al., 2001), but again, the low sensitivity requires hyperpolarization, which adds a level of complication and requires specific expertise and relatively costly equipment. Our technique can easily be implemented using conventional high-resolution NMR hardware, and this constitutes a clear advantage over other techniques.

5 Conclusion

We have presented a singlet-assisted version of the well-known diffusion tensor imaging technique that provides access to measurements of the full diffusion tensor of molecules diffusing within porous media with large pores. The diffusion tensor can be used to access structural information such as fractional anisotropy, pore geometry, and orientation, as well as tortuosity, an important parameter that has so far been inaccessible to NMR, since conventional DTI fails to accurately measure it in structures with pores above 50–100 microns in size. Structures containing such large pores include battery electrodes, scaffoldings for tissue engineering, and certain rocks.

Data availability statement

The raw data supporting the conclusions of this article will be made available by the authors, without undue reservation.

Author contributions

GM: methodology development, investigation, and formal analysis. FG: methodology development, investigation, and resources. SR: investigation and formal analysis. GP: conceptualization, methodology development, supervision, validation, funding acquisition, and writing—review and editing. All authors contributed to the article and approved the submitted version.

Funding

This research was supported by the EPSRC UK (grant no: EP/N033558/1) and the Leverhulme Trust Research Project (grant no: RPG-2019-298).

Acknowledgments

The authors would like to thank Monique C. Tourell for useful discussions.

Conflict of interest

The authors declare that the research was conducted in the absence of any commercial or financial relationships that could be construed as a potential conflict of interest.

Publisher's note

References

Ahuja, P., Sarkar, R., Vasos, P. R., and Bodenhausen, G. (2009). Diffusion coefficients of biomolecules using long-lived spin states. *J. Am. Chem. Soc.* 131 (22), 7498–7499. doi:10.1021/ja902030k

Basser, P. J., and Jones, D. K. (2002). Diffusion-tensor MRI: Theory, experimental design and data analysis - a technical review. *NMR Biomed.* 15 (7-8), 456–467. doi:10.1002/nbm.783

Basser, P. J., Mattiello, J., and LeBihan, D. (1994). MR diffusion tensor spectroscopy and imaging. *Biophysical J.* 66 (1), 259–267. doi:10.1016/s0006-3495(94)80775-1

Basser, P. J., and Pierpaoli, C. (1996). Microstructural and physiological features of tissues elucidated by quantitative-diffusion-tensor MRI. *J. Magn. Reson B* 111 (3), 209–219. doi:10.1006/jmrb.1996.0086

Bullitt, E., Gerig, G., Pizer, S. M., Lin, W. L., and Aylward, S. R. (2003). Measuring tortuosity of the intracerebral vasculature from MRA images. *Ieee Trans. Med. Imaging* 22 (9), 1163–1171. doi:10.1109/Tmi.2003.816964

Callaghan, P. T. (2011). *Translational dynamics & magnetic resonance*. Oxford: Oxford University Press.

Gobel, M., Godehardt, M., and Schladitz, K. (2017). Multi-scale structural analysis of gas diffusion layers. *J. Power Sources* 355, 8–17. doi:10.1016/j.jpowsour.2017.03.086

Hurlimann, M. D., Helmer, K. G., Latour, L. L., and Sotak, C. H. (1994). Restricted diffusion in sedimentary rocks. Determination of surface-area-to-volume ratio and surface relaxivity. *J. Magnetic Reson. Ser. A* 111 (2), 169–178. doi:10.1006/jmra.1994.1243

Jones, D. K., Horsfield, M. A., and Simmons, A. (1999). Optimal strategies for measuring diffusion in anisotropic systems by magnetic resonance imaging. *Magn. Reson Med.* 42 (3), 515–525. doi:10.1002/(sici)1522-2594(199909)42:3<515::aid-mrm14>3.0.co;2-q

Kuchel, P. W., Coy, A., and Stilbs, P. (1997). NMR "diffusion-diffraction" of water revealing alignment of erythrocytes in a magnetic field and their dimensions and membrane transport characteristics. *Magnetic Reson. Med.* 37 (5), 637–643. doi:10.1002/mrm.1910370502

Latour, L. L., Mitra, P. P., Kleinberg, R. L., and Sotak, C. H. (1993). Time-Dependent diffusion-coefficient of fluids in porous-media as a probe of surface-to-volume ratio. *J. Magnetic Reson. Ser. A* 101 (3), 342–346. doi:10.1006/jmra.1993.1056

Mair, R. W., Hurlimann, M. D., Sen, P. N., Schwartz, L. M., Patz, S., and Walsworth, R. L. (2001). Tortuosity measurement and the effects of finite pulse widths on xenon gas diffusion NMR studies of porous media. *Magn. Reson. Imaging* 19 (3-4), 345–351. doi:10.1016/S0730-725x(01)00247-8

Momot, K. I., Pope, J. M., and Wellard, R. M. (2011). "Digital processing of diffusion-tensor images of avascular tissues," in *Medical image processing. Biological and medical Physics, biomedical engineering*. Editor G. Dougherty (New York: Springer).

Mori, S., and Tournier, J. D. (2013). *Introduction to diffusion tensor imaging: And higher order models*. Second edition. Amsterdam, Netherlands: Elsevier Inc. doi:10.1016/C2011-0-07607-X

Park, S., Lee, J.-W., and Popov, B. N. (2012). A review of gas diffusion layer in PEM fuel cells: Materials and designs. *Int. J. Hydrogen Energy* 37 (7), 5850–5865. doi:10.1016/j.ijhydene.2011.12.148

Pierpaoli, C., Jezzard, P., Basser, P. J., Barnett, A., and DiChiro, G. (1996). Diffusion tensor MR imaging of the human brain. *Radiology* 201 (3), 637–648. doi:10.1148/radiology.201.3.8939209

Pileio, G., Carravetta, M., and Levitt, M. H. (2010). Storage of nuclear magnetization as long-lived singlet order in low magnetic field. *Proc. Natl. Acad. Sci. U. S. A.* 107 (40), 17135–17139. doi:10.1073/pnas.1010570107

Pileio, G., Dumez, J.-N., Pop, I.-A., Hill-Cousins, J. T., and Brown, R. C. D. (2015). Real-space imaging of macroscopic diffusion and slow flow by singlet tagging MRI. *J. Magnetic Reson.* 252, 130–134. doi:10.1016/j.jmr.2015.01.016

Pileio, G. Ed. (2020). "Long-lived nuclear spin order: Theory and applications" in *New Developments in NMR* (London: Royal Society of Chemistry). doi:10.1039/9781788019972

Pileio, G., and Ostrowska, S. (2017). Accessing the long-time limit in diffusion NMR: The case of singlet assisted diffusive diffraction q-space. *J. Magn. Reson* 285, 1–7. doi:10.1016/j.jmr.2017.10.003

Pileio, G. (2017). Singlet NMR methodology in two-spin-1/2 systems. *Prog. Nucl. Magn. Reson Spectrosc.* 98-99, 1–19. doi:10.1016/j.pnmrs.2016.11.002

Poonawalla, A. H., and Zhou, X. J. (2004). Analytical error propagation in diffusion anisotropy calculations. *J. Magnetic Reson. Imaging* 19 (4), 489–498. doi:10.1002/jmri.20020

Price, W. S., Nara, M., and Arata, Y. (1997). A pulsed field gradient NMR study of the aggregation and hydration of parvalbumin. *Biophys. Chem.* 65 (2-3), 179–187. doi:10.1016/s0301-4622(97)00003-3

Price, W. S. (2009). *NMR studies of translational motion*. Cambridge: Cambridge University Press.

Price, W. S., Tsuchiya, F., Suzuki, C., and Arata, Y. (1999). Characterization of the solution properties of Pichia farinosa killer toxin using PGSE NMR diffusion measurements. *J. Biomol. NMR* 13 (2), 113–117. doi:10.1023/a:1008394716710

Sarkar, R., Ahuja, P., Vasos, P. R., and Bodenhausen, G. (2008). Measurement of slow diffusion coefficients of molecules with arbitrary scalar couplings via long-lived spin states. *ChemPhysChem* 9 (16), 2414–2419. doi:10.1002/cphc.200800476

Stejskal, E. O., and Tanner, J. E. (1965). Spin diffusion measurements: Spin echoes in the presence of a time-dependent field gradient. *J. Chem. Phys.* 42 (1), 288–292. doi:10.1063/1.1695690

Stevanato, G., Hill-Cousins, J. T., Hakansson, P., Roy, S. S., Brown, L. J., Brown, R. C. D., et al. (2015). A nuclear singlet lifetime of more than one hour in room-temperature solution. *Angew. Chemie-International Ed.* 54 (12), 3740–3743. doi:10.1002/anie.201411978

Tayler, M. C. D., and Levitt, M. H. (2011). Singlet nuclear magnetic resonance of nearly-equivalent spins. *Phys. Chem. Chem. Phys.* 13 (13), 5556–5560. doi:10.1039/c0cp02293d

Thorat, I. V., Stephenson, D. E., Zacharias, N. A., Zaghib, K., Harb, J. N., and Wheeler, D. R. (2009). Quantifying tortuosity in porous Li-ion battery materials. *J. Power Sources* 188 (2), 592–600. doi:10.1016/j.jpowsour.2008.12.032

Tourell, M. C., Pop, I.-A., Brown, L. J., Brown, R. C. D., and Pileio, G. (2018). Singlet-assisted diffusion-NMR (SAD-NMR): Redefining the limits when measuring tortuosity in porous media. *Phys. Chem. Chem. Phys.* 20 (20), 13705–13713. doi:10.1039/C8CP00145F

frontiers | Frontiers in Chemistry

TYPE Original Research
PUBLISHED 10 August 2023
DOI 10.3389/fchem.2023.1239964

OPEN ACCESS

EDITED BY
Bogdan-George Rusu,
Institute of Macromolecular Chemistry "Petru Poni", Romania

REVIEWED BY
Angélique Bousquet,
Université Clermont Auvergne, France
Phitsanu Poolcharuansin,
Mahasarakham University, Thailand

*CORRESPONDENCE
Ioana-Laura Velicu,
laura.velicu@uaic.ro

RECEIVED 14 June 2023
ACCEPTED 31 July 2023
PUBLISHED 10 August 2023

CITATION
Matei T, Tiron V, Jijie R, Bulai G, Velicu I-L, Cristea D and Crăciun V (2023), Band-gap engineering of zirconia by nitrogen doping in reactive HiPIMS: a step forward in developing innovative technologies for photocatalysts synthesis.
Front. Chem. 11:1239964.
doi: 10.3389/fchem.2023.1239964

Band-gap engineering of zirconia by nitrogen doping in reactive HiPIMS: a step forward in developing innovative technologies for photocatalysts synthesis

Teodora Matei[1], Vasile Tiron[2], Roxana Jijie[2], Georgiana Bulai[3], Ioana-Laura Velicu[1]*, Daniel Cristea[4] and Valentin Crăciun[5,6]

[1]Faculty of Physics, Alexandru Ioan Cuza University of Iasi, Iasi, Romania, [2]Research Center on Advanced Materials and Technologies, Department of Exact and Natural Sciences, Institute of Interdisciplinary Research, Alexandru Ioan Cuza University of Iasi, Iasi, Romania, [3]Integrated Center of Environmental Science Studies in the North-Eastern Development Region (CERNESIM), Department of Exact and Natural Sciences, Institute of Interdisciplinary Research, Alexandru Ioan Cuza University of Iasi, Iasi, Romania, [4]Department of Materials Science, Faculty of Materials Science and Engineering, Transilvania University, Brasov, Romania, [5]National Institute for Laser, Plasma and Radiation Physics, Măgurele, Romania, [6]Extreme Light Infrastructure for Nuclear Physics, Măgurele, Romania

In the global context of climate change and carbon neutrality, this work proposes a strategy to improve the light absorption of photocatalytic water-splitting materials into the visible spectrum by anion doping. In this framework, reactive high power impulse magnetron sputtering (HiPIMS) of a pure Zr target in $Ar/N_2/O_2$ gas mixture was used for the deposition of crystalline zirconium oxynitride ($ZrO_{2-x}N_x$) thin films with variable nitrogen doping concentration and energy band-gap. The nitrogen content into these films was controlled by the discharge pulsing frequency, which controls the target surface poisoning and peak discharge current. The role of the nitrogen doping on the optical, structural, and photocatalytic properties of $ZrO_{2-x}N_x$ films was investigated. UV-Vis-NIR spectroscopy was employed to investigate the optical properties and to assess the energy band-gap. Surface chemical analysis was performed using X-ray photoelectron spectroscopy, while structural analysis was carried out by X-ray diffraction. The increase in the pulse repetition frequency determined a build-up in the nitrogen content of the deposited $ZrO_{2-x}N_x$ thin films from ~10 to ~25 at.%. This leads to a narrowing of the optical band-gap energy from 3.43 to 2.20 eV and endorses efficient absorption of visible light. Owing to its narrow bandgap, $ZrO_{2-x}N_x$ thin films obtained by reactive HiPIMS can be used as visible light-driven photocatalyst. For the selected processing conditions (pulsing configuration and gas composition), it was found that reactive HiPIMS can suppress the hysteresis effect for a wide range of frequencies, leading to a stable deposition process with a smooth transition from compound to metal-sputtering mode.

KEYWORDS

reactive HiPIMS, band-gap engineering, photocatalytic activity, hysteresis effect, zirconium oxynitride thin film

1 Introduction

Solar energy, by utilizing various pathways for conversion, has the potential to play a vital role in the ambitious global pursuit of achieving net-zero greenhouse gas emissions by 2050. Despite claims from the harshest critics that the manufacturing of photovoltaic and photocatalytic integrated systems consumes significant amounts of energy and relies on the extraction of finite Earth minerals with severe environmental impacts, these technologies are continuously advancing. In fact, solar energy has already reached a point where it is cost-competitive with traditional methods of power generation. Furthermore, the implementation of effective circular economy strategies, along with the ongoing development of the mineral recycling industry, aims to minimize the negative consequences associated with mining. This makes solar energy an environmentally friendly technology, representing an extraordinary source of renewable and green energy. Photocatalytic technologies, such as solar fuels production, self-cleaning capabilities, and environmental remediation, have the potential to significantly contribute to the growth of sustainable energy markets.

In this context, zirconium oxide (ZrO_2), commonly known as zirconia, stands out as an exceptional, unique, and highly versatile semiconductor. It finds widespread use due to its remarkable properties, including a high melting point, thermal stability, resistance to corrosion and hardness, chemical inertness, good biocompatibility, and optical transparency. The combination of these exceptional properties opens up a range of interesting and attractive applications. For instance, zirconia can be employed in indoor and outdoor architectural coatings, conventional and flexible optoelectronic devices (Venkataraj et al., 2002), shape memory alloys (Jette et al., 2021), and, of particular significance in the pursuit of decarbonization, as photocatalysts for hydrogen fuel production (Teeparthi et al., 2018; Besisa and Ewais, 2021).

However, when it comes to solar energy applications, zirconia photocatalysts face a challenge due to their wide band-gap [$E_g \simeq 5.1$ eV (Teeparthi et al., 2018)]. This characteristic leads to low efficiency in utilizing solar energy. In addition to charge separation and charge utilization efficiencies, the overall efficiency of a photocatalyst in converting solar energy depends directly on its ability to harness solar energy effectively. One approach to enhance this crucial aspect of a photocatalyst is by manipulating its band gap through band gap engineering, thereby extending its light absorption range from ultraviolet (UV) to visible light. One feasible method to achieve this is by introducing nitrogen as a dopant into the zirconium oxide lattice. This approach narrows the optical band gap, allowing for tailored optical performance and rendering the photocatalyst sensitive to visible light.

Strategies to produce Zr oxynitrides ($ZrO_{2-x}N_x$) involve two main approaches: controlled oxidation of zirconium nitride (Wiame et al., 1998) and nitridation of zirconia (Lerch, 1996). However, both of these methods typically require high processing temperatures, which can limit their application when dealing with heat-sensitive materials that need to be coated. In industrial-scale production, the synthesis of metal oxynitrides, including Zr oxynitrides, often relies on reactive magnetron sputtering. This method offers several advantages (Bräuer et al., 2010). Firstly, it allows for the deposition of high-density films and coatings with excellent thickness uniformity and strong adhesion to substrates. Additionally, reactive magnetron sputtering enables high deposition rates, providing efficient production capabilities. The process also offers good controllability, allowing for precise manipulation of the deposition parameters. Moreover, it demonstrates long-term stability, ensuring consistent and reliable outcomes. Furthermore, reactive magnetron sputtering is a relatively cost-effective deposition method, making it economically viable for large-scale production. Lastly, it offers the advantage of being able to uniformly coat large and heat-sensitive materials, expanding its potential applications.

Reactive magnetron sputtering is a process commonly used in thin film deposition. It involves sputtering a metallic target in a gas mixture of argon and a reactive gas. The compound coating is formed through the chemical reaction between the sputtered material and the reactive gas species at the substrate. The chemical composition of the resulting compound film can be controlled by adjusting the flux ratio of the sputtered material and the reactive gas. During reactive sputtering, particularly in the metal oxide mode, a phenomenon known as hysteresis effect can occur. This effect arises due to the formation of a compound film on the target surface and the inner walls of the deposition chamber. This effect can lead to process instability and significantly reduced sputtering efficiency (Greene, 2017). To ensure a stable and reproducible deposition process, it is necessary to suppress or eliminate this hysteresis effect. In addition to stabilizing the reactive deposition process, it is also important to control the transition between metal and compound-sputtering modes. This enables the growth of stoichiometric compound thin films at high deposition rates. When two different reactive gases are used, more complex processes come into play, including mixed target poisoning mechanisms (Van Bever et al., 2022), double hysteresis (Depla et al., 2006), and "process trapping" effects (Báranková et al., 1995). In such cases, experimental findings have shown that the transition zone and the width of the hysteresis loop depend strongly on the mass flow rates of oxygen and nitrogen (Martin and Rousselot, 1999). However, Severin et al. (2006) demonstrated that by using two reactive gases, such as oxygen and nitrogen, instead of just one (e.g., oxygen), it is possible to stabilize the transition zone.

The operation of magnetron sputtering in a high-power pulsed regime offers several advantages, including the ability to achieve transient regimes where physical and chemical processes can rapidly evolve under optimal conditions. This ensures excellent process stability and reproducibility. High-power impulse magnetron sputtering (HiPIMS) is a variant of this technique, characterized by the application of unipolar power pulses with high magnitude, low frequency, and low duty cycle to the conventional sputtering magnetron cathode (Kouznetsov et al., 1999). These pulses result in a high instantaneous plasma density. The elevated plasma density in HiPIMS facilitates the generation of highly ionized fluxes consisting of both metal and gas species, whose energy and direction can be controlled during the film deposition process using electric and/or magnetic fields (Tiron et al., 2012). The energetic ion bombardment occurring during film deposition enhances the synthesis of materials with superior properties compared to those obtained through conventional magnetron sputtering (Sarakinos et al., 2010). When compared to reactive direct current magnetron sputtering (dcMS), reactive HiPIMS, if configured properly, allows for the

suppression or elimination of the undesired hysteresis effect without the need for feedback control systems (Sarakinos et al., 2008; Aiempanakit et al., 2011). Wallin et al. propose that the elimination or suppression of the hysteresis effect during reactive HiPIMS could be attributed to factors such as high erosion rate during the pulse, limited target oxidation between pulses, and gas rarefaction effects in front of the target (Wallin and Helmersson, 2008).

In terms of process stability, one of the challenges encountered in the reactive HiPIMS process is the occurrence of arcing. However, there are strategies to suppress both arcing and hysteresis effects in reactive HiPIMS, and one such strategy is the use of short pulses. By employing short pulse durations, there is less time for charge accumulation, which effectively suppresses the development of arcing on the target surface (Tiron et al., 2020). Additionally, when maintaining a constant average power, shorter pulse durations result in higher pulsing frequencies. This, in turn, reduces target poisoning between pulses (Tiron and Sirghi, 2015), thereby suppressing the hysteresis effect. Furthermore, when aiming to synthesize highly efficient photocatalysts for sustainable development goals, it is crucial to consider environmentally friendly and versatile manufacturing technologies. HiPIMS is well-regarded in the coating industry as an excellent green and eco-friendly processing technology. It not only offers an attractive combination of properties and performances but also aligns with the goal of utilizing environmentally friendly manufacturing techniques.

The approach adopted in this study to address the hysteresis effect and control the nitrogen incorporation in zirconia films involves the use of reactive HiPIMS conditions, an optimal gas mixture of Ar-O_2-N_2, and a suitable pulsing configuration. This strategy has been previously employed to finely adjust the nitrogen content and optical band-gap in other transition metal oxynitrides, such as ZnO_xN_y (Tiron and Sirghi, 2015; Tiron et al., 2017) and TiO_xN_y (Demeter et al., 2017).

A crucial factor in controlling the nitrogen content is the low oxygen content in the gas mixture. By introducing a low amount of oxygen into the discharge, the incorporation of oxygen atoms into the coating is limited, allowing the un-oxidized metal atoms to bond with the less reactive nitrogen atoms.

Additionally, the use of short HiPIMS pulses plays a significant role in suppressing both the hysteresis effect and arcing, leading to enhanced process stability. These benefits are achieved without the need for specific approaches (Vlček et al., 2013) or feedback control systems (Sproul et al., 2005).

The photocatalytic activity of the $ZrO_{2-x}N_x$ thin films was evaluated through the photodegradation tests. The results provide insight into the films' ability to facilitate the degradation of the MB dye under visible-light exposure, demonstrating their potential for practical applications in photocatalysis.

2 Experimental details

The experiments were conducted in a high vacuum stainless steel chamber using specific equipment and parameters. A Zr sputtering target with a diameter of 50 mm and a thickness of 3 mm, possessing a purity of 99.95%, was utilized. The target was mounted on a 2" magnetron cathode configured with an unbalanced type II magnetic field, according to Window and Savvides classification (Window and Savvides, 1986).

A gas mixture comprising of high-purity argon (99.999%, flow rate of 50 sccm), nitrogen (99.999%, flow rate of 1 sccm), and oxygen (99.999%, flow rate of 0.1 sccm) was employed as the sputtering gas. The total pressure within the chamber was set to 0.8 Pa. To generate the required electrical pulses, a pulsing unit (home-built high-power pulse generator) was utilized, receiving a constant voltage from a DC power supply. The applied pulses were unipolar HiPIMS pulses with a consistent duration of 10 μs and a constant amplitude of −700 V. Various repetition frequencies were employed, ranging from 300 to 1500 Hz.

$ZrO_{2-x}N_x$ thin films were deposited onto Si (100) and quartz substrates placed 7 cm away from the target. For comparison, a reference ZrO_2 film was synthesized using a pulse repetition frequency of 800 Hz and flow rates of 50 sccm for argon, 1 sccm for oxygen, and 0 sccm for nitrogen. The deposition process did not involve any substrate bias or heating. The deposition time was set to 30 min, and the deposition rate was measured using a quartz crystal microbalance rate monitor (Q-pod, Inficon), which was positioned near the port-substrate location. Before the thin film deposition at a specific repetition frequency, a 5-min target pre-sputtering process was conducted. This step aimed to eliminate any contaminants present on the target surface and to establish stable operational conditions for the deposition process.

During the experiments, the discharge voltage and current were monitored using a digital oscilloscope (Le Croy WaveSurfer 434) equipped with a high-voltage probe (TesTec, 1:100) and a current probe (Pearson, 1 V/1A). These probes were connected to the magnetron feedthrough to capture the time evolution of the discharge parameters.

To investigate process stability and understand the relationship between the film's stoichiometry and target coverage, time-resolved optical emission spectroscopy (TR-OES) measurements were performed (Tiron et al., 2020). The optical radiation emitted by the entire plasma was concentrated onto the aperture of the monochromator using a collimating lens. Subsequently, an optical fibre was installed outside the vacuum chamber, directed towards the target surface, to transmit the focused radiation to the monochromator for further analysis. TR-OES allows for the analysis of the optical emission spectra over time, providing valuable insights into the stability of the deposition process and its impact on the resulting film's composition.

The optical transmittance of the deposited films on quartz substrates was measured across a wide wavelength range of 190–1100 nm. This measurement was carried out using a UV-Vis-NIR spectrophotometer (Evolution 300 from Thermo Scientific). The transmittance measurements enabled the evaluation of the films' optical behaviour, and the energy band-gap (E_g) was determined through Tauc plot analysis. This analysis helps to understand the film's optical properties, particularly the energy required for electronic transitions.

The chemical composition of the deposited films was analysed using X-ray Photoelectron Spectroscopy (XPS) with an ESCALB Xi + XPS system. Monochromatic AlK_α radiation was used as the X-ray source. Initially, survey scans were performed, consisting of 5 scans with a pass energy of 50.0 eV and a step size of 0.5 eV. This was followed by high-resolution scans of the core level regions of Zr, N,

C, and O, with 5 scans at a pass energy of 20.0 eV and a step size of 0.1 eV.

To remove surface contaminants, a 5-min 500 eV Ar ion sputtering step was conducted, and the XPS acquisition was repeated. The binding energies of the XPS spectra were referenced to the adventitious C1s position at 284.8 eV, providing a standard reference point for accurate analysis.

X-ray diffraction (XRD) measurements were employed to investigate the structural properties and phase analysis of the samples. The XRD patterns were recorded in the 20°-80° 2θ range, with an angle step of 0.02° and a scan speed of 1°/min. A Shimadzu LabX XRD-6000 diffractometer equipped with a CuK_α radiation source (λ = 1.54059 Å) was used in Bragg-Brentano configuration.

To evaluate the photocatalytic efficiency of the synthesized ZrO_2_x films, the degradation of MB under visible light irradiation was performed. The ZrO_xN_y films, deposited on 1 cm × 1 cm quartz substrates, were placed in a PS well with a diameter of 15.6 mm. The PS well contained 3 mL of MB solution with a concentration of 12 μg/mL, obtained from Sigma Aldrich, Darmstadt, Germany.

The experimental setup involved illuminating the $ZrO_{2-x}N_x$ films with a visible lamp emitting light with a wavelength greater than 400 nm. The incident light flux was maintained at 25 mW/cm^2 (Demeter et al., 2017). The photocatalytic reaction took place in ambient air. Before the irradiation process, the MB solution with the $ZrO_{2-x}N_x$ films was kept in the dark for 30 min to establish an absorption-desorption equilibrium.

The change in MB concentration over time during the irradiation process was monitored using a Specord 210 Plus UV-Vis spectrophotometer from Analytik Jena, Germany. The concentration values were determined based on a constructed calibration graph (y = 0.083 + 0.091x) specific to the MB dye. The degradation efficiency of the photocatalytic process was calculated using the following equation:

$$Degradation\,(\%) = \frac{C_0 - C}{C_0} \times 100 \quad (1)$$

where C_0 is the initial concentration of dye after 30 min stored in dark conditions, while C is the dye concentration after a certain irradiation time.

3 Results and discussion

3.1 Process stabilization and stoichiometry control

3.1.1 Deposition rate

Understanding the behaviour of the reactive HiPIMS process is crucial for controlling process stability, deposition rate, and the properties of the deposited films, especially their chemical composition. In this study, the relationship between target coverage and process stability, specifically the hysteresis effect, was investigated by studying the influence of pulse repetition frequency on the deposition rate. The pulse frequency was varied between 300 and 1500 Hz to observe the transition from compound (oxide) sputtering mode to metal-sputtering mode. It is important to note that all the $ZrO_{2-x}N_x$ films were deposited at repetition frequencies within the transition zone of 800–1200 Hz.

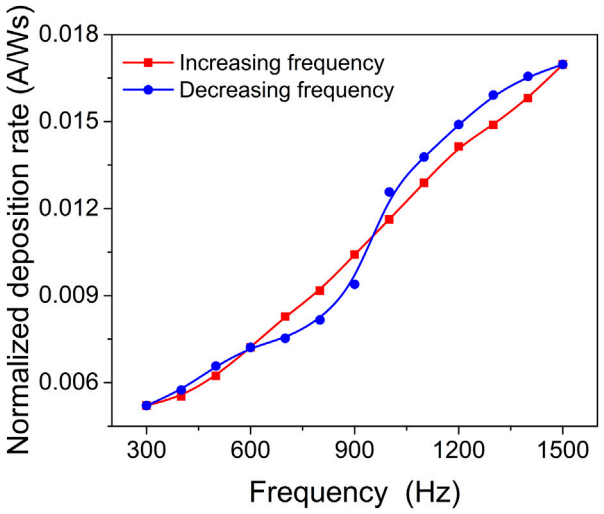

FIGURE 1
Deposition rate normalized to the average power applied to the target as a function of pulsing frequency.

Figure 1 depicts the influence of pulse repetition frequency on the deposition rate. As the average power of the HiPIMS discharge changed with the pulsing frequency (while pulse duration and amplitude were kept constant), the deposition rate was normalized to the average power. By varying the pulsing repetition frequency, a suppression of the hysteresis effect was observed, along with a smooth transition from the poisoned to metallic sputtering target mode.

These findings indicate that adjusting the pulse repetition frequency in the reactive HiPIMS process can effectively control the hysteresis effect and achieve a stable deposition process. The transition from compound sputtering mode to metallic sputtering mode can be achieved by selecting an appropriate pulsing repetition frequency. This knowledge is valuable for optimizing the deposition process and obtaining films with desired properties and chemical composition.

The suppression of hysteresis in the reactive HiPIMS discharge can be attributed to several factors. Firstly, the high erosion rate during the pulse and limited target poisoning between pulses contribute to reduced target poisoning (Sarakinos et al., 2008; Wallin and Helmersson, 2008). This means that the target surface is effectively cleaned during the pulses, and there is less build-up of deposited material between pulses. Additionally, the gas rarefaction effect, which occurs when the time between pulses is short enough to prevent gas refill in front of the target, can also contribute to hysteresis suppression (Kubart et al., 2011). This effect becomes more pronounced with increasing peak current.

In this study, as the pulse frequency increases, the power-normalized deposition rate gradually increases due to the increase in the target's effective sputtering yield. It is important to note that a small amount of oxygen was added to the sputtering gas mixture, resulting in a coexistence of a nitride and an oxide compound system at the target surface. The sputtering yield of the

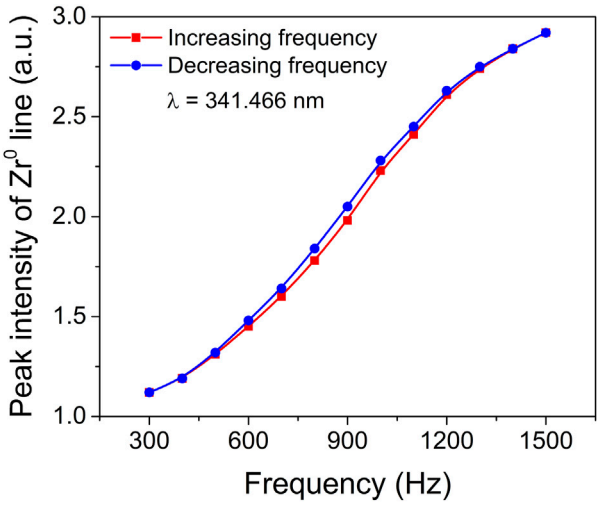

FIGURE 2
Peak intensity of Zr^0 (341.466 nm) optical emission spectral line as a function of pulsing frequency.

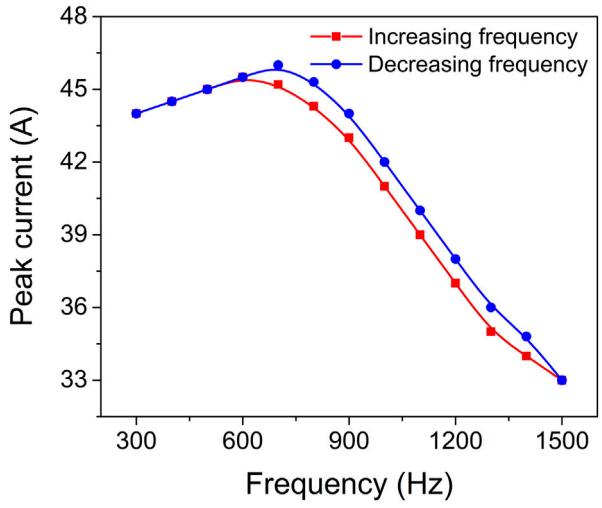

FIGURE 3
Peak current as a function of pulsing frequency.

nitride is higher than that of the corresponding oxide due to the lower binding energy of the nitride. As the pulsing frequency increases, the oxide compound is gradually removed from the target surface, shifting the surface composition from predominantly metal oxide to predominantly metal nitride, and finally to predominantly metal. This transition leads to an increase in the effective sputtering yield.

The high erosion rate during the pulses effectively cleans the target surface, while the reduced plasma off-time and limited plasma activation during the pulse off-time contribute to decreased target poisoning (Sarakinos et al., 2008). The synergistic effect between the increase in effective sputtering yield and the decrease in ion peak current (reduced ion return effect) results in a maximum deposition rate observed at high pulsing repetition frequencies.

Overall, by increasing the pulsing frequency in the reactive HiPIMS process, the hysteresis effect is suppressed through enhanced target surface cleaning, reduced target poisoning, and a favourable shift in the target surface composition towards metal nitride. These factors contribute to an increased deposition rate and improved process stability.

3.1.2 Plasma emission

In order to gain a more comprehensive understanding of the hysteresis behaviour and process stability, a detailed investigation was carried out using time-resolved optical emission spectroscopy (TR-OES). The main objective was to explore the relationship between the deposition rate and the coverage of the target material. TR-OES proved to be a highly valuable technique in this study, as it provided crucial insights into the coverage of the target compound, which is directly related to the abundance of excited metallic species present in the plasma. To establish a correlation between the deposition rate and target coverage, the intensity of a specific Zr optical emission line at 341.466 nm was carefully recorded at various pulsing frequencies. This particular Zr spectral line is known to exhibit the highest intensity in plasma optical emission spectroscopy (Figure S1). By examining Figure 2, which illustrates the influence of pulsing frequency on the peak intensity of the Zr optical emission spectral line, we can observe the significant impact that varying pulsing frequencies have on the observed intensity levels. This comprehensive investigation utilizing TR-OES and the analysis of the Zr optical emission line intensity provides valuable insights into the intricate interplay between the deposition rate, target coverage, and the pulsing frequency. Such understanding is crucial for optimizing process stability and further enhancing our knowledge of hysteresis behaviour in the studied system.

Figure 3 depicts the gradual decrease in peak current within the frequency range of 700–1500 Hz. Interestingly, despite this trend, the peak intensity of the Zr0 optical emission spectral line exhibits a gradual increase as the pulse frequency rises. This implies that the intensity of the Zr^0 optical emission line during the pulse, and consequently the presence of Zr atoms in the gas phase, further intensify with higher pulse repetition frequencies. The observed increase in pulse frequency results in the gradual removal of the oxide compound from the target surface. Therefore, the surface transitions from being predominantly covered by metal oxide to being predominantly covered by metal nitride, and eventually to being predominantly covered by metal. The smooth transition depicted in Figure 2 demonstrates that this shift from oxide sputtering to metal sputtering occurs without any sudden jumps or steep variations, indicating a remarkably stable process. This analysis highlights the dynamic relationship between pulse frequency, target surface composition, and the resulting emission behaviour. The findings provide valuable insights into the hysteresis behaviour and process stability, shedding light on the intricate mechanisms governing the transition from oxide to metal sputtering modes.

3.1.3 Discharge peak current

To further explore the impact of deposition conditions on target coverage and process stability, the target peak current was measured as a function of pulse repetition frequency. Time evolution of the

target voltage and discharge current during HiPIMS of Zr target in argon, nitrogen and oxygen gas mixture at pressure 0.8 Pa and repetition frequency 1 kHz are depicted in Supplementary Figure S2. Figure 3 illustrates the results of this investigation. By keeping the pulse duration constant at a specific value, it was observed that varying the pulse frequency led to a corresponding change in the peak current. In particular, increasing the pulsing frequency from 700 to 1500 Hz resulted in a linear increase in the average power, ranging from 80 to 140 W, while simultaneously causing a linear decrease in the peak current, from 46 to 33 A. This trend indicates a smooth transition from a predominantly oxidized target to a predominantly nitrided one. The narrow hysteresis loop, spanning only 1 A, along with the monotonic and linear relationship between peak current and pulsing frequency, point towards excellent process stability. Consequently, within this specific frequency range, the reactive HiPIMS technology offers a remarkable capability to control the chemical composition of $ZrO_{2-x}N_x$ thin films through the modulation of peak current. This insight provides valuable opportunities to precisely tailor the properties of the thin films based on the desired chemical composition, enabling enhanced control over the overall performance and functionality of the materials.

The difference in discharge current behaviour between the compound and metal-sputtering modes can be attributed to the varying target surface coverage by oxide compounds, which has a significant impact on the secondary electron emission yield (Hippler et al., 2023).

In this work, we have observed a somewhat surprising phenomenon where the peak current during predominantly oxide mode HiPIMS of a Zr target is higher compared to the peak current during predominantly nitride mode HiPIMS. This finding contrasts with the results reported by Depla et al. (2009), who found that during reactive DCMS of a Zr target, the secondary electron emission yield (SEEY) of Zr oxide is lower than that of Zr nitride and much lower than that of Zr metal. As a result, for the same applied voltage, the discharge current should be lower during the oxide mode DCMS of a Zr target.

Interestingly, our results are more consistent with the findings reported by Aiempanakit et al. (2013) for the oxide mode HiPIMS of a Ti target. They discovered a significant difference in the discharge behavior between DCMS and HiPIMS. In oxide mode HiPIMS of a Ti target, they observed a peak current that is much higher (about two times) compared to the metal mode HiPIMS of pure Ti target.

To explain the difference in discharge behavior between DCMS and HiPIMS, Aiempanakit et al. (2013) conducted ion mass spectrometry measurements. They found that during reactive DCMS, the discharge is primarily governed by Ar^+ induced SEEY of the target surface. However, during reactive HiPIMS, the discharge is mainly governed by O^+ induced SEEY of the target surface. The increased fraction of O^+ ions in the total ionic current to the target, coupled with preferential sputtering of oxygen atoms and O^+ ion back-attraction, results in a large ionic current and an increased effective SEEY. Additionally, the self-sputtering by O^+ ions of an oxidized target leads to an increased release of secondary electrons due to the high ionization potential of 13.62 eV for O^+.

These findings provide valuable insights into the complex discharge behavior and secondary electron emission processes occurring during oxide mode HiPIMS and help to understand the observed peak current differences between oxide and nitride modes of HiPIMS for different target materials.

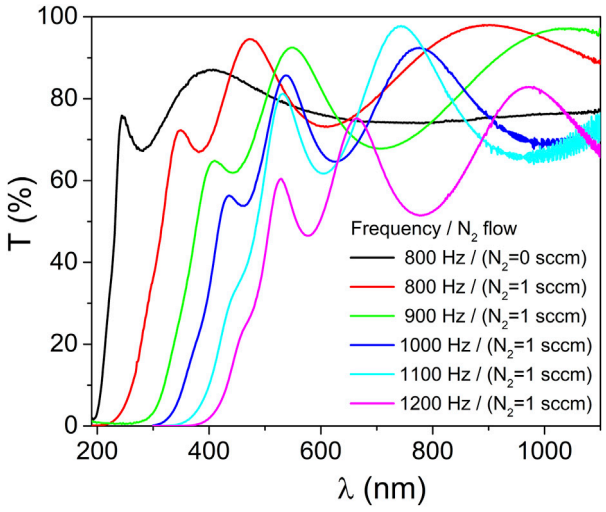

FIGURE 4
Optical transmittance of the ZrO_2 and $ZrO_{2-x}N_x$ coatings prepared at different pulsing repetition frequencies.

Based on the reported findings by Aiempanakit et al. (2013) for the oxide sputtering mode of a Ti target, it is evident that the behaviour of reactive HiPIMS of Zr target can differ from conventional dcMS. In the case of reactive HiPIMS, the higher discharge peak current observed in the oxide-sputtering mode compared to the metal/nitride-sputtering regime can be attributed to the contribution of two factors: the O^{1+} ion recycling process and the higher O^{1+} induced secondary electron emission yield (SEEY) of the oxidized Zr target surface.

During the predominantly oxide sputtering mode, there is a steep increase in the oxygen ion concentration, likely caused by the reduced sputtering yield of the oxidized metal and the limited amount of metal available (Aiempanakit et al., 2013). This is accompanied by a steep increase in the discharge current. The preferential sputtering of oxygen from the target surface, driven by the high oxygen partial sputtering yields, leads to the replacement of sputtered oxygen atoms by back-attracted O^{1+} ions. This dynamic process affects the target cleaning and contributes to the O^{1+} induced SEEY of the oxidized target, which is higher compared to the metal mode.

Since the Zr target exhibits similar behaviour to the Ti target in terms of secondary electron emission yield (SEEY), it can be expected that the same discharge current behaviour occurs during the predominantly oxide mode HiPIMS of the Zr target. As the pulsing frequency increases, the higher amount of Zr atoms available leads to more oxygen consumption, resulting in less target oxidation and a lower O^{1+} induced SEEY. Consequently, the target peak current decreases. Therefore, the higher discharge peak current observed in the oxide-sputtering mode compared to the metal/nitride-sputtering mode in reactive HiPIMS is likely influenced by the interplay of the O^{1+} ion recycling process, the higher O^{1+} induced SEEY of the oxidized target surface, and the dynamics of target oxidation and consumption. However, as values O^{1+} and Ar^+

10.3389/fchem.2023.1239964

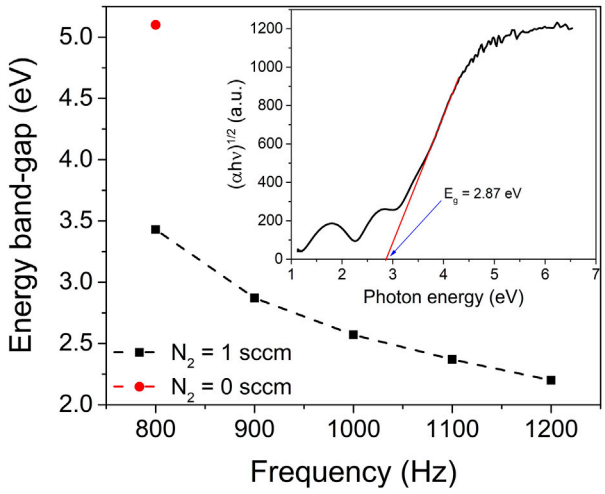

FIGURE 5
Optical band-gap of ZrO_2 (red point) and $ZrO_{2-x}N_x$ thin films (black points) prepared at different pulsing repetition frequencies. The inset shows the Tauc plot used to estimate the optical band-gap of the $ZrO_{2-x}N_x$ thin film deposited at pulsing frequency of 900 Hz. The dashed line in the figure guides the eye to help visualize trends or patterns in the data.

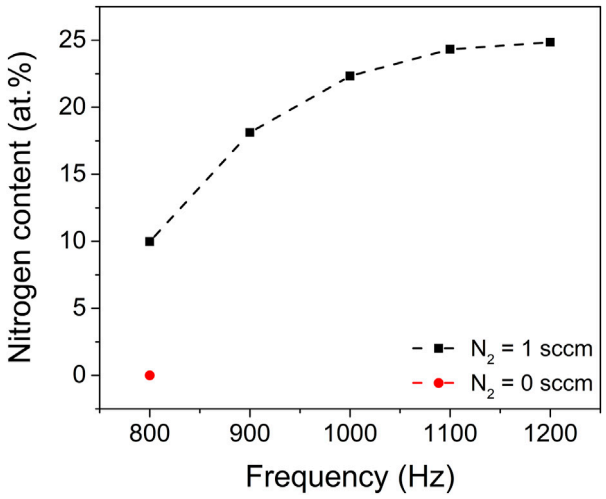

FIGURE 6
Nitrogen content in the ZrO_2 (red point) and $ZrO_{2-x}N_x$ thin films (black points) prepared at different pulsing repetition frequencies. The dash-dotted line in the figure was drawn to guide the eye.

induced SEEY of the oxidized Zr target surface are not known exactly, the results provide qualitative rather than quantitative information.

3.2 Thin films properties

3.2.1 Optical properties

The optical properties of the ZrO_2 and $ZrO_{2-x}N_x$ thin films were characterized using transmittance measurements in the wavelength range of 190–1100 nm. Figure 4 presents the optical transmittance spectra of the thin films deposited at various pulsing repetition frequency values, ranging from 800 to 1200 Hz. The reference spectrum corresponds to the optical transmittance of a zirconia (ZrO_2) thin film deposited at 800 Hz.

As depicted in Figure 4, a clear observation can be made regarding the optical properties of the ZrO_2 and $ZrO_{2-x}N_x$ films. It is evident that the optical absorption edge gradually shifts towards longer wavelengths as the HiPIMS pulse repetition frequency increases. This shift indicates a decrease in the band-gap energy of the $ZrO_{2-x}N_x$ films with higher repetition frequencies. The change in band-gap energy suggests a modification in the electronic structure of the films, potentially leading to enhanced light absorption in the visible range.

In addition to the shifting absorption edge, another notable feature in Figure 4 is the variation in the interference fringes. With increasing pulse repetition frequency, the separation between consecutive maxima of the interference fringes decreases. This observation implies that the thickness of the $ZrO_{2-x}N_x$ thin films increases as the repetition frequency is raised. The controlled tuning of film thickness through pulsing parameters is of significant interest in tailoring the optical and functional properties of thin films for various applications.

To quantitatively determine the energy band-gap, the $(\alpha h\nu)^{1/2}$ vs. hν Tauc plot was utilized, with the linear portion of the plot being analysed. In the inset of Figure 5, this linear fit is presented, with the exponent of 1/2 chosen. This exponent is characteristic of the allowed indirect transition, which predominantly governs the optical absorption behaviour in zirconia thin films (Pinzón et al., 2014). By fitting the linear region, the band-gap energy of the ZrO_2 and $ZrO_{2-x}N_x$ thin films can be accurately determined, providing insights into their optoelectronic properties and potential applications in various fields.

The obtained optical band-gap value of the zirconia thin film deposited solely in an Ar-O_2 atmosphere (without nitrogen gas) aligns well with the literature-reported value for ZrO_2 thin films (5.1 eV). This agreement indicates the reliability and accuracy of the deposition process and measurement techniques employed in this study.

As the pulsing repetition frequency increases from 800 to 1200 Hz, the energy band-gap of the $ZrO_{2-x}N_x$ thin films exhibits a gradual decrease from 3.43 to 2.20 eV. The narrowing of the band-gap with increasing repetition frequency (for $f < 1000$ Hz) can be attributed, with a high degree of certainty, to the variation in nitrogen content within the deposited films. The incorporation of nitrogen introduces deep-acceptor energy levels within the band-gap, in close proximity to the valence band (Kumari et al., 2015). This alteration in the energy levels within the band-gap leads to a narrowing of the optical band-gap. For repetition frequencies higher than 1000 Hz, the observed band gap narrowing, as the frequency increases, could be attributed to a phase change. This phase transition may be connected to the presence of Zr_2ON_2 and Zr_3N_4 phases, both of which have much lower band gap energies compared to ZrO_2 or $ZrO_{2-x}N_x$. Previous reports have cited band gap values between 1.5 and 2.6 eV for Zr_2ON_2 (Thapa et al., 2022) and between 0.6 and 1.1 eV for Zr_3N_4 (Yablonskikh et al., 2014). Moreover, the optical properties of the thin films could also be influenced by the presence of internal stress. The combination of

TABLE 1 Measured values for thickness (*t*), energy band-gap (E_g) and elemental composition (*at.*%) for the $ZrO_{2-x}N_x$ thin films deposited at different pulse repetition frequencies.

f (Hz)	800	900	1000	1100	1200
t (nm)	140	180	220	260	300
E_g (eV)	3.43	2.87	2.57	2.37	2.20
N (at.%)	10.0	18.1	22.3	24.3	24.9
O (at.%)	57.0	49.0	45.5	42.4	42.0
Zr (at.%)	33.0	32.9	32.2	33.3	33.1

phase changes and internal stress within the films may collectively contribute to the observed alterations in their optical characteristics.

By narrowing the optical band-gap, the $ZrO_{2-x}N_x$ films exhibit improved light absorption in the visible region of the electromagnetic spectrum. This enhanced light absorption in the visible range is advantageous for photocatalytic applications, as it enables the utilization of a broader range of photons and facilitates more efficient utilization of solar energy. Consequently, the photocatalytic performance of $ZrO_{2-x}N_x$ thin films can be significantly improved, offering promising opportunities for their application as efficient photocatalysts in various environmental and energy-related processes.

3.2.2 Chemical composition and bonding states

The nitrogen incorporation and chemical bonding states in the $ZrO_{2-x}N_x$ thin films were analysed using X-ray Photoelectron Spectroscopy (XPS). Figure 6 illustrates the nitrogen atom concentration within the $ZrO_{2-x}N_x$ films prepared at various pulsing repetition frequencies.

The XPS results reveal a clear trend: as the pulsing repetition frequency increases, the nitrogen content within the films also increases. This observation suggests that the nitrogen gas plays a crucial role in the incorporation of nitrogen atoms into the $ZrO_{2-x}N_x$ films during the deposition process.

Furthermore, it is noteworthy that the nitrogen content tends to approach a saturation value at high pulsing repetition frequencies, specifically above 1100 Hz. This implies that there might be an optimal range of pulsing repetition frequencies that allows for maximum nitrogen incorporation into the films. Beyond this range, further increasing the repetition frequency might not lead to significant changes in the nitrogen content.

The XPS analysis provides valuable insights into the nitrogen incorporation and chemical bonding states within the $ZrO_{2-x}N_x$ films, highlighting the influence of the pulsing repetition frequency on these properties. This information contributes to a better understanding of the film's composition and can guide the optimization of deposition parameters for desired film characteristics.

Table 1 presents the estimated values for thickness, energy band-gap, and elemental composition of the $ZrO_{2-x}N_x$ thin films deposited at different pulse repetition frequencies.

At low pulsing repetition frequency values, the HiPIMS discharge operates in reactive mode, where the target surface is predominantly covered by metal oxide. This is because oxygen has a high reactivity, favouring the formation of metal-oxygen bonds over metal-nitrogen bonds. The combination of lower sputtering yield of metal oxide and the high reactivity of oxygen leads to less nitrogen incorporation into the growing film. In this regime, the presence of oxygen dominates the reaction, inhibiting the bonding between Zr and nitrogen atoms. As the pulsing repetition frequency increases, the target surface transitions from being predominantly covered by metal oxide to predominantly covered by metal nitride. This is attributed to the higher sputtering yield of metal nitride compared to metal oxide. Additionally, the limited amount of oxygen present in the working gas mixture (with a low O_2 partial pressure of only 0.2%) contributes to an oxygen deficit in the deposited films. This oxygen deficit allows for the formation of bonding sites between the Zr atoms and the less reactive nitrogen atoms. The higher sputtering yield of the nitride is attributed to its characteristic binding energy, which is generally three times smaller than that of the corresponding oxide. However, as the pulsing repetition frequency is further increased, the nitrogen incorporation into the film tends to saturate. This is because the discharge transitions from a compound (nitride) sputtering mode to a metal sputtering mode, leading to a noticeable increase in the sputtered Zr atoms in the gas phase. At very low repetition frequencies (less than 200 Hz), a full oxidation of the growing film would be expected if the deposition rate is very low, and the available oxygen is sufficient to completely oxidize the sputtered Zr atoms.

It is important to note that the formation of metal nitrides is energetically less favourable than the formation of metal oxides due to the higher reactivity of oxygen. The enthalpy of formation of metal nitrides is generally lower than that of the corresponding oxide. Consequently, the formation of metal-oxygen bonds is energetically more favourable than metal-nitrogen bonds, and oxygen tends to prevail over nitrogen in the reaction. Overall, by controlling the pulsing repetition frequency in the HiPIMS process, it is possible to manipulate the surface composition and promote the incorporation of nitrogen into the deposited films, resulting in the formation of $ZrO_{2-x}N_x$ thin films with tailored properties for specific applications.

In the high-resolution XPS spectra of Zr 3d, O 1s, and N 1s recorded from the $ZrO_{2-x}N_x$ thin films deposited at a pulsing frequency of 900 Hz, after Ar sputter-etching, several important features were observed. Figure 7A shows the deconvolution of the Zr 3d spectrum, which resulted in four peaks corresponding to two pairs of doublets. The most intense doublet, with binding energies of approximately 181.2 eV and 183.6 eV, corresponds to the Zr $3d_{5/2}$ and Zr $3d_{3/2}$ core levels. These peaks are assigned to Zr^{4+} bonded to O^{2-}, indicating the presence of ZrO_2 in the thin film.

The lower doublet, positioned at around 182.2 eV and 184.6 eV, is attributed to Zr^{4+} bonded to O and N, suggesting the formation of Zr-O-N bonds in the $ZrO_{2-x}N_x$ lattice (Mejía et al., 2022). The presence of Zr-O-N bonds indicates that an oxygen atom is replaced by a nitrogen atom within the ZrO_2 lattice. It is important to note that this lower doublet assigned to Zr-O-N bonds is absent in the high-resolution XPS spectra of Zr 3d recorded from the ZrO_2 thin film, which was deposited without nitrogen.

The separation between the peaks of the doublets in the Zr 3d spectrum is approximately 2.4 eV. The less intense doublet, assigned to Zr-O-N bonds, has a slightly higher binding energy compared to the doublet associated with Zr-O bonds (ZrO_2) due to the less electronegativity of nitrogen in Zr-O-N bonds. This observation is

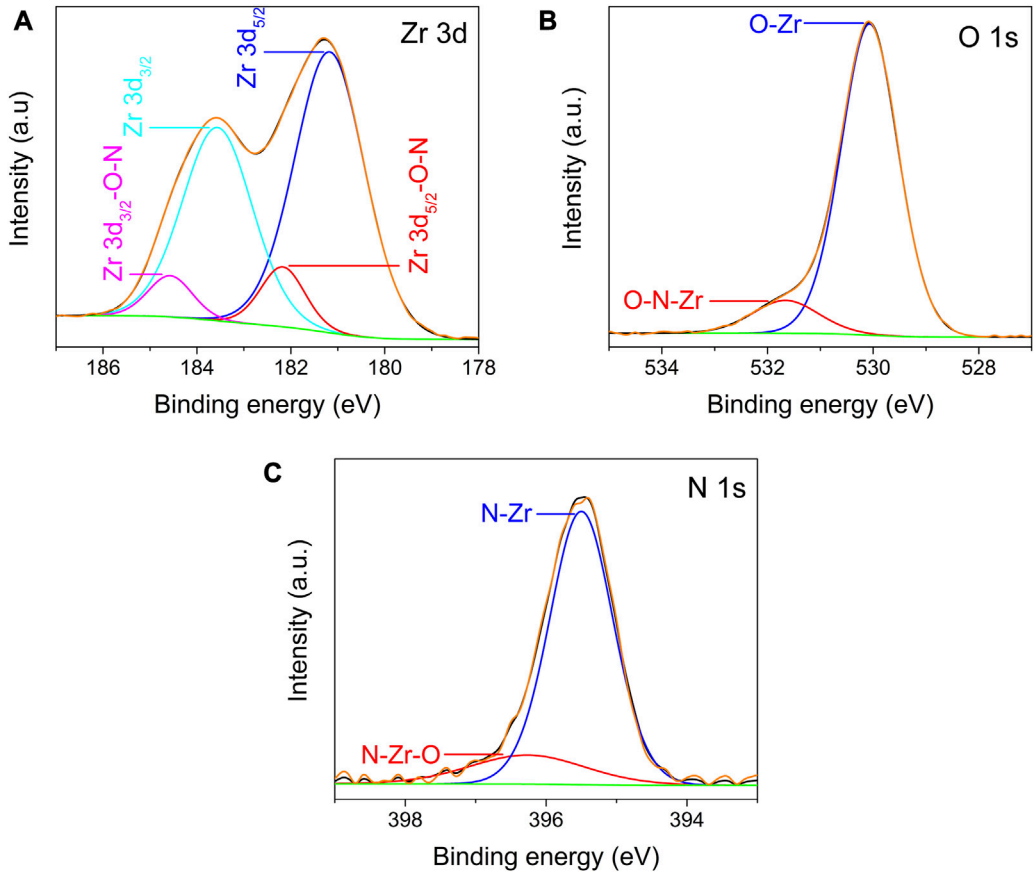

FIGURE 7
High resolution XPS spectra of Zr 3d **(A)**, O 1s **(B)** and N 1s **(C)** recorded from $ZrO_{2-x}N_x$ deposited at pulsing frequency of 900 Hz, after cleaning using Ar ion sputtering.

consistent with the formation of Zr-O-N bonds and further confirms the nitrogen incorporation into the $ZrO_{2-x}N_x$ thin films.

The high-resolution XPS spectra of O 1s and N 1s (Figures 7B,C) provide additional insights into the chemical states and bonding in the $ZrO_{2-x}N_x$ thin films.

In the high-resolution XPS spectrum of O 1s (Figure 7B), two distinct peaks were observed. The first peak, centred at around 530.1 eV, is attributed to O-Zr bonds within the ZrO_2 lattice. This peak corresponds to the oxygen atoms bonded to zirconium in the ZrO_2 structure. The second peak, detected at approximately 531.5 eV, has been assigned by various researchers to Zr-N-O bonds in the $ZrO_{2-x}N_x$ lattice (Cubillos et al., 2014a; Cubillos et al., 2017). This peak indicates the presence of oxygen atoms bonded to both zirconium and nitrogen atoms within the $ZrO_{2-x}N_x$ structure. The observation of the Zr-N-O bonding peak further confirms the nitrogen incorporation in the $ZrO_{2-x}N_x$ thin films.

Regarding the N 1s high-resolution XPS spectrum, it was deconvoluted considering two contributions (Figure 7C). The peak centred at around 395.5 eV is associated with N atoms four-coordinated to zirconium (N-Zr bonds) (Signore et al., 2007). This peak corresponds to nitrogen atoms directly bonded to zirconium atoms in the $ZrO_{2-x}N_x$ lattice. The peak detected at approximately 396.2 eV is tentatively assigned to Zr-N-O bonds in the $ZrO_{2-x}N_x$ lattice based on previous XPS data reported in the literature (Roman et al., 2011) and considering the XPS results discussed earlier. This peak represents the presence of nitrogen atoms bonded to zirconium and oxygen atoms within the $ZrO_{2-x}N_x$ structure. The broad width of this peak may be attributed to the presence of impurities on the film surface, such as oxy/carbo-nitrides. These impurities can influence the XRD peak characteristics and contribute to the observed broadening (Jaimes-Ochoa et al., 2019).

The deconvolution of the O 1s and N 1s high-resolution XPS spectra provides valuable information about the chemical bonding states in the $ZrO_{2-x}N_x$ films, confirming the presence of both Zr-N-O and N-Zr bonds in the lattice. These results, together with elemental composition listed in Table 1, support the successful incorporation of nitrogen into the ZrO_2 lattice by oxygen substitution and the formation of $ZrO_{2-x}N_x$ films.

The narrowing of the bandgap by increasing the pulsing repetition frequency is strongly correlated with the variation of nitrogen content in the deposited films, resulting in the introduction of deep-acceptor energy levels in the bandgap (Kumari et al., 2015). This change in the energy bandgap can also be attributed to the covalent-bond character between nitrogen and oxygen, which reduces the strong electronegativity of oxygen in Zr-O ionic bonds observed in the ZrO_2 lattice (Cubillos et al., 2014b). Additionally, the substitution of oxygen atoms with nitrogen

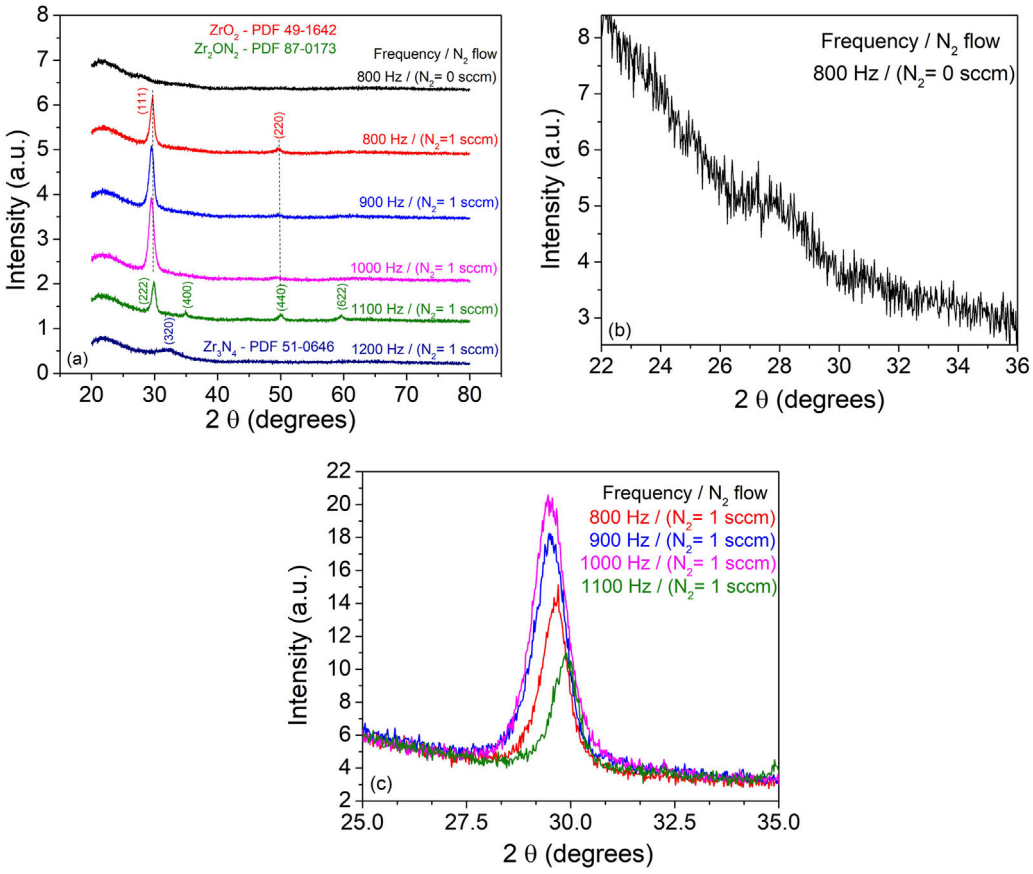

FIGURE 8
XRD patterns recorded from ZrO_2 and $ZrO_{2-x}N_x$ thin films deposited on quartz substrates at room temperature and different pulse repetition frequencies.

atoms generates oxygen vacancies within the $ZrO_{2-x}N_x$ lattice, which, combined with the reduced bandgap, can significantly enhance the photocatalytic performance under visible light irradiation. This improvement is attributed to the increased absorption of visible light by the $ZrO_{2-x}N_x$ thin films, leading to enhanced photocatalytic activity.

3.2.3 Structural analysis

The XRD analysis of the films deposited on quartz substrate revealed interesting findings, as shown in Figure 8. The diffractogram of the sample deposited without N_2 predominantly exhibited an amorphous or near-amorphous microstructure, with a weak crystallographic signal at ~27.8° that could correspond to the (111) main peak of the thermodynamically stable monoclinic ZrO_2 structure. This suggests that the film deposited without nitrogen had limited crystallinity.

In contrast, for the film deposited in the presence of N_2 at 800 Hz pulsing repetition frequency, two distinct diffraction lines were observed, indicating the presence of a distorted cubic ZrO_2 phase. The shift of the XRD peaks towards lower 2θ angles compared to the polycrystalline bulk position can be attributed to the energetic ion bombardment during the film deposition process (Hovsepian et al., 2014; Cemin et al., 2019). The inclusion of nitrogen in the zirconium oxide structure can also contribute to compressive residual stress within the film, further shifting the diffraction lines (Nordseth et al., 2019). With increasing pulsing repetition frequencies up to 1000 Hz, the intensity and displacement of the diffraction from the (111) crystallographic plane became more pronounced. This suggests a preferential crystallographic ordering and a possible improvement in crystallinity. However, it should be noted that the increasing thickness of the samples could also contribute to the higher peak intensity. For the sample deposited at 1100 Hz, the observed diffraction lines were assigned to the cubic Zr_2ON_2 phase and the wide peak at ~32.14° was associated with the (320) crystallographic plane of the Zr_3N_4 structure. These results are consistent with the XPS measurements, which indicated an increase in nitrogen content with the pulsing repetition frequency.

The estimated crystallite average size, ranging between 8 and 12 nm, using Scherrer's equation and the Pseudo-Voigt fit of the main peaks, showed no dependency on the pulsing repetition frequency. This suggests that the crystallite size was not significantly affected by the variations in the deposition conditions.

Overall, the XRD analysis provided valuable insights into the structural properties and phase composition of the deposited films, confirming the presence of different phases and crystallographic structures depending on the deposition conditions and nitrogen incorporation.

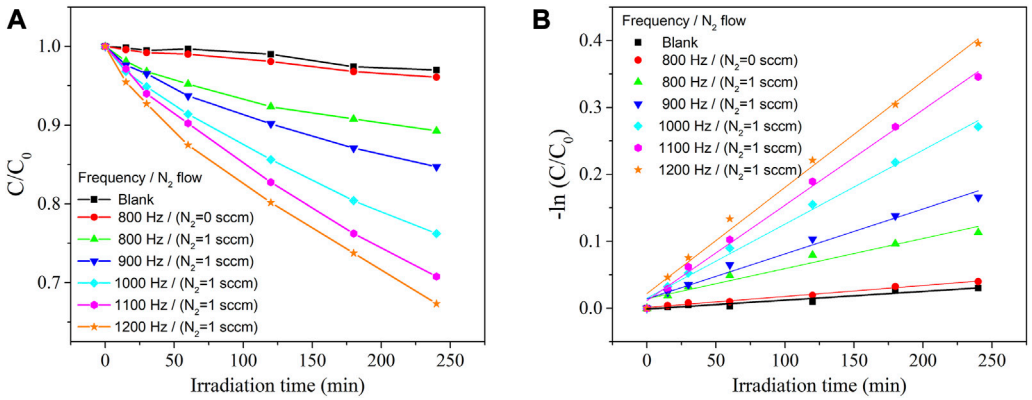

FIGURE 9
Degradation of MB dye under visible-light irradiation in the absence (blank) and presence of catalysts **(A)** and its pseudo-first-order kinetic analysis **(B)**.

The results illustrated and discussed in the previous sections concerning the influence of the repetition frequency on the measured deposition rate, intensity of Zr^0 optical emission spectral line and target peak current allow a more comprehensive understanding of the variation in the stoichiometry of the films.

3.2.4 Photocatalytic activity assessment

The photocatalytic activity of the $ZrO_{2-x}N_x$ films was evaluated by studying the photodegradation of the organic MB dye under visible-light irradiation. Figure 9A presents the change in MB concentration as a function of irradiation time for the $ZrO_{2-x}N_x$ catalysts obtained under different plasma processing conditions. In the absence of a photocatalyst (blank experiment), no significant changes in the MB concentration were observed under visible-light irradiation, indicating that the dye does not undergo spontaneous degradation in the absence of a catalyst.

The ZrO_2 thin film, with its wide optical band-gap (E_g = 5.1 eV), exhibited a very low decomposition rate, where only approximately 4% of the initial organic dye was decomposed after 4 h of visible-light irradiation (λ > 400 nm). This confirms the limited photocatalytic activity of ZrO_2 under visible-light conditions due to its large band-gap.

In contrast, improved photocatalytic activity was observed for the N-doped zirconia samples, which can be attributed to the narrowing of the band-gap. As mentioned earlier, increasing the pulsing repetition frequency led to an increase in the nitrogen content in the films and a gradual decrease in the optical band-gap. This band-gap narrowing is believed to enhance the absorption of visible light and promote the generation of photoexcited charge carriers, thus facilitating the photocatalytic degradation of MB.

The results of the photocatalytic tests demonstrate the potential applicability of the $ZrO_{2-x}N_x$ films as visible-light-driven photocatalysts for organic dye degradation. The band-gap engineering through nitrogen incorporation offers a promising strategy for enhancing the photocatalytic performance of ZrO_2-based materials.

The narrowing of the band-gap in $ZrO_{2-x}N_x$ films through nitrogen doping enables the absorption of a greater number of visible-light photons, leading to the generation of more electron-hole pairs and improved photocatalytic behaviour. As shown in Figure 9, the $ZrO_{2-x}N_x$ films with narrower band-gaps (films deposited at higher pulsing frequencies) exhibit higher efficiency as photocatalysts for the degradation of MB dye under visible-light irradiation.

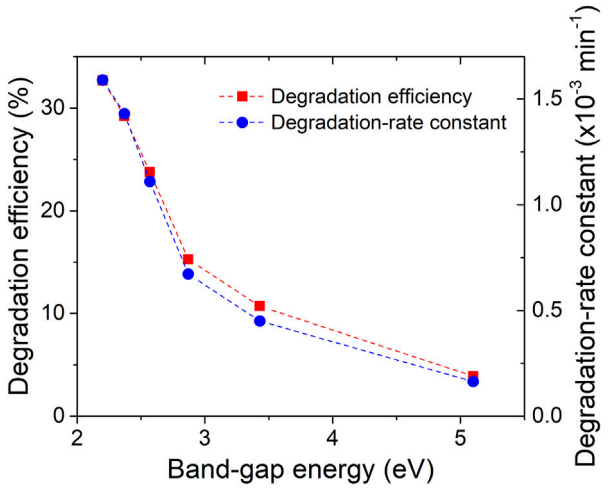

FIGURE 10
Degradation efficiency and degradation-rate constant vs. energy band-gap of ZrO_xN_y thin films.

To quantitatively analyse the degradation kinetics, the MB degradation-rate constant (k) was determined by fitting the kinetic data obtained from the linear fitting curves of -ln(C/C0) versus irradiation time (Figure 9B). The excellent linearity of the plots indicates that the photodegradation rate of MB follows a pseudo-first-order kinetic reaction: -ln(C/C0) = kt, where k represents the photodegradation-rate constant (Nazir et al., 2021). Furthermore, the calculated MB degradation efficiency and degradation-rate constant (k) were plotted against the energy band-gap of the $ZrO_{2-x}N_x$ samples in Figure 10. It can be observed that as the energy band-gap decreases (due to nitrogen doping), the MB degradation efficiency and the degradation-rate constant increase.

This correlation confirms the influence of the band-gap on the photocatalytic performance of $ZrO_{2-x}N_x$ films. The narrower band-gap allows for more efficient utilization of visible light and promotes higher photocatalytic activity.

These findings highlight the potential of nitrogen-doped $ZrO_{2-x}N_x$ films as effective photocatalysts for visible-light-driven degradation of organic dyes, offering a promising avenue for various environmental and energy-related applications.

The decrease in the energy band gap of $ZrO_{2-x}N_x$ films from 5.1 to 2.2 eV leads to a gradual increase in MB degradation efficiency from 4.0% to 32.7% after 4 h of visible-light irradiation. Simultaneously, the degradation-rate constant increases by a factor of ten. It is important to note that the efficiency of the films is lower compared to zirconia nanoparticles (Teeparthi et al., 2018) due to their lower specific surface area, which limits the number of available active sites for photocatalytic reactions.

Figure 10 further illustrates the relationship between enhanced photocatalytic activity and the decreasing band gap in N-doped zirconia. The narrower band gap allows for better utilization of visible light, facilitating the migration of more photo-excited electrons from the valence band (VB) to the conduction band (CB) of the catalyst. This enhanced migration leads to the generation of more holes in the VB, which can react with adsorbed water molecules on the catalyst's surface to produce hydroxyl radicals ($^{\bullet}OH$). Additionally, the conduction band electrons can react with dissolved oxygen to generate superoxide anions (O_2^-). The combined presence of VB holes, hydroxyl radicals, and superoxide anions acts as oxidizing and reducing agents in the decomposition reactions of organic contaminants.

These mechanisms highlight the role of nitrogen doping in promoting visible-light-driven photocatalytic activity by enabling efficient utilization of light energy and facilitating the generation of reactive species for organic degradation. While the films may have lower efficiency compared to nanoparticles, their unique properties and potential for integration into various applications make them promising materials for future photocatalysis studies.

Indeed, while the optical band gap energy of the $ZrO_{2-x}N_x$ photocatalyst plays a significant role in determining the degradation efficiency, it is important to consider that other factors can also influence the overall photocatalytic performance. Morphology, size, and crystallinity of the photocatalyst are additional factors that can impact photocatalytic activity (Tiron et al., 2022). These factors affect the specific surface area, surface reactivity, charge carrier mobility, and light absorption properties of the material, all of which contribute to the overall photocatalytic performance.

In conclusion, the narrow band gap of the $ZrO_{2-x}N_x$ thin film obtained through reactive HiPIMS makes it a promising candidate for visible-light-driven photocatalytic decomposition of organic contaminants. However, to fully optimize the photocatalytic performance, it is crucial to consider and optimize other factors such as morphology, size, and crystallinity, along with the band gap energy. Further research and development in these areas will contribute to the advancement of efficient and effective photocatalytic materials for environmental remediation applications.

4 Conclusion

The incorporation of nitrogen into ZrO_2 thin films using reactive HiPIMS with carefully selected process conditions allows for precise control over the nitrogen content. By adjusting the pulsing repetition frequency, a gradual transition from compound to metal sputtering mode is achieved, effectively suppressing hysteresis, and ensuring process stability. The reactive gas mixture, consisting of Ar, N_2, and O_2, combined with short pulse durations, facilitates this transition.

The introduction of nitrogen into the crystal structure of the thin films leads to significant changes in their optical properties. The decrease in band-gap energy is directly correlated to the nitrogen content in the films. By varying the pulsing frequency within the range of 800–1200 Hz, crystalline $ZrO_{2-x}N_x$ thin films with nitrogen contents ranging from approximately 10–25 at.% and optical band gaps ranging from 3.43 to 2.20 eV can be deposited at room temperature.

The suitability of $ZrO_{2-x}N_x$ thin films for visible-light driven photocatalysis was verified by conducting photodegradation tests with methylene blue (MB) organic dye as a representative contaminant. The results revealed that the photocatalytic activity of N-doped zirconia improves with an increase in N content. This enhancement in photocatalytic performance is attributed to the narrower energy band gap achieved through nitrogen doping. The ability to tune the nitrogen content in the films provides a means to optimize the photocatalytic performance.

The chemical composition and deposition rate of the coatings can be analytically described based on the variation of the peak current, as supported by experimental findings. This analytical approach offers insights into the relationship between deposition parameters and film properties.

The combination of a narrow band-gap energy, increasing deposition rate, and stable deposition process makes this research a promising solution for addressing energy and environmental challenges. It sheds light on new trends and strategies for developing innovative technologies in the synthesis and doping of advanced photocatalytic materials.

Data availability statement

The original contributions presented in the study are included in the article/Supplementary Material, further inquiries can be directed to the corresponding author.

Author contributions

TM: synthesis, data curation. VT: conceptualization, synthesis, data curation, writing-reviewing, editing and supervision. RJ: data curation, writing-original draft. GB: synthesis, data curation. I-LV: conceptualization, writing-reviewing and editing. DC: synthesis, data curation. VC: data curation and funding acquisition. All authors contributed to the article and approved the submitted version.

Funding

The authors gratefully acknowledge financial support from Romanian Ministry of Research, Innovation and Digitalization, UEFISCDI, under projects PN-III-P1-1.1-TE-2019-1209, PCE104/2022, PED580/2022 and Project LAPLAS VII—contract no. 30N/2023.

Conflict of interest

The authors declare that the research was conducted in the absence of any commercial or financial relationships that could be construed as a potential conflict of interest.

Publisher's note

All claims expressed in this article are solely those of the authors and do not necessarily represent those of their affiliated organizations, or those of the publisher, the editors and the reviewers. Any product that may be evaluated in this article, or claim that may be made by its manufacturer, is not guaranteed or endorsed by the publisher.

Supplementary material

The Supplementary Material for this article can be found online at: https://www.frontiersin.org/articles/10.3389/fchem.2023.1239964/full#supplementary-material

References

Aiempanakit, M., Aijaz, A., Lundin, D., Helmersson, U., and Kubart, T. (2013). Understanding the discharge current behavior in reactive high power impulse magnetron sputtering of oxides. *J. Appl. Phys.* 113, 133302. doi:10.1063/1.4799199

Aiempanakit, M., Kubart, T., Larsson, P., Sarakinos, K., Jensen, J., and Helmersson, U. (2011). Hysteresis and process stability in reactive high power impulse magnetron sputtering of metal oxides. *Thin Solid Films* 519, 7779–7784. doi:10.1016/j.tsf.2011.06.021

Báranková, H., Berg, S., Carlsson, P., and Nender, C. (1995). Hysteresis effects in the sputtering process using two reactive gases. *Thin Solid Films* 260, 181–186. doi:10.1016/0040-6090(94)06501-2

Besisa, D. H. A., and Ewais, E. M. M. (2021). Black zirconia composites with enhanced thermal, optical and mechanical performance for solar energy applications. *Sol. Energy Mater. Sol. Cells* 225, 111063. doi:10.1016/j.solmat.2021.111063

Bräuer, G., Szyszka, B., Vergöhl, M., and Bandorf, R. (2010). Magnetron sputtering – milestones of 30 years. *Vacuum* 84, 1354–1359. doi:10.1016/j.vacuum.2009.12.014

Cemin, F., Abadias, G., Minea, T., and Lundin, D. (2019). Tuning high power impulse magnetron sputtering discharge and substrate bias conditions to reduce the intrinsic stress of TiN thin films. *Thin Solid Films* 688, 137335. doi:10.1016/j.tsf.2019.05.054

Cubillos, G. I., Bethencourtb, M., Olaya, J. J., Alfonso, J. E., and Marcoe, J. F. (2014b). The influence of deposition temperature on microstructure and corrosion resistance of ZrO_xN_y/ZrO_2coatings deposited using RF sputtering. *Appl. Surf. Sci.* 309, 181–187. doi:10.1016/j.apsusc.2014.04.215

Cubillos, G. I., Mendozab, M. E., Alfonso, J. E., Blanco, G., and Bethencourt, M. (2017). Chemical composition and microstructure of zirconium oxynitride thin layers from the surface to the substrate-coating interface. *Mater. Charact.* 131, 450–458. doi:10.1016/j.matchar.2017.07.035

Cubillos, G. I., Olaya, J. J., Bethencourt, M., Cifredo, G., and Blanco, G. (2014a). Structural changes in ZrO_xN_y/ZrO_2 coatings deposited through spray pyrolisis-nitriding. *Rev. Mex. Física* 60, 233–242.

Demeter, A., Samoila, F., Tiron, V., Stanescu, D., Magnan, H., Straticiuc, M., et al. (2017). Visible-light photocatalytic activity of TiO_xN_y thin films obtained by reactive multi-pulse High Power Impulse Magnetron Sputtering. *Surf. Coatings Technol.* 324, 614–619. doi:10.1016/j.surfcoat.2016.10.011

Depla, D., Mahieu, S., and De Gryse, R. (2009). Magnetron sputter deposition: Linking discharge voltage with target properties. *Thin Solid Films* 517, 2825–2839. doi:10.1016/j.tsf.2008.11.108

Depla, D., Tomaszewski, H., Buyle, G., and De Gryse, R. (2006). Influence of the target composition on the discharge voltage during magnetron sputtering. *Surf. Coatings Technol.* 201, 848–854. doi:10.1016/j.surfcoat.2005.12.047

Greene, J. E. (2017). Review Article: Tracing the recorded history of thin-film sputter deposition: From the 1800s to 2017. *J. Vac. Sci. Technol. A* 35, 05C204. doi:10.1116/1.4998940

Hippler, R., Cada, M., Mutzke, A., and Hubicka, Z. (2023). Pulse length dependence of a reactive high power impulse magnetron (HiPIMS)discharge. *Plasma Sources Sci. Technol.* 32, 055013. doi:10.1088/1361-6595/acd5fc

Hovsepian, P. E., Sugumaran, A. A., Purandare, Y., Loch, D. A. L., and Ehiasarian, A. P. (2014). Effect of the degree of high power impulse magnetron sputtering utilisation on the structure and properties of TiN films. *Thin Solid Films* 562, 132–139. doi:10.1016/j.tsf.2014.04.002

Jaimes-Ochoa, C. J., Quintero, J., and Ospina, R. (2019). Obtaining ZrN, ZrO, ZrC powder in a nitrogen atmosphere by means of a Ball Mill. *J. Phys. Conf. Ser.* 1247, 012040. doi:10.1088/1742-6596/1247/1/012040

Jette, J., Rohmer, J., Wegner, M., and Quandt, E. (2021). Fabrication of stable monoclinic zirconia-based ceramics. *Ceram. Int.* 47, 8692–8696. doi:10.1016/j.ceramint.2020.11.093

Kouznetsov, V., Macák, K., Schneider, J. M., Helmersson, U., and Petrov, I. (1999). A novel pulsed magnetron sputter technique utilizing very high target power densities. *Surf. Coatings Technol.* 122, 290–293. doi:10.1016/S0257-8972(99)00292-3

Kubart, T., Aiempanakit, M., Andersson, J., Nyberg, T., Berg, S., and Helmersson, U. (2011). Studies of hysteresis effect in reactive HiPIMS deposition of oxides. *Surf. Coatings Technol.* 205, S303–S306. doi:10.1016/j.surfcoat.2011.01.019

Kumari, R., Sahai, A., and Goswami, N. (2015). Effect of nitrogen doping on structural and optical properties of ZnO nanoparticles. *Prog. Nat. Sci. Mater. Int.* 25, 300–309. doi:10.1016/j.pnsc.2015.08.003

Lerch, M. (1996). Nitridation of zirconia. *J. Am. Ceram. Soc.* 79 (10), 2641–2644. doi:10.1111/j.1151-2916.1996.tb09028.x

Martin, N., and Rousselot, C. (1999). Instabilities of the reactive sputtering process involving one metallic target and two reactive gases. *J. Vac. Sci. Technol. A* 17, 2869–2878. doi:10.1116/1.581953

Mejía, C. P., Vanegas, H. S., and Olaya, J. J. (2022). Electrochemical and optical behavior of ZrN-Ag coatings deposited by means of DC reactive magnetron sputtering technique. *Coatings* 12, 754. doi:10.3390/coatings12060754

Nazir, A., Latif, S., Adil, S. F., Kuniyil, M., Imran, M., Hatshan, M. R., et al. (2021). Photocatalytic degradation of cefixime trihydrate by bismuth ferrite nanoparticles. *Materials* 15, 213. doi:10.3390/ma15010213

Nordseth, Ø., Kumar, R., Bergum, K., Chilibon, I., Foss, S. E., and Monakhov, E. (2019). Nitrogen-doped Cu_2O thin films for photovoltaic applications. *Materials* 12, 3038. doi:10.3390/ma12183038

Pinzón, M. J., Alfonso, J. E., Olaya, J. J., Cubillos, G. I., and Romero, E. (2014). Influence of the electrical power applied to the target on the optical and structural properties of ZrON films produced via RF magnetron sputtering in a reactive atmosphere. *Thin Solid Films* 572, 184–188. doi:10.1016/j.tsf.2014.09.006

Roman, D., Bernardi, J., de Amorim, C., de Souza, F., Spinelli, A., Giacomellid, C., et al. (2011). Effect of deposition temperature on microstructure and corrosion resistance of ZrN thin films deposited by DC reactive magnetron sputtering. *Mater. Chem. Phys.* 130, 147–153. doi:10.1016/j.matchemphys.2011.06.013

Sarakinos, K., Alami, J., Klever, C., and Wuttig, M. (2008). Process stabilization and enhancement of deposition rate during reactive high power pulsed magnetron sputtering of zirconium oxide. *Surf. Coatings Technol.* 202, 5033–5035. doi:10.1016/j.surfcoat.2008.05.009

Sarakinos, K., Alami, J., and Konstantinidis, S. (2010). High power pulsed magnetron sputtering: A review on scientific and engineering state of the art. *Surf. Coatings Technol.* 204, 1661–1684. doi:10.1016/j.surfcoat.2009.11.013

Severin, D., Kappertz, O., Kubart, T., Nyberg, T., Berg, S., Pflug, A., et al. (2006). Process stabilization and increase of the deposition rate in reactive sputtering of metal oxides and oxynitrides. *Appl. Phys. Lett.* 88, 161504. doi:10.1063/1.2196048

Signore, M. A., Rizzo, A., Mirenghi, L., Tagliene, M. A., and Capello, A. (2007). Characterization of zirconium oxynitride films obtained by radio frequency magnetron reactive sputtering. *Thin Solid Films* 515, 6798–6804. doi:10.1016/j.tsf.2007.02.033

Sproul, W. D., Christie, D. J., and Carter, D. C. (2005). Control of reactive sputtering processes. *Thin Solid Films* 491, 1–17. doi:10.1016/j.tsf.2005.05.022

Teeparthi, S. R., Awin, E. W., and Kumar, R. (2018). Dominating role of crystal structure over defect chemistry in black and white zirconia on visible light photocatalytic activity. *Sci. Rep.* 8, 5541. doi:10.1038/s41598-018-23648-0

Thapa, B., Patterson, R. J., Conibeer, G., and Shrestha, S. (2022). Investigating electronic, optical, and phononic properties of bulk γ-m2on$_2$ and β-$M_7O_8N_4$ (M = Hf and Zr) insulators using density functional theory. *ACS Omega* 7, 9196–9205. doi:10.1021/acsomega.1c05649

Tiron, V., Ciolan, M. A., Bulai, G., Mihalache, G., Lipsa, F. D., and Jijie, R. (2022). Efficient removal of methylene blue and ciprofloxacin from aqueous solution using flower-like nanostructured ZnO coating under UV irradiation. *Nanomaterials* 12, 2193. doi:10.3390/nano12132193

Tiron, V., Sirghi, L., and Popa, G. (2012). Control of aluminum doping of ZnO:Al thin films obtained by high-power impulse magnetron sputtering. *Thin Solid Films* 520, 4305–4309. doi:10.1016/j.tsf.2012.02.079

Tiron, V., and Sirghi, L. (2015). Tuning the band gap and nitrogen content of ZnO_xN_y thin films. *Surf. Coatings Technol.* 282, 103–106. doi:10.1016/j.surfcoat.2015.10.017

Tiron, V., Velicu, I.-L., Matei, T., Cristea, D., Cunha, L., and Stoian, G. (2020). Ultra-short pulse HiPIMS: A strategy to suppress arcing during reactive deposition of SiO_2 thin films with enhanced mechanical and optical properties. *Coatings* 10, 633. doi:10.3390/coatings10070633

Tiron, V., Velicu, I.-L., Stanescu, D., Magnan, H., and Sirghi, L. (2017). High visible light photocatalytic activity of nitrogen-doped ZnO thin films deposited by HiPIMS. *Surf. Coatings Technol.* 324, 594–600. doi:10.1016/j.surfcoat.2016.11.087

Van Bever, J., Strijckmans, K., and Depla, D. (2022). A computational study of the double hysteresis phenomenon during reactive sputtering. *J. Phys. D Appl. Phys.* 55, 355302. doi:10.1088/1361-6463/ac761c

Venkataraj, S., Kappertz, O., Weis, H., Drese, R., Jayavel, R., and Wuttig, M. (2002). Structural and optical properties of thin zirconium oxide films prepared by reactive direct current magnetron sputtering. *J. Appl. Phys.* 92, 3599–3607. doi:10.1063/1.1503858

Vlček, J., Rezek, J., Houška, J., Čerstvý, R., and Bugyi, R. (2013). Process stabilization and a significant enhancement of the deposition rate in reactive high-power impulse magnetron sputtering of ZrO_2 and Ta_2O_5 films. *Surf. Coatings Technol.* 236, 550–556. doi:10.1016/j.surfcoat.2013.10.052

Wallin, E., and Helmersson, U. (2008). Hysteresis-free reactive high power impulse magnetron sputtering. *Thin Solid Films* 516, 6398–6401. doi:10.1016/j.tsf.2007.08.123

Wiame, H., Centeno, M. A., Picard, S., Bastians, P., and Grange, P. (1998). Thermal oxidation under oxygen of zirconium nitride studied by XPS, DRIFTS, TG-MS. *J. Eur. Ceram. Soc.* 18, 1293–1299. doi:10.1016/S0955-2219(98)00056-9

Window, B., and Savvides, N. (1986). Charged particle fluxes from planar magnetron sputtering sources. *J. Vac. Sci. Technol. A Vac. Surfaces, Films* 4, 196–202. doi:10.1116/1.573470

Yablonskikh, M., Dzivenko, D., Bourguille, J., Riede, R., Magnano, E., Parmigiani, F., et al. (2014). Electronic structure and band gap of oxygen bearing c-Zr3N4 and of c-Hf3N4 by soft X-ray spectroscopy. *Phys. Status Solidi A* 211, 835–842. doi:10.1002/pssa.201330338

frontiers | Frontiers in Chemistry

TYPE Original Research
PUBLISHED 08 November 2023
DOI 10.3389/fchem.2023.1290745

OPEN ACCESS

EDITED BY
Panwang Zhou,
Shandong University, China

REVIEWED BY
Yongqing Li,
Liaoning University, China
Ying Shi,
Jilin University, China

*CORRESPONDENCE
Yongjin Peng,
hunterpyj2016@163.com

RECEIVED 08 September 2023
ACCEPTED 16 October 2023
PUBLISHED 08 November 2023

CITATION
Ma T, Huang H, Liu Y and Peng Y (2023), Theoretical investigation on a simple turn on fluorescent probe for detection of biothiols based on coumarin unit. *Front. Chem.* 11:1290745. doi: 10.3389/fchem.2023.1290745

Theoretical investigation on a simple turn on fluorescent probe for detection of biothiols based on coumarin unit

Tianhao Ma[1], He Huang[2], Yuling Liu[2] and Yongjin Peng[2]*

[1]Affiliated 3rd Hospital, Jinzhou Medical University, Jinzhou, China, [2]College of Bio-Informational Engineering, Jinzhou Medical University, Jinzhou, China

The discovery of a simple and efficient detection method for biothiols would be scientifically significant due to the crucial role of them in various physiological processes. Recently, a simple fluorescent probe, DEMCA-NBSC, based on coumarin fragments, was developed by Ding et al., and provided an efficient way for real-time sensing of biothiols both *in vivo* and vitro. Theoretical insights to the fluorescence sensing mechanism of the probe were provided in this work. Details of the electron transfer process in the probe under optical excitation and the fluorescent character of the probe were analyzed using a quantum mechanical method. All these theoretical results could inspire the development of a highly convenient and efficient fluorescent probe to sense biothiols both *in vivo* and vitro.

KEYWORDS

fluorescent probe, biothiols, quantum mechanical, electron transfer, proton transfer

1 Introduction

Biothiols, including cysteine (Cys), homocysteine (Hcy), and glutathione (GSH), have strong REDOX and nucleophilic properties (Gothland et al., 2023; Liu and Liu, 2023; Pandya et al., 2023; Qu et al., 2023). As the main chemical antioxidants, biothiols protect cells and tissues from endogenous reactive oxygen species (ROS) and free radicals (Mezhnina et al., 2022; Villavicencio-Tejo et al., 2022; Chen et al., 2023). They are involved in information transmission, cell growth and apoptosis, protein formation, immune regulation, and other processes in living systems. Cys can assist in the synthesis of antioxidant GSH and maintain intracellular homeostasis of oxidation and reduction (Takagi et al., 2012; Blasco et al., 2018). It can also take advantage of the reversible oxidation of glutathione disulfide (GSSG) to protect the thiol-containing proteins and enzymes from injury by free radicals, peroxidation, and heavy metals.

Biothiols are involved in many transfer and detoxification processes, including cell growth, REDOX, and so on. The normal level of Cys in the human body (30–200 μmol/L) is essential to maintain the tertiary and quaternary structure of proteins; Cys is also an important source of sulfide in the human metabolism process (Weerapana et al., 2010; Kisty et al., 2023; das Neves et al., 2023; Cao et al., 2023). Excess Cys in the human body could lead to rheumatoid arthritis, Parkinson's, and Alzheimer's disease. Cys deficiency, meanwhile, can induce developmental delays in children and cause edema, liver injury, and skin injury (Pang et al., 2020; Wang et al., 2023). The normal serum concentration of Hcy in healthy adults is 9–13 μmol/L. When the concentration of Hcy in serum is higher than 15 μmol/L,

TABLE 1 Parameters of the four stable probe conformations.

	α	ΔG (kcal/mol) E1 was taken as References
E1	27°	0
E2	42°	4.31
K1	0°	4.60
K2	180°	11.07

hyperhomocysteinemia could be induced (Ganguly and Alam, 2015; Zhong et al., 2023). GSH is the most abundant non-protein mercaptan in cells. The normal concentration *in vivo* is between 1 and 10 mmol/L, and it plays a key role in the control of oxidative stress of the cell apoptosis in a REDOX stable state (Huang et al., 2023; Swiderski et al., 2023). Abnormality in GSH concentration is also observed as a signal for many diseases, such as AIDS, cancer, lung damage, and Parkinson's disease (Su et al., 2020; Niu et al., 2021).

In view of the importance of biothiols, accurate detection of its concentration and distribution in the organism are important for disease assessment and diagnosis. Fluorescence analysis technology has great potential for concentration monitoring and intracellular imaging of biothiols *in vivo* due to its high sensitivity, simple operation, and low levels of damage to biological samples (Liu et al., 2021; Zhou et al., 2023a; Zhang et al., 2023).

To date, many fluorescent probes have been developed to detect biothiols, although many have a specific response to only one of the biothiols (Long et al., 2022; Kaushik et al., 2023; Si et al., 2023; Tang et al., 2023; Wu et al., 2023). However, there is a close relationship between different biothiols. A change in one biothol in specific cellular metabolic processes may lead to another biothol changing, and many diseases are associated with the combination of two or more biothiols. Therefore, detecting two or more biothiols simultaneously is more valuable for biological research and disease diagnosis (Hao et al., 2022; Hou et al., 2022; Jiang et al., 2022; Li et al., 2022; Ma et al., 2022; Zhou et al., 2023b; Peng et al., 2023; Zhu et al., 2023).

In 2014, Guo et al. reported the first dual-signal fluorescent probe for simultaneous detection of Cys and GSH (Liu et al., 2014). In 2018, Yin's research group synthesized a functional fluorescent probe through which biothiols such as Cys, Hcy, and GSH could be distinguished by three different emission channels (Yin et al., 2019). In 2019, Song's research group constructed the first case of a fluorescent probe that can detect Cys, Hcy, GSH, and H_2S simultaneously within four light-emitting channels (Zhang et al., 2019). Along with the continuous progress of the design concept, the study of fluorescent probes with the ability to detect biothiols simultaneously has become a hot topic in biological and medical field (Raut and Sahoo, 2021; Ding et al., 2023a; Du et al., 2023; Kaushik et al., 2023; Shellaiah and Sun, 2023; Zhang et al., 2023).

Although recently some related work has been done, the application of fluorescent probes for rapid simultaneous detection of biothiols in both vivo and vitro is still a hot topic. Ding et al. successfully designed and developed a simple fluorescent probe, namely, DEMCA-NBSC, based on coumarin fragments, which presented remarkable emission enhancement and exhibited yellow-green fluorescence after the addition of biothiols (Hcy/Cys/GSH), and the intensified emission response was ascribed to biothiols inducing the cleavage of NBSC group to form a fluorescent compound, DEMCA-OH, which exhibited a strong aggregation-induced emission (AIE) property (Ding G. et al., 2023). The rupture of an S-O bond occurred when the probe DEMCA-NBSC contacted with biothiols. DEMCA-OH was then successfully formed and was the sensing mechanism of DEMCA-NBSC for biothiols which has been confirmed and reported according to the literature (Chen et al., 2022; Goswami et al., 2022). The colorimetrical and fluorescent responses to Cys, Hcy, and GSH was confirmed in reference 45.

It is worth mentioning that DEMCA-NBSC exhibits a rapid response (within 3 min), high selectivity, outstanding sensitivity, and lower detection limits (0.236, 0.223, and 0.365 μM for Cys, GSH,

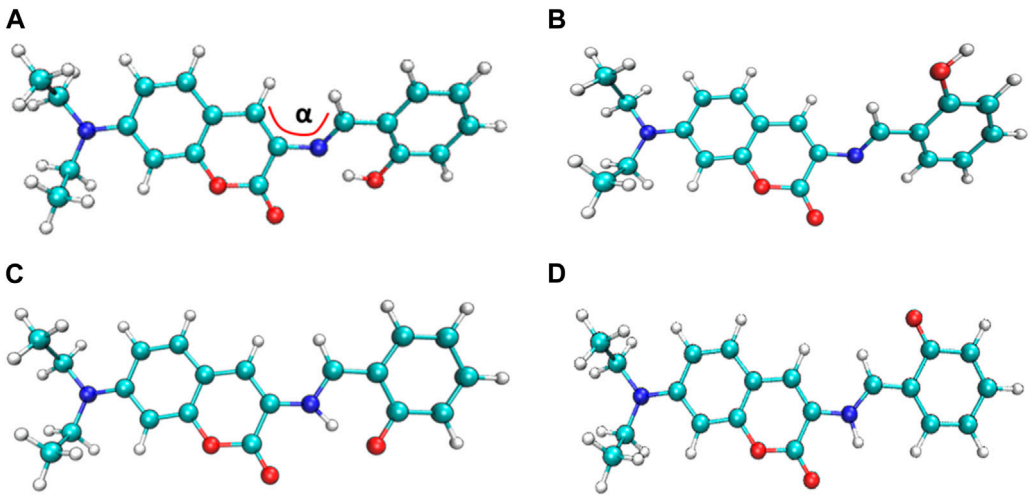

FIGURE 1
The four most stable probe conformations of probe DEMCA-OH. **(A)** E1 **(B)** E2 **(C)** K1 **(D)** K2.

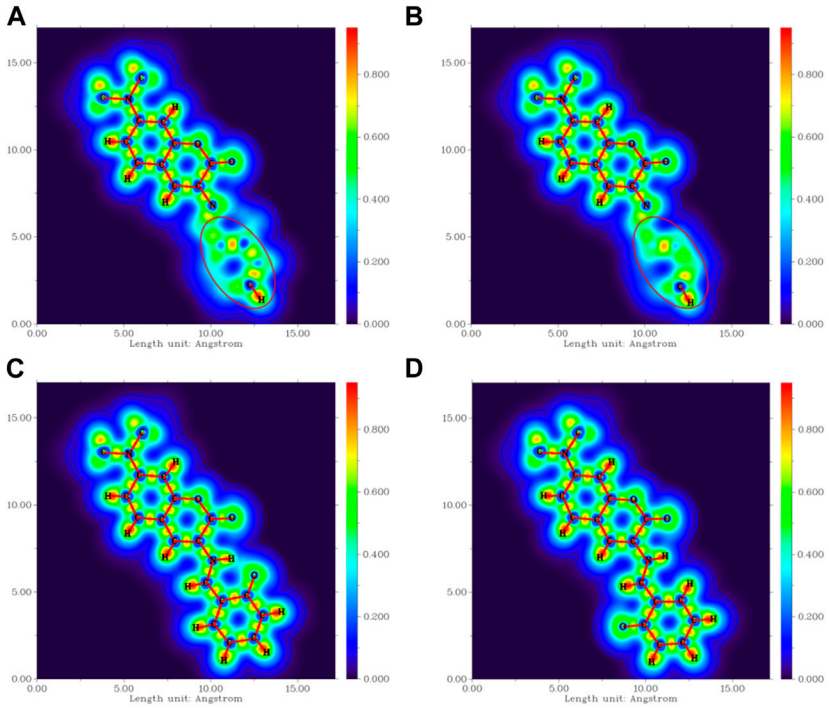

FIGURE 2
The localized orbital locator projection on the naphthalene ring plane in the four-probe conformation **(A)** E1 **(B)** E2 **(C)** K1 **(D)** K2.

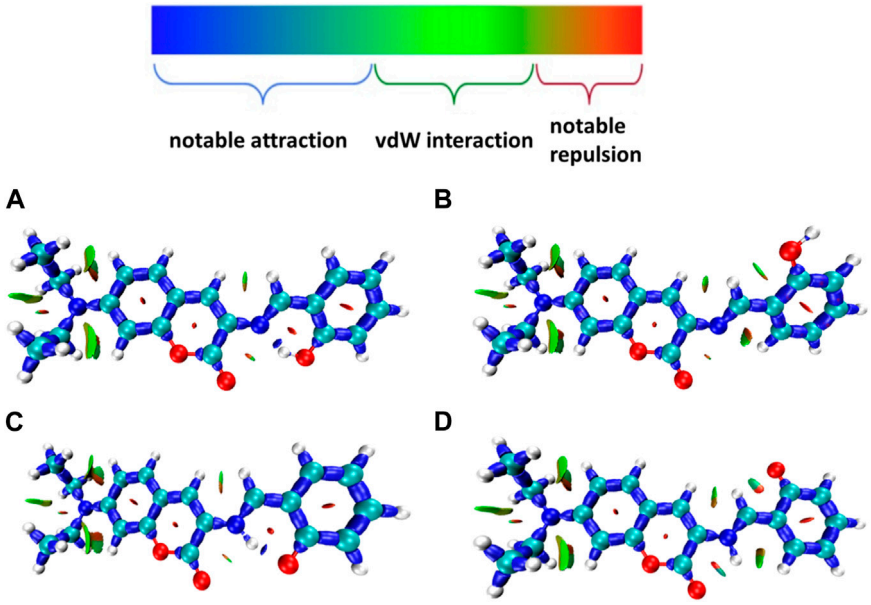

FIGURE 3
Many interactions between adjacent atoms in four probe molecules **(A)** E1 **(B)** E2 **(C)** K1 **(D)** K2.

and Hcy, respectively) to biothiols. This probe provides an effective tool for the real-time detection of biothiols both *in vivo* and vitro.

Due to the excellent properties, such as simple synthetic procedure, low cytotoxicity, outstanding sensitivity, and high selectivity, the probe DEMCA-NBSC offered an efficient approach for biothiols detection in and out of biological systems, and has a potential application in diagnostics. In this work, the fluorescent mechanism of the probe DEMCA-NBSC

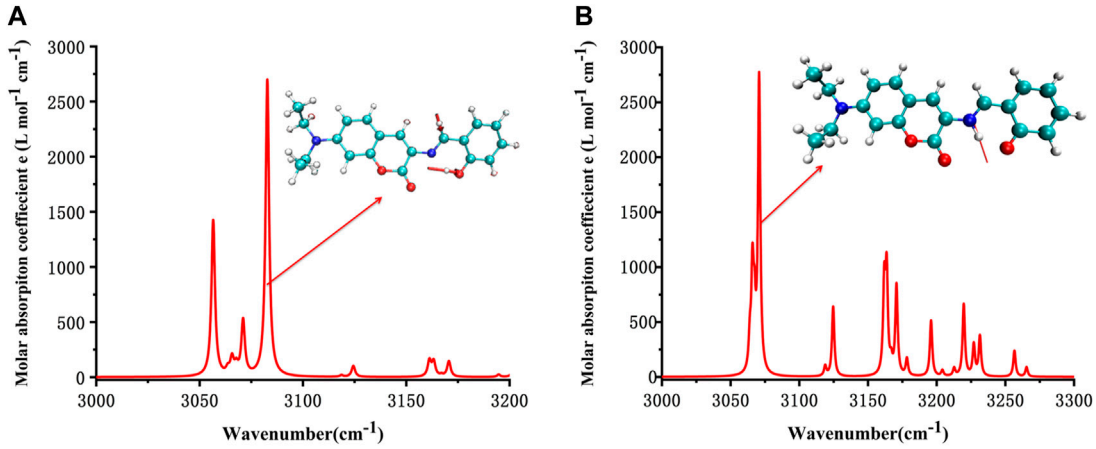

FIGURE 4
Simulated IR spectrum of **(A)** E1 and **(B)** K1.

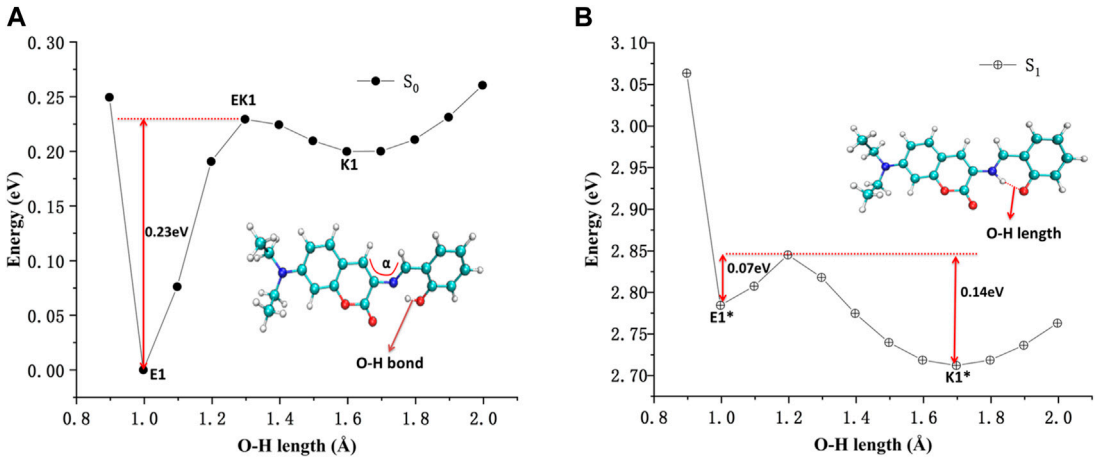

FIGURE 5
The potential energy curves of DEMCA-OH **(A)** ground state and **(B)** first excited state.

and the remaining compound DEMCA-OH were investigated in detail using a quantum mechanical method. The electronic structure analysis on the ground S_0 and first excited S_1 states of the probe DEMCA-NBSC revealed the electron transfer process of the probe under optical excitation. By means of electronic structure, intramolecular interaction, IR spectrum, potential energy scan curve, energy surface hopping dynamics, and charge analysis on the remaining compound DEMCA-OH, the typical excited state intramolecular proton transfer (ESIPT) process that caused the fluorescence phenomenon in DEMCA-OH was investigated in detail. The comprehensive analysis on the probe DEMCA-NBSC and remaining compound DEMCA-OH could provide deep insights into the structure-function relationship of the fluorescent probes.

All these theoretical results could provide insights for understanding the fluorescent principle and building highly effective fluorescent probes for detection of biothiols simultaneously in biological samples.

2 Conformation search, electronic structure, and fluorescent properties

The processes of the conformation search for DEMCA-OH were as follows.

(1) Using Confab (O'Boyle et al., 2011) to obtain initial conformations of DEMCA-OH;
(2) Conducting batch structural optimization using Crest to invoke the xtb program under the GFN2-xTB method (Bannwarth et al., 2019);
(3) Invoking isostat in the Molclus (Lu, 2021) program to screen out several stable probe conformations with the local lowest free energy;
(4) Using the functional and basis set combination B3LYP, PBE0, M06-2x and CAM-B3LYP/def2-TZVPD in structure optimization and analyzing the corresponding vibrational frequency on the stable probe conformations obtained from

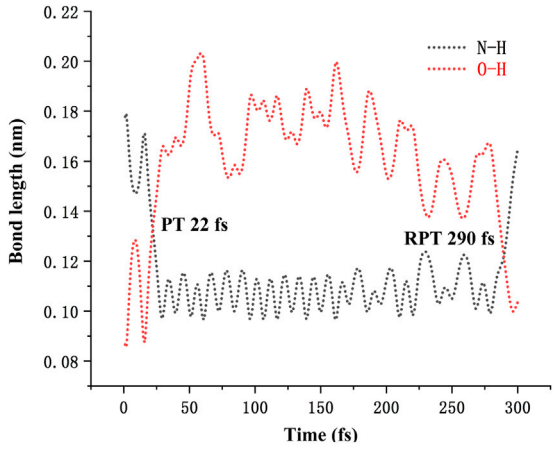

FIGURE 6
The variation of O-H and N-H bond length in S_1 state of DEMCA-OH.

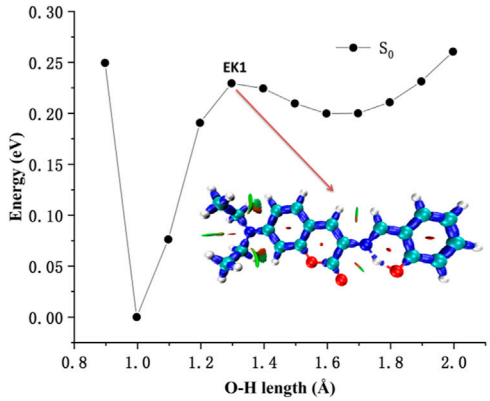

FIGURE 7
The interaction within transition state EK1.

step (3) within the ORCA program (Neese, 2018). Zero negative frequency was found within the optimized structure, which confirmed the local minimum energy of the corresponding structure (Ahlrichs and Ahlrichs, 2005; Grimme et al., 2011; Yu et al., 2016; Ghosh et al., 2018). Similar results were obtained in the probe structure optimization using the four functional as B3LYP, PBE0, M06-2x and CAM-B3LYP. For clarity, the results of the CAM-B3LYP/def2-TZVPD combination were used for the following analysis. The wB2GP-PLYP/def2-TZVPD combination was used in single point energy and TDDFT calculation to obtain the free energy with high precision according to the benchmark research (Grimme and Grimme, 2010; Brauer et al., 2014; Grimme and Grimme, 2014; Boese, 2015; Peng et al., 2021; Liu et al., 2022; Lin et al., 2023; Liu et al., 2023). An SMD model was used in the calculation within a solvent environment (Zhou et al., 2015; Martins and Martins, 2019; Zhao et al., 2021; Zhao et al., 2022). Most of the figures in this work were rendered by means of VMD 1.9.3 software (Humphrey et al., 1995) and the analyses were finished by using the Multiwfn 3.8 (dev) code (Chen and Chen, 2012).

(5) The electronic structure and fluorescent properties of probe were obtained based on the DFT and TDDFT results by ORCA program.

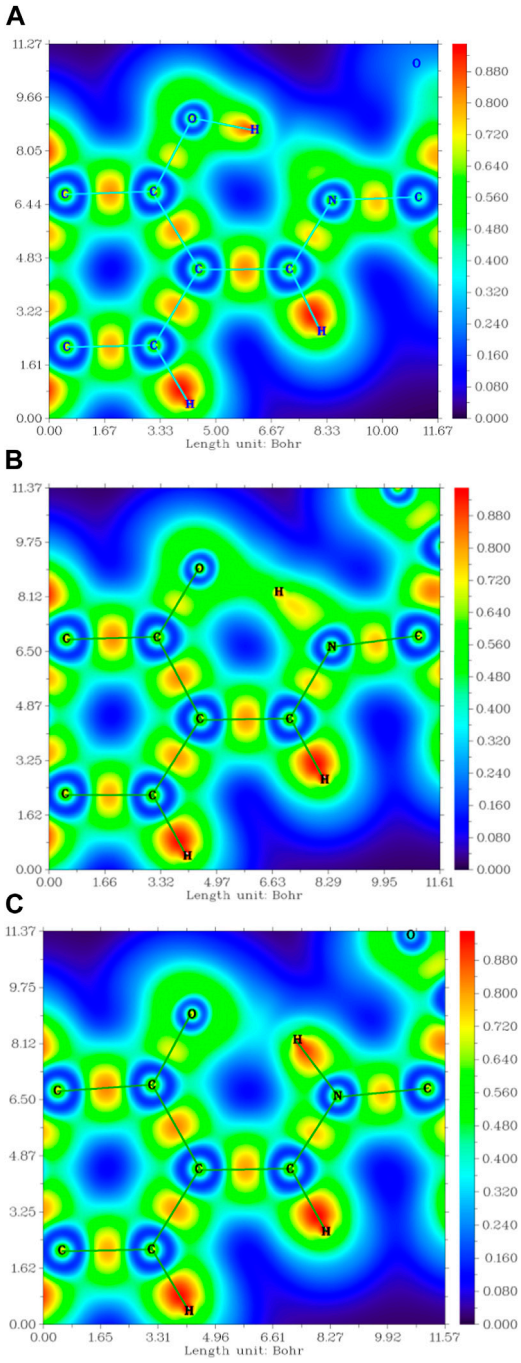

FIGURE 8
The 2D projection of the LOL in the N-H-O hydrogen bond area within **(A)** E1, **(B)** EK1, and **(C)** K1.

10.3389/fchem.2023.1290745

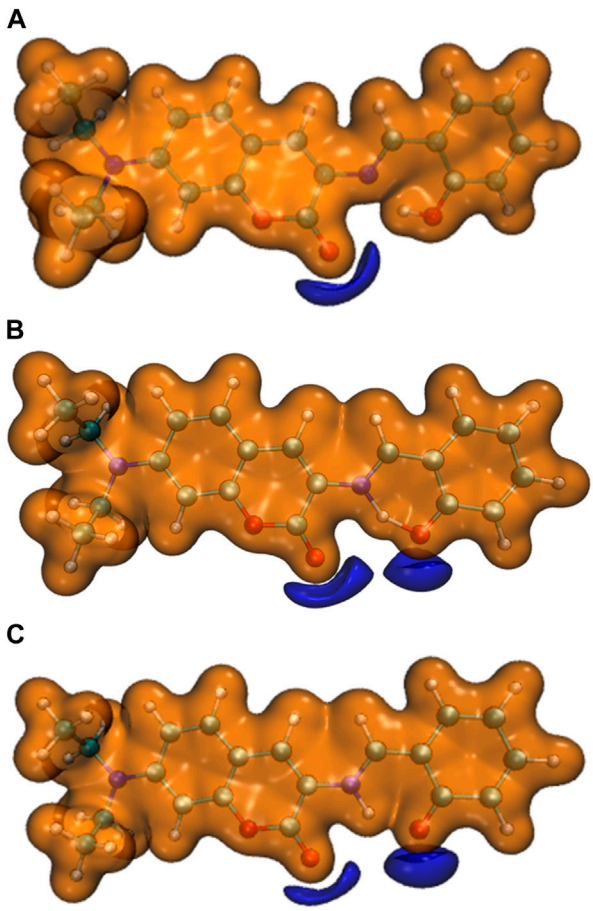

FIGURE 9
The static electrical potential of **(A)** E1, **(B)** EK1, and **(C)** K1 (orange: isovalue = 0.05 a.u. ,purple: isovalue = −0.05 a.u.).

(6) The dynamics on the excited state of the probe were conducted using the Newton-X program (Barbatti et al., 2014).

3 Results and discussion

The four most stable conformations of probe DEMCA-OH (named E1, E2, K1, and K2) are shown in Figure 1 and summarized in Table 1. Apart from the two end ethenyl, the whole planar structure is shown in molecule K1 and K2, while there are different dihedral values α between the benzene and naphthalene ring within the molecule E1 and E2. The potential energy scan curve on dihedral angle α is provided in Supplementary Figure S1 for reference. The localized orbital locator projection on the naphthalene ring plane in the four-probe conformation clearly indicated the planar structure in molecule K1 and K2. Meanwhile a larger dihedral value α between the benzene and naphthalene ring within the E2 molecule than E1 molecule is also clearly shown in Figure 2.

Many kinds of interactions between adjacent atoms in the four probe molecules are depicted in Figure 3. It could be clearly inferred that the hydrogen bond interaction of N . . . O-H and N-H . . . O in E1 and K1 molecule respectively led to the much lower free energy and more stable structure compared with E2 and K2 molecules. E1 and K1 molecules were the most commonly found and used conformation for the biothiols probe according to reference 45. Therefore, only E1 and K1 probe molecules were considered for the electron excitation and emission process analysis. The clear difference between the structure of E1 and K1 molecules is intuitively shown in their simulated IR spectrum (Figure 4).

It can be seen from the simulated IR spectrum that O-H stretch vibration in E1 (3,081 cm^{-1}, as shown by the red arrow both in Figure 4A and the inset E1 molecule) has a similar intensity to the N-H stretch vibration in K1 molecule (3,073 cm^{-1}, as shown by the red arrow both in Figure 4B and the inset K1 molecule). But the different spectrum shape in this wavenumber range (3,000–3,300 cm^{-1}) indicated the clear difference between the structure of E1 and K1 molecules.

The potential energy curves of ground state and first excited state of DEMCA-OH are constructed in Figure 5. It can be clearly concluded that the Enol form (E1, O-H bond length with about

TABLE 2 The main electron excitation processes in the probe molecule.

Probe	Electronic transition[a]	Excitation energy (nm)	Oscillator strength	Composition[b]	CI[c]
E1	$S_0 \rightarrow S_1$	438	0.9816	H → L	0.6815
K1	$S_0 \rightarrow S_1$	443	1.0521	H → L	0.6908
NBSC	$S_0 \rightarrow S_1$	421	0.0014	H → L	0.7103

[a]Only the excited states with oscillator strengths larger than 0.1 were considered.
[b]H stands for HOMO, and L stands for LUMO.
[c]Coefficient of the wave function for each excitation was in absolute value.

TABLE 3 The main electron emission processes in the probe molecule.

Compound	Electronic transition[a]	Emission energy (nm)	Oscillator strength	Composition[b]	CI[c]
E1	$S_1 \rightarrow S_0$	485	0.9945	H → L	0.6726
K1	$S_1 \rightarrow S_0$	567	1.1014	H → L	0.6017
NBSC	$S_1 \rightarrow S_0$	493	0.0087	H → L	0.7015

a,b,c same indication as in Table 1.

10.3389/fchem.2023.1290745

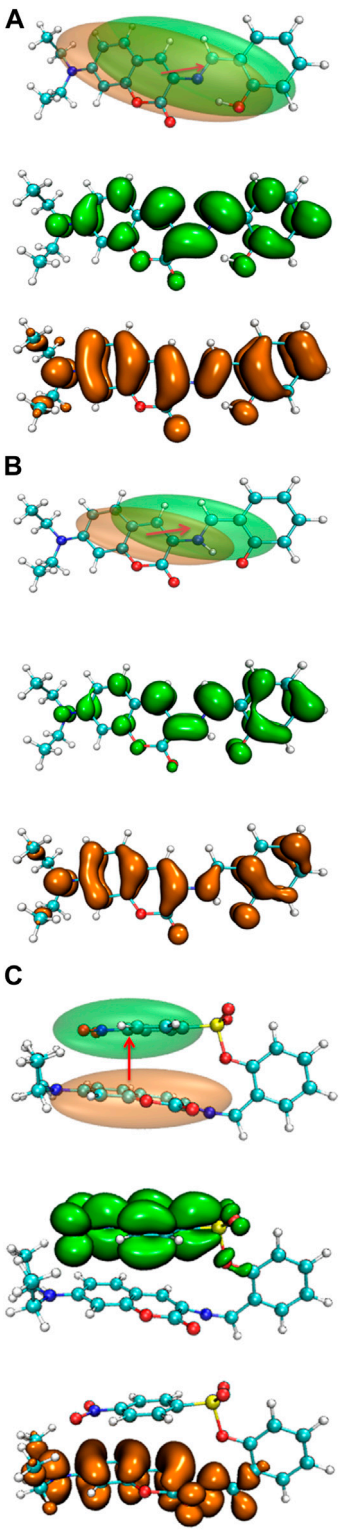

FIGURE 10
The electron density difference between the S_0 and S_1 of **(A)** E1, **(B)** K1, and **(C)** DEMCA-NBSC.

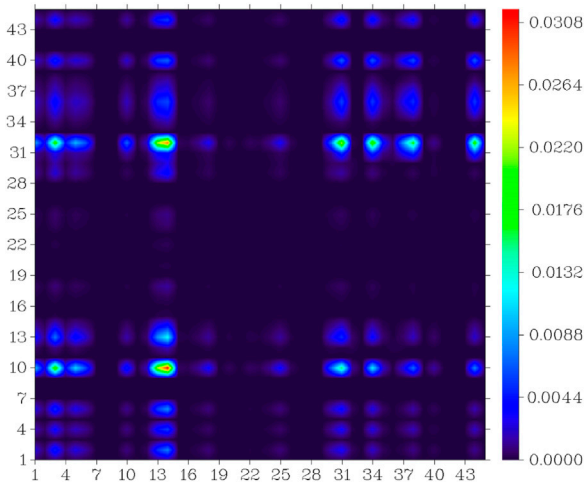

FIGURE 11
Atom-atom electron transfer heat map of the E1 molecule from S_0 to S_1.

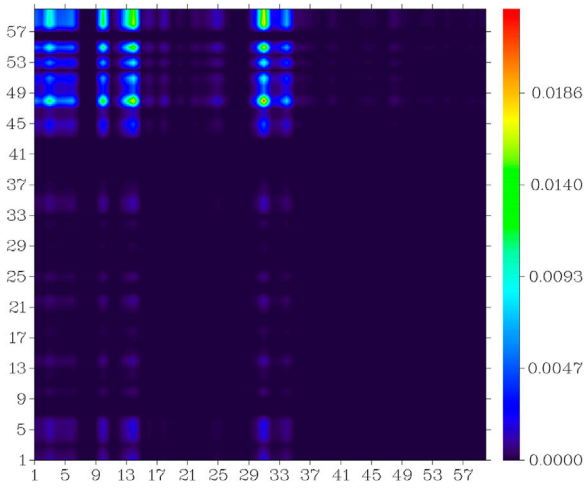

FIGURE 12
Atom-atom electron transfer heat map of the DEMCA-NBSC molecule from S_0 to S_1.

1.0 Å) was the most stable ground state (S_0) for the DEMCA-OH, while the Keto* form (K1*, O-H bond length with about 1.7 Å and N-H bond length with about 1.0 Å) was the most stable first excited state (S_1) for DEMCA-OH. Meanwhile, the energy barrier from E1* to K1* and E1 to K1 were 0.07 eV and 0.23eV respectively which led to the typical ESIPT process in the optical excitation of the DEMCA-OH. Dual emission band with different wavelengths corresponding to the E1* to E1 and K1* to K1 process could be obtained from this mechanism, which was consistent with the experimental results.

The energy surface hopping dynamics between the first excited state and ground state of DEMCA-OH was analyzed through the NX program. During the sufficient simulation time (300fs), the variation of O-H bond length was in the range of 0.8–2.1 Å. The proton transfer (PT, 22 fs) and reversed proton transfer (RPT, 290 fs) process shown in Figure 6 indicated the low energy barrier between the E1* and K1* state of probe DEMCA-OH. Meanwhile, the energy barrier from K1* to E1* (0.14 eV) was twice as much as the energy

TABLE 4 The calculated [experimental (Ding et al., 2023b)] excitation and emitting fluorescence wavelength of the probes.

Probe	λ_{ex} (wB2GP-PLYP in DMF, nm)	λ_{ex} (experimental in DMF, nm)	λ_{em} (wB2GP-PLYP in DMF, nm)	λ_{em} (experimental in DMF, nm)
E1	438	450	485	500
K1	443	450	567	575
NBSC	421	430	493	500

barrier from K1* to E1* (0.07 eV), which led to the longer duration in K1* over E1* as shown in the statistical results on the energy surface hopping dynamics of DEMCA-OH S_1 state. The theoretical results were consistent with the larger measured fluorescent intensity with ESIPT emission (K1* to K1) over normal emission (E1* to E1), as shown in Figure 1 of reference [45].

The interaction within transition state EK1 (O-H bond length 1.3 Å and N-H bond length 1.2 Å) from E1 to K1 was demonstrated in the potential energy curve of ground state S_0 of DEMCA-OH, as shown in Figure 7. It was further confirmed that hydrogen bond interaction of N . . . O-H and N-H . . . O had a crucial role in the stability of the structure of DEMCA-OH. The 2D projection of the LOL in the N-H-O hydrogen bond area within E1, EK1, and K1 molecules is shown in Figure 8 and clearly indicates the electron distribution variation while the proton transfers between adjacent oxygen and nitrogen atoms. From Figures 7, 8, it can be concluded that competition between the strength of hydrogen bond interactions of N . . . O-H and N-H . . . O led to the stable molecular structure of DEMCA-OH. Due to the higher electric negativity of oxygen than nitrogen, the strength of O-H over N-H made E1 the preferable stable ground state structure of DEMCA-OH over K1.

Furthermore, the proton transfer also influenced the static electrical potential of the molecule, especially the neighbor area of the two adjacent oxygen atoms, as shown in Figure 9. It can be seen that when the O-H hydrogen bond was formed in E1, the shared electrons between oxygen and hydrogen reduced the absolute value of the static electrical potential near the oxygen atom. While the N-H hydrogen bond was formed in K1, the absolute value of the static electrical potential near the oxygen atom was clearly larger than that in the E1 molecule.

The main electron excitation and emission processes in the probe molecule DEMCA are summarized in Table 2 and Table 3 respectively. It can be seen that the main orbital composition correlated to the electron excitation and emission processes in the probes was between the highest occupied molecular orbital (homo) and lowest unoccupied molecular orbital (lumo). Compared with the E1 molecule, there were larger stoke shifts between the wavelengths of electron excitation and emissions within the K1 molecule, which was consistent with the experimental results (Ding et al., 2023b). Meanwhile, the oscillator strength of the electron transition from S_1 to S_0 in NBSC molecules was smaller than that within the E1 and K1 molecules, which was also found in the experimental results (Ding et al., 2023b).

The electron density difference between the S_0 and S_1 of E1 and K1 are shown in Figure 10. The electrons were excited from the hole area (orange part) to the electron area (green part). The absorption and emission bands in E1 and K1 could be due to the (π,π) transition with intramolecular local charge transfer character. While the corresponding absorption and emission bands in NBSC should be produced by a non-local charge transfer process, as shown in Figure 10C.

In the S_0 to S_1 electron excitation process, the biggest electron donor and acceptor atoms were N (No.14) and C (No.10 and No.32) respectively (atom numbers were referred to Supplementary Figure S2), which was indicated in the atom-atom electron transfer heat map of the E1 molecule (Figure 11). Two end ethylene groups (atom No.15-No.28) were hardly involved in this process, which is indicated in Figure 11 as well. For clarity, the similar atom-atom electron transfer heat map of the K1 molecule with the E1 molecule was not depicted here. The atom-atom electron transfer heat map of DEMCA-NBSC molecule (Figure 12, atom numbers are referred to in Supplementary Figure S3) clearly indicated the non-local intra charge transfer character from S_0 to S_1 electron excitation process just as the results mentioned before.

The theoretical and experimental center wavelengths of the absorption and emission bands of the probes are summarized in Table 4. Although there was a clear deviation from the experimental wavelength, a similar trend of wavelength varying with the experimental value was found in the calculation. It can be seen that there are larger stoke shifts between absorption and emission wavelengths in the K1 molecule than the E1 molecule from both the theoretical and experimental results.

4 Conclusion

The different stable conformations of probe DEMCA-OH were found through a quantum mechanical method. The E1 and K1 form received lower energy due to the hydrogen bond interaction which stabilized the structure of the probe. The low energy barrier between their first excited state E1* and K1* indicated the typical ESIPT process within the optical excitation on the probe DEMCA-OH. The energy surface hopping dynamics analysis on the first excited state further confirmed that the ESIPT process happened in the electronic excitation of the probe DEMCA-OH. Meanwhile, the electron density difference analysis between the ground state and first excited state indicated a non-local intramolecular charge transfer process in DEMCA-NBSC rather than a local intramolecular charge transfer process (π,π transition), which occurred in DEMCA-OH when the molecules were under optical excitation. All these results provide insights into preparing a wide range of fluorescent probes and expanding the potential for widespread use in bio-medical applications.

Data availability statement

The original contributions presented in the study are included in the article/Supplementary Material, further inquiries can be directed to the corresponding author.

Author contributions

TM: Data curation, Writing–original draft. HH: Data curation, Software, Writing–original draft. YL: Data curation, Writing–original draft. YP: Conceptualization, Funding acquisition, Investigation, Writing–original draft.

Funding

The author(s) declare financial support was received for the research, authorship, and/or publication of this article. This work was funded by the Natural Science Foundation of Liaoning Province (2022-MS-389, 20180550512, JYTQN201923).

Conflict of interest

The authors declare that the research was conducted in the absence of any commercial or financial relationships that could be construed as a potential conflict of interest.

Publisher's note

All claims expressed in this article are solely those of the authors and do not necessarily represent those of their affiliated organizations, or those of the publisher, the editors and the reviewers. Any product that may be evaluated in this article, or claim that may be made by its manufacturer, is not guaranteed or endorsed by the publisher.

Supplementary material

The Supplementary Material for this article can be found online at: https://www.frontiersin.org/articles/10.3389/fchem.2023.1290745/full#supplementary-material

References

Ahlrichs, F. R., and Ahlrichs, R. (2005). Balanced basis sets of split valence, triple zeta valence and quadruple zeta valence quality for H to Rn: design and assessment of accuracy. *Phys. Chem. Chem. Phys.* 7, 3297–3305. doi:10.1039/b508541a

Bannwarth, C., Grimme, S. S., and Grimme, S. (2019). GFN2-xTB-An accurate and broadly parametrized self-consistent tight-binding quantum chemical method with multipole electrostatics and density-dependent dispersion contributions. *J. Chem. Theory Comput.* 15, 1652–1671. doi:10.1021/acs.jctc.8b01176

Barbatti, M., Ruckenbauer, M., Plasser, F., Pittner, J., Granucci, G., Lischka, M. H., et al. (2014). Newton-X: a surface-hopping program for nonadiabatic molecular dynamics. *WIREs Comput. Mol. Sci.* 4, 26–33. doi:10.1002/wcms.1158

Blasco, N., Cámara, Y., Núñez, E., Beà, A., Barés, G., Forné, C., et al. (2018). Cardiomyocyte hypertrophy induced by Endonuclease G deficiency requires reactive oxygen radicals accumulation and is inhibitable by the micropeptide humanin. *Redox Biol.* 16, 146–156. doi:10.1016/j.redox.2018.02.021

Boese, A. D. (2015). Basis set limit coupled-cluster studies of hydrogen-bonded systems. *Mol. Phys.* 113, 1618–1629. doi:10.1080/00268976.2014.1001806

Brauer, B., Martin, M. K. J. M. L., and Martin, J. M. L. (2014). Some observations on counterpoise corrections for explicitly correlated calculations on noncovalent interactions. *J. Chem. Theory Comput.* 10, 3791–3799. doi:10.1021/ct500513b

Cao, Q., Zhang, J. B., Sun, D. Y., Fu, J. T., Wu, W. B., Chen, X. F., et al. (2023). Pyroptosis, metabolism, and oxidation in tumorigenesis: mechanisms and therapeutic implications. *Antioxidants Redox Signal.* 39 (7-9) 6, 512–530. doi:10.1089/ars.2023.0257

Chen, T. F., and Chen, F. (2012). Multiwfn: a multifunctional wavefunction analyzer. *J. Comput. Chem.* 33, 580–592. doi:10.1002/jcc.22885

Chen, X. G., Mei, Y., and Song, Q. H. (2022). A 3-(2′-nitro vinyl)-4-phenylselenyl coumarin as a fluorescent probe for distinguishing detection of Cys/Hcy and GSH. *Dyes And Pigments* 203, 110312. doi:10.1016/j.dyepig.2022.110312

Chen, Y., Shui, M., Yuan, Q., Vong, C. T., Yang, Z., Wang, Z. S., et al. (2023). Wielding the double-edged sword: redox drug delivery systems for inflammatory bowel disease. *J. Control. Release* 358, 510–540. doi:10.1016/j.jconrel.2023.05.007

das Neves, R. P., Chagoyen, M., Martinez-Lorente, A., Iniguez, C., Calatrava, A., Calabuig, J., et al. (2023). Each cellular compartment has a characteristic protein reactive cysteine ratio determining its sensitivity to oxidation. *Antioxidants* 12, 1274–2062. doi:10.3390/antiox12061274

Ding, G., Wang, X., Luo, D., Meng, S., Zhou, L., Fan, Y., et al. (2023b). A simple ESIPT combines AIE character "turn on" fluorescent probe for Hcy/Cys/GSH detection and cell imaging based on coumarin unit. *Dyes And Pigments* 208, 110762. doi:10.1016/j.dyepig.2022.110762

Ding, W., Yao, S., Chen, Y., Wu, Y., Li, Y., He, W., et al. (2023a). A near-infrared fluorescent and photoacoustic probe for visualizing biothiols dynamics in tumor and liver. *Molecules* 28, 2229–2463. doi:10.3390/molecules28052229

Du, W., Gong, X.-L., Tian, Y., Zhu, X., Peng, Y., and Wang, Y.-W. (2023). Coumarin-based fluorescence probe for differentiated detection of biothiols and its bioimaging in cells. *Biosensors-Basel* 13, 447–7902. doi:10.3390/bios13040447

Ganguly, P., and Alam, S. F. (2015). Role of homocysteine in the development of cardiovascular disease. *Nutr. J.* 14, 6–6627. doi:10.1186/1475-2891-14-6

Ghosh, S., Verma, P., Cramer, C. J., Truhlar, L. D. G., and Truhlar, D. G. (2018). Combining wave function methods with density functional theory for excited states. *Chem. Rev.* 118, 7249–7292. doi:10.1021/acs.chemrev.8b00193

Goswami, R., Karthick, K., Das, S., Rajput, S., Seal, N., Pathak, B., et al. (2022). Brønsted acid-functionalized ionic Co(II) framework: a tailored vessel for electrocatalytic oxygen evolution and size-exclusive optical speciation of biothiols. *ACS Appl. Mat. Interfaces* 14, 29773–29787. doi:10.1021/acsami.2c05299

Gothland, A., Jary, A., Grange, P., Leducq, V., Beauvais-Remigereau, L., Dupin, N., et al. (2023). Harnessing redox disruption to treat human herpesvirus 8 (HHV-8) related malignancies. *Antioxidants* 12, 84–2214. doi:10.3390/antiox12010084

Grimme, L. S., and Grimme, S. (2010). Assessment of TD-DFT methods and of various spin scaled CIS(D) and CC2 versions for the treatment of low-lying valence excitations of large organic dyes. *J. Chem. Phys.* 132. doi:10.1063/1.3418614

Grimme, L. S., and Grimme, S. (2014). Double-hybrid density functionals. *WIREs Comput. Mol. Sci.* 4, 576–600. doi:10.1002/wcms.1193

Grimme, S., Goerigk, S. L., and Goerigk, L. (2011). Effect of the damping function in dispersion corrected density functional theory. *J. Comput. Chem.* 32, 1456–1465. doi:10.1002/jcc.21759

Hao, Y.-Q., Zhang, Y.-T., Zhu, D.-D., Luo, L.-J., Chen, L., Tang, Z.-L., et al. (2022). Dual-emission fluorescent probe for discriminative sensing of biothiols. *Chin. J. Of Anal. Chem.* 50, 100153. doi:10.1016/j.cjac.2022.100153

Hou, H., Liu, Q., Liu, X., Fu, S., Zhang, H., Li, S., et al. (2022). Dual response site fluorescent probe for highly sensitive detection of cys/hcy and GSH *in vivo* through two different emission channels. *Biosensors* 12, 1056. doi:10.3390/bios12111056

Huang, J., Yang, X., Zhang, J., Wang, F., and Tang, X. (2023). The correlation between *Helicobacter pylori* immunoglobulin G seropositivity and plasma homocysteine levels in adults. *Mediat. Inflamm.* 23, 1–6. doi:10.1155/2023/7590549

Humphrey, W., Schulten, A. K., and Schulten, K. K. (1995). VMD: visual molecular dynamics. *J. Mol. Graph.* 14, 33–38. doi:10.1016/0263-7855(96)00018-5

Jiang, H., Yin, G., Gan, Y., Yu, T., Zhang, Y., Yin, H. P., et al. (2022). A multisite-binding fluorescent probe for simultaneous monitoring of mitochondrial homocysteine, cysteine and glutathione in live cells and zebrafish. *Chin. Chem. Lett.* 33, 1609–1612. doi:10.1016/j.cclet.2021.09.036

Kaushik, R., Nehra, N., Zimcik, V. P., and Zimcik, P. (2023). Near-Infrared probes for biothiols (cysteine, homocysteine, and glutathione): a comprehensive review. *Acs Omega* 8, 98–126. doi:10.1021/acsomega.2c06218

Kisty, E. A., Saart, E. C., and Weerapana, E. (2023). Identifying redox-sensitive cysteine residues in mitochondria. *Antioxidants* 12, 992–1615. doi:10.3390/antiox12050992

Li, S., Huo, F., Yin, Y. C., and Yin, C. (2022). A dual-response NIR probe reveals positive correlation between biothiols and viscosity under cellular stress change. *Chem. Commun.* 58, 4881–4884. doi:10.1039/d2cc00668e

Lin, X. Y., Sun, S. H., Liu, Y. T., Shi, Q. Q., Peng, J. J. Y. J., and Peng, Y. J. (2023). Thiophene and diaminobenzo- (1,2,5-thiadiazol)- based DAD-type near-infrared fluorescent probe for nitric oxide: a theoretical research. *Front. Chem.* 10, 990979. doi:10.3389/fchem.2022.990979

Liu, E. J. C., and Liu, J. (2023). Mitochondrial calcium and reactive oxygen species in cardiovascular disease. *Cardiovasc. Res.* 119, 1105–1116. doi:10.1093/cvr/cvac134

Liu, J., Sun, Y.-Q., Huo, Y., Zhang, H., Wang, L., Zhang, P., et al. (2014). Simultaneous fluorescence sensing of Cys and GSH from different emission channels. *J. Am. Chem. Soc.* 136, 574–577. doi:10.1021/ja409578w

Liu, P., Liu, Y. L., Huang, H., Peng, G.Y.-j., and Peng, Y. J. (2023). Theoretical investigation on FRET strategy of ratio metric fluorescent probe sensing hydrogen sulfide. *Spectrochimica Acta Part A Mol. Biomol. Spectrosc.* 289, 122223. doi:10.1016/j.saa.2022.122223

Liu, Y., Yu, Y., Zhao, Q., Tang, C., Zhang, H., Qin, Y., et al. (2021). Fluorescent probes based on nucleophilic aromatic substitution reactions for reactive sulfur and selenium species: recent progress, applications, and design strategies. *Coord. Chem. Rev.* 427, 213601. doi:10.1016/j.ccr.2020.213601

Liu, Y.-l., Peng, H.Y.-j., and Peng, Y.-j. (2022). Fluorescent probe for simultaneous detection of human serum albumin and sulfite: a theoretical analysis. *J. Mol. Struct.* 1255, 132441. doi:10.1016/j.molstruc.2022.132441

Long, L., Yuan, F., Yang, X., Ruan, P., Chen, X., Li, L., et al. (2022). On-site discrimination of biothiols in biological fluids by a novel fluorescent probe and a portable fluorescence detection device. *Sensors Actuators B Chem.* 369, 132211. doi:10.1016/j.snb.2022.132211

Lu, T. (2021). Molclus program. Version 1.9.9.3 http://www.keinsci.com/research/molclus.html (Accessed february 11, 2021).

Ma, Y., Wang, Y., Hui, X., Lin, B., Yuan, Y., Lv, X. R., et al. (2022). Dual-molecular targeted NIR II probe with enhanced response for head and neck squamous cell carcinoma imaging. *Nanotechnology* 33, 225101. doi:10.1088/1361-6528/ac56f9

Martins, E. L. J. B. L., and Martins, J. B. L. (2019). Analysis of lowest energy transitions at TD-DFT of pyrene in vacuum and solvent. *J. Mol. Model.* 25, 183–188. doi:10.1007/s00894-019-4065-9

Mezhnina, V., Ebeigbe, O. P., Kondratov, A. R. V., and Kondratov, R. V. (2022). Circadian control of mitochondria in reactive oxygen species homeostasis. *Antioxidants Redox Signal.* 37, 647–663. doi:10.1089/ars.2021.0274

Neese, F. (2018). Software update: the ORCA program system, version 4.0. *Wiley Interdiscip. Rev. Comput. Mol. Sci.* 8 (1), e1327. doi:10.1002/wcms.1327

Niu, B., Liao, K., Zhou, Y., Wen, T., Quan, G., Pan, X., et al. (2021). Application of glutathione depletion in cancer therapy: enhanced ROS-based therapy, ferroptosis, and chemotherapy. *Biomaterials* 277, 121110–125483. doi:10.1016/j.biomaterials.2021.121110

O'Boyle, N. M., Vandermeersch, T., Flynn, C. J., Hutchison, A. R. G. R., and Hutchison, G. R. (2011). Confab - systematic generation of diverse low-energy conformers. *J. Cheminform.* 3, 8–16. doi:10.1186/1758-2946-3-8

Pandya, J. D., Musyaju, S., Modi, H. R., Cao, Y., Flerlage, W. J., Huynh, L., et al. (2023). Comprehensive evaluation of mitochondrial redox profile, calcium dynamics, membrane integrity and apoptosis markers in a preclinical model of severe penetrating traumatic brain injury. *Free Radic. Biol. Med.* 198, 44–58. doi:10.1016/j.freeradbiomed.2023.02.001

Pang, X., Dong, J., Gao, L., Wang, L., Yu, S., Kong, J., et al. (2020). Dansyl-peptide dual-functional fluorescent chemosensor for Hg2+ and biothiols. *Dyes And Pigments* 173, 107888–113614. doi:10.1016/j.dyepig.2019.107888

Peng, Y. J., Wang, H.C.-j., and Wang, C. J. (2021). DFT investigation on electronic structure, chemical bonds and optical properties of Cu6(SR)6 nanocluster. *Chem. Phys. Lett.* 780, 138898. doi:10.1016/j.cplett.2021.138898

Peng, Z., Li, Z., Zhou, T., Wu, D., Wang, E., Ma, C., et al. (2023). Visualizing biothiols *in vivo* using a dual-channel sensitive fluorescent probe. *Dyes And Pigments* 214, 111230. doi:10.1016/j.dyepig.2023.111230

Qu, L., Chen, H., Chen, H., Shi, C., Li, H., Lian, W., et al. (2023). Nanoparticles containing biocompatible radicals based on 1,2,4-benzotriazinyl for reactive oxygen species scavenging in living cells. *ACS Appl. Nano Mat.* 6, 5781–5788. doi:10.1021/acsanm.3c00209

Raut, J., and Sahoo, P. P. (2021). Detection of biothiols using some novel chemosensors: an overview. *Mini-Reviews Org. Chem.* 18, 867–884. doi:10.2174/1570193x17999201109212903

Shellaiah, M., and Sun, K. W. (2023). Review on carbon dot-based fluorescent detection of biothiols. *Biosensors-Basel* 13, 335–2162. doi:10.3390/bios13030335

Si, L., Fu, Q., Shi, Z., Zhang, T., Hou, Q., Ai, Z. S., et al. (2023). The fluorescent detection of biothiols and antimicrobial study based on copper(I) iodide coordination polymer. *Dyes And Pigments* 215, 111228. doi:10.1016/j.dyepig.2023.111228

Su, P., Zhu, Z., Tian, Y., Liang, L., Wu, W., Cao, J., et al. (2020). A TAT peptide-based ratiometric two-photon fluorescent probe for detecting biothiols and sequentially distinguishing GSH in mitochondria. *Talanta* 218, 121127. doi:10.1016/j.talanta.2020.121127

Swiderski, J., Sakkal, S., Apostolopoulos, V., Zulli, A., and Gadanec, L. K. (2023). Combination of taurine and black pepper extract as a treatment for cardiovascular and coronary artery diseases. *Nutrients* 15, 2562–3501. doi:10.3390/nu15112562

Takagi, T., Naito, Y., Uchiyama, K., Fukui, A., Yoriki, H., Tsuji, T., et al. (2012). Tu1891 intestinal peroxiredoxin-6 is a predictive marker for the outcome of the treatment with granulocyte and monocyte adsorption in patients with ulcerative colitis. *Gastroenterology* 142, S871–S871. doi:10.1016/s0016-5085(12)63378-2

Tang, R., Wang, C., Zhou, X., Feng, M., Li, Z., Chen, Y. G., et al. (2023). An aggregation induced emission chalcone fluorescent probe with large Stokes shift for biothiols detection. *Spectrochimica Acta Part A Mol. Biomol. Spectrosc.* 300, 122870. doi:10.1016/j.saa.2023.122870

Villavicencio-Tejo, F., Olesen, M. A., Aranguiz, A., and Quintanilla, R. A. (2022). Activation of the Nrf2 pathway prevents mitochondrial dysfunction induced by caspase-3 cleaved tau: implications for alzheimer's disease. *Antioxidants* 11, 515–2057. doi:10.3390/antiox11030515

Wang, R., Zhang, T., Zhang, W., Chen, B., Liu, J., Liu, G., et al. (2023). Microperoxidase-11 functionalized nanozyme with enhanced peroxidase-mimicking activities for visual detection of cysteine. *Anal. Chim. Acta* 67, 2332–2345. doi:10.1016/j.aca.2023.341386

Weerapana, E., Wang, C., Simon, G. M., Richter, F., Khare, S., Dillon, M. B. D., et al. (2010). Quantitative reactivity profiling predicts functional cysteines in proteomes. *Nature* 468, 790–795. doi:10.1038/nature09472

Wu, Y., Guo, X., Ma, X., Zhu, Y., Zeng, Y. H., and Zeng, H. (2023). Novel near-infrared frequency up-conversion luminescence probe for monitoring biothiols *in vitro* and *in vivo*. *Sensors Actuators B Chem.* 385, 133705. doi:10.1016/j.snb.2023.133705

Yin, G., Niu, T., Yu, T., Gan, Y., Sun, X., Yin, P., et al. (2019). Simultaneous visualization of endogenous homocysteine, cysteine, glutathione, and their transformation through different fluorescence channels. *Angew. Chem. Int. Ed.* 58, 4557–4561. doi:10.1002/anie.201813935

Yu, H. S., Li, S. L., and Truhlar, D. G. (2016). Perspective: Kohn-Sham density functional theory descending a staircase. *J. Chem. Phys.* 145, 130901. doi:10.1063/1.4963168

Zhang, H., Xu, L., Chen, W., Huang, J., Huang, C., Song, J. X., et al. (2019). Simultaneous discrimination of cysteine, homocysteine, glutathione, and H2S in living cells through a multisignal combination strategy. *Anal. Chem.* 91, 1904–1911. doi:10.1021/acs.analchem.8b03869

Zhang, Y., Wang, Y., Ni, H., Huang, W., Xu, P., and Ji, M. (2023). An off-on quinoxaline-based fluorescent probe for lighting up biothiols in living cells and zebrafish. *Tetrahedron* 139, 133433–135476. doi:10.1016/j.tet.2023.133433

Zhao, G., Shi, W., Xin, X., Li, F. Y., and Li, Y. (2022). Solvent dependence of ESIPT process in 2-(2-carbonmethoxy-3,4-dichloro-6-hydroxyphenyl) compounds. *J. Mol. Liq.* 354, 118807. doi:10.1016/j.molliq.2022.118807

Zhao, G. J., Yang, Y. F., Zhang, C. Y., Li, Y. Z. Y., and Li, Y. Q. (2021). The theoretical study of excited-state intramolecular proton transfer of N, N,-bis (salicylidene)-(2-(3″4′-diaminophenyl) benzothiazole). *J. Luminescence* 230, 117741. doi:10.1016/j.jlumin.2020.117741

Zhong, X., He, R., You, S., Liu, B., Wang, X., and Mao, J. (2023). The roles of aerobic exercise and folate supplementation in hyperhomocysteinemia- accelerated atherosclerosis. *Acta Cardiol. Sin.* 39(2), 309–318. doi:10.6515/acs.202303_39(2).20221027a

Zhou, B., Wang, B., Bai, M., Dong, M., and Tang, X. (2023a). Fluorescent probe for highly selective detection of cysteine in living cells. *Spectrochimica Acta Part a-Molecular And Biomol. Spectrosc.* 294, 122523. doi:10.1016/j.saa.2023.122523

Zhou, M., Zhao, J., Cui, Y., Wang, Q., Dai, Y., Xia, P. L., et al. (2015). Theoretical study on the excited-state intramolecular proton-transfer reaction of 10-hydroxybenzo[h]quinoline in methanol and cyclohexane. *J. Luminescence* 161, 1–6. doi:10.1016/j.jlumin.2014.12.049

Zhou, S., Ding, X., Zhao, Y., Luo, J. W., and Luo, W. (2023b). A flavone-based long-wavelength fluorescent probe to detect biothiols *in vitro* and *in vivo*. *Chin. J. Of Org. Chem.* 43, 178–185. doi:10.6023/cjoc202206016

Zhu, G.-B., Gao, J., Zhang, M.-Y., He, L., Han, H.-H., Zang, Y., et al. (2023). Iodine substitution compromises the aggregation-induced emission (AIE) property and enhances the biothiol sensitivity of quinoline-malononitrile-based fluorescent probes. *Dyes And Pigments* 215, 111246. doi:10.1016/j.dyepig.2023.111246

frontiers | Frontiers in Chemistry

TYPE Original Research
PUBLISHED 02 February 2024
DOI 10.3389/fchem.2024.1355238

OPEN ACCESS

EDITED BY
Panwang Zhou,
Shandong University, China

REVIEWED BY
Anex Jose,
Stanford University, United States
Zhigang Yang,
Shenzhen University, China

*CORRESPONDENCE
Xueying Ji,
jixueying@163.com

†These authors have contributed equally to this work

RECEIVED 13 December 2023
ACCEPTED 23 January 2024
PUBLISHED 02 February 2024

CITATION
Mi L, Niu C, Chen J, Han F and Ji X (2024), Development of an activatable far-red fluorescent probe for rapid visualization of hypochlorous acid in live cells and mice with neuroinflammation.
Front. Chem. 12:1355238.
doi: 10.3389/fchem.2024.1355238

Development of an activatable far-red fluorescent probe for rapid visualization of hypochlorous acid in live cells and mice with neuroinflammation

Long Mi[1†], Changhe Niu[2†], Jianqiang Chen[1], Feng Han[1] and Xueying Ji[1*]

[1]Department of Radiology, Department of Ophthalmology, The First Affiliated Hospital of Hainan Medical University, Hainan Medical University, Haikou, China, [2]Wuhan Children's Hospital, Tongji Medical College, Huazhong University of Science and Technology, Wuhan, China

Recent investigations have suggested that abnormally elevated levels of HOCl may be tightly related to the severity of neuroinflammation. Although some successes have been achieved, fluorescent probes with far-red fluorescence emission and capable of detecting HOCl with high specificity in pure aqueous solution are still urgently needed. Herein, a responsive far-red fluorescent probe, DCI-H, has been constructed to monitor HOCl activity *in vivo* and *in vitro*. DCI-H could rapidly respond to HOCl within 120 s and had a low detection limit for HOCl of 1.5 nM. Importantly, physiologically common interfering species, except for HOCl, did not cause a change in the fluorescence intensity of DCI-HOCl at 655 nm. The results of confocal imaging demonstrated the ability of DCI-H to visualize endogenous HOCl produced by MPO-catalyzed H_2O_2/Cl^- and LPS stimulation. With the assistance of DCI-H, upregulation of HOCl levels was observed in the mice model of LPS-induced neuroinflammation. Thus, we believed that DCI-H provided a valuable tool for HOCl detection and diagnosis of inflammation-related diseases.

KEYWORDS

far-red fluorescent probe, hypochlorous acid, oxidative stress, LPS-induced neuroinflammation, bioimaging

Introduction

Reactive oxygen species (ROS) are a class of anions, free radicals, and neutral small molecules generated by the normal metabolism of intracellular oxygen, including superoxide anion, peroxynitrite, singlet oxygen, hydrogen peroxide, hypochlorous acid (HOCl) and so on (Sies and Jones, 2020; Sun et al., 2020). Endogenous ROS can act as second messengers and are involved in regulating a series of physiological processes, such as redox balance and signal transduction (Linley et al., 2012; Ye et al., 2015; Sies et al., 2022). In living organisms, HOCl is an important ROS, mainly produced in the respiratory burst process of neutrophils (Elbim and Lizard, 2009; Güngör et al., 2009). A large body of research evidence shows that low concentrations of HOCl in organisms can regulate redox balance and resist the invasion of pathogens, while high concentrations of HOCl can cause oxidative damage to biologically active molecules (Goud et al., 2008; Guo et al., 2020; Shakya et al., 2023). For example, overexpression of HOCl can not only react with amnio,

sulfhydryl, and thioethers groups to destroy the spatial structures of proteins and lead to protein inactivation but also react with nitrogen-containing bases to make nucleic acid lose the ability to assemble biological macromolecules (Dharmaraja, 2017). Hydrogen peroxide (H_2O_2) and chloride ion react to generate endogenous HOCl under the catalysis of myeloperoxidase (MPO) (Winterbourn and Kettle, 2000; Ulfig and Leichert, 2021), and the change of HOCl level is closely associated with the occurrence and development of numerous diseases, such as arthritis (Stamp et al., 2012), liver cirrhosis (Whiteman et al., 2005; Jaeschke and Hasegawa, 2006), kidney injury (Malle et al., 2003), and neuronal degeneration (Yap et al., 2006; Ray and Katyal, 2016). Neuroinflammation is associated with chronically activated glial cells (astrocytes and microglia) in the brain, a process that generates large amounts of ROS (Wang et al., 2018; Shukuri et al., 2021). Therefore, the development of a rapid and sensitive method for detecting HOCl is of great significance for diagnosing neuroinflammation.

Currently, routine detection of HOCl includes high-performance liquid chromatography, electrochemistry, gas chromatography, and capillary electrophoresis. However, these techniques are unable to detect HOCl directly and *in situ* in cells or *in vivo* (Zhang et al., 2018). To circumvent this limitation, small-molecule fluorescent probes have attracted much attention due to their high sensitivity, rapid response, simplicity, and excellent selectivity. Numerous HOCl fluorescent probes based on diverse fluorophores, such as coumarin (Samanta and Govindaraju, 2019; He et al., 2020a; He et al., 2020b; Ma et al., 2020; Nguyen et al., 2020; Nie et al., 2020), naphthalimide (Cheng et al., 2021; Fang and Dehaen, 2021; Wang et al., 2021; Tian et al., 2022; Wang et al., 2022), rhodamine (Lu et al., 2020; Yang et al., 2020; Zeng et al., 2023), and boron dipyrromethene (Shi et al., 2021; Bi et al., 2023; Mahanta et al., 2023), have been developed successively. The widespread use of some of the reported fluorescent probes in biological applications was still constrained by certain factors, for example, the limitation of fluorescence emission wavelengths to the visible region or the need for large amounts of organic solvents in the detection system (Dong et al., 2020; Kwon et al., 2022).

With those in mind, a novel far-red fluorescent probe DCI-H was developed. This probe exhibited excellent selectivity, fast response, and high sensitivity to HOCl. In PBS solution, HOCl promoted the release of fluorophore DCI-OH from DCI-H through a specific removal reaction of N, N-dimethylthiocarbamate, resulting in fluorescence enhancement at 655 nm. Noticeably, DCI-H had low cytotoxicity and successfully imaged endogenous HOCl in cells. In addition, the far-red fluorescence emission of DCI-H achieved real-time imaging of HOCl in mice models of LPS-induced neuroinflammation using DCI-HOCl.

Results and discussion

Design and synthesis of DCI-H

Dicyanoisophorone (DCI) was a common fluorophore used for the construction of fluorescent probes with large Stoke shifts, far-red emission properties, superior photostability, and convenient synthesis methods. A novel responsive fluorescent probe, DCI-H, was designed using DCI as the core fluorophore and N, N-dimethylthiocarbamate as the HOCl recognition site (Scheme 1A). With the introduction of chlorine atoms into the molecular backbone of DCI-OH, the pKa value could be lowered to ensure that its fluorescence emission under physiological pH conditions remained in the far-red region (Wang et al., 2020). The chemical structure of DCI-H was well characterized by 1H NMR, 13C NMR, and MS (Supplementary Figure S1–S4). The sensing mechanism of DCI-H toward HOCl was shown in Scheme 1B. Specifically, HOCl first oxidized N, N-dimethylthiocarbamate to form intermediate DCI-N, followed by the release of DCI-OH via a hydrolysis reaction. In order to further confirm this sensing process, mass spectrometry was applied to analyze the solution of DCI-H in the absence or presence of HOCl. Supplementary Figure S4 clearly showed that DCI-H itself exhibited a major peak at m/z = 410.1010, corresponding to DCI-H ([M-H]-); the product after reaction with HOCl demonstrated a major peak at m/z = 323.0890, corresponding to DCI-OH ([M-H]-) (Supplementary Figure S5).

Spectral response of DCI-H toward HOCl

Having obtained DCI-H, its spectral properties were investigated in PBS solution (pH 7.4, 10 mM, 1% acetonitrile) in detail. With 490 nm as the excitation wavelength, the blank DCI-H exhibited weak fluorescence (Figure 1A). This property provided a low background starting state for subsequent experiments to observe the HOCl-induced fluorescence changes. The fluorescence intensity of DCI-H was gradually boosted upon increasing the HOCl concentration from 0 μM to 18 μM (Figure 1B). The addition of 18 μM HOCl induced a fluorescence enhancement at 655 nm up to 17-fold compared with DCI-H itself. Such a significant fold change in fluorescence intensity indicated that DCI-H was highly sensitive for *in vitro* detection of HOCl and held the potential to be utilized in cellular and *in vivo* experiments. The fluorescence intensity value of DCI-H at 655 nm was selected to establish the relationship with HOCl concentration. The fluorescence intensity varied significantly in the presence of 1 μM HOCl while saturating at 18 μM. Data analysis further confirmed that there was a linear relationship between fluorescence intensity at 655 nm and HOCl concentration (0–4 μM), with a fitting equation of F_{665} = 20,939.7 [HOCl] + 5594.21 (R^2 = 0.99). The limit of detection was found to be 1.5 nM in terms of the equation of LOD = 3δ/k (Figure 1C). The fluorescence intensity of DCI-H at 655 nm under continuous excitation with 490 nm light changed little within 360 s, which proved that the N, N-dimethylthiocarbamate did not undergo hydrolysis and displayed excellent stability. Upon the addition of HOCl, the fluorescence intensity increased rapidly within 60 s and remained stable after 120 s, suggesting that DCI-H had an extremely fast response to HOCl (Figure 1D). DIC-H showed negligible changes in fluorescence intensity over a wide pH range from 3.0 to 11.0, indicating that it is not susceptible to pH interference from the biological environment. When HOCl was added to the solution of DIC-H in different pH values, its fluorescence response at pH 3.0–6.0 was weak; however, the response was pronounced in the pH range of 6.0–11.0, especially reaching a maximum at pH 8.0–9.0 (Figure 1E). At physiological pH 7.4, the fluorescence response of DIC-H to HOCl was sufficient for subsequent biological experiments. Selectivity was a very important factor in evaluating the

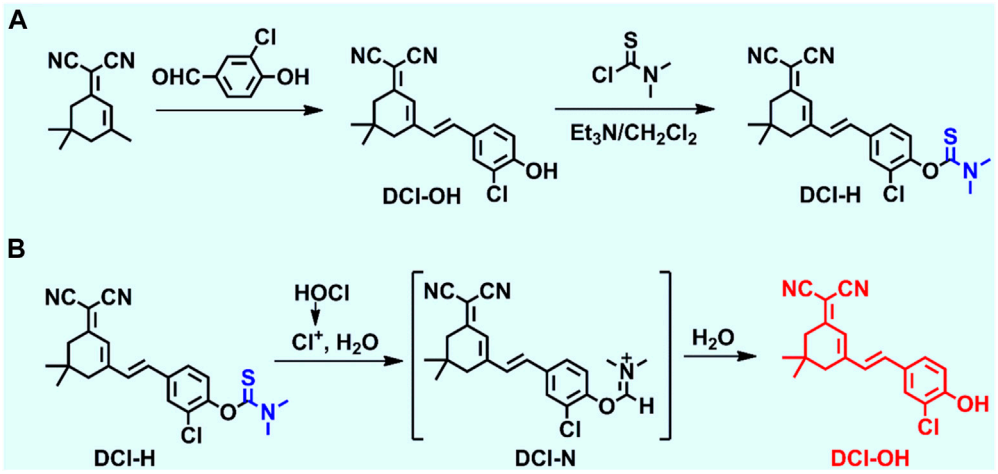

SCHEME 1
(A) Synthetic route of DCI-H. **(B)** The proposed reaction mechanism of DCI-H toward HOCl.

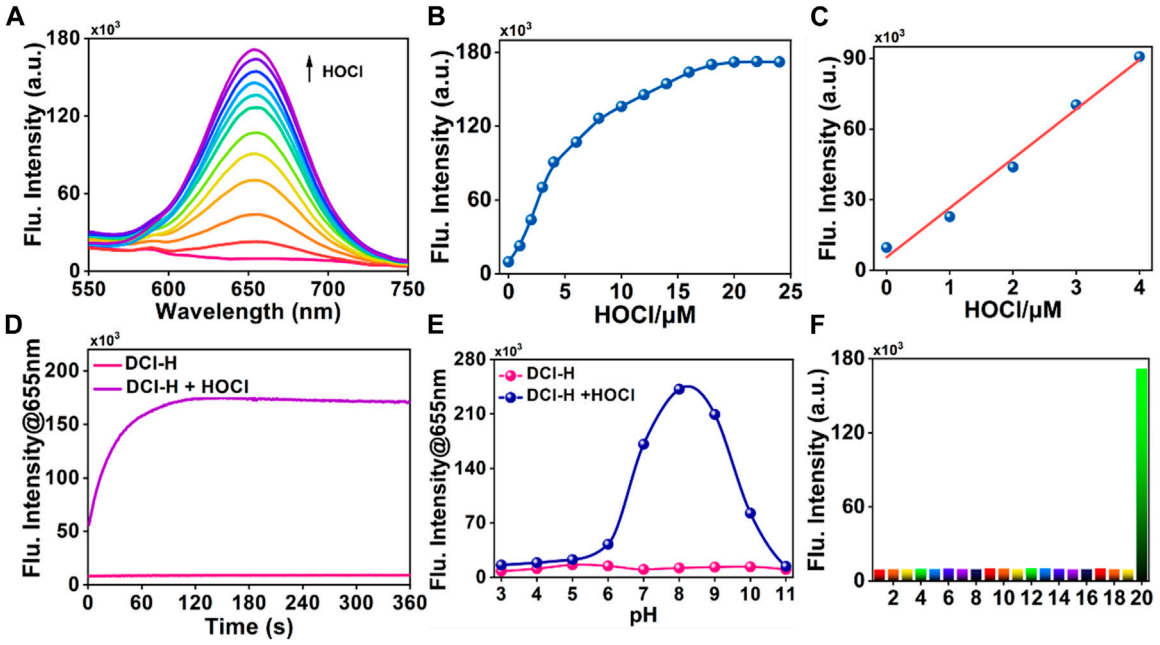

FIGURE 1
Fluorescence response of DCI-H toward HOCl. **(A)** Fluorescence spectra of DCI-H (10 μM) upon exposure to various HOCl concentrations (0, 1, 2, 3, 4, 6, 8, 10, 12, 14, 16, 18 μM). **(B)** Fluorescence intensities at 655 nm as a function of HOCl concentrations (0–24 μM). **(C)** Linearity between fluorescence intensity of DCI-H at 655 nm and HOCl concentration (0–4 μM). **(D)** Time-dependent fluorescence change of DCI-H at 655 nm in the presence or absence of HOCl (18 μM). **(E)** Effects of pH on the fluorescence of DCI-H at 655 nm in the presence or absence of HOCl (18 μM). **(F)** Fluorescence intensities of DCI-H at 655 nm in the presence of a series of potential interfering analytes (100 μM): 1) Met, 2) Gly, 3) Glu, 4) His, 5) S^{2-}, 6) $S_2O_3^{2-}$, 7) SO_3^{2-}, 8) SO_4^{2-}, 9) F^-, 10) K^+, 11) Na^+, 12) Mg^{2+}, 13) Al^{3+}, 14) Ca^{2+}, 15) Fe^{3+}, 16) H_2O_2, 17) $^1O_2$, 18) Cys, 19) GSH, 20) HOCl (18 μM). λ_{ex} = 490 nm.

performance of DCI-H. As shown in Figure 1F, DCI-H gave weak fluorescence responses to common biological species, such as amino acids (Met, Gly, Glu, His), anions (S^{2-}, $S_2O_3^{2-}$, SO_3^{2-}, SO_4^{2-}, F^-), metal ions (K^+, Na^+, Mg^{2+}, Al^{3+}, Ca^{2+}, Fe^{3+}), reactive oxygen species (H_2O_2, $^1O_2$), and thiols (Cys, GSH). Only HOCl triggered an intensive fluorescence response, which ensured its potential for application in complex biological samples.

In situ monitoring endogenous HOCl activity in live cells

Considering the high selectivity and sensitivity of DCI-H, its potential application for direct intracellular monitoring of HOCl was further evaluated. First of all, to confirm biocompatibility, RAW264.7 cells were treated with varying concentrations of

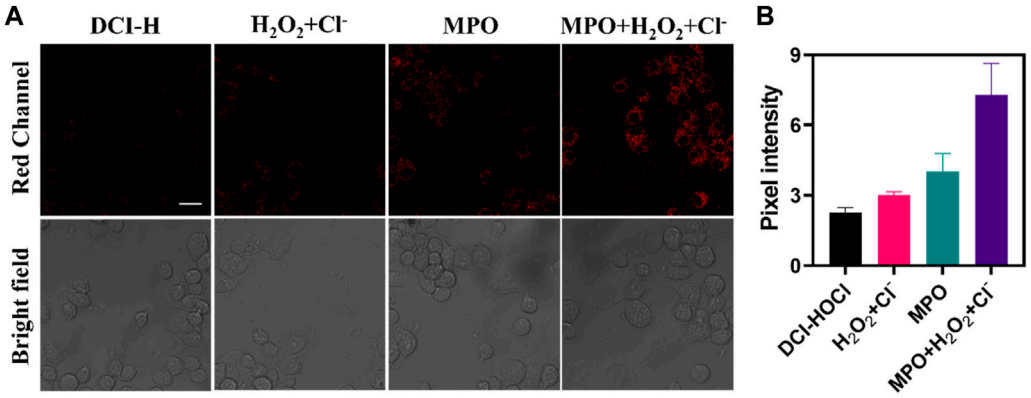

FIGURE 2
Confocal fluorescence images of RAW264.7 cells. **(A)** The cells were incubated with DCI-H (10 μM) for 30 min or preincubated with 100 μM H_2O_2/1 mM Cl-, 100 ng/mL MPO, 100 μM H_2O_2/1 mM Cl-/100 ng/mL MPO for 1 h respectively, followed by incubation with DCI-H for 30 min. **(B)** Pixel intensity from images of **(A)**. Data are presented as mean values with ±s.d. (n = 3). Scale bar: 20 μm.

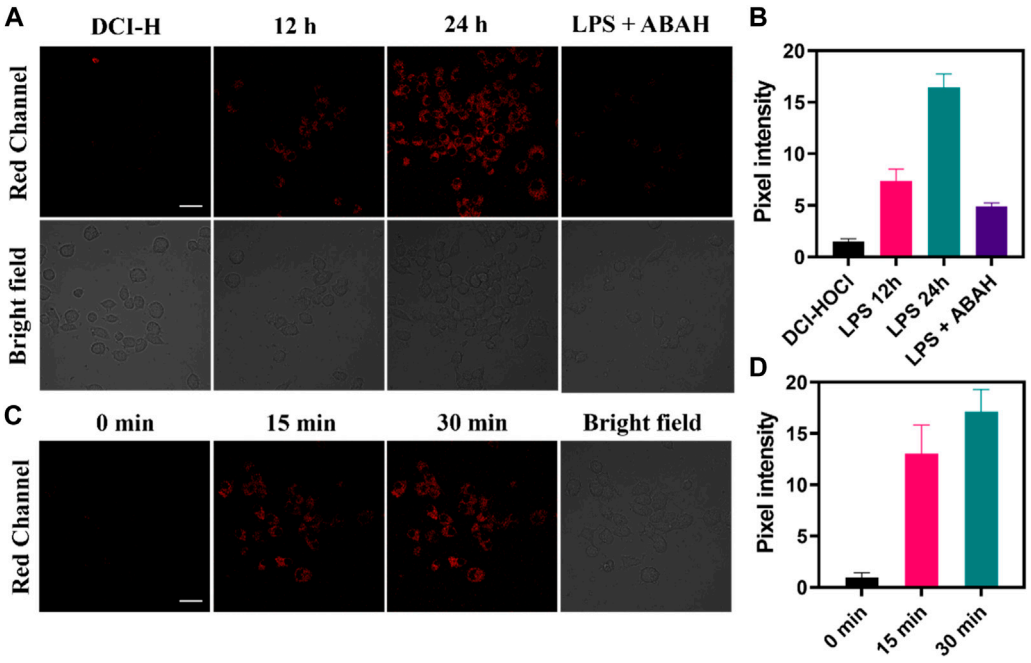

FIGURE 3
Confocal fluorescence images of RAW264.7 cells. **(A)** The cells were stimulated with 0.5 μg mL−1 LPS for 12 h, 24 h or 0.5 μg mL−1 LPS/100 μM ABAH for 24 h, and then incubated with DCI-H (10 μM) for 30 min. **(B)** Pixel intensity from images of **(A)**. **(C)** The cells were stimulated with 0.5 μg mL−1 LPS for 24 h, and then incubated with DCI-HOCl for 0 min, 15 min, 30 min. **(D)** Pixel intensity from images of **(C)**. Data are presented as mean values with ±s.d. (n = 3). Scale bar: 20 μm.

DCI-H and cell viability was examined. As depicted in Supplementary Figure S6, after 24 h of incubation, the cells did not show significant cytotoxicity even at a concentration of 30 μM. MPO catalyzed the reaction between H_2O_2 and chloride ions to produce HOCl, which had a potent oxidizing capacity. This excess of MPO and HOCl might cause oxidative stress and damage to cells. In Figure 2, DCI-H fluoresced relatively weakly in the red channel after incubation with cells alone for 30 min. In contrast, the red channel fluorescence was slightly enhanced upon incubation with H_2O_2/Cl- or MPO. After treatment with MPO, H_2O_2, and Cl-, the red channel fluorescence was significantly augmented, suggesting that MPO catalyzed the generation of a large amount of endogenous HOCl by H_2O_2/Cl-. These data demonstrated that DCI-H could effectively image MPO-generated HOCl in living cells and was expected to serve as a simple tool to explore the different states of the cellular microenvironment with respect to the endogenous HOCl level.

The oxidative stress process was accompanied by the upregulation of HOCl levels, so the application of DCI-H in the

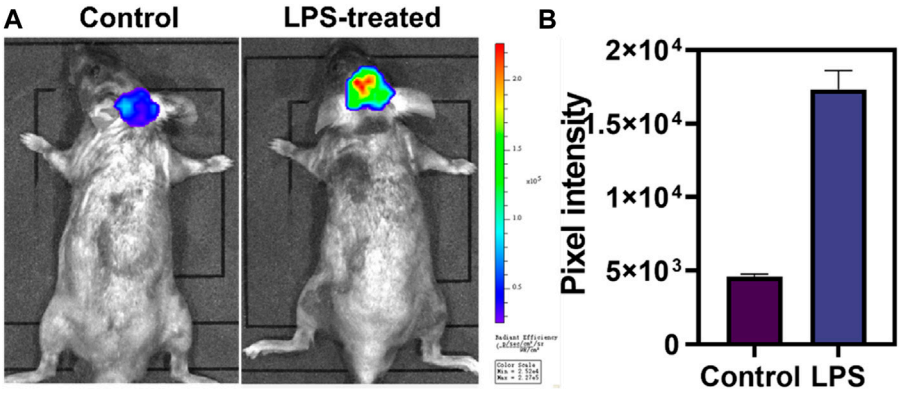

FIGURE 4
Evaluation of HOCl in neuroinflammation with DCI-H. **(A)** The normal and LPS-induced neuroinflammation mice were intracranially injected with DCI-H, respectively. **(B)** Pixel intensity from images of **(A)**. Data are presented as mean values with ±s.d. (n = 3).

LPS-induced cellular inflammation model was explored. As shown in Figure 3A, incubating RAW264.7 cells with DCI-H for 30 min, only very weak fluorescence was observed in the red channel. The cells were stimulated with LPS for 12 h or 24 h followed by incubation with DCI-H for 30 min, and the red channel fluorescence was apparently strengthened compared with that of the DCI-H group. The intensity of fluorescence in the red channel of LPS-treated cells for 24 h was higher than that for 12 h, which indicated that the longer the time of LPS-stimulated cells, the higher the level of endogenous HOCl (Figure 3B). 4-aminobenzhydrazide, an inhibitor of MPO, was able to inhibit the production of HOCl inside the cell. Upon treatment of cells with LPS/ABAH for 24 h, fluorescence in the red channel was suppressed. Subsequently, real-time dynamic imaging of HOCl by DCI-H was investigated at the cellular level. The cells were first stimulated with LPS for 24 h to induce upregulation of HOCl levels followed by incubating with DCI-H and imaged at 0 min, 15 min, and 30 min (Figure 3C). It can be seen that DCI-H showed a gradual enhancement trend with the extension of time (Figure 3D). The above experimental results of confocal fluorescence imaging indicated that DCI-H could be indicative of the detection of HOCl levels in LPS-induced cell models.

Fluorescence imaging of LPS-induced neuroinflammation *in vivo*

Motivated by the superior performance in cellular imaging, we intended to validate the ability of DCI-H to monitor HOCl in a model of neuroinflammation. LPS triggered a series of microglial cell responses to cause neuroinflammation by interacting with the membrane receptor Toll-like receptor 4 (Allendorf et al., 2020). In light of this, C57BL/6J mice were injected intraperitoneally with LPS to mimic neuroinflammation. As illustrated in Figure 4, normal mice were injected intracranially with DCI-H and imaged 30 min later, which revealed weak fluorescence in the mice's brains. Surprisingly, when mice were injected intraperitoneally with LPS for a week to induce neuroinflammation, followed by intracranial injection of DCI-H, significant fluorescence enhancement was observed in the brains of mice. The above experimental results demonstrated that HOCl expression level was upregulated in the brains of mice with LPS-induced neuroinflammation, and DCI-H was able to image this process dynamically.

Conclusion

In summary, a responsive far-red fluorescent probe, DCI-H, was designed and synthesized, which could be directly employed for the detection of HOCl activity. *In vitro* analysis in PBS solution revealed that DCI-H had ultra-high sensitivity, rapid response, and high selectivity for HOCl. Most importantly, it could also dynamically monitor the fluctuation of intracellular HOCl levels in real time via DCI-H. DCI-H was successfully applied to *in vivo* imaging of LPS-induced neuroinflammation model mice, from which it was found that the levels of HOCl in the brains of neuroinflammatory mice were significantly elevated and much higher than that of normal mice. Thus, DCI-H had the potential to be exploited as an effective chemical tool for discovering the biological functions of HOCl and related disease diagnosis.

Materials and general experimental methods

For details, see Supplementary Material.

Synthesis of (E)-O-(2-chloro-4-(2-(3-(dicyanomethylene)-5,5-dimethylcyclohex-1 -en-1-yl)vinyl) phenyl) dimethylcarbamothioate (DCI-H). DCI-OH was synthesized according to the previously reported procedure. DCI-OH (324 mg, 1.0 mmol) was dissolved in dry dichloromethane (10 mL), and then the reaction system was cooled to 0 °C. Diethylamino thionyl chloride (369 mg, 3.0 mmol) and triethylamine (0.5 mL) were added slowly and sequentially. The reaction mixture was brought to room temperature and stirred overnight. The reaction was monitored by TLC. Upon completion of the reaction, the solvent was removed by distillation under reduced pressure. The resulting product was purified by silica gel column chromatography (eluent gradient: 25% ethyl acetate/75% petroleum ether) to give the desired compound (205 mg, 50% yield). ^{1}H NMR

(400 MHz, $CDCl_3$): δ 7.56 (s, 1H), 7.42 (d, J = 8.4 Hz, 1H), 7.17 (d, J = 8.4 Hz, 1H), 6.94 (s, 2H), 6.84 (s, 1H), 3.46 (s, 3H), 3.38 (s, 3H), 2.59 (s, 2H), 2.43 (s, 2H), 1.07 (s, 6H); ^{13}C NMR (100 MHz, $CDCl_3$): δ 185.96, 169.04, 153.01, 150.49, 134.83, 134.50, 130.36, 128.91, 128.41, 126.33, 125.70, 124.23, 113.29, 112.49, 79.43, 43.48, 42.92, 39.12, 38.92, 32.01, 27.97; HRMS m/z: $C_{22}H_{22}ClN_3OS$ $[M-H]^+$ calcd for 410.1094 found 410.1010.

Data availability statement

The original contributions presented in the study are included in the article/Supplementary Material, further inquiries can be directed to the corresponding author.

Ethics statement

The animal study was approved by Institutional Animal Care and Use Committee of Hainan Medical University (protocol code HYLL-2021-133 and date of approval 12 April 2021). The study was conducted in accordance with the local legislation and institutional requirements.

Author contributions

XJ: Conceptualization, Project administration, Supervision, Writing–review and editing. LM: Data curation, Methodology, Writing–original draft. CN: Data curation, Methodology, Writing–original draft. JC: Data curation, Methodology, Writing–original draft. FH: Data curation, Methodology, Writing–original draft.

Funding

The author(s) declare financial support was received for the research, authorship, and/or publication of this article. This research was funded by the Hainan Provincial Natural Science Foundation of China (821MS0832) and Hainan Province Clinical Medical Center (2021), Hainan Province Health and Wellness Industry Research Project (21A200120).

Conflict of interest

The authors declare that the research was conducted in the absence of any commercial or financial relationships that could be construed as a potential conflict of interest.

Publisher's note

All claims expressed in this article are solely those of the authors and do not necessarily represent those of their affiliated organizations, or those of the publisher, the editors and the reviewers. Any product that may be evaluated in this article, or claim that may be made by its manufacturer, is not guaranteed or endorsed by the publisher.

Supplementary material

The Supplementary Material for this article can be found online at: https://www.frontiersin.org/articles/10.3389/fchem.2024.1355238/full#supplementary-material

References

Allendorf, D. H., Franssen, E. H., and Brown, G. C. (2020). Lipopolysaccharide activates microglia via neuraminidase 1 desialylation of Toll-like Receptor 4. *New J. Chem.* 155 (4), 403–416. doi:10.1111/jnc.15024

Bi, S., Yang, T., An, K., Zhou, B., and Han, Y. (2023). A benzo BODIPY based fluorescent probe for selective visualization of hypochlorous acid in living cells and zebrafish. *Spectrochim. Acta. A.* 299, 122860. doi:10.1016/j.saa.2023.122860

Cheng, W., Xue, X., Gan, L., Jin, P., Zhang, B., Guo, M., et al. (2021). Individual and successive detection of H2S and HClO in living cells and zebrafish by a dual-channel fluorescent probe with longer emission wavelength. *Anal. Chim. Acta.* 1156, 338362. doi:10.1016/j.aca.2021.338362

Dharmaraja, A. T. (2017). Role of reactive oxygen species (ROS) in therapeutics and drug resistance in cancer and bacteria. *J. Med. Chem.* 60 (8), 3221–3240. doi:10.1021/acs.jmedchem.6b01243

Dong, S., Zhang, L., Lin, Y., Ding, C., and Lu, C. (2020). Luminescent probes for hypochlorous acid *in vitro* and *in vivo*. *Analyst* 145 (15), 5068–5089. doi:10.1039/d0an00645a

Elbim, C., and Lizard, G. (2009). Flow cytometric investigation of neutrophil oxidative burst and apoptosis in physiological and pathological situations. *Cytom. Part. A.* 75A (6), 475–481. doi:10.1002/cyto.a.20726

Fang, Y., and Dehaen, W. (2021). Fluorescent probes for selective recognition of hypobromous acid: achievements and future perspectives. *Molecules* 26 (2), 363. doi:10.3390/molecules26020363

Goud, A. P., Goud, P. T., Diamond, M. P., Gonik, B., and Abu-Soud, H. M. (2008). Reactive oxygen species and oocyte aging: role of superoxide, hydrogen peroxide, and hypochlorous acid. *Free. Radic. Biol. Med.* 44 (7), 1295–1304. doi:10.1016/j.freeradbiomed.2007.11.014

Güngör, N., Knaapen, A. M., Munnia, A., Peluso, M., Haenen, G. R., Chiu, R. K., et al. (2009). Genotoxic effects of neutrophils and hypochlorous acid. *Mutagenesis* 25 (2), 149–154. doi:10.1093/mutage/gep053

Guo, C., Davies, M. J., and Hawkins, C. L. (2020). Role of thiocyanate in the modulation of myeloperoxidase-derived oxidant induced damage to macrophages. *Redox. Biol.* 36, 101666. doi:10.1016/j.redox.2020.101666

He, L., Xiong, H., Wang, B., Zhang, Y., Wang, J., Zhang, H., et al. (2020a). Rational design of a two-photon ratiometric fluorescent probe for hypochlorous acid with a large Stokes shift. *Anal. Chem.* 92 (16), 11029–11034. doi:10.1021/acs.analchem.0c00030

He, X., Chen, H., Xu, C., Fan, J., Xu, W., Li, Y., et al. (2020b). Ratiometric and colorimetric fluorescent probe for hypochlorite monitor and application for bioimaging in living cells, bacteria and zebrafish. *J. Hazard. Mat.* 388, 122029. doi:10.1016/j.jhazmat.2020.122029

Jaeschke, H., and Hasegawa, T. (2006). Role of neutrophils in acute inflammatory liver injury. *Liver. Int.* 26 (8), 912–919. doi:10.1111/j.1478-3231.2006.01327.x

Kwon, N., Chen, Y., Chen, X., Kim, M. H., and Yoon, J. (2022). Recent progress on small molecule-based fluorescent imaging probes for hypochlorous acid (HOCl)/hypochlorite (OCl^-). *Dyes. Pigments.* 200, 110132. doi:10.1016/j.dyepig.2022.110132

Linley, J. E., Ooi, L., Pettinger, L., Kirton, H., Boyle, J. P., Peers, C., et al. (2012). Reactive oxygen species are second messengers of neurokinin signaling in peripheral sensory neurons. *P P. Natl. Acad. Sci.* 109 (24), E1578–E1586. doi:10.1073/pnas.1201544109

Lu, P., Zhang, X., Ren, T., and Yuan, L. (2020). Molecular engineering of ultra-sensitive fluorescent probe with large Stokes shift for imaging of basal HOCl in tumor cells and tissues. *Chin. Chem. Lett.* 31 (11), 2980–2984. doi:10.1016/j.cclet.2020.08.016

Ma, C., Zhong, G., Zhao, Y., Zhang, P., Fu, Y., and Shen, B. (2020). Recent development of synthetic probes for detection of hypochlorous acid/hypochlorite. *Spectrochim. Acta. A.* 240, 118545. doi:10.1016/j.saa.2020.118545

Mahanta, C. S., Ravichandiran, V., and Swain, S. P. (2023). Recent developments in the design of new water-soluble boron dipyrromethenes and their applications: an updated review. *ACS Appl. Bio. Mat.* 6 (8), 2995–3018. doi:10.1021/acsabm.3c00289

Malle, E., Buch, T., and Grone, H. J. (2003). Myeloperoxidase in kidney disease. *Kidney. Int.* 64 (6), 1956–1967. doi:10.1046/j.1523-1755.2003.00336.x

Nguyen, V. N., Heo, S., Kim, S., Swamy, K. M. K., Ha, J., Park, S., et al. (2020). A thiocoumarin-based turn-on fluorescent probe for hypochlorite detection and its application to live-cell imaging. *Sensors. Actuat. B-Chem.* 317, 128213. doi:10.1016/j.snb.2020.128213

Nie, J., Sun, H., Miao, B., and Ni, Z. (2020). A novel coumarin-based ratiometric near-infrared fluorescence probe for hypochlorous acid in living cells. *Dyes. Pigments.* 181, 108590. doi:10.1016/j.dyepig.2020.108590

Ray, R. S., and Katyal, A. (2016). Myeloperoxidase: bridging the gap in neurodegeneration. *Neurosci. Biobehav. Rev.* 68, 611–620. doi:10.1016/j.neubiorev.2016.06.031

Samanta, S., and Govindaraju, T. (2019). Unambiguous detection of elevated levels of hypochlorous acid in double transgenic AD mouse brain. *ACS Chem. Neurosci.* 10 (12), 4847–4853. doi:10.1021/acschemneuro.9b00554

Shakya, S., Pyles, K. D., Albert, C. J., Patel, R. P., Mccommis, K. S., and Ford, D. A. (2023). Myeloperoxidase-derived hypochlorous acid targets human airway epithelial plasmalogens liberating protein modifying electrophilic 2-chlorofatty aldehydes. *Redox. Biol.* 59, 102557. doi:10.1016/j.redox.2022.102557

Shi, W.-J., Feng, L.-X., Wang, X., Huang, Y., Wei, Y.-F., Huang, Y.-Y., et al. (2021). A near-infrared-emission aza-BODIPY-based fluorescent probe for fast, selective, and "turn-on" detection of HClO/ClO^-. *Talanta* 233, 122581. doi:10.1016/j.talanta.2021.122581

Shukuri, M., Uchino, M., Sakamaki, T., Onoe, S., Hosoi, R., Todoroki, K., et al. (2021). *Ex vivo* imaging and analysis of ROS generation correlated with microglial activation in rat model with acute neuroinflammation induced by intrastriatal injection of LPS. *Biochem. Biophys. Res. Commun.* 584, 101–106. doi:10.1016/j.bbrc.2021.11.008

Sies, H., Belousov, V. V., Chandel, N. S., Davies, M. J., Jones, D. P., Mann, G. E., et al. (2022). Defining roles of specific reactive oxygen species (ROS) in cell biology and physiology. *Nat. Rev. Mol. Cell. Bio.* 23 (7), 499–515. doi:10.1038/s41580-022-00456-z

Sies, H., and Jones, D. P. (2020). Reactive oxygen species (ROS) as pleiotropic physiological signalling agents. *Nat. Rev. Mol. Cell. Bio.* 21 (7), 363–383. doi:10.1038/s41580-020-0230-3

Stamp, L. K., Khalilova, I., Tarr, J. M., Senthilmohan, R., Turner, R., Haigh, R. C., et al. (2012). Myeloperoxidase and oxidative stress in rheumatoid arthritis. *Rheumatology* 51 (10), 1796–1803. doi:10.1093/rheumatology/kes193

Sun, Y., Lu, Y., Saredy, J., Wang, X., Drummer Iv, C., Shao, Y., et al. (2020). ROS systems are a new integrated network for sensing homeostasis and alarming stresses in organelle metabolic processes. *Redox. Biol.* 37, 101696. doi:10.1016/j.redox.2020.101696

Tian, M., Xu, J., Ma, Q., Li, L., Yuan, H., Sun, J., et al. (2022). A novel lysosome-located fluorescent probe for highly selective determination of hydrogen polysulfides based on a naphthalimide derivative. *Spectrochim. Acta. A.* 268, 120708. doi:10.1016/j.saa.2021.120708

Ulfig, A., and Leichert, L. I. (2021). The effects of neutrophil-generated hypochlorous acid and other hypohalous acids on host and pathogens. *Cell. Mol. Life Sci.* 78 (2), 385–414. doi:10.1007/s00018-020-03591-y

Wang, K., Liu, Y., Liu, C., Zhu, H., Li, X., Yu, M., et al. (2022). A new-type HOCl-activatable fluorescent probe and its applications in water environment and biosystems. *Sci. Total. Environ.* 839, 156164. doi:10.1016/j.scitotenv.2022.156164

Wang, S. M., Lim, S. W., Wang, Y. H., Lin, H. Y., Lai, M. D., Ko, C. Y., et al. (2018). Astrocytic CCAAT/Enhancer-binding protein delta contributes to reactive oxygen species formation in neuroinflammation. *Redox. Biol.* 16, 104–112. doi:10.1016/j.redox.2018.02.011

Wang, S. S., Du, S. Y., He, X., Qi, Y. M., Li, X. L., Rong, R. X., et al. (2021). Nucleus-targeting imaging and enhanced cytotoxicity based on naphthalimide derivatives. *Bioorg. Chem.* 115, 105188. doi:10.1016/j.bioorg.2021.105188

Wang, Y., Zhang, W., Ma, T., Li, D., Zhou, Y., Zhang, X., et al. (2020). A new chloro-substituted dicyanoisophorone-based near-infrared fluorophore with a larger Stokes shift and its application for detecting cysteine in cells and *in vivo*. *New J. Chem.* 44 (36), 15432–15438. doi:10.1039/d0nj02913k

Whiteman, M., Rose, P., Siau, J. L., Cheung, N. S., Tan, G. S., Halliwell, B., et al. (2005). Hypochlorous acid-mediated mitochondrial dysfunction and apoptosis in human hepatoma HepG2 and human fetal liver cells: role of mitochondrial permeability transition. *Free. Radic. Biol. Med.* 38 (12), 1571–1584. doi:10.1016/j.freeradbiomed.2005.02.030

Winterbourn, C. C., and Kettle, A. J. (2000). Biomarkers of myeloperoxidase-derived hypochlorous acid. *Free. Radic. Biol. Med.* 29 (5), 403–409. doi:10.1016/s0891-5849(00)00204-5

Yang, J., Fan, M., Sun, Y., Zhang, M., Xue, Y., Zhang, D., et al. (2020). A near-infrared fluorescent probe based on phosphorus-substituted rhodamine for deep imaging of endogenous hypochlorous acid *in vivo*. *Sensors. Actuat. B-Chem.* 307, 127652. doi:10.1016/j.snb.2019.127652

Yap, Y. W., Whiteman, M., Bay, B. H., Li, Y., Sheu, F. S., Qi, R. Z., et al. (2006). Hypochlorous acid induces apoptosis of cultured cortical neurons through activation of calpains and rupture of lysosomes. *J. Neurochem.* 98 (5), 1597–1609. doi:10.1111/j.1471-4159.2006.03996.x

Ye, Z. W., Zhang, J., Townsend, D. M., and Tew, K. D. (2015). Oxidative stress, redox regulation and diseases of cellular differentiation. *BBA-Gen. Subj.* 1850 (8), 1607–1621. doi:10.1016/j.bbagen.2014.11.010

Zeng, S., Liu, X., Kafuti, Y. S., Kim, H., Wang, J., Peng, X., et al. (2023). Fluorescent dyes based on rhodamine derivatives for bioimaging and therapeutics: recent progress, challenges, and prospects. *Chem. Soc. Rev.* 52 (16), 5607–5651. doi:10.1039/d2cs00799a

Zhang, R., Song, B., and Yuan, J. (2018). Bioanalytical methods for hypochlorous acid detection: recent advances and challenges. *Trac. Trends. Anal. Chem.* 99, 1–33. doi:10.1016/j.trac.2017.11.015

frontiers | Frontiers in Chemistry

TYPE Original Research
PUBLISHED 11 March 2024
DOI 10.3389/fchem.2024.1382443

OPEN ACCESS

EDITED BY
Fuminori Misaizu,
Tohoku University, Japan

REVIEWED BY
Kiichirou Koyasu,
The University of Tokyo, Japan
Sungyul Lee,
Kyung Hee University, Republic of Korea

*CORRESPONDENCE
Xianglei Kong,
kongxianglei@nankai.edu.cn
Suzana Veličković,
vsuzana@vin.bg.ac.rs

RECEIVED 05 February 2024
ACCEPTED 27 February 2024
PUBLISHED 11 March 2024

CITATION
Xu S, Liu X, Hou Y, Kou M, Xu X, Veljković F, Veličković S and Kong X (2024), Structures and growth pathways of $Au_nCl_{n+3}^-$ (n ≤ 7) cluster anions.
Front. Chem. 12:1382443.
doi: 10.3389/fchem.2024.1382443

Structures and growth pathways of $Au_nCl_{n+3}^-$ (n ≤ 7) cluster anions

Shiyin Xu[1], Xinhe Liu[1], Yameng Hou[1], Min Kou[1], Xinshi Xu[1], Filip Veljković[2], Suzana Veličković[2]* and Xianglei Kong[1,3]*

[1]State Key Laboratory of Elemento-Organic Chemistry, Frontiers Science Center for New Organic Matter, College of Chemistry, Nankai University, Tianjin, China, [2]"VINCA" Institute of Nuclear Sciences—National Institute of the Republic of Serbia, University of Belgrade, Belgrade, Serbia, [3]Tianjin Key Laboratory of Biosensing and Molecular Recognition, College of Chemistry, Nankai University, Tianjin, China

Gold chloride clusters play an important role in catalysis and materials chemistry. Due to the diversity of their species and isomers, there is still a dearth of structural studies at the molecular level. In this work, anions of $Au_nCl_{n+3}^-$ and $Au_nCl_{n+5}^-$ (n = 2–4) clusters were obtained by laser desorption/ionization mass spectrometry (LDI MS), and the most stable isomers of $Au_nCl_{n+3}^-$ were determined after a thorough search and optimization at the TPSSh/aug-cc-pVTZ/ECP60MDF level. The results indicate that all isomers with the lowest energy have a planar zigzag skeleton. In each species, there is one Au(III) atom at the edge connected with four Cl atoms, which sets it from the other Au(I) atoms. Four growth pathways for $Au_nCl_{n+3}^-$ (n = 2–7) clusters are proposed (labelled R1, R2, R3 and R4). They are all associated with an aurophilic contact and are exothermic. The binding energies tend to stabilize at ~ −41 kcal/mol when the size of the cluster increases in all pathways. The pathway R1, which connects all the most stable isomers of the respective clusters, is characterized by cluster growth due to aurophilic interactions at the terminal atom of Au(I) in the zigzag chains. In the pathway of R4 involving Au-Au bonding in its initial structures (n ≤ 3), the distance between intermediate gold atoms grows with cluster size, ultimately resulting in the transfer of the intermediate Au-Au bonding into aurophilic interaction. The size effect on the structure and aurophilic interactions of these clusters will be better understood based on these discoveries, potentially providing new insights into the active but elusive chemical species involved in the corresponding catalytic reactions or nanoparticle synthesis processes.

KEYWORDS

gold chloride clusters, mass spectrometry, aurophilic interaction, growth pathway, structural optimization

1 Introduction

Gold chemistry is one of the most rapidly developing chemical fields. The synthesis and growth mechanisms of gold nanoparticles are important topics that have attracted the attention of researchers in recent decades. The Brust-Schiffrin two-phase method, in which $AuCl_4$ is reduced by sodium borohydride in the presence of an alkanethiol (Brust et al., 1994), is a widely used approach for the synthesis of small gold nanoparticles. Originally, it was assumed that the Au(I) thiolate polymers were formed as intermediates prior to the final reduction of the gold thiolate nanoparticles (Templeton et al., 2000; Murray, 2008; Sardar et al., 2009). However, Goulet and Lennox found that changing the ratio of thiol ligand to Au(III) salt from 4:1 to 2:1 did not lead to the formation of Au(I) thiolate

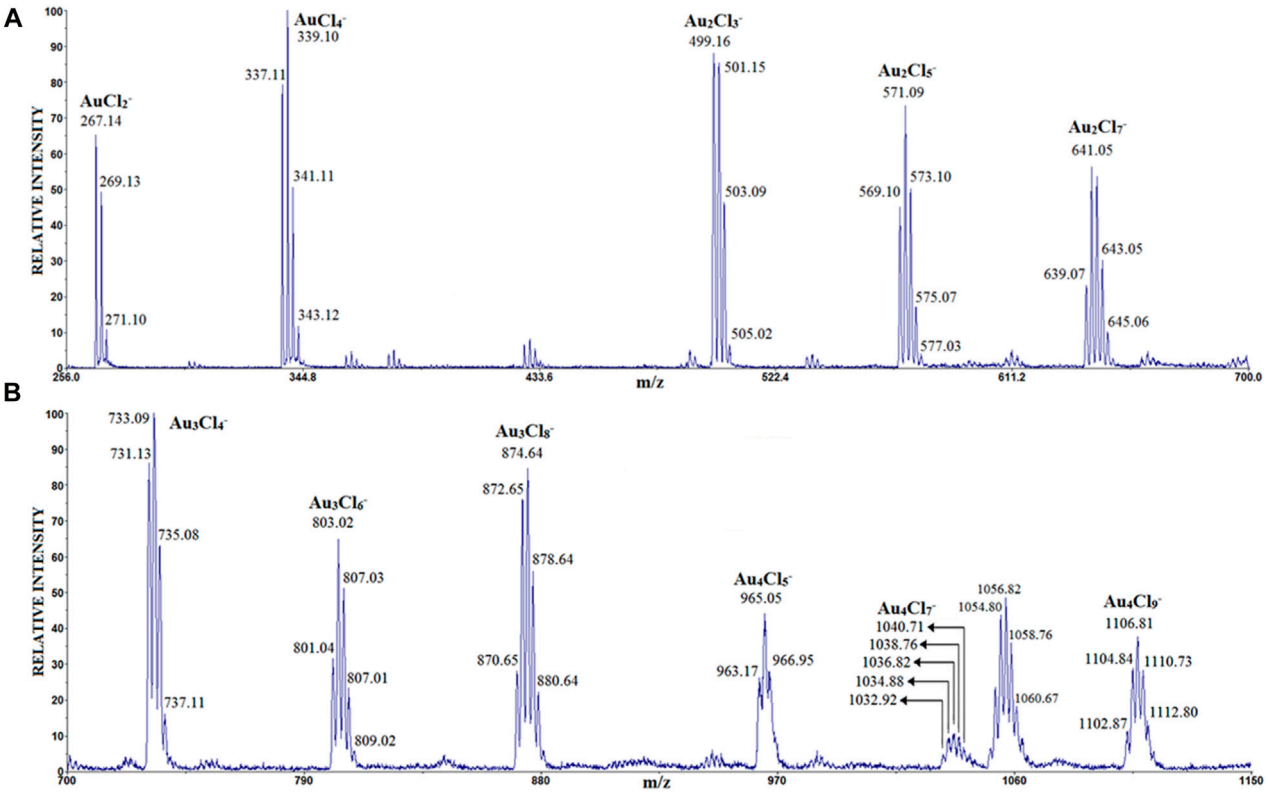

FIGURE 1
The LDI mass spectrum of $AuCl_4H$ obtained in the negative ion mode: **(A)** *m/z* 200–700 and **(B)** *m/z* 700–1,150). The attribution of peaks observed at ~ m/z 1,056 that are differently spaced from the series of Au halide clusters (shown in b) needs further identification.

oligomers, but to the reduction of $Au(I)X_2^-$ (X = halide), casting doubt for the first time that Au(I) thiolate oligomers are reaction intermediates (Goulet and Lennox, 2010). Research by Li *et al.* supports this view and suggests that metal nucleation centers form before metal-sulfur bonds are formed (Li et al., 2011). Barngrover *et al.* have shown that $Au(I)X_2^-$ (X = halide) is an important precursor for the synthesis of larger size gold nanoclusters (Barngrover et al., 2015).

Thanks to the above-mentioned works, gold halides and their corresponding clusters have become the subject of research in recent years (Davies et al., 2016; Cao et al., 2019; Zhang et al., 2020). For example, it is realized that the acetylene hydrochlorination over an Au/C catalyst involves the formation of Au-Cl related complexes (Davies et al., 2016), and so do the Au-catalyzed intramolecular hydroarylation reactions (Zhang et al., 2020). It should be noted that the properties of gold are influenced by relativistic effects (Theilacker et al., 2015; Jerabek et al., 2017), which is why the d^{10} electrons of the inner shell must also be taken into account when forming compounds and clusters. One of the most striking phenomena in this context is the aurophilic interaction. The short Au···Au distance observed in crystals is attributed to the weak interaction defined as "aurophilicity" or "aurophilic interaction" (Schmidbaur et al., 1988a; Schmidbaur et al., 1988b; Scherbaum et al., 1988). Aurophilic interactions bring the metal atoms closer together and contribute significantly to the stability of the corresponding clusters. Typically, the aurophilic interaction appears to act between closed-shell gold atoms and the Au^{+1} oxidation state. It is also characterized by the linear coordination of n = 2 of the gold atoms. To date, there are numerous studies that attempt to illustrate how aurophilicity can influence the structures of gold halide clusters. Schwerdtfeger *et al.* found that all coin metal(I) halide tetramers should have a square ring structure with a butterfly D_{2d} symmetry. However, gold(I) phosphane chloride and bromide tetramers have structures with planar gold cores due to gold-gold interactions (Schwerdtfeger et al., 2004). Rabilloud reported the lowest energy isomers of Au_nBr_n and Au_nI_n (n = 2–6). The cyclic isomers of tetramers and pentamers are non-planar to strengthen both the interactions between gold and halide atoms and those between neaby gold atoms (Rabilloud, 2012). Ma *et al.* have shown that all $Au_nCl_{n+1}^-$ ($2 \le n \le 7$) ions are characterized by a zigzag structure, suggesting that the aurophilic interaction plays a key role in such clusters (Ma et al., 2019b). Ma *et al.* also showed that $Au_{2n}Cl$ (n = 1–4) and Au_nCl_{n+1} ($2 \le n \le 7$) clusters can be experimentally obtained by matrix assisted laser desorption ionization mass spectrometry of $AuCl_4H$ (Ma et al., 2019a). Lemke investigated the formation of $[AuCl_{2-x}OH_x]^+(H_2O)_n$ (x = 0.1), $[AuCl_2]^+(HCl)_2(H_2O)_n$ and $[Au_2Cl_{5-x}OH_x]^+(H_2O)_n$ (x = 0.1) using electrospray ionization mass spectrometry and theoretical calculations. His calculations show that the microsolvation-induced localization of electrons enhances the Au···Au interaction in the singly bridged clusters (Lemke, 2014).

Because thiolate-for-chloride ligand exchange can happen at low barrier heights (Barngrover and Aikens, 2012), it is easy for the

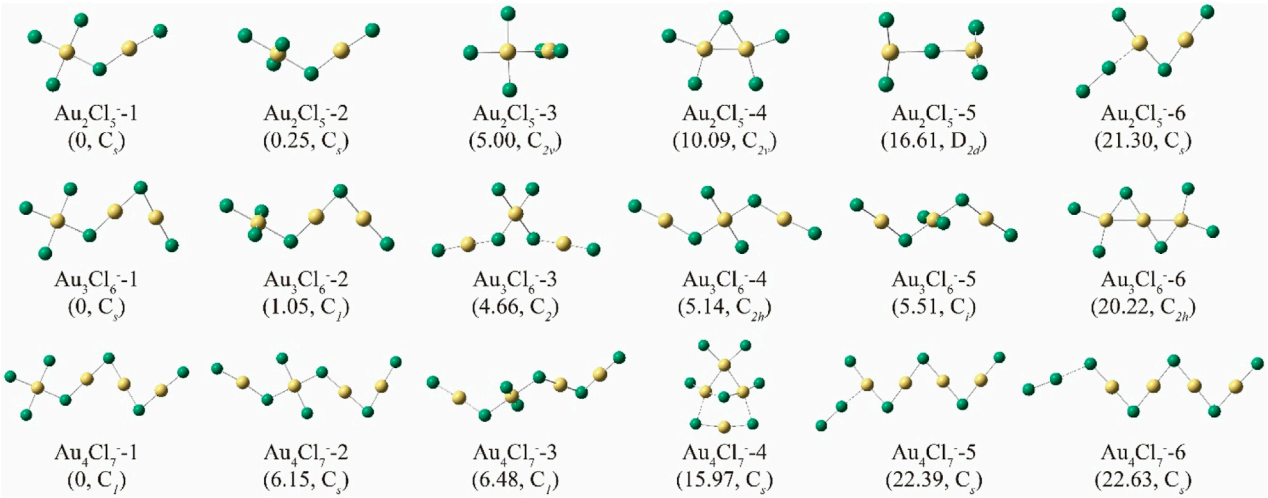

FIGURE 2
Structures of the top 6 isomers of $Au_nCl_{n+3}^-$ (n = 2–4). Their relative energies (ΔE, in kcal mol^{-1}) and symmetry are shown in parentheses.

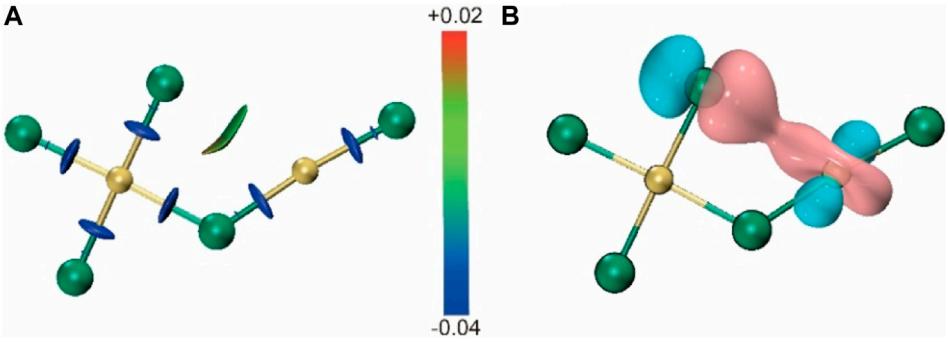

FIGURE 3
(A) IRI calculated for $Au_2Cl_5^-$-1 cluster ions. **(B)** AdNDP calculated for $Au_2Cl_5^-$-1 cluster ions.

precursors of gold-chloride clusters or nanoparticles to form gold-chloride-thiolate or gold-thiolate clusters or nanoparticles by exchanging ligands. Therefore, understanding the structures of various series of gold chloride clusters, their growth pathways, and related kinetics is crucial for the growth of relevant gold nanoparticles. Despite the aforementioned studies on gold chloride clusters (Schwerdtfeger et al., 2004; Srivastava and Misra, 2014; Ma et al., 2019a; Ma et al., 2019b), there is still a gap in the study of polychlorinated gold cluster anions (for example, $Au_nCl_{n+3}^-$) and their growth pathways. In this paper, we attempt to reveal the stability, structural regularity and cluster growth patterns of $Au_nCl_{n+3}^-$ clusters by experimental methods and theoretical calculations. The most stable structures of the clusters and the relative binding properties within them as well as the trends of binding energy changes along the different growth paths are calculated and analyzed. The results are helpful in predicting relevant clusters with larger sizes and may also provide clues for the synthesis of one- or two-dimensional nanostructures from the unit of gold chloride.

2 Experimental

The experiments in this work were performed with a matrix-assisted laser desorption/ionization mass spectrometer, MALDI MS, (Voyager-DE PRO Sciex, Foster City, CA, United States) equipped with a time-of-flight (TOF) mass analyzer. This mass spectrometer contains an ultraviolet nitrogen laser (wavelength 337 nm, pulse width 3 ns and repetition rates of 20.00 Hz). The other instrumental parameters were: accelerating voltage 20,000 V, grid voltage 94%, laser intensity of 1,300 a. u., and number of laser shots 300 and delayed extraction time of 100 ns.

To avoid interference of matrix on cluster ions or potential unexpected reactions, the mass spectra were obtained using the laser desorption/ionization (LDI) method without the use of conventional or other matrices. The sample was aqueous $AuCl_4H$ solutions (2.5 g/dm^3) (99.99%, CAS no.: 12453-07-1) prepared in deionized water (Millipore) immediately prior to the experiment. Subsequently, 0.5 μL of the $AuCl_4H$ solution was applied to the stainless target spot, the target spot left to dry at

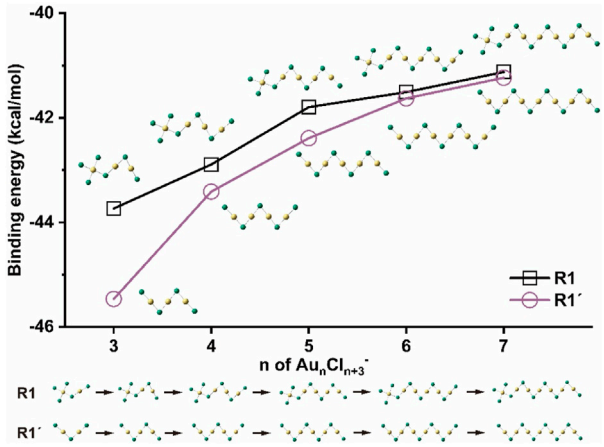

FIGURE 4
Binding energies of $Au_nCl_{n+3}^-$ (n = 3–7) on the pathway of R1 and those of $Au_nCl_{n+1}^-$ (n = 3–7) on the pathway of R1′.

room temperature and placed in the source area of the mass spectrometer.

2.1 Computation

NKCS program (Zhou et al., 2021) has been applied here to search for global minimum structures of $Au_nCl_{n+3}^-$ (n = 2, 3, 4) clusters, and some other structures on the suggested growth pathways are constructed manually based on their structural similarity. All structures have been optimized by the Gaussian 09 program at the level of TPSSh with the Stuttgart energy-consistent relativistic pseudopotentials ECP60MDF and the corresponding valence basis set of MDF60 for Au and aug-cc-pVTZ for Cl. All structures are further checked by frequency calculations to make sure they are true energy minima in their potential energy surfaces (PESs). Besides, IRI (Interaction Region Indicator) (Lu and Chen, 2021), ELF (Electron Localization Function) (Lu and Chen, 2011) and AdNDP (Adaptive natural density partitioning) (Zubarev and Boldyrev, 2008) analysis have been carried out to investigate their bonding properties using Multiwfn program (Lu and Chen, 2012).

3 Results and discussion

The results of our previous studies have shown that the method of LDI mass spectrometry is suitable for the investigation of gold chloride clusters. For example, a series of Au_nCl_{n+1}, Au_nCl_{n-1} and Au_nCl_nH type cluster anions were obtained by laser ablation of $AuCl_4H$ (20 mg/mL) in the presence of graphene as a matrix. By reducing the $AuCl_4H$ concentration tenfold (2 mg/mL), the anions $Au_{2n}Cl^-$ and Au_{2n+1} (n = 1–4) could also be detected. A Nd:YAG laser (355 nm) was used for these experiments. The amount of sample applied to the target was 1 mL.

In contrast to the above conditions, here the amount of sample applied to the target was twice as small, desorption and ionization of the sample was performed with an N_2 laser, mass spectra were obtained without using a matrix, while the concentration of $AuCl_4H$ was 2.5 mg/mL, similar to the previous experiments. Under these conditions, the anion clusters $Au_nCl_{n+1}^-$, (n = 1–4), $Au_nCl_{n+3}^-$ and $Au_nCl_{n+5}^-$ (n = 2, 3, 4) were identified in the LDI mass spectrum in negative mode, as shown in Figures 1A,B (for the sake of clarity, the mass spectrum is divided into two parts: a) *m/z* 200–700 and b) *m/z* 700–1,150).

The peak with the highest intensity corresponds to the anion $AuCl_4^-$, which was not identified in previous work. The cluster anions of the type $Au_nCl_{n+1}^-$ (discovered earlier), $Au_nCl_{n+3}^-$ and $Au_nCl_{n+5}^-$ show a significant intensity for n = 1–4. The anion $Au_4Cl_7^-$ has the lowest intensity.

To determine the most stable structures of $Au_nCl_{n+3}^-$ (n = 2–4) cluster anions, extensive structures were generated, optimized and compared based on the cluster search program of NKCS (Zhou et al., 2021). Considering that the most stable structures of $Au_nCl_{n+1}^-$ are typically characterized by zigzag structures (Ma et al., 2019b), some similar structures were also generated by manually adding two Cl atoms. The top 6 isomers with the lowest energies of $Au_nCl_{n+3}^-$ (n = 2–4) are shown in Figure 2. For simplicity, we can divide the Au_2Cl_5 structures into two categories, those with Au-Au bonds and those without. The Au-Au bonds mentioned here refer to those with typical covalent bonding properties, with bond lengths of less than 2.72 Å (Cordero et al., 2008). And the aurophilic interactions, which typically have a distance between 2.72 and 3.32 Å, are not considered to be the Au-Au bonds discussed here (Sculfort and Braunstein, 2011).

For $Au_2Cl_5^-$, it can be stated that the first two isomers, Au_2Cl_5-1 and −2, are characterized by their zigzag skeleton, which is similar to the previously reported structure of $Au_2Cl_3^-$ (Ma et al., 2019b). The two isomers, which have only Au-Cl connections, are very close in energy. Both can be considered as structures formed by the fusion of structural units of $AuCl_4^-$ and $AuCl_2^-$ by eliminating a Cl atom from two different angles. The difference in their dihedral angles leads to an energy gap of 0.25 kcal/mol. Further analysis based on the interaction region indicator (IRI) and adaptive natural density partitioning (AdNAP) (Zubarev and Boldyrev, 2008; Lu and Chen, 2021) shows that the energy difference is due to the in-plane interaction between the separated chlorine and gold atoms on both sides caused by the coordination between the d orbitals of the gold atoms and the p orbitals of the chlorine atoms (Figure 3). In both structures, the distance between the two gold atoms is greater than 3.32 Å, indicating the absence of the aurophilic interaction. The third stable isomer, Au_2Cl_5-3, is characterized by an Au-Au bond with a length of 2.72 Å and has a relative energy 5.00 kcal/mol higher than Au_2Cl_5-1. The planar structure of Au_2Cl_5-4 has an Au-Au bond with a length of 2.72 Å and a C_{2v} symmetry, but is 10.09 kcal/mol less stable than the top isomer. The isomer Au_2Cl_5-6 also has a zigzag skeleton and can be regarded as a structure formed by attaching a chlorine molecule to the gold atom in the most stable isomer of $Au_2Cl_3^-$.

For the anion $Au_3Cl_6^-$, the first two isomers are characterized by similar skeletons to $Au_2Cl_5^-$ −1 and −2, but the energy difference due to the weak coordination in the plane between the gold and chlorine atoms has increased to 1.05 kcal/mol, much greater than that between $Au_2Cl_5^-$ −1 and −2. The isomers of $Au_3Cl_6^-$ −3, −4 and −5 also have similar structures, which can be

TABLE 1 Structural parameters (with the method of TPSSh and the basis sets of ECP60MDF for Au and aug-cc-pVTZ for Cl) of the isomers of $Au_nCl_{n+1}^-$ and $Au_nCl_{n+3}^-$ (n = 2–7) on the pathways of R1′ and R1 (ref to Supplementary Figure S4), respectively; Bond Lengths are in A and angles are in degrees.

Clusters	<Au^a Cl Au^b	<Au^b Cl Au^b	Au^a–Au^b	Au^b–Au^b
$Au_2Cl_3^-$		95.94		3.46
$Au_3Cl_4^-$		79.02		2.97
$Au_4Cl_5^-$		79.43		2.96
$Au_5Cl_6^-$		78.11		2.94
$Au_6Cl_7^-$		77.91		2.94
$Au_7Cl_8^-$				2.93
$Au_2Cl_5^-$	117.14		3.99	
$Au_3Cl_6^-$	112.95	77.29	3.91	2.92
$Au_4Cl_7^-$	111.38	76.95	3.87	2.91
$Au_5Cl_8^-$	109.83	77.43	3.84	2.92
$Au_6Cl_9^-$	109.74	77.32	3.84	2.92
$Au_7Cl_{10}^-$	109.21	77.47	3.82	2.92

a Representing Au(III),b representing Au(I).

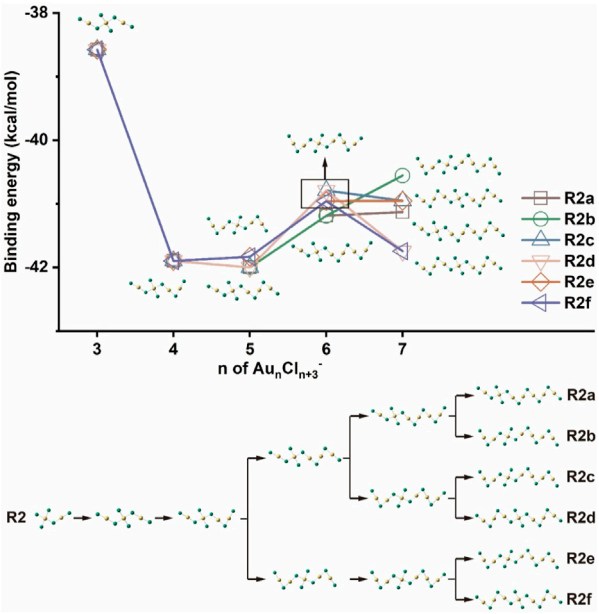

FIGURE 5
Binding energies of $Au_nCl_{n+3}^-$ (n = 3–7) according to the growth route of R2.

treated as if they were formed by inserting the $AuCl_4$ unit into the chain of $Au_2Cl_3^-$. Therefore, the three isomers have similar energies. The isomer $Au_2Cl_5^-$-6, which has a relative energy of 20.22 kcal/mol, is characterized by its planar structure with a C_{2h} symmetry and the two consecutive Au-Au bonds.

Similar results are found in the structures of $Au_4Cl_7^-$. As shown in Figure 2, the most stable isomer of $Au_4Cl_7^-$ can be regarded as a natural extension of the structures of $Au_2Cl_5^-$-1 and $Au_3Cl_6^-$-1. The isomers with an $AuCl_4$ unit ($Au_4Cl_7^-$-2) inserted in the centre of the zigzag skeleton can increase the energy by 6.15 and 6.48 kcal/mol, respectively (this corresponding to the isomers of $Au_4Cl_7^-$ −3 and −4). Some isomers with Au-Au bonds are also observed with a relative energy of almost 16 kcal/mol. And the isomers of $Au_4Cl_7^-$ −5 and −6 can be considered as products formed by attaching the Cl_2 molecule to the frameworks of $Au_4Cl_5^-$ at different positions.

The similarity and inheritance of the structures shown in Figure 2 also provide information about their probable growth processes. Roughly, these structures can be divided into two types: one is based on the zigzag skeleton of $Au_nCl_{n+1}^-$ clusters with two Cl atoms added at appropriate positions, and the other is the type with more complex topological connections that are not significantly related to the zigzag skeleton. Among them, the first category accounts for the majority. Considering the continuity of these structures, four different pathways have been proposed and investigated here. The structures of the most stable isomers of $Au_nCl_{n+3}^-$ (n = 2–4) are all characterized by a zigzag skeletons starting with the $AuCl_4^-$ unit. To better understand the corresponding growth process, cluster ions with similar structures but larger sizes ($Au_nCl_{n+3}^-$, n = 5–7) were also optimized, and their structures are shown in the proposed growth path R1 in Figure 4. This path R1 is very similar to the previously proposed path R1′ for $Au_nCl_{n+1}^-$ clusters (Ma et al., 2019b). The binding energy of each step in R1 is calculated based on:

$$Au_{n-1}Cl_{n+2}^- + AuCl \rightarrow Au_nCl_{n+3}^- \ (n = 3\text{-}7, \textit{with the structures shown in R1 in Fig. 4}) \quad (1)$$

For comparison, the binding energy of each step for clusters of $Au_nCl_{n+1}^-$ (n = 3–7) in R1′ is also calculated at the same level:

$$Au_{n-1}Cl_n^- + AuCl \rightarrow Au_nCl_{n+1}^- \ (n = 3\text{-}7, \textit{with the structures shown in R1′ in Fig. 4}) \quad (2)$$

Figure 4 shows the binding energies of the two types of clusters as functions of the cluster sizes in the paths of R1 and

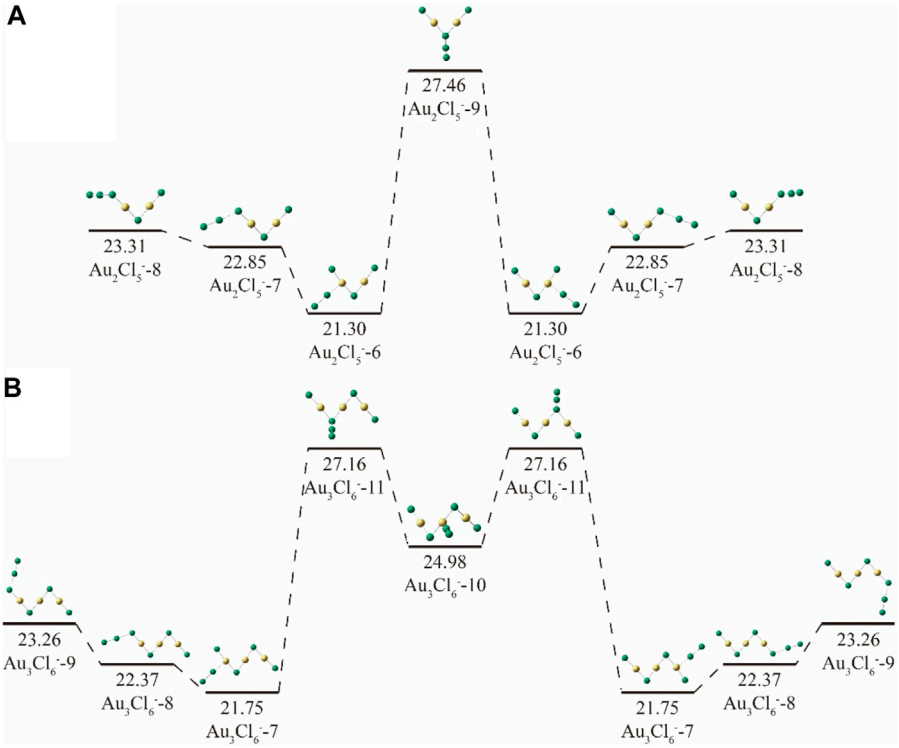

FIGURE 6
The relative energies of **(A)** $Au_2Cl_5^-$-n (n = 6–9) and **(B)** $Au_nCl_{n+3}^-$ (n = 7–11) cluster ions.

R1'. The result shows that the growth process in R1 is exergonic, with ΔE between −41 and −44 kcal/mol, indicating that the pathway of R1 is thermodynamically favorable. As the size of the cluster increases and the zigzag skeleton chain becomes longer, the energy released decreases, which is very similar to the R1′-pathway in the case of $Au_nCl_{n+1}^-$. For clusters with a size of n > 6, the binding energies of both pathways are very close to each other and gradually converge to a stable value of about −41 kcal/mol.

Table 1 compares the most important geometric parameters of the structures in both paths. The Au-Au distance in $Au_2Cl_5^-$ is 3.99 Å, which is significantly longer than that in $Au_2Cl_3^-$ (3.46 Å). The electron localization function (ELF) profiles for both structures show no electron pair density between two Au atoms, indicating that there is no aurophilic interaction in either case. As the size of the cluster of $Au_nCl_{n+3}^-$ increases, the left-side terminal Au-Au distance, which represents the length between trivalent and monovalent gold atoms, gradually shortens to 3.82 Å. This distance is much longer than the terminal Au-Au distance in the case of $Au_nCl_{n+1}^-$ (2.97–2.93 Å) and also the sum of the van der Waals radii of two gold atoms (3.32 Å). However, all Au–Au distances between monovalent gold atoms in the clusters of $Au_nCl_{n+3}^-$ (n = 3–7) are 2.92 Å, which is slightly shorter than the distances in $Au_nCl_{n+1}^-$. These distances show the significant aurophilic interactions in the clusters, which are also confirmed by the ELF calculation results (Supplementary Figure S3). The results show that the structural difference between the clusters of $Au_nCl_{n+3}^-$ and $Au_nCl_{n+1}^-$ is mainly in the terminal trivalent gold unit. The structural features in the following zigzag skeletons, together with the binding energies, converge more and more to a fixed value with increasing size.

As already mentioned, Figure 2 shows another class of isomers that differ from those in R1 by a change in the position of the trivalent gold atom. Instead of the terminal position, the trivalent gold atom can also be located anywhere within the zigzag chain, leading to various isomers with total energies 5–7 kcal/mol higher than the corresponding isomers with the lowest energies. The pathways for the formation of such isomers are discussed and shown in Figure 5 as route 2 (R2). In pathway R1, the trivalent gold atoms are fixed at one end of the chain, and the clusters extend only along the side of the monovalent gold, while in the first step of R2, the chain extends on the other side of the Au(III) unit and forms a sandwich-like Au(III) inside. The chain can then be further extended on both sides of the Au(I) unit to form different or identical structures along different paths. As can be seen in Figure 5, the growth path away from the Au(III) unit releases more energy (R2a), which is thermodynamically advantageous. The result is consistent with that reported in R1, i.e., the Au(I) units tend to bond with each other to strengthen the aurophilic interactions so that they stay away from the Au(III) unit. Therefore, the binding energy in the most favorable pathway in R2 (R2a) also tends to stabilize at −41 kcal/mol as the cluster size increases, which is similar to that in the R1 pathway. As shown in Supplementary Table S1, aurophilic interactions can be clearly found when the distance between the nearby Au atoms is taken into account. Here, no aurophilic interaction can be found between the Au(III) and Au(I) atoms, but the distances between the nearby Au(I) atoms in

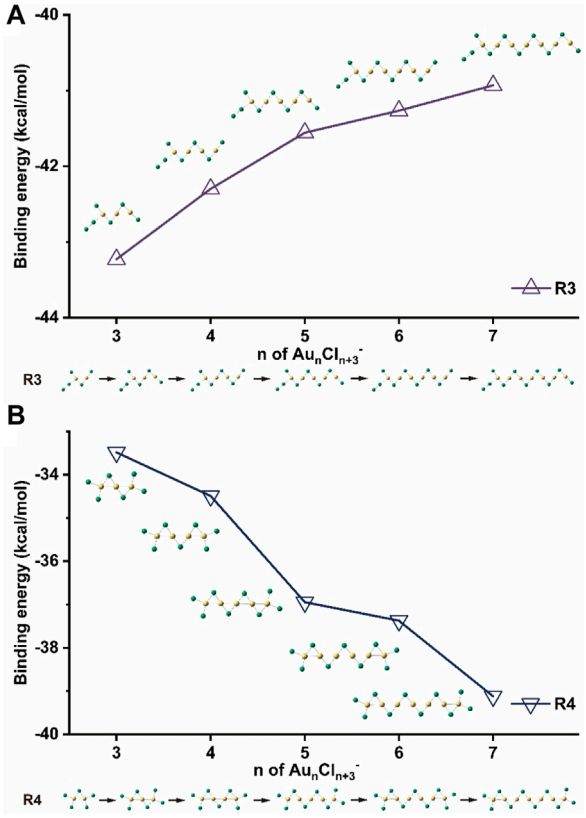

FIGURE 7
Binding energies of $Au_nCl_{n+3}^-$ (n = 3–7) according to growth routes of **(A)** R3, and **(B)** R4.

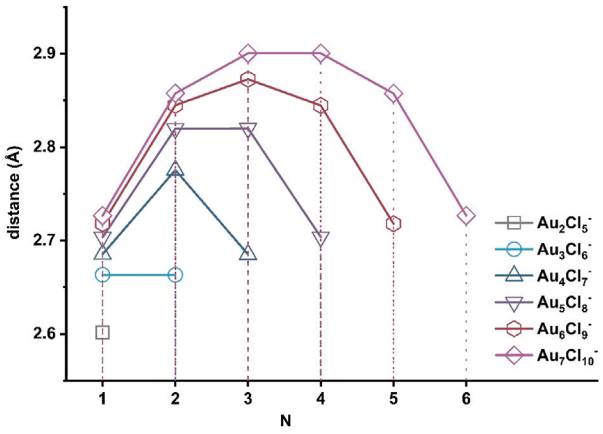

FIGURE 8
Adjacent Au-Au(N) lengths (in A) in $Au_nCl_{n+3}^-$ (n = 2–7) isomers, which are shown in the pathway of R4 (Figure 7). The N in the abscissa indicates the *N*th Au-Au distance counted from left terminals to right terminals.

the isomers shown in R2 are typically 2.87–2.90 Å, even shorter than those of the most stable isomers reported in R1.

All isomers in R1 and R2 contain an Au(III) unit. However, it is possible that the cluster can also form by appending a Cl_2 unit to the previously reported zigzag skeleton of $Au_nCl_{n+1}^-$, as shown by the isomers of $Au_2Cl_5^-$-6, $Au_3Cl_6^-$-7 and $Au_4Cl_7^-$-5 shown in Figure 2 and Supplementary Figure S2. These isomers are interesting due to their structural diversity and possible isomerization pathways, even though their relative energies are higher than those of the most stable isomers by more than 20 kcal/mol. They can be treated as complexes formed by the anchoring of a Cl_2 unit to the skeleton of $Au_nCl_{n+1}^-$. It has been shown that each atom of the zigzag skeleton can act as an anchor. Even with the same anchoring position, different isomers can be formed due to the different anchoring angles. Figure 6A shows these four isomers of $Au_2Cl_5^-$. Among these isomers, the one in which the Cl_2 unit is anchored to the Au(I) atom ($Au_2Cl_5^-$-6) has the lowest energy, while the isomer in which the Cl_2 unit is anchored to the middle Cl atom has a higher relative energy by 6.16 kcal/mol. Among the isomers anchored at the edge of the Cl atom, two isomers are both stable due to their anchoring directions, with energies of 2.01 and 1.55 kcal/mol higher than the isomer of $Au_2Cl_5^-$-6. Although the isomerization barriers between these isomers have not yet been calculated, it is believed that it is possible to move the Cl_2 unit along the zigzag edge of the skeleton of $Au_nCl_{n+1}^-$ by manipulating the Cl_2 unit by appropriate experimental methods. In addition to these isomers shown here, there are other isomers in which the two Cl atoms (instead of the Cl_2 unit) are anchored to the edge of the skeleton from both sides ($Au_2Cl_5^-$-10 and $Au_2Cl_5^-$-11, see Supplementary Figure S1) or from both Cl atoms ($Au_2Cl_5^-$-12, see Supplementary Figure S1), although their energies are much higher. For $Au_3Cl_6^-$, more anchor positions were found for the Cl_2 unit (Figure 6B). Similar to $Au_2Cl_5^-$, the isomer anchored with the edge Au atom is the most stable isomer of this type, and the isomer anchored with the edge Cl atom is the second most stable. Other isomers anchored with middle Cl atoms or Au atoms in the zigzag skeleton are less stable than the most stable isomer by 5.41 and 2.18 kcal/mol, respectively.

Starting from the most stable structure, in which the Cl_2 unit is anchored to the Au atom at the edge, a different pathway for the growth of isomers of this type is proposed and shown in Figure 7 as route 3 (R3). The binding energies and the main geometrical parameters of the structures in R3 are shown and listed in Figure 7 and Supplementary Table S2, respectively. Similar to the paths R1' for $Au_nCl_{n+1}^-$ and R1 for $Au_nCl_{n+3}^-$, the absolute values of the binding energy decrease from 43 kcal/mol to 41 kcal/mol with increasing size of the cluster. Obviously, the aurophilic interaction is filled with the zigzag chains, with a typical Au-Au distance of 2.94 Å and Au-Cl-Au angle of 78°, both of which are close to those in the clusters of $Au_nCl_{n+1}^-$.

The isomers of $Au_2Cl_5^-$-4 and $Au_3Cl_6^-$-5 with symmetric planar structure are different from the zigzag structures. Although their relative energies are higher, the Au-Au bonds present inside the clusters suggest that they may have a completely different growth path. Therefore, the corresponding isomers with n = two to seven and the path of R4 were calculated and shown in Figure 7. The heat released during these exothermic processes increases with the size of the cluster. Figure 8 shows the distances between nearby gold atoms in these structures, where the N stands for the *N*th gold atom in the corresponding structures counted from the left. As can be seen in the figure, the Au-Au distances in the four clusters increase with n ≥ 4 along the molecular chains, reaching maximum values and then decreasing to values close to the initial values. The Au-Au distances

in clusters with n ≤ 3 are always smaller than 2.72 Å, highlighting the dominant role of Au-Au bonding, while the distances in the middle parts of clusters with larger sizes (n = 6, 7) are between 2.72 Å and 3.32 Å, indicating the existence of an aurophilic interaction (Supplementary Table S3). The structural transition from Au-Au bonding to aurophilic interaction occurs for the cluster with n = 4. It can be naturally assumed that aurophilic interactions along the chains are a feature of isomers with larger sizes in the R4 pathway, although the Au-Au bonds may still exist at the two ends.

It should be mentioned that the cluster of $Au_nCl_{n+5}^-$ (n = 2, 3, 4) were also identified in the LDI mass spectrum (Figure 1). The preliminary theoretical calculations for these culsters show that their structures may retain the similar configuration. Due to the diversity and complexity of their structures, further research is still underway on their most stable structures and growth pathways. We hope these results can help to understand the structure, interactions, and properties of such cluster ions more systematically.

4 Conclusion

In summary, cluster anions of $Au_nCl_{n+3}^-$ (n = 2–4) were obtained by LDI mass spectrometry. Their most stable isomers were studied in detail and finally optimized at the TPSSh/aug-cc-pVTZ/ECP60MDF level. The results show that the isomers with the lowest energy for the clusters $Au_nCl_{n+3}^-$ (n = 2–4) have similar structures, all characterized by a zigzag skeleton. Compared to the most stable structures of $Au_nCl_{n+1}^-$ reported previously, the two Cl atoms have been added to the edge gold atom to give it an oxidation state of +3, canceling the original aurophilic interaction with the edge gold atom (if present). Furthermore, the gold-chlorine coordination results in the most stable isomers having a planar structure. Based on these results, four growth pathways for $Au_nCl_{n+3}^-$ (n = 2–7) clusters are proposed. These pathways are exothermic processes, and the Au(I)···Au(I) interactions are present in all of them. For the pathway R1, which connects all the most stable isomers of the corresponding clusters, it is found that the growth of the clusters tends to occur at the end of the Au(I) due to the aurophilic interactions between Au(I) and Au(I), and the Au(III) preferentially remains at the other end of the zigzag chain. For the pathways of R1, R2 and R3, the binding energies tend to stabilize at −41 kcal/mol as the size of the cluster increases.

The pathway of the R4 is different. In this pathway, which contains an Au-Au bond in its initial structures (n ≤ 3), the released heat increases and the distance between the intermediate gold atoms increases with increasing cluster size, which eventually leads to the transformation of the intermediate Au-Au bond into an aurophilic interaction.

All these pathways lead to structures with similar one-dimensional zigzag chains stabilized by aurophilic interactions with similar energies. These results not only help us to better understand the size effect on the structure and aurophilic interactions of these clusters, but may also reflect some new information about the active but elusive species in related catalytic reactions or nanoparticle synthesis processes.

Data availability statement

The datasets presented in this study can be found in online repositories. The names of the repository/repositories and accession number(s) can be found in the article/Supplementary Material.

Author contributions

SX: Data curation, Formal Analysis, Writing–original draft. XL: Data curation, Investigation, Writing–original draft. YH: Investigation, Visualization, Writing–original draft. MK: Data curation, Investigation, Writing–original draft. XX: Methodology, Writing–original draft. FV: Investigation, Methodology, Writing–review and editing. SV: Conceptualization, Formal Analysis, Investigation, Methodology, Project administration, Supervision, Writing–review and editing. XK: Conceptualization, Data curation, Formal Analysis, Funding acquisition, Investigation, Methodology, Supervision, Writing–review and editing.

Funding

The author(s) declare that financial support was received for the research, authorship, and/or publication of this article. The authors gratefully acknowledge financial support from the National Natural Science Foundation of China (Grant Nos. 22174076 and 21627801), and the Ministry of Education, Science and Technological Development of the Republic of Serbia (grant No 451-03-66/2024-03/200017).

Conflict of interest

The authors declare that the research was conducted in the absence of any commercial or financial relationships that could be construed as a potential conflict of interest.

The author(s) declared that they were an editorial board member of Frontiers, at the time of submission. This had no impact on the peer review process and the final decision.

Publisher's note

Supplementary material

The Supplementary Material for this article can be found online at: https://www.frontiersin.org/articles/10.3389/fchem.2024.1382443/full#supplementary-material

References

Barngrover, B. M., and Aikens, C. M. (2012). The golden pathway to thiolate-stabilized nanoparticles: following the formation of gold(I) thiolate from gold(III) chloride. *J. Am. Chem. Soc.* 134, 12590–12595. doi:10.1021/ja303050s

Barngrover, B. M., Manges, T. J., and Aikens, C. M. (2015). Prediction of nonradical Au(0)-containing precursors in nanoparticle growth processes. *J. Phys. Chem. A* 119, 889–895. doi:10.1021/jp509676a

Brust, M., Walker, M., Bethell, D., Schiffrin, D. J., and Whyman, R. (1994). Synthesis of thiol-derivatised gold nanoparticles in a two-phase Liquid-Liquid system. *J. Chem. Soc. Chem. Commun.* 7, 801–802. doi:10.1039/c39940000801

Cao, S., Yang, M., Elnabawy, A. O., Trimpalis, A., Li, S., Wang, C., et al. (2019). Single-atom gold oxo-clusters prepared in alkaline solutions catalyse the heterogeneous methanol self-coupling reactions. *Nat. Chem.* 11, 1098–1105. doi:10.1038/s41557-019-0345-3

Cordero, B., Gómez, V., Platero-Prats, A. E., Revés, M., Echeverría, J., Cremades, E., et al. (2008). Covalent radii revisited. *Dalton Trans.*, 2832–2838. doi:10.1039/b801115j

Davies, C. J., Miedziak, P. J., Brett, G. L., and Hutchings, G. J. (2016). Vinyl chloride monomer production catalysed by gold: a review. *Chin. J. Catal.* 37, 1600–1607. doi:10.1016/s1872-2067(16)62482-8

Goulet, P. J. G., and Lennox, R. B. (2010). New insights into brust-schiffrin metal nanoparticle synthesis. *J. Am. Chem. Soc.* 132, 9582–9584. doi:10.1021/ja104011b

Jerabek, P., von der Esch, B., Schmidbaur, H., and Schwerdtfeger, P. (2017). Influence of relativistic effects on bonding modes in M(II) dinuclear complexes (M = Au, Ag, and Cu). *Inorg. Chem.* 56, 14624–14631. doi:10.1021/acs.inorgchem.7b02434

Lemke, K. H. (2014). Gold chloride clusters with Au(III) and Au(I) probed by FT-ICR mass spectrometry and MP2 theory. *Phys. Chem. Chem. Phys.* 16, 7813. doi:10.1039/c3cp55109a

Li, Y., Zaluzhna, O., Xu, B., Gao, Y., Modest, J. M., and Tong, Y. J. (2011). Mechanistic insights into the brust-schiffrin two-phase synthesis of organo-chalcogenate-protected metal nanoparticles. *J. Am. Chem. Soc.* 133, 2092–2095. doi:10.1021/ja1105078

Lu, T., and Chen, F. (2011). Meaning and functional form of the electron localization function. *Acta Phys. Chim. Sin.* 27, 2786–2792. doi:10.3866/pku.Whxb20112786

Lu, T., and Chen, F. (2012). Multiwfn: a multifunctional wavefunction analyzer. *J. Comput. Chem.* 33, 580–592. doi:10.1002/jcc.22885

Lu, T., and Chen, Q. (2021). Interaction region indicator: a simple real space function clearly revealing both chemical bonds and weak interactions. *Chemistry–Methods* 1, 231–239. doi:10.1002/cmtd.202100007

Ma, Y., Bian, S., Shi, Y., Fan, X., and Kong, X. (2019a). Greatly enhanced electron affinities of $Au_{2n}Cl$ clusters (n = 1–4): effects of chlorine doping. *ACS Omega* 4, 17295–17300. doi:10.1021/acsomega.9b01981

Ma, Y., Bian, S., Shi, Y., Fan, X., and Kong, X. (2019b). Size effect on aurophilic interaction in gold-chloride cluster anions of $Au_nCl_{n+1}^-$ ($2 \le n \le 7$). *ACS Omega* 4, 650–654. doi:10.1021/acsomega.8b02907

Murray, R. W. (2008). Nanoelectrochemistry: metal nanoparticles, nanoelectrodes, and nanopores. *Chem. Rev.* 108, 2688–2720. doi:10.1021/cr068077e

Rabilloud, F. (2012). Structure and bonding in coinage metal halide clusters M_nX_n, M = Cu, Ag, Au; X = Br, I; n = 1–6. *J. Phys. Chem. A* 116, 3474–3480. doi:10.1021/jp300756h

Sardar, R., Funston, A. M., Mulvaney, P., and Murray, R. W. (2009). Gold nanoparticles: past, present, and future. *Langmuir* 25, 13840–13851. doi:10.1021/la9019475

Scherbaum, F., Grohmann, A., Huber, B., Krüger, C., and Schmidbaur, H. (1988). Aurophilicity as a consequence of relativistic effects: the hexakis(triphenylphosphaneaurio)methane dication $[(Ph_3PAu)_6C]^{2\oplus}$. *Angew. Chem. Int. Ed.* 27, 1544–1546. doi:10.1002/anie.198815441

Schmidbaur, H., Graf, W., and Müller, G. (1988a). Weak intramolecular bonding relationships: the conformation-determining attractive interaction between gold(I) centers. *Angew. Chem. Int. Ed.* 27, 417–419. doi:10.1002/anie.198804171

Schmidbaur, H., Scherbaum, F., Huber, B., and Müller, G. (1988b). Polyauriomethane compounds. *Angew. Chem. Int. Ed.* 27, 419–421. doi:10.1002/anie.198804191

Schwerdtfeger, P., Krawczyk, R. P., Hammerl, A., and Brown, R. (2004). A comparison of structure and stability between the group 11 halide tetramers M_4X_4 (M = Cu, Ag, or Au; X = F, Cl, Br, or I) and the group 11 chloride and bromide phosphanes $(XMPH_3)_4$. *Inorg. Chem.* 43, 6707–6716. doi:10.1021/ic0492744

Sculfort, S., and Braunstein, P. (2011). Intramolecular d^{10}-d^{10} interactions in heterometallic clusters of the transition metals. *Chem. Soc. Rev.* 40, 2741–2760. doi:10.1039/c0cs00102c

Srivastava, A. K., and Misra, N. (2014). The highest oxidation state of Au revealed by interactions with successive Cl ligands and superhalogen properties of $AuCl_n$ (n = 1-6) species. *Int. J. Quantum Chem.* 114, 1513–1517. doi:10.1002/qua.24717

Templeton, A. C., Wuelfing, W. P., and Murray, R. W. (2000). Monolayer-protected cluster molecules. *Acc. Chem. Res.* 33, 27–36. doi:10.1021/ar9602664

Theilacker, K., Schlegel, H. B., Kaupp, M., and Schwerdtfeger, P. (2015). Relativistic and solvation effects on the stability of gold(III) halides in aqueous solution. *Inorg. Chem.* 54, 9869–9875. doi:10.1021/acs.inorgchem.5b01632

Zhang, J., Simon, M., Golz, C., and Alcarazo, M. (2020). Gold-catalyzed atroposelective synthesis of 1,1′-Binaphthalene-2,3′-diols. *Angew. Chem. Int. Ed.* 59, 5647–5650. doi:10.1002/anie.201915456

Zhou, M., Xu, Y., Cui, Y., Zhang, X., and Kong, X. (2021). Search for global minimum structures of P_{2n+1}^+ (n = 1–15) using xTB-based basin-hopping algorithm. *Front. Chem.* 9, 694156. doi:10.3389/fchem.2021.694156

Zubarev, D. Y., and Boldyrev, A. I. (2008). Developing paradigms of chemical bonding: adaptive natural density partitioning. *Phys. Chem. Chem. Phys.* 10, 5207. doi:10.1039/b804083d

frontiers | Frontiers in Chemistry

TYPE Review
PUBLISHED 26 June 2024
DOI 10.3389/fchem.2024.1407561

OPEN ACCESS

EDITED BY
Raquel Eugenia Galian,
University of Valencia, Spain

REVIEWED BY
Yadong Zhou,
China Jiliang University, China
Gustavo F. S. Andrade,
Juiz de Fora Federal University, Brazil
Luciana Schmidt,
Universitat Politècnica de València, Spain

*CORRESPONDENCE
Krishanu Ray,
kray@som.umaryland.edu

RECEIVED 27 March 2024
ACCEPTED 17 May 2024
PUBLISHED 26 June 2024

CITATION
Dasgupta S and Ray K (2024), Plasmon-enhanced fluorescence for biophotonics and bio-analytical applications.
Front. Chem. 12:1407561.
doi: 10.3389/fchem.2024.1407561

Plasmon-enhanced fluorescence for biophotonics and bio-analytical applications

Souradip Dasgupta[1] and Krishanu Ray[1,2]*

[1]Division of Vaccine Research, Institute of Human Virology, University of Maryland School of Medicine, Baltimore, MD, United States, [2]Department of Biochemistry and Molecular Biology, University of Maryland School of Medicine, Baltimore, MD, United States

Fluorescence spectroscopy serves as an ultrasensitive sophisticated tool where background noises which serve as a major impediment to the detection of the desired signals can be safely avoided for detections down to the single-molecule levels. One such way of bypassing background noise is plasmon-enhanced fluorescence (PEF), where the interactions of fluorophores at the surface of metals or plasmonic nanoparticles are probed. The underlying condition is a significant spectral overlap between the localized surface plasmon resonance (LSPR) of the nanoparticle and the absorption or emission spectra of the fluorophore. The rationale being the coupling of the excited state of the fluorophore with the localized surface plasmon leads to an augmented emission, owing to local field enhancement. It is manifested in enhanced quantum yields concurrent with a decrease in fluorescence lifetimes, owing to an increase in radiative rate constants. This improvement in detection provided by PEF allows a significant scope of expansion in the domain of weakly emitting fluorophores which otherwise would have remained unperceivable. The concept of coupling of weak emitters with plasmons can bypass the problems of photobleaching, opening up avenues of imaging with significantly higher sensitivity and improved resolution. Furthermore, amplification of the emission signal by the coupling of free electrons of the metal nanoparticles with the electrons of the fluorophore provides ample opportunities for achieving lower detection limits that are involved in biological imaging and molecular sensing. One avenue that has attracted significant attraction in the last few years is the fast, label-free detection of bio-analytes under physiological conditions using plasmonic nanoparticles for point-of-care analysis. This review focusses on the applications of plasmonic nanomaterials in the field of biosensing, imaging with a brief introduction on the different aspects of LSPR and fabrication techniques.

KEYWORDS

plasmon-enhanced fluorescence, biophotonic applications, analytical applications, radiative decay rate, fluorescence

1 Introduction

Light–matter interactions manifested by absorption, emission, and scattering have paved the way for the design and applications of fluorophores in a variety of real-time problems such as organic electronics, biosensors, and photocatalysis (Spitzberg et al., 2019; Rivera and Kaminer, 2020; Peng et al., 2022a; Kumar et al., 2022; Zhang et al., 2023; Zhang et al., 2024). The wavelength of light in the solar spectrum typically ranges in a few hundreds

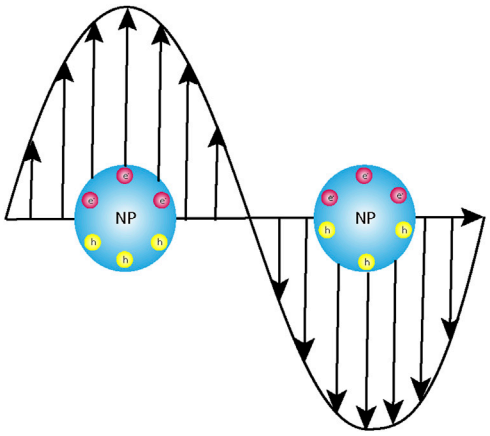

FIGURE 1
Schematic representation of the interaction of the electromagnetic light wave with the instantaneously created dipole post-photoexcitation leading to localized surface plasmon resonance (LSPR).

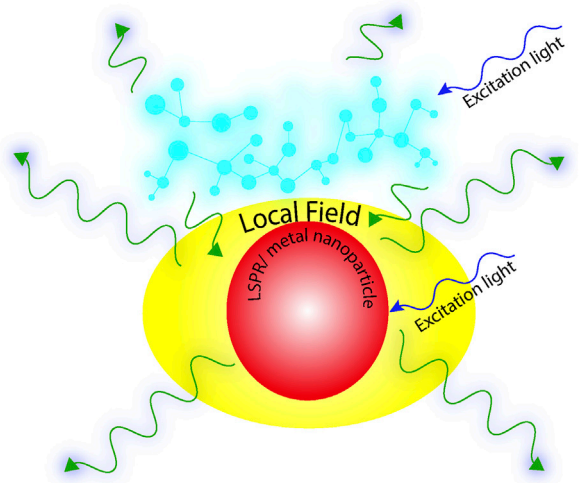

FIGURE 2
Schematic representation of plasmon-enhanced fluorescence (PEF).

of nanometres. However, the size of the fluorogenic molecules or the plasmonic nanoparticles under investigation posed a serious lacuna to the extent of these interactions and, consequently, their applications. With the advent of nanomaterials, these could be subsided to a certain extent. When organic fluorophores are irradiated by monochromatic light, a section of the molecules lying in the ground state gets excited, and the extra energy is finally released as photons; the process is defined as photoluminescence. The augmented spectral intensity observed in metal nanoparticles is attributed to the excitation of the localized surface plasmon resonance (LSPR) that results in the higher-extinction cross sections of the plasmonic nanoparticles (Lukyanchuk et al., 2010). The above discussion necessitates a very brief overview of plasmons and plasmonic nanoparticles. When metal surfaces are irradiated with light, which is known to be an electromagnetic wave, there is an oscillation of the free electrons because of the formation of a dipole. These combined oscillations are defined as plasmons. In the dipole so formed, the electrons migrate to restore its initial configuration, but the electromagnetic waves which still oscillate force the electrons of the material to oscillate at the same frequency as that of the irradiating light (Figure 1). This is when the fundamental condition of resonance is achieved. The prerequisite is that the wavelength of the irradiating light has to be greater than or equal to the frequency of the plasmons. The easiest and most convenient way to modulate the plasmon resonance of a metal nanoparticle is to engineer the shape and size of the particles or shelling it with a non-conducting material like silica of varying thicknesses. Randomly distributed arrays of homogenous or heterogeneous nanostructures with variable sizes ranging up to tens of nanometres are much smaller than the wavelength of the interacting electromagnetic radiation and, thus, provide further scope of modulation in their optical properties (Lakowicz, 2005; Lakowicz et al., 2008; Ray et al., 2009a; Szmacinski et al., 2009; Wurtz et al., 2011; Li et al., 2017; Nicholls et al., 2017; Vestler et al., 2018).

Now, if a fluorophore molecule comes in the vicinity of the plasmonic nanoparticles, then there might arise a condition where resonance is achieved between the frequency of the fluorophore emission and that of the plasmon resonance. Under such circumstances, because of elastic scattering, an enhanced emission at the same frequency as that of the fluorophore could be observed. This phenomenon is defined as plasmon-enhanced fluorescence (Figure 2). Ideally, a significant overlap between the LSPR of the metal nanoparticle and the absorption/emission spectra of the fluorophore is a prerequisite condition to achieve optimal PEF (Lu et al., 2011). With an aim of providing amplified signals for advanced techniques like surface-enhanced Raman scattering (SERS), tip-enhanced fluorescence (TEF), and other single-molecule fluorescence methods, this tool has proved its omnipresence (Hartschuh, 2008; Schmid et al., 2013; Li et al., 2021; Sim et al., 2022; Li et al., 2023). As discussed earlier, the entire phenomenon of plasmon-enhanced fluorescence is based on the fundamental principle of the enhancement of the electromagnetic field, owing to the coupling of the incident light frequency with the frequency of the surface plasmons, and it has a very strong dependence on the shape, size, and interparticle separation distance in the metal nanostructures (Laible et al., 2021; Yang et al., 2023). There are specific domains within the nanostructures where the electric fields are intensely confined within the noble metal (Au, Ag, etc.) nanostructures, and these regions are defined as plasmonic "hotspots." Engineering the interparticle gap proved to be an efficient pathway to modulate the plasmon resonance and, consequently, the electromagnetic fields. It has already been established that with the decrease in interparticle gap size, the localized electromagnetic field shows an exponential increase. Since this interparticle gap and topography play a vital role in LSPR, this gap has sparked significant interest in recent years (Laible et al., 2018; Dai et al., 2020; Laible et al., 2020).

The distance between the fluorophore and the metal nanoparticle plays a vital role in PEF (Ray et al., 2007). Before the advent of PEF, it was widely established that when metal surfaces are in close proximity of excited fluorophores, there is an ample chance that the excited fluorophores lose their excess energy by availing a non-radiative channel, i.e., resonance energy transfer, and

as a consequence, quenching could be observed (Alivisatos et al., 1987; Yeltik et al., 2013; Wang et al., 2020a). In a recent report, this phenomenon of quenching in the presence of metal nanoparticles of Pd was successfully exploited to develop and design the ultrasensitive detection of fluorescently labelled DNA and proteins (Li et al., 2015). In some cases, a fluorophore attached directly to a metal surface may form an entirely separate entity with different photophysics altogether. The surface plasmon-enhanced electromagnetic field hence presents a situation where the PEF may be superseded by surface plasmon-induced quenching, and hence, an optimization is necessary. Thus, an appropriate spacer of specific thickness is needed to balance these two counterintuitive phenomena. In another recent report, polyelectrolyte multilayers were efficiently used as spacers to achieve enhanced fluorescence signals from lanthanide-doped conversion nanoparticles (UCNPs) with AuNRs. The enhancement in emission was demonstrated to be dependent on both the thickness of the dielectric polyelectrolyte multilayer spacers and the size of the AuNRs (Feng et al., 2015). Another contemporary report demonstrated that for randomly oriented fluorophores, maximum enhancement in fluorescence could be observed for substrate side detection with spacers having a low refractive index viz. Teflon, SiO_2, etc. (Akimov and Sun, 2017). The discovery of surface plasmon polaritons in the 1950s provided the necessary impetus that led to the development of SERS in the mid-1970s (Fleischmann et al., 1974). The last couple of decades have witnessed a significant growth in this field, with applications demonstrated in various domains viz. optical and photovoltaic devices, bioanalytics, etc. (Liu et al., 2018; Spitzberg et al., 2019; Peng et al., 2022a; Kumar et al., 2022). This review primarily focusses on the bio-analytical applications of plasmonic nanoparticles in fluorescence in the last 20 years.

2 Basics of plasmon-enhanced fluorescence

When an ensemble of molecules is irradiated with light, a certain fraction of the molecules residing in the ground state absorbs the energy and is promoted to the higher excited states. Excited-state depopulation occurs mainly by two pathways, namely, radiative and non-radiative. The non-radiative pathways, which usually involve internal conversion (IC) and intersystem crossing (ISC), are usually faster and occur in the femtosecond–picosecond time regime. Emission efficiency or fluorescence quantum yield is defined as the ratio of the radiative rate constants and sum of all rate constants (Eq. 2). Physically, it is a measure of the probability of the depopulation of the excited state by fluorescence rather than any other non-radiative pathway (Eq. 1).

$$\phi_f^{sample} = \phi_f^{reference} \cdot \frac{\frac{F_{sample}}{1-10^{-A_{sample}}}}{\frac{F_{reference}}{1-10^{-A_{reference}}}} \cdot \left(\frac{n_{sample}}{n_{reference}}\right)^2 \ldots\ldots \text{eqn}, \quad (1)$$

$$\phi_f = \frac{k_r}{k_r + k_{nr}} \ldots\ldots \text{eqn}, \quad (2)$$

where F_{sample} and $F_{reference}$ are the integrated emission intensity and A_{sample} and $A_{reference}$ are the absorbance at the excitation wavelength of the sample and reference, respectively. ϕ_f^{ref} is the emission quantum yield of the reference. n is the refractive index of the medium used for sample and fluorescence. k_r and k_{nr} are the radiative and non-radiative rate constants, respectively.

Fluorescence lifetime is another intrinsic parameter which is defined as the average time a molecule spends in the excited state. It is mathematically coined as the reciprocal of the sum of all rate constants (Eq. 3):

$$\tau_f = \frac{1}{k_r + k_{nr}} \ldots\ldots \text{eqn}. \quad (3)$$

For dilute solutions, the Lambert–Beer law holds good, i.e., absorbance is a linear function of concentration, i.e., $A = \epsilon cl$ = log P_0-log P, where A is the absorbance or optical density, ϵ is the molar absorption coefficient, c is the concentration of the sample, l is the path length through which the light traverses, and P_0 is the excitation power. Emission intensity, which is defined as $F = QP_0\ (1–10^{-\epsilon cl})$, is directly proportional to the power of the excitation light and the concentration of the sample until an inner-filter effect crops in. The point is that quantum yield and lifetimes are better parameters than intensity since both are independent of the power of excitation light.

When the plasmon nanoparticle–fluorophore conjugate is irradiated with light of a specific wavelength having power P_0, both the metal nanoparticle and the fluorophore absorb the energy, which results in a molecular excited state of the fluorophore and an LSPR in the plasmon nanoparticle, provided the conditions discussed above are met. Now, if the placement of the molecule is beyond the energy transfer distance, then possibilities of excited-state relaxation by non-radiative pathways like Forster resonance energy transfer (FRET) are eliminated. If the electromagnetic local field generated by the LSPR couples with that of the fluorophore, PEF could be observed. This enhancement in near-field intensity (E) leads to a change in the excitation power $<|E|^2.P_0>$ in the region of the local field, which, consequently, results in an increase in the radiative rate constant (k_r) (Aroca, 2006; Koya et al., 2021). Thus, experimentally, the parameter we end up recording is enhanced emission intensity concomitant with a decrease in fluorescence lifetime (τ_f) in the near-field region of the plasmonic nanoparticle. On the contrary, in the far field, scattered frequencies from the plasmons interact with frequencies of the emitters, resulting in an enhanced electromagnetic field.

3 Fabrication of plasmonic nanomaterials

The role of shape, size, and interparticle distances in influencing the plasmonic hotspot and, in turn, the enhanced electromagnetic field has been briefly discussed in the *Introduction* section of this report. In order to achieve tunability and often periodicity in the placement of the metal, atoms play a vital role. Attaining nanometer-scale sensitivity demands state-of-the-art fabrication technologies.

3.1 Top-down approaches

3.1.1 Electron beam lithography

Conventional lithographic techniques have limitations in spatial resolution, which restricts their use in fabricating subwavelength-scale

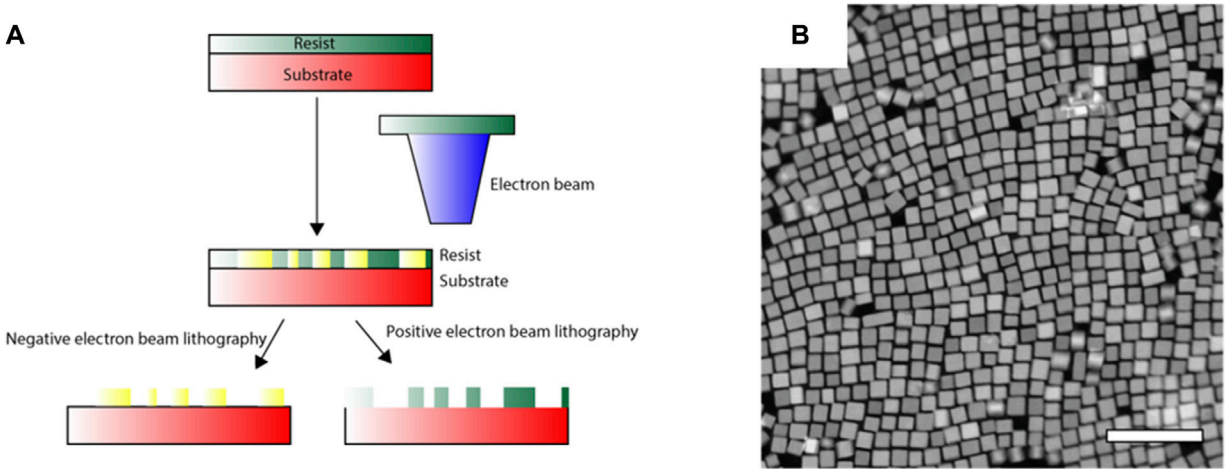

FIGURE 3
(A) Schematic representation of the electron beam lithography (EBL) technique. **(B)** Example depicting structural modifications in FSn:In_2O_3 nanoparticles using EBL (Roccapriore et al., 2022).

features, a necessity for their use in the visible-wavelength domain. The diffraction limit of light used in conventional photolithography is usually in the order of hundreds of nanometres, which in electron beam lithography (EBL), significantly improves to tens of nanometres, allowing the fabrication of detailed structures (Qin et al., 2021; Roccapriore et al., 2022). After covering the surface of the substrate with a resist, the electron beams are allowed to impinge on specific areas of the sample that results in directing writing on the resist layer (Figure 3A). Part of the resist layer is then etched with a developer viz. acetone. A subnanometer metal film is then deposited on the etched structure, followed by lifting-off to obtain the metal plasmonic nanomaterial (Figure 3B).

3.1.2 Focused ion beam lithography

In focused ion beam (FIB) lithography, heavy-mass atoms viz. Ga are usually used to bombard the substrate surface for direct-write patterning. FIB mainly relies on high-energy, short-range secondary electrons instead of both the primary and secondary electrons, which plays a role in EBL. Thus, "resists," which constitute a very important component of EBL, are not required in this case. The ions which are used in this method are massive compared to electrons used in EBL. Hence, the wavelength is smaller, which consequently results in less scattering than in the former. It can be used to directly mill a pattern on a substrate for prototyping of plasmonic nanomaterials (Morimoto et al., 1986). However, in some cases, there is Ga ion contamination that alters the very nature of the plasmonic nanomaterials. Recent technologies using He- and Ne-based FIBs have been proven to be successful in reducing this issue (Boden et al., 2011).

3.1.3 Direct laser writing

Direct laser writing (DLW) or multiphoton lithography relies on the principle of two photon absorptions that induce a drastic change in the solubility of the resist. In this case, well-desired structuring is carried out by irradiating photoresists with a monochromatic beam of light. It serves as a diverse, efficient technology for the fabrication of sub-micron-resolved 3D nanostructures (Bernardeschi et al., 2021). Coupling DLW with electrochemical metal deposition serves as a very efficient methodology to fabricate complex 3D plasmonic nanomaterials. However, a point to note in this case is the spatial resolution that can be achieved here, i.e., 100–150 nm. However, when combined with stimulated emission depletion microscopy, the best achievable resolution can be up to 50 nm (Fischer and Wegener, 2011; Elmeranta et al., 2016).

3.2 Bottom-up self-assembly approaches

In addition to top-down approaches, another relatively convenient way of the preparation of plasmonic materials involves the use of building blocks in order to achieve complex nanostructures of homogenous chemical composition in the solution itself. Molecular interactions like hydrogen bonds, van der Waals forces, and stacking interactions constitute the major forces that cause self-assembly of the building blocks at the nanoscale. Because of their much lower cost and intrinsically additive nature, bottom-up approaches have been widely used in the past decade for the fabrication of plasmonic nanomaterials (Ozin et al., 2009; Tang et al., 2020). Plasmon coupling is a process which heavily relies on the spatial arrangement of the nanostructures within the assembly, and hence, a very brief discussion on the complex interplay of underlying entropic and other interparticle forces mentioned becomes relevant in this context. Some of the commonly used bottom-up approaches involve sol–gel processing, chemical vapour deposition (CVD), laser pyrolysis, and colloidal self-assembly. The sol–gel process involves the mixing of dispersed solid nanoparticles in a homogenous liquid to invoke the formation of three dimensional agglomerates of specific morphologies (Kumar et al., 2019). Electrotuneable voltage-controlled self-assembly of plasmonic nanoparticles at the interface of two immiscible electrolyte solutions was successfully evoked to obtain nanoplasmonic liquid mirrors (Montelongo et al., 2017). In CVD, one of the substrate surfaces is exposed to a volatile precursor to obtain nanomaterials of varied shapes, sizes, and

thicknesses. Using vanadyl acetylacetonate ($VO(acac)_2$) powder as a volatile precursor, nanomaterials with different morphologies were prepared utilizing CVD (Wang et al., 2010). Trimeric and heptameric clusters of Au nanoshells exhibiting pronounced Fano resonance were obtained on drying polymer-coated nanoshells (Fan et al., 2010). In colloidal self-assembly, for example, the plasmonic nanoparticles are usually capped by a layer of passivating ligands known as stabilizers or capping agents, which prevents chemical changes. There is a solvation layer surrounding the nanoparticles because of electrostatic interactions, and these interactions counter the van der Waals attractive forces (Bishop et al., 2009; He et al., 2012; Li et al., 2020). The mechanism of the aggregation of plasmonic nanoparticles is analogous to polymerization reactions. In some cases, oligomers that are formed from the aggregation of individual plasmonic monomers serve as the repeating unit, whereas in others, particle assembly at very low rates favours long-chain formation, following the chain growth pathway. It has been found that the side bonding sites on the individual repeating units of the plasmonic oligomers are more than the terminating sites, and hence, side chain polymerization becomes kinetically favoured (Wang et al., 2012). These techniques for the preparation of plasmonic nanoparticles directly from solution have been extensively used over decades. In a recent report, using an electrochemically driven self-assembly process, trimeric Au nanolenses having an interparticle size of sub 2 nm were synthesized (Lloyd et al., 2017). The first report on the synthesis of Al nanocrystals using oleic acid as the capping agent and $(CH_3)_2C_2H_5NAlH_3$ as the precursor varied the relative proportion of the solvents viz. tetrahydrofuran (THF) and dioxane to achieve size tunability (McClain et al., 2015). The concept again is to moderate the electrostatic interactions operating out of solvation and the van der Waals forces (Jacobson et al., 2020). In recent days, modified DNA structures are widely being used as templates for the synthesis of plasmonic nanomaterials (Liu and Liedl, 2018; Wang et al., 2020b). In a seminal work by Rothemund, a 7-kilobase single-stranded DNA scaffold was efficiently twisted into several 2D nanostructures using a technology which he termed as "DNA origami" (Rothemund, 2006).

4 Plasmonic nanomaterials: role of metals

Plasmonic nanomaterials have generated significant interest in the past decade because of their diversified applications, owing to plasmonic coupling spanning the entire wavelength, i.e., from ultraviolet to infrared (Alivisatos et al., 1987). It has been discussed earlier (Section 2) that in plasmonic nanostructures, free-space electromagnetic energy is confined to ultrasmall regions defined as "hotspots." The LSPR can be effectively tuned by engineering the size and structure of the nanomaterials (viz. nanoparticles of various sizes and shapes, nanodiscs, nanorods, etc.) and also the dielectric properties of the metals. Because of the ease in the modulation of the LSPR, the optical properties can also be tuned to cover the entire range of the spectrum. Nanoporous gold nanomaterials had been, for a very long time, used for tunability in the visible-to-IR range. Varying the size of a monolayer of polystyrene beads over Au nanodiscs prepared by the deposition of gold and silver alloys on a Si wafer helps in tuning the diameter of the Au nanoparticles (Zhao et al., 2014). In another report, a silver halide electroreduction process was utilized to achieve tunability in pore size and diameter (Seok et al., 2018). However, in recent days, the focus is on Al-based plasmonic nanostructures owing to their natural abundance and long range of tunability, ranging from the UV to the IR region of the spectrum (Jacobson et al., 2020). However, preparation of size-controlled Al nanocrystals did not receive initial impetus, owing to the very high reactivity of this alkaline earth material in the presence of ambient oxygen (O_2) and water (H_2O). Hallas et al. synthesized crystalline Al nanocubes by using a transition metal catalyst viz. Tebbe's reagent with an excess of AlH_3 in THF. This was one of the first reports that expanded the use of a conventional transition metal catalyst in tuning the shape of metal nanoparticles (Clark et al., 2019). Al may prove to be a successful alternative to Au and Ag plasmonic nanomaterials, owing to its natural abundance and higher plasmon tunability (Tian et al., 2017). However, the unstable nature and very high reactivity have impeded the real-time applications of these plasmonic nanomaterials. Another metal that has been investigated very recently in this line is rhodium (Rh). Clavero et al. demonstrated chemical reduction on self-assembled micelles with trisodium hexachlorodate (Na_3RhCl_6) as the Rh precursor to obtain nanoporous Rh nanostructures (Clavero, 2014).

5 Substrates for PEF

The first report of PEF involved the enhancement of the emission intensity of fluorescein isothiocyanate (FITC) and rhodamine 6G on rugged silver islands (Chen et al., 1980). Later studies by Glass et al. delineated the role of the degree of overlap of the emission and absorption spectra on the enhancement of the fluorescence intensity (Glass et al., 1980). Following these developments, many different fabrication techniques were brought to light. We broadly categorize these into two subsections. The first section provides a brief overview of the physical modifications that have been effective in bringing about PEF. The second section elaborates a few of the wet chemical techniques that are broadly being used.

5.1 Physical modifications

5.1.1 Metal islands and hybrid nanostructures

PEF for fluorophores emitting in the visible region of the spectrum has been widely studied using silver nanoparticles. In one of the initial reports on the enhancement of tryptophan emission in proteins, the enhancement of the emission intensity of *N*-acetyl-1-tryptophanamide (NATA), a tryptophan analogue could be observed close to the Ag nanostructured surfaces (Figure 4A) (Ray et al., 2008a). In one of the initial reports on the enhancement of the emission of semiconductor quantum dots in the presence of plasmonic nanoparticles, Ray et al. demonstrated a several-fold enhancement of the emission intensity of CdTe quantum dots on silver island films (SIFs). This, coupled with single-molecule blinking experiments, delineated the intricacies of heterogeneity in the emission enhancement on glass and SIF surfaces (Ray et al., 2006).

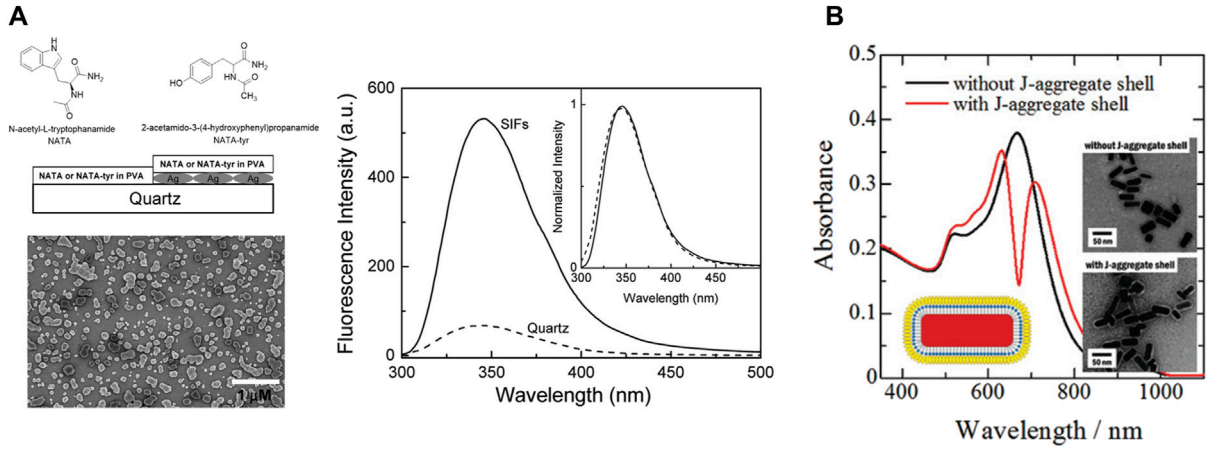

FIGURE 4
(A) Emission spectra of the 15-nm PVA film containing NATA on quartz and silver island films (SIFs) (Ray et al., 2008a). **(B)** Change in the absorption spectra of shelling Au nanorods with J-aggregated cyanine dyes (Yoshida et al., 2009).

5.1.2 Plasmonic nanoparticles with a capping layer

The spatial proximity between the fluorophore and the plasmonic nanoparticles is a vital factor to induce PEF (Section 2). The easiest way to achieve that is to deposit a layer of the fluorophores on the plasmonic surface. However, there are a couple of drawbacks in this case; first, there is always a possibility of Forster resonance energy transfer leading to quenching instead of enhancement (Section 2) (Glass et al., 1980). Second, a simple mixing might lead to the formation of an entirely different species. To prevent these, plasmonic nanoparticles are coated with a layer of organic polymers, which prevents them from coalescing. It has a major influence on the self-assembly process of the plasmonic nanomaterials and also helps in modulating the distance between the plasmonic surface and the exciton material. In a recent report, the role of capping layers was demonstrated using a library of gold nanourchins (NUs), where the observed coupling values were higher in the presence of the capping layer. The formation of the plexitonic hybrids was also significantly influenced by the extent of dye aggregation (Peruffo et al., 2021). Yoshida et al. efficiently synthesized hetero-nanostructures consisting of a Au-nanorod core with an inner spacer and an outer spacer of J-aggregated cyanine dye. They demonstrated that such double-layered composite structures provide flexibility in controlling the plasmon–exciton coupling (Figure 4B) (Yoshida et al., 2009).

5.2 Wet chemical modifications

5.2.1 Nanoprisms

In a simple, robust, and cost-effective technique, silver (Ag) nanoprisms were reportedly synthesized by reducing Ag^+ in $AgNO_3$ using a solution of sodium borohydride ($NaBH_4$) (Figure 5A). The reaction time and colour were indicative of the size of the nanoprisms (Frank et al., 2010). Other photochemical techniques can also provide a meticulous control of the prism size.

5.2.2 Nanowires

The Ag nanowire is another exotic plasmonic nanocrystal that has been used widely in various applications. One of the initial reports of synthesis demonstrated a seed-assisted route, where a platinum (Pt) nanoparticle seed was first synthesized by the reduction of platinum chloride ($PtCl_2$) with ethylene glycol, followed by the addition of $AgNO_3$ and polyvinyl pyrollidone (PVP), which allowed the formation of Ag nanoparticles. The pre-synthesized Pt nanoparticles acted as the template for the epitaxial growth of the Ag nanoparticles. When these nanoparticles were heated at high temperatures, because of Ostwald ripening, they could not retain their spherical shape and gradually started forming wires of size ranging from 30 to 40 nm (Figure 5B). A meticulous control over the size of the wires could be achieved by varying the reaction temperature and also the proportion of PVP to $AgNO_3$ (Sun et al., 2002).

5.2.3 Core–shell plasmonic nanomaterials

In core–shell nanomaterials, the core (typically a metal nanoparticle) is coated by another dielectric compound, which prevents the core from coming into direct contact with the surrounding environment and, hence, increases its stability. This broadens its scope by enabling the modulation of the plasmonic properties of the core. Optically transparent SiO_2 is one of the widely used shelling materials. The prerequisites of an ideal shelling material include a uniform, ultrathin layer that prevents the plasmonic core from coming into direct contact with the solution. Using (3-aminopropyl)trimethoxysilane (APTMS) as the linker and Na_2SiO_3 as the Si precursor, thin (2 nm) shelling was demonstrated efficiently at higher temperatures (100 C). The reaction duration was varied to obtain shells of varied thicknesses (Krajczewski and Kudelski, 2019).

5.2.4 Nanotriangles

In recent years, truncated triangular pyramid-shaped plasmonic nanomaterials have attracted significant interest, owing to the anisotropic distribution of the LSPR and

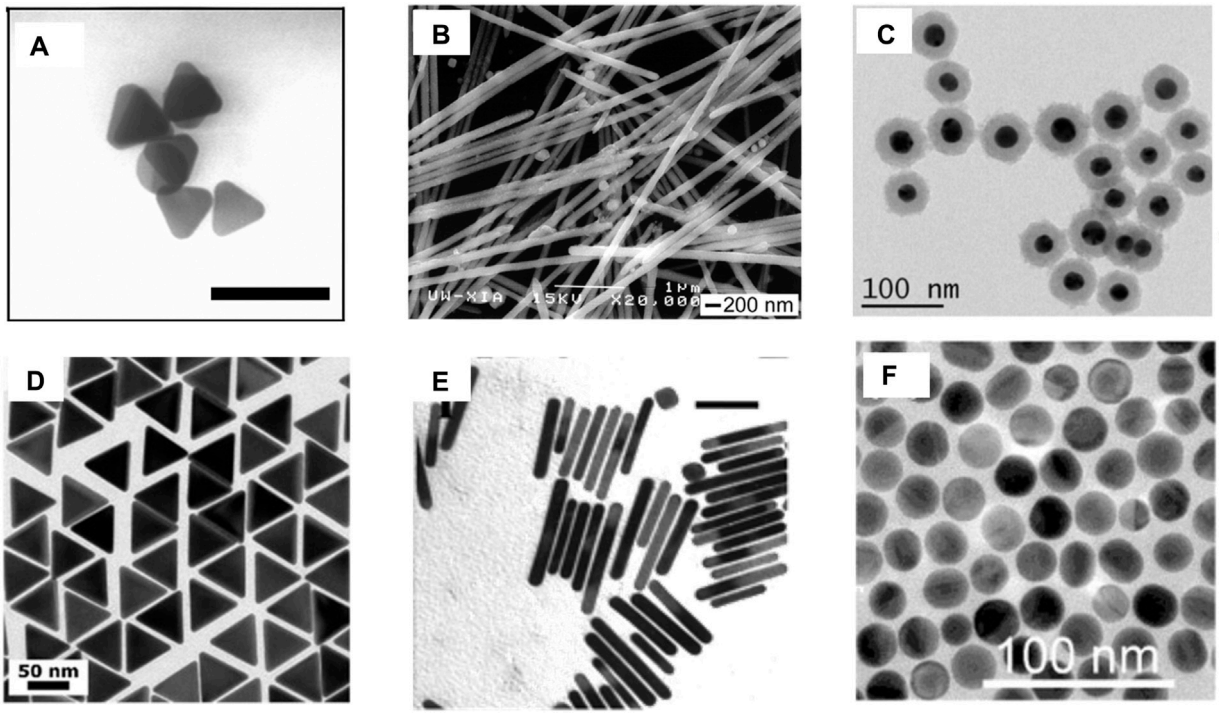

FIGURE 5
(A) Ag nanoprisms having an average lateral dimension of 40 ± 5 nm and an average thickness of 8.5 ± 1.4 nm; the bar corresponds to 100 nm (Frank et al., 2010). **(B)** SEM images of Ag nanowires with n_{PVP}/n_{AgNO3} = 1.5 (Sun et al., 2002). **(C)** TEM images of AuNP@SiO_2 of uniform thickness (Gogoi et al., 2021). **(D)** TEM images of 60-nm gold nanotriangles (Scarabelli and Liz-Marzán, 2021). **(E)** TEM images of gold NRs with plasmon band energies at 1,250 nm; the bar corresponds to 50 nm (Nikoobakht and El-Sayed, 2003). **(F)** TEM AuNS with diameters 24 ± 2 nm (Ruan et al., 2014).

generation of a strong electromagnetic local field, which consequently results in spectral tunability from the visible to the IR domain (Section 2). In a recent report, gold nanotriangles (AuNTs) were synthesized using the time-tested seeded growth technique in which Au (III) in $HAuCl_4$ was first reduced to Au using $NaBH_4$ as the reducing agent. Subsequently, the Au nanocrystal seeds thus obtained were aged and diluted in a cetyltrimethylammonium chloride (CTAC). The seeds were subsequently transferred into two growth solutions of CTAC, NaI, and $HAuCl_4$, which ensures the formation of AuNTs (Figure 5D) (Scarabelli and Liz-Marzán, 2021).

5.2.5 Nanospheres and nanorods

The most widely used plasmonic nanomaterials in biomedicine and photonic devices involve the use of spherical gold nanoparticles (AuNPs) and nanorods (AuNRs) (Ruan et al., 2014; Zheng et al., 2021). The reason behind the choice is their ease of synthesis, stability, and fairly strong LSPR couplings in the visible and NIR ranges. However, AuNRs have spherical symmetry, which limits their LSPR response only to the visible range. This problem was, however, bypassed in AuNRs, where, because of anisotropic LSPR, increased flexibility in the modulation of the LSPR could be achieved. In a modified seeded growth method, AuNPs were prepared with a surfactant CTAB in the seed formation phase, followed by a growth solution in which the Ag content was changed to obtain NRs with modulated aspect ratios (Nikoobakht and El-Sayed, 2003).

6 Examples of fluorescence enhancement

6.1 Role of hyperbolic metasurfaces in the enhancement of spontaneous emission

Nitrogen vacancy (NV) sites in nanodiamonds are a distinct example of solid-state nanoemitters displaying a broadband emission spectrum. Owing to their significant stability, they can serve as a unique and robust single photon source. The spin-selective optical transitions in nanodiamonds diversify their scope of applications in various fields. However, the extraction of the generated photon from the NV centres becomes a strenuous task, owing to longer fluorescence lifetimes and fewer numbers of photons. A recent report demonstrated the use of alternately layered, stacked silica–silver thin films in a pyramidal shape that aided in Purcell enhancement due to plasmonic coupling (Figure 6) (Zheng et al., 2023). In a contemporary report, resonance indicators of nanodiamonds and gold (RING) nanoassemblies were fabricated by modifying biotin-capped nanodiamonds and Au nanoparticles by the hybridization of complementary DNA sequences (Liang et al., 2023). It was demonstrated that the transition dynamics of the nitrogen-vacancy centres aids in higher local density of states and correspondingly enhances the oscillator strength because of a closed nanocavity. Using the concept of DNA assembly, RING nanoassemblies with different proportions of nanodiamonds and AuNPs were prepared to decipher the role of closed nanocavity in the enhancement of fluorescence of the NVs (Liang et al., 2023).

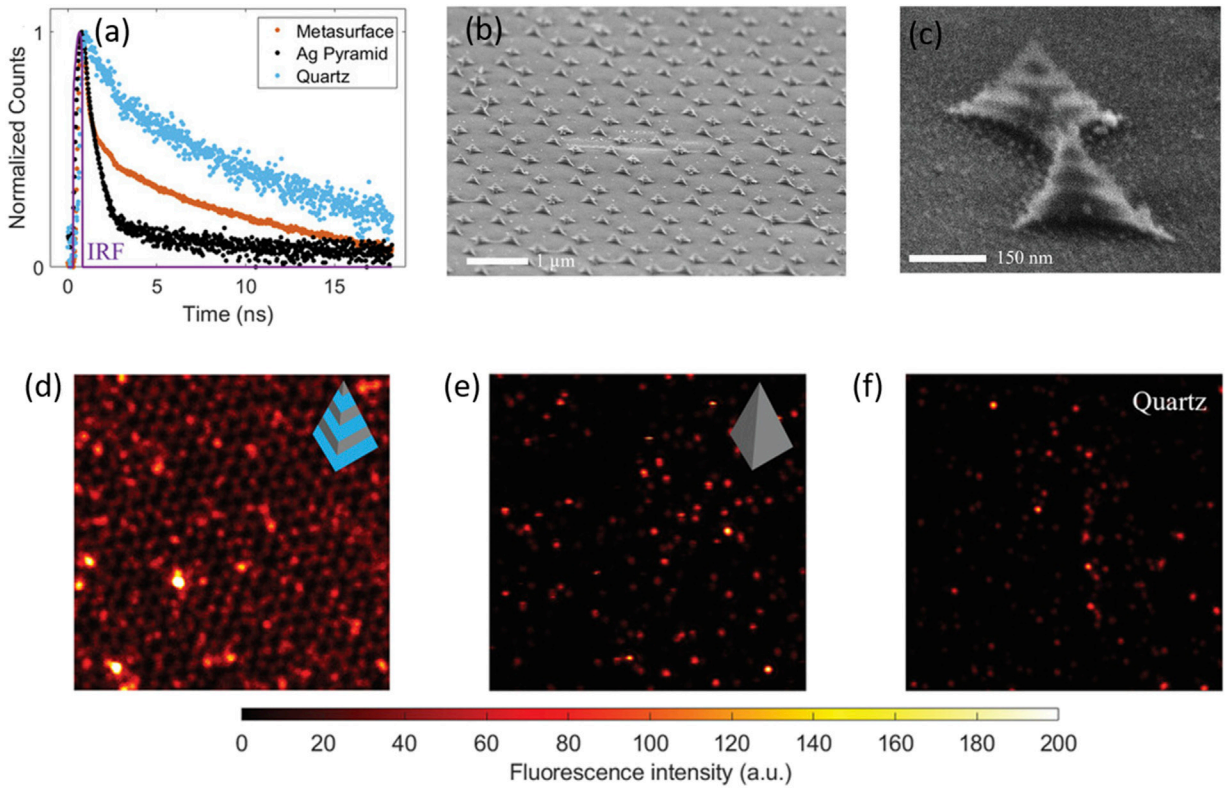

FIGURE 6
(A) Temporal parameters of the pyramidal metasurface: **(A)** fluorescence decays of the nitrogen vacancies (NVs) on different surfaces: black (Ag pyramid), blue (quartz), and yellow (pyramidal heterostructure) **(B,C)**. SEM images of the fabricated heterostructures at different magnifications **(D,E,F)**. The fluorescence intensity images of NV centres measured on the pyramidal metasurface, the Ag nanopyramid, and the quartz substrate, respectively, in a dimension of ≈14 μm × 14 μm with an excitation wavelength of 532 nm (Zheng et al., 2023).

6.2 Applications in fluorescence imaging

Fluorescence imaging is an excellent non-invasive method for the real-time monitoring of various physiological processes with the best spatial and temporal resolutions (Ntziachristos, 2010). However, small penetration depths and a moderate signal-to-noise ratio are an impediment to many such applications. The augmentation of the fluorescence signal because of the coupling of free electrons on the nanomaterial surface and the excited-state fluorophore not only leads to a plasmon-enhanced fluorescence but also contributes to better detection limits (Hong et al., 2014). Spatiotemporal properties of fluorescein-conjugated Au nanoparticles were delineated using a combination of fluorescence-lifetime imaging microscopy (FLIM) and direct reflectance (DR), which paved the way for multimodal bioimaging. A decrease in the fluorescence lifetime of fluorescein due to a change in the radiative rate constant in the near-field region of the AuNPs was successfully exploited to detect tumour surfaces (Section 2; Figure 7) (Fixler et al., 2014).

However, until very recently, the concept of plasmon-enhanced fluorescence for fluorescence imaging in the NIR region was limited. By the electrostatic assembly of fluorescent polymer dots on the surface of silica-coated gold nanorods, PEF could be observed. Since it was already established that PEF is a distance-dependent phenomenon, where the spatial distance between the plasmonic nanoparticle and the fluorescent probe plays a vital role, the thickness of the Si coating was varied to optimize the maximum enhancement (Anger et al., 2006). It was finally employed to probe the cerebral vasculature in live mice (Peng et al., 2022b). However, only two NIR probes, indocyanine green (λ_{em} = 828 nm) and methylene blue (λ_{em} = 686 nm) nm, have been clinically approved. So, the recent focus is on imaging in the short-wave infrared (SWIR) (900–1,700 nm) window. First, reduced autofluorescence and, second, lesser photon scattering have enabled SWIR imaging at significantly better depths within the tissue. Utilizing the concept of plasmon-enhanced fluorescence, commercially available SWIR dye IR-E1050-AuNR composites were successfully used for the *in vivo* imaging of ovarian cancer (Huang et al., 2021).

6.3 In molecular sensing

PEF is a phenomenon that is associated with augmented fluorescence concomitant with an increase in the radiative rate constant. Using this very concept, PEF has been very effectively used in the past decade as a tool for sensing different analytes, biomolecules, nucleic acids, etc. (Gao et al., 2023; Lu et al., 2023; Rippa et al., 2024). The present technique of specific RNA quantification involves complementary base pairing between a

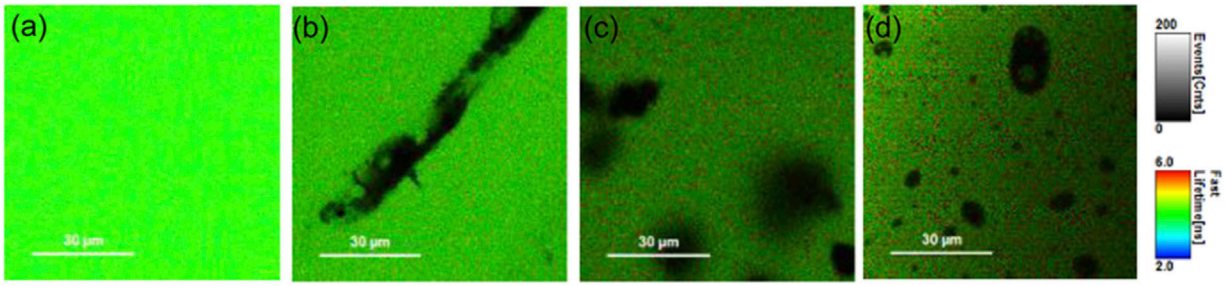

FIGURE 7
FLIM images of phantoms containing 50 µM fluorescein with **(A)** 0, **(B)** 2, and **(C)** 4 mg/mL of GNRs **(D)**. FLIM image of a phantom containing 50 µM fluorescein with 20 µg/mL of GNSs. The grayscale bar represents fluorescence intensity in counts/ms. The coloured scale bar displays the fluorescence lifetimes in nanoseconds (Fixler et al., 2014).

target RNA and the nucleic acid probe. However, sensitivity and rapidity are two major challenges in this methodology. In a PEF-based technique, a target RNA is first annealed, followed by labelling with a fluorogenic probe, and finally adhered to the SIFs, where enhanced fluorescence was observed because of PEF (Aslan et al., 2006). Using fluorescence lifetime correlation spectroscopy (FLCS) as an efficient tool, a 5-fold enhancement in the emission of cyanine 5 (Cy5) was reported in the presence of 50-nm Ag colloidal particles (Ray et al., 2008b). In another report, the deposition of a 10-nm Ag film on Klarite, a commercially available SERS substrate, resulted in the 50-fold enhancement in fluorescence of streptavidin-conjugated Alexa 674 (A647) (Ray and Lakowicz, 2013). The biotin–streptavidin host–guest system immobilized on an Au surface showed an enhancement in the fluorescence of the labelled streptavidin moiety, owing to plasmon-enhanced fluorescence. Utilizing this concept, a unique DNA chip was engineered using a biotinylated catcher probe that can track the DNA-binding kinetics (Tawa and Knoll, 2004). Utilizing the same concept, a solid surface-based immunoassay was developed, which could detect human chorionic gonadotropin (hCG) hormone in serum with LOD as low as 0.3 mIU mL^{-1} (~6 × 10^{-13} mol L^{-1}) (Vareiro et al., 2005). An ultrasensitive biochip for surface plasmon-enhanced fluorescence assays was developed, which could detect IgG molecules at concentrations as small as 11 pM (Toma et al., 2013). Silver island films were used to enhance the fluorescence intensity of myoglobin immunoassay if labelled with the Alexa Fluor 647 dye (Matveeva et al., 2007). The concept of plasmon-enhanced fluorescence was exploited to develop an Au@ polymer dot-based fluorescent immunoassay platform that can detect a prostate-specific antigen (PSA) with as less as 10 µL of the blood sample within 10 min (You et al., 2019). The proposition of thin Al films can also serve as an efficient substrate for metal-enhanced fluorescence with probes like NATA and tyrosine (Chowdhury et al., 2009). Another label-free approach of detecting tryptophan-containing proteins involved the augmentation of the tryptophan fluorescence in the presence of Al nanostructures (Ray et al., 2009b). In the last few years, there has been immense progress in the direction of label-free bioassays and sensing using the concept of plasmon-enhanced fluorescence (Figure 8) (Reinhard et al., 2007; Dai et al., 2022; Roy et al., 2023). The absolute quantification of membrane protein expression on cell surfaces is imperative to early cancer detection. For example, peptide–AuNP nanoprobes were designed and developed for the quantitative estimation of integrin GPIIB/IIIa, which, using NIR two-photon microscopy, could be directly visualized (Gao et al., 2015). Similarly, Ag–aptamer clusters were developed, which could provide significant quantitative insights into mIgM in live cells (Liu et al., 2014). In a recent report, a TiO_2 cluster-based biosensing platform was demonstrated, which could track the expression levels of N-cadherin, an important biomarker of epithelial-to-mesenchymal transition (EMT) in malignant cells (Han et al., 2021). The use Au-Se-peptide nanoprobes in mapping the role of drugs viz. curcumin and 7-ethyl-10-hydroxycamptothecin in apoptosis in malignant cells was another significant advancement in this domain (Pan et al., 2019). The design and development of label-free assays is another field that attracts significant attraction. A highly controlled assembly of peptide-functionalized Au nanoparticles was demonstrated to be a sensitive label-free assay for the detection of blood coagulation factor XIII (Chandrawati and Stevens, 2014). The fabrication of a plasmonic nanogap cavity using colloidal Ag nanocubes on top of Au films resulted in field enhancements, which, when coupled with a PED4 assay, resulted in an ~100-fold enhancement in fluorescence, which aided in the detection of an important cardiac biomarker viz. B-type natriuretic peptide (BNP) (Cruz et al., 2020).

6.4 Plasmon-enhanced fluorescence: DNA origami

DNA origami is a technique based on the molecular self-assembly, which can serve as a template for the fabrication of discrete, complex nanostructures using a bottom-up approach. The complex interactions between the plasmonic nanoparticles and fluorophores can be engineered by immobilization on a 3D origami structure. The specificity of nucleic acid binding makes DNA origami an efficient tool for tuning the arrangement of plasmonic nanomaterials for enhanced emission. The DNA connector configuration plays a vital role in controlling the placement of a plasmonic particle. In the shear configuration, after antiparallel hybridization of the same terminal ends, a perpendicular orientation of the duplex with respect to the bound surface is achieved. On the contrary, in the zipper configuration, protrusion of the different terminal ends is

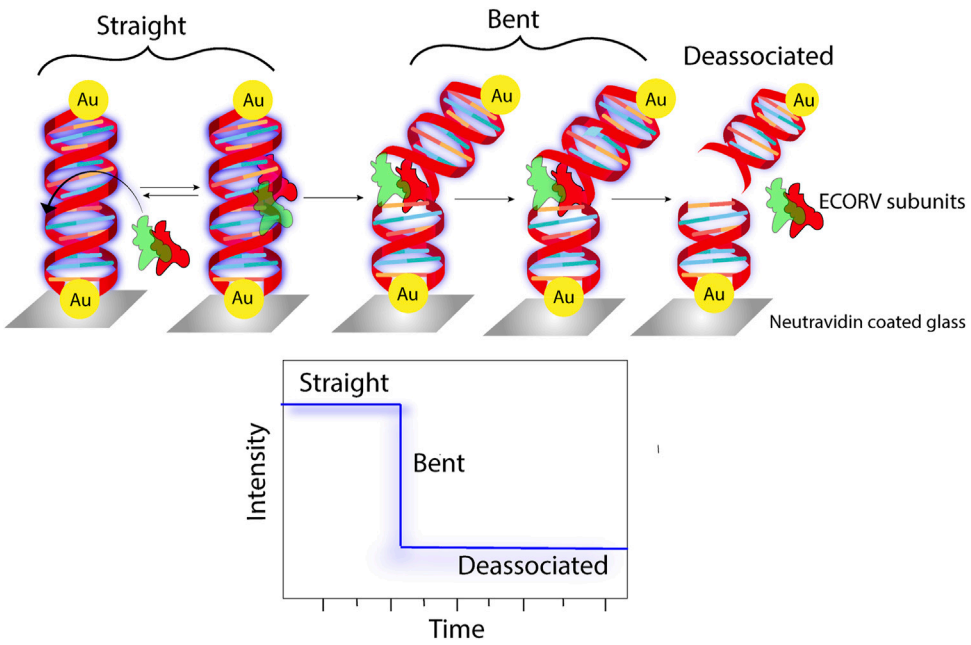

FIGURE 8
Schematic representation of fluorescence being used as a parameter to track the enzymatic cleavage of Au-tethered dsDNA (Reinhard et al., 2007).

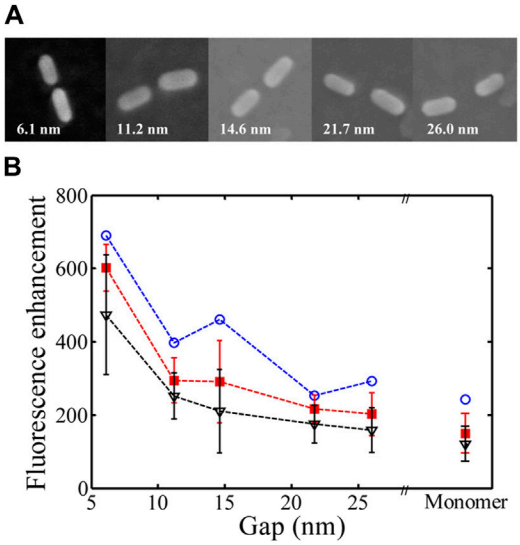

FIGURE 9
(A) SEM images of AuNR dimers with different gaps. **(B)** Dependence of fluorescence enhancement on distance (Zhang et al., 2015).

observed, which, on binding, results in a tangential orientation. Schreiber et al. used hybrid nanostructures with varying distances between the fluorescent probe and metal nanoparticles to demonstrate a $1/d^4$ distance-dependent quenching model (Schreiber et al., 2014). The use of Au nanoparticles for fluorescence enhancement is restricted to the NIR region, which was overcome by fabricating gold nanorod dimers on a DNA origami template. Using ATTO 655 as the fluorescent probe and engineering the distances between the nanorod tip and the probe, it was shown that an optimum distance of 6.1 nm was most favourable for achieving a 473-fold fluorescence enhancement (Figure 9) (Zhang et al., 2015). Similar studies were subsequently carried out using AgNPs having a higher scattering cross section (Vietz et al., 2017). In another report along the same line, different hybrid nanoparticle–DNA origami assemblies were used to explore the distance dependence on local field enhancement in monomeric and dimeric AuNPs (Pal et al., 2013).

6.5 Single-molecule detection

Another important domain where PEF finds significant use is single-molecule detection. One of the major issues with single-molecule fluorescence is the low signal-to-noise ratio. In biological systems, coupled with that is the issue of undesired analyte molecules contributing to spurious signals. Thus, the fluorescence from the target analyte must be isolated from the erroneous contributions (Ray et al., 2006; Ray et al., 2008c; Ray et al., 2015). In a seminal work using self-assembled dimeric nanoantennas (DNs) with a modified DNA origami template, higher fluorescence enhancement could be achieved compared to antennas fabricated by top-down lithography approaches. Even in the presence of a quencher like $NiCl_2$, a 5,468-fold fluorescence enhancement with ATTO 647N could be observed, which aided in single-molecule detection at concentrations of 25 μM (Puchkova et al., 2015). In another work, Au bowtie nanoantennas fabricated using electron beam lithography on 50-nm-thick ITO-coated quartz coverslips were used for the fluorescence enhancement of a NIR emissive TPQDI probe. A 1,348-fold fluorescence enhancement was reported (Kinkhabwala et al., 2009). Orrit et al. reported the single-molecule fluorescence enhancement of crystal violet (CV) up to

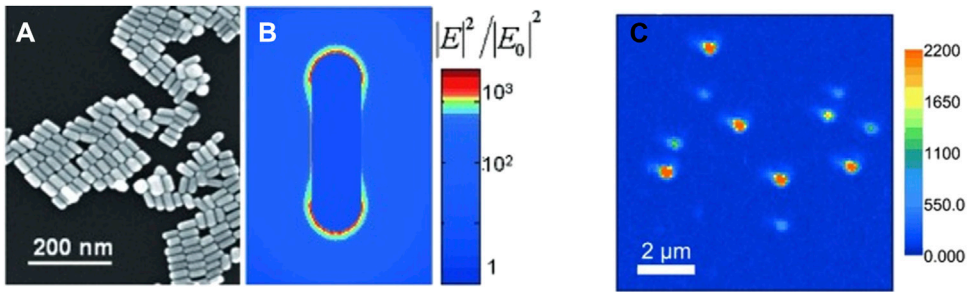

FIGURE 10
SEM image of **(A)** drop of the gold nanorod. **(B)** Map of the near-field optical intensity. **(C)** Single-molecule imaging of SMD enhanced by AuNRs (Yuan et al., 2013).

1,100 times in the presence of AuNRs (Figure 10). The underlying concept is that a molecule prefers diffusing through the ideal position where the enhancement is maximum. Using high-fluorophore concentrations, the fluorescence enhancement of a single CV molecule in the presence of AuNRs was demonstrated (Yuan et al., 2013).

6.6 Devices based on plasmon-enhanced fluorescence

Small optical reading devices have recently proved to be indispensable, providing rapidity and cost effectiveness to certain diagnostic assays and conventional laboratory tests. Exploiting the computational capabilities and imaging abilities of commercially available smartphone devices, early diagnosis of diseases and quantitative detection of viruses like HIV and other chronic ailments have been developed recently (Inci et al., 2013; Rad et al., 2015; Nguyen et al., 2023). A handheld miniature microscopy device based on the principle of plasmon-enhanced fluorescence, coupled with a smartphone, could efficiently image 50-nm fluorescent beads. In the same report, the detection of 80 fluorophores was demonstrated in each diffraction-limited spot using the handheld microscope, which paved the way for the design and development of nanophotonic devices (Wei et al., 2017). An assembly of ZnO nanorod arrays in a microfluidic system, along with a photodetector, was successfully used for the point-of-care (POC) detection of cancer biomarkers viz. carcinoembryonic antigen, α-fetoprotein, etc. (Hu et al., 2013). A similar kind of assembly using ZnO nanorods with cyanine 3 (Cy3) and Cy5 served as an immunoassay for the detection of carcinoembryonic antigens (Liu et al., 2016). In brief, many different plasmonic nanostructures can be widely utilized in different biosensing platforms including point-of-care diagnostics (Semeniak et al., 2023). Plasmonic Au-nanoparticle platforms allow for the accurate detection and quantification of type 1 diabetes antibodies, overcoming the shortcomings of non-specific binding in ELISA, which makes it an important contender for point-of-care diagnostics (Zhang et al., 2014). A plasmonic gold nano-island chip was designed and fabricated for the efficient diagnosis of myocardial infarction (MI). The serum biomarkers viz. cardiac troponin I showed ~130-fold enhanced NIR fluorescence in the presence of the plasmonic nanomaterial, which leads to quantitative detections with superior sensitivity to standard immunoassays (Xu et al., 2020).

7 Summary and perspective

This review delves into the recent advancements in plasmonic materials, with a specific focus on their ability to amplify fluorescence through near-field interactions and placing particular emphasis on the potential of utilizing plasmon-enhanced fluorescence for various photonic and analytical applications. The augmented spectral intensity in metal nanoparticles owing to the excitation of the LSPR results in the higher-extinction cross sections of the plasmonic nanoparticles, which leads to an enhancement in emission. This has been successfully employed in the domains of single-molecule detection, imaging, and the development of fluorescence-based biosensors. The theory will continue evolving and probe into the intricate details of molecular-level interactions between the plasmonic metamaterial and the quantum emitter. The past decade has witnessed a growth in the development of novel plasmonic materials, particularly focussing on semiconductors and conducting oxides. This exciting frontier holds immense promise for extending the spectral range of plasmonic effects beyond the limitations of traditional noble metals like gold and silver and other metals like aluminium. Accordingly, all of these plasmonic materials offer exciting possibilities for manipulating light across a broader spectrum of the UV-vis-IR regimes. This expanded range opens doors for innovative applications in the areas of enhanced biosensing and advanced optoelectronics. By enabling plasmonic interactions with biomolecules in UV-vis-IR regions, these materials could lead towards more sensitive and specific detection techniques for medical diagnostics. Tailoring the spectral response of plasmonic materials could potentially pave the way for the development of miniaturized and high-performance optical devices with functionalities like light modulation and switching.

Point-of-care testing is poised to benefit significantly from the development of planar plasmonic substrates. These plasmonic substrates can be fabricated using two main approaches: top-down nanofabrication techniques for precise patterning and the bottom-up nanoparticle assembly for potentially scalable production. Both approaches have shown promise in creating surfaces that enhance fluorescence for protein or DNA/RNA microarrays. This advancement could lead to rapid, portable diagnostic tools with increased sensitivity for detecting various diseases and biological markers. Despite a growth in research on plasmonic structures designed to enhance fluorescence for diagnostic and biosensing

applications, there remains a significant gap between these promising tools and their translation into clinically relevant platforms that can effectively navigate the complexities of real-world biological systems. Even though plasmonic structures face some limitations, continued research and development hold promise towards notable improvements in the fields of photonics and optical sensing. By overcoming these challenges, a plethora of possibilities in manipulating light at the nanoscale can be accomplished, leading to advancements in the areas of ultrasensitive biosensing, ultracompact photonic circuits, and enhanced light-harvesting technologies.

Author contributions

SD: writing–original draft and writing–review and editing. KR: writing–original draft and writing–review and editing.

Funding

The author(s) declare that financial support was received for the research, authorship, and/or publication of this article. The authors acknowledge the funding support by the National Institute of Allergy and Infectious Diseases of the National Institutes of Health under Award Numbers R01-AI172487 and R61-AI176561 (KR). The content is solely the authors' responsibility and does not necessarily represent the official views of the National Institutes of Health.

Conflict of interest

The authors declare that the research was conducted in the absence of any commercial or financial relationships that could be construed as a potential conflict of interest.

Publisher's note

All claims expressed in this article are solely those of the authors and do not necessarily represent those of their affiliated organizations, or those of the publisher, the editors, and the reviewers. Any product that may be evaluated in this article, or claim that may be made by its manufacturer, is not guaranteed or endorsed by the publisher.

References

Akimov, Y., and Sun, S. (2017). Spacer-controlled emission of randomly oriented fluorophores enhanced with surface plasmon-polaritons. *Phys. Chem. Chem. Phys.* 19 (13), 8706–8714. doi:10.1039/C7CP00151G

Alivisatos, A. P., Arndt, M. F., Efrima, S., Waldeck, D. H., and Harris, C. B. (1987). Electronic energy transfer at semiconductor interfaces. I. Energy transfer from two-dimensional molecular films to Si(111). *J. Chem. Phys.* 86 (11), 6540–6549. doi:10.1063/1.452396

Anger, P., Bharadwaj, P., and Novotny, L. (2006). Enhancement and quenching of single-molecule fluorescence. *Phys. Rev. Lett.* 96 (11), 113002. doi:10.1103/PhysRevLett.96.113002

Aroca, R. (2006). *Surface-enhanced vibrational spectroscopy*. China: John Wiley & Sons.

Aslan, K., Huang, J., Wilson, G. M., and Geddes, C. D. (2006). Metal-enhanced fluorescence-based rna sensing. *J. Am. Chem. Soc.* 128 (13), 4206–4207. doi:10.1021/ja0601179

Bernardeschi, I., Ilyas, M., and Beccai, L. (2021). A review on active 3d microstructures via direct laser lithography. *Adv. Intell. Syst.* 3 (9), 2100051. doi:10.1002/aisy.202100051

Bishop, K. J., Wilmer, C. E., Soh, S., and Grzybowski, B. A. (2009). Nanoscale forces and their uses in self-assembly. *Small* 5 (14), 1600–1630. doi:10.1002/smll.200900358

Boden, S. A., Moktadir, Z., Bagnall, D. M., Mizuta, H., and Rutt, H. N. (2011). Focused helium ion beam milling and deposition. *Microelectron. Eng.* 88 (8), 2452–2455. doi:10.1016/j.mee.2010.11.041

Chandrawati, R., and Stevens, M. M. (2014). Controlled assembly of peptide-functionalized gold nanoparticles for label-free detection of blood coagulation factor xiii activity. *Chem. Commun.* 50 (41), 5431–5434. doi:10.1039/C4CC00572D

Chen, C. Y., Davoli, I., Ritchie, G., and Burstein, E. (1980). Giant Raman scattering and luminescence by molecules adsorbed on Ag and Au metal island films. *Surf. Sci.* 101 (1), 363–366. doi:10.1016/0039-6028(80)90631-7

Chowdhury, M. H., Ray, K., Gray, S. K., Pond, J., and Lakowicz, J. R. (2009). Aluminum nanoparticles as substrates for metal-enhanced fluorescence in the ultraviolet for the label-free detection of biomolecules. *Anal. Chem.* 81 (4), 1397–1403. doi:10.1021/ac802118s

Clark, B. D., Jacobson, C. R., Lou, M., Renard, D., Wu, G., Bursi, L., et al. (2019). Aluminum nanocubes have sharp corners. *ACS Nano* 13 (8), 9682–9691. doi:10.1021/acsnano.9b05277

Clavero, C. (2014). Plasmon-induced hot-electron generation at nanoparticle/metal-oxide interfaces for photovoltaic and photocatalytic devices. *Nat. Photonics* 8 (2), 95–103. doi:10.1038/nphoton.2013.238

Cruz, D. F., Fontes, C. M., Semeniak, D., Huang, J., Hucknall, A., Chilkoti, A., et al. (2020). Ultrabright fluorescence readout of an inkjet-printed immunoassay using plasmonic nanogap cavities. *Nano Lett.* 20 (6), 4330–4336. Epub 20200514. doi:10.1021/acs.nanolett.0c01051

Dai, F., Horrer, A., Adam, P.-M., and Fleischer, M. (2020). Accessing the hotspots of cavity plasmon modes in vertical metal–insulator–metal structures for surface enhanced Raman scattering. *Adv. Opt. Mater.* 8 (7), 1901734. doi:10.1002/adom.201901734

Dai, S., Li, W., Xu, R., Wang, X., Li, Q., Dou, M., et al. (2022). Label-free fluorescence quantitative detection platform on plasmonic silica photonic crystal Microsphere array. *Anal. Chem.* 94 (51), 17939–17946. doi:10.1021/acs.analchem.2c04000

Elmeranta, M., Vicidomini, G., Duocastella, M., Diaspro, A., and de Miguel, G. (2016). Characterization of nanostructures fabricated with two-beam dlw lithography using sted microscopy. *Opt. Mater Express* 6 (10), 3169–3179. doi:10.1364/OME.6.003169

Fan, J. A., Wu, C., Bao, K., Bao, J., Bardhan, R., Halas, N. J., et al. (2010). Self-assembled plasmonic nanoparticle clusters. *Science* 328 (5982), 1135–1138. doi:10.1126/science.1187949

Feng, A. L., You, M. L., Tian, L., Singamaneni, S., Liu, M., Duan, Z., et al. (2015). Distance-dependent plasmon-enhanced fluorescence of upconversion nanoparticles using polyelectrolyte multilayers as tunable spacers. *Sci. Rep.* 5 (1), 7779. doi:10.1038/srep07779

Fischer, J., and Wegener, M. (2011). Three-dimensional direct laser writing inspired by stimulated-emission-depletion microscopy [invited]. *Opt. Mater Express* 1 (4), 614–624. doi:10.1364/OME.1.000614

Fixler, D., Nayhoz, T., and Ray, K. (2014). Diffusion reflection and fluorescence lifetime imaging microscopy study of fluorophore-conjugated gold nanoparticles or nanorods in solid phantoms. *ACS Photonics* 1 (9), 900–905. doi:10.1021/ph500214m

Fleischmann, M., Hendra, P. J., and McQuillan, A. J. (1974). Raman spectra of pyridine adsorbed at a silver electrode. *Chem. Phys. Lett.* 26 (2), 163–166. doi:10.1016/0009-2614(74)85388-1

Frank, A. J., Cathcart, N., Maly, K. E., and Kitaev, V. (2010). Synthesis of silver nanoprisms with variable size and investigation of their optical properties: a first-year undergraduate experiment exploring plasmonic nanoparticles. *J. Chem. Educ.* 87 (10), 1098–1101. doi:10.1021/ed100166g

Gao, L., Liu, M., Ma, G., Wang, Y., Zhao, L., Yuan, Q., et al. (2015). Peptide-conjugated gold nanoprobe: intrinsic nanozyme-linked immunsorbant assay of integrin expression level on cell membrane. *ACS Nano* 9 (11), 10979–10990. doi:10.1021/acsnano.5b04261

Gao, S., Zhou, R., Samanta, S., Qu, J., and Ohulchanskyy, T. Y. (2023). Recent advances in plasmon-enhanced luminescence for biosensing and bioimaging. *Anal. Chim. Acta* 1254, 341086. doi:10.1016/j.aca.2023.341086

Glass, A. M., Liao, P. F., Bergman, J. G., and Olson, D. H. (1980). Interaction of metal particles with adsorbed dye molecules: absorption and luminescence. *Opt. Lett.* 5 (9), 368. doi:10.1364/ol.5.000368

Gogoi, H., Maddala, B. G., Ali, F., and Datta, A. (2021). Role of solvent in electron-phonon relaxation dynamics in core-shell Au–Sio2 nanoparticles. *ChemPhysChem* 22 (21), 2201–2206. doi:10.1002/cphc.202100592

Han, Y., Qiu, C., Li, J., Gao, F., Yuan, Q., Tang, Y., et al. (2021). Metal cluster-based electrochemical biosensing system for detecting epithelial-to-mesenchymal transition. *ACS Sensors* 6 (6), 2290–2298. doi:10.1021/acssensors.1c00339

Hartschuh, A. (2008). Tip-enhanced near-field optical microscopy. *Angew. Chem. Int. Ed.* 47 (43), 8178–8191. doi:10.1002/anie.200801605

He, L., Hu, Y., Wang, M., and Yin, Y. (2012). Determination of solvation layer thickness by a magnetophotonic approach. *ACS Nano* 6 (5), 4196–4202. Epub 20120427. doi:10.1021/nn3007288

Hong, G., Diao, S., Chang, J., Antaris, A. L., Chen, C., Zhang, B., et al. (2014). Through-skull fluorescence imaging of the brain in a new near-infrared window. *Nat. Photonics* 8 (9), 723–730. doi:10.1038/nphoton.2014.166

Hu, W., Lu, Z., Liu, Y., Chen, T., Zhou, X., and Li, C. M. (2013). A portable flow-through fluorescent immunoassay lab-on-a-chip device using zno nanorod-decorated glass capillaries. *Lab. Chip* 13 (9), 1797–1802. doi:10.1039/c3lc41382a

Huang, S., Lin, C.-W., Qi, J., Iyer, A. M., He, Y., Li, Y., et al. (2021). Surface plasmon-enhanced short-wave infrared fluorescence for detecting sub-millimeter-sized tumors. *Adv. Mater.* 33 (7), 2006057. doi:10.1002/adma.202006057

Inci, F., Tokel, O., Wang, S., Gurkan, U. A., Tasoglu, S., Kuritzkes, D. R., et al. (2013). Nanoplasmonic quantitative detection of intact viruses from unprocessed whole blood. *ACS Nano* 7 (6), 4733–4745. doi:10.1021/nn3036232

Jacobson, C. R., Solti, D., Renard, D., Yuan, L., Lou, M., and Halas, N. J. (2020). Shining light on aluminum nanoparticle synthesis. *Accounts Chem. Res.* 53 (9), 2020–2030. doi:10.1021/acs.accounts.0c00419

Kinkhabwala, A., Yu, Z., Fan, S., Avlasevich, Y., Müllen, K., and Moerner, W. E. (2009). Large single-molecule fluorescence enhancements produced by a bowtie nanoantenna. *Nat. Photonics* 3 (11), 654–657. doi:10.1038/nphoton.2009.187

Koya, A. N., Zhu, X., Ohannesian, N., Yanik, A. A., Alabastri, A., Proietti Zaccaria, R., et al. (2021). Nanoporous metals: from plasmonic properties to applications in enhanced spectroscopy and photocatalysis. *ACS Nano* 15 (4), 6038–6060. Epub 20210402. doi:10.1021/acsnano.0c10945

Krajczewski, J., and Kudelski, A. (2019). Shell-isolated nanoparticle-enhanced Raman spectroscopy. *Front. Chem.* 7, 410. Epub 20190604. doi:10.3389/fchem.2019.00410

Kumar, A., Choudhary, P., Kumar, A., Camargo, P. H. C., and Krishnan, V. (2022). Recent advances in plasmonic photocatalysis based on tio(2) and noble metal nanoparticles for energy conversion, environmental remediation, and organic synthesis. *Small* 18 (1), e2101638. Epub 20210815. doi:10.1002/smll.202101638

Kumar, K. V. A., Balu, A., Ramachandran, A., Unnikrishnan, N. V., and Selvaraj, N. B. (2019). Sol-gel synthesized plasmonic nanoparticles and their integration into dye sensitized solar cells. *Appl. Surf. Sci.* 491, 670–674. doi:10.1016/j.apsusc.2019.05.344

Laible, F., Braun, K., Hauler, O., Eberle, M., Kern, D. P., Meixner, A. J., et al. A flexible platform for controlled optical and electrical effects in tailored plasmonic break junctions. (*Nanophotonics*, 2020) 9(6):1391–1400. doi:10.1515/nanoph-2019-0472

Laible, F., Gollmer, D. A., Dickreuter, S., Kern, D. P., and Fleischer, M. (2018). Continuous reversible tuning of the gap size and plasmonic coupling of bow tie nanoantennas on flexible substrates. *Nanoscale* 10 (31), 14915–14922. doi:10.1039/c8nr03575j

Laible, F., Horneber, A., and Fleischer, M. (2021). Mechanically tunable nanogap antennas: single-structure effects and multi-structure applications. *Adv. Opt. Mater.* 9 (20), 2100326. doi:10.1002/adom.202100326

Lakowicz, J. R. (2005). Radiative decay engineering 5: metal-enhanced fluorescence and plasmon emission. *Anal. Biochem.* 337 (2), 171–194. doi:10.1016/j.ab.2004.11.026

Lakowicz, J. R., Ray, K., Chowdhury, M., Szmacinski, H., Fu, Y., Zhang, J., et al. (2008). Plasmon-controlled fluorescence: a new paradigm in fluorescence spectroscopy. *Analyst* 133 (10), 1308–1346. doi:10.1039/B802918K

Li, C., Huang, Y., Li, X., Zhang, Y., Chen, Q., Ye, Z., et al. (2021). Towards practical and sustainable sers: a review of recent developments in the construction of multifunctional enhancing substrates. *J. Mater. Chem. C* 9 (35), 11517–11552. doi:10.1039/D1TC02134F

Li, H., Sun, D.-e., and Liu, Z. (2015). Ultrasensitive biosensing platform based on the luminescence quenching ability of plasmonic palladium nanoparticles. *Chem. – A Eur. J.* 21 (13), 4944–4948. doi:10.1002/chem.201406633

Li, J.-F., Li, C.-Y., and Aroca, R. F. (2017). Plasmon-enhanced fluorescence spectroscopy. *Chem. Soc. Rev.* 46 (13), 3962–3979. doi:10.1039/C7CS00169J

Li, Z., Devasenathipathy, R., Wang, J., Yu, L., Liang, Y., Sheng, H., et al. (2023). Direct observation of the plasmon-enhanced palladium catalysis with single-molecule fluorescence microscopy. *Nano Res.* 16 (7), 8817–8826. doi:10.1007/s12274-023-5548-7

Li, Z., Wang, W., and Yin, Y. (2020). Colloidal assembly and active tuning of coupled plasmonic nanospheres. *Trends Chem.* 2 (7), 593–608. doi:10.1016/j.trechm.2020.03.008

Liang, L., Zheng, P., Jia, S., Ray, K., Chen, Y., and Barman, I. (2023). Plasmonic nanodiamonds. *Nano Lett.* 23 (12), 5746–5754. doi:10.1021/acs.nanolett.3c01514

Liu, B., Monshat, H., Gu, Z., Lu, M., and Zhao, X. (2018). Recent advances in merging photonic crystals and plasmonics for bioanalytical applications. *Analyst* 143 (11), 2448–2458. doi:10.1039/C8AN00144H

Liu, C., Meng, F., Zheng, W., Xue, T., Jin, Z., Wang, Z., et al. (2016). Plasmonic zno nanorods/Au substrates for protein microarrays with high sensitivity and broad dynamic range. *Sensors Actuators B Chem.* 228, 231–236. doi:10.1016/j.snb.2016.01.019

Liu, N., and Liedl, T. (2018). DNA-assembled advanced plasmonic architectures. *Chem. Rev.* 118 (6), 3032–3053. doi:10.1021/acs.chemrev.7b00225

Liu, R., Zhai, J., Liu, L., Wang, Y., Wei, Y., Jiang, X., et al. (2014). Spatially marking and quantitatively counting membrane immunoglobulin M in live cells via Ag cluster–aptamer probes. *Chem. Commun.* 50 (27), 3560–3563. doi:10.1039/C3CC49036J

Lloyd, J. A., Ng, S. H., Liu, A. C. Y., Zhu, Y., Chao, W., Coenen, T., et al. (2017). Plasmonic nanolenses: electrostatic self-assembly of hierarchical nanoparticle trimers and their response to optical and electron beam stimuli. *ACS Nano* 11 (2), 1604–1612. doi:10.1021/acsnano.6b07336

Lu, G., Zhang, T., Li, W., Hou, L., Liu, J., and Gong, Q. (2011). Single-molecule spontaneous emission in the vicinity of an individual gold nanorod. *J. Phys. Chem. C* 115 (32), 15822–15828. doi:10.1021/jp203317d

Lu, Y.-C., Darius, E., Lien, M.-C., Yeh, I. H., Shi, H.-F., Huang, Y.-H., et al. (2023). Two-dimensional Cs2agbibr6-based biosensor for selective and sensitive detection of cardiac biomarker troponin I. *ACS Appl. Nano Mater.* 6 (24), 23022–23028. doi:10.1021/acsanm.3c04385

Luk yanchuk, B., Zheludev, N. I., Maier, S. A., Halas, N. J., Nordlander, P., Giessen, H., et al. (2010). The Fano resonance in plasmonic nanostructures and metamaterials. *Nat. Mater* 9 (9), 707–715. Epub 20100823. doi:10.1038/nmat2810

Matveeva, E. G., Gryczynski, I., Barnett, A., Leonenko, Z., Lakowicz, J. R., and Gryczynski, Z. (2007). Metal particle-enhanced fluorescent immunoassays on metal mirrors. *Anal. Biochem.* 363 (2), 239–245. Epub 20070126. doi:10.1016/j.ab.2007.01.030

McClain, M. J., Schlather, A. E., Ringe, E., King, N. S., Liu, L., Manjavacas, A., et al. (2015). Aluminum nanocrystals. *Nano Lett.* 15 (4), 2751–2755. doi:10.1021/acs.nanolett.5b00614

Montelongo, Y., Sikdar, D., Ma, Y., McIntosh, A. J. S., Velleman, L., Kucernak Anthony, R., et al. (2017). Electrotunable nanoplasmonic liquid mirror. *Nat. Mater.* 16 (11), 1127–1135. doi:10.1038/nmat4969

Morimoto, H., Sasaki, Y., Saitoh, K., Watakabe, Y., and Kato, T. (1986). Focused ion beam lithography and its application to submicron devices. *Microelectron. Eng.* 4 (3), 163–179. doi:10.1016/0167-9317(86)90009-2

Nguyen, T. M., Chung, J. H., Bak, G.-H., Kim, Y. H., Kim, M., Kim, Y.-J., et al. (2023). Multiarray biosensor for diagnosing lung cancer based on gap plasmonic color films. *ACS Sensors* 8 (1), 167–175. doi:10.1021/acssensors.2c02001

Nicholls, L. H., Rodríguez-Fortuño, F. J., Nasir, M. E., Córdova-Castro, R. M., Olivier, N., Wurtz, G. A., et al. (2017). Ultrafast synthesis and switching of light polarization in nonlinear anisotropic metamaterials. *Nat. Photonics* 11, 628–633. doi:10.1038/s41566-017-0002-6

Nikoobakht, B., and El-Sayed, M. A. (2003). Preparation and growth mechanism of gold nanorods (nrs) using seed-mediated growth method. *Chem. Mater.* 15 (10), 1957–1962. doi:10.1021/cm020732l

Ntziachristos, V. (2010). Going deeper than microscopy: the optical imaging frontier in biology. *Nat. Methods* 7 (8), 603–614. doi:10.1038/nmeth.1483

Ozin, G. A., Hou, K., Lotsch, B. V., Cademartiri, L., Puzzo, D. P., Scotognella, F., et al. (2009). Nanofabrication by self-assembly. *Mater. Today* 12 (5), 12–23. doi:10.1016/S1369-7021(09)70156-7

Pal, S., Dutta, P., Wang, H., Deng, Z., Zou, S., Yan, H., et al. (2013). Quantum efficiency modification of organic fluorophores using gold nanoparticles on DNA origami scaffolds. *J. Phys. Chem. C* 117 (24), 12735–12744. doi:10.1021/jp312422n

Pan, W., Liu, X., Wan, X., Li, J., Li, Y., Lu, F., et al. (2019). Rapid preparation of Au–Se–peptide nanoprobe based on a freezing method for bioimaging. *Anal. Chem.* 91 (24), 15982–15987. doi:10.1021/acs.analchem.9b04616

Peng, L., Liu, Y., Zhang, J., Zhang, Z., Liu, Z., Fang, X., et al. (2022a). Surface plasmon-enhanced nir-ii fluorescence in a multilayer nanoprobe for through-skull mouse brain imaging. *ACS Appl. Mater Interfaces* 14 (34), 38575–38583. Epub 20220817. doi:10.1021/acsami.2c11218

Peng, L., Liu, Y., Zhang, J., Zhang, Z., Liu, Z., Fang, X., et al. (2022b). Surface plasmon-enhanced nir-ii fluorescence in a multilayer nanoprobe for through-skull mouse brain imaging. *ACS Appl. Mater. Interfaces* 14 (34), 38575–38583. doi:10.1021/acsami.2c11218

Peruffo, N., Mancin, F., and Collini, E. (2021). Plexcitonic nanohybrids based on gold nanourchins: the role of the capping layer. *J. Phys. Chem. C* 125 (36), 19897–19905. doi:10.1021/acs.jpcc.1c05862

Puchkova, A., Vietz, C., Pibiri, E., Wünsch, B., Sanz Paz, M., Acuna, G. P., et al. (2015). DNA origami nanoantennas with over 5000-fold fluorescence

enhancement and single-molecule detection at 25 μm. *Nano Lett.* 15 (12), 8354–8359. doi:10.1021/acs.nanolett.5b04045

Qin, N., Qian, Z.-G., Zhou, C., Xia, X.-X., and Tao, T. H. (2021). 3d electron-beam writing at sub-15 Nm resolution using spider silk as a resist. *Nat. Commun.* 12 (1), 5133. doi:10.1038/s41467-021-25470-1

Rad, M. Z., Ghuchani, S. R., Bahaadinbeigy, K., and Khalilzadeh, M. M. (2015). Real time recognition of heart attack in a smart phone. *Acta Inf. Med.* 23 (3), 151–154. Epub 20150525. doi:10.5455/aim.2015.23.151-154

Ray, K., Badugu, R., and Lakowicz, J. R. (2006). Metal-enhanced fluorescence from cdte nanocrystals: a single-molecule fluorescence study. *J. Am. Chem. Soc.* 128 (28), 8998–8999. doi:10.1021/ja061762i

Ray, K., Badugu, R., and Lakowicz, J. R. (2007). Sulforhodamine adsorbed Langmuir–Blodgett layers on silver island films: effect of probe distance on the metal-enhanced fluorescence. *J. Phys. Chem. C* 111 (19), 7091–7097. doi:10.1021/jp067635q

Ray, K., Badugu, R., Szmacinski, H., and Lakowicz, J. R. (2015). Several hundred-fold enhanced fluorescence from single fluorophores assembled on silver nanoparticle–dielectric–metal substrate. *Chem. Commun.* 51 (81), 15023–15026. doi:10.1039/C5CC03581C

Ray, K., Chowdhury, M. H., and Lakowicz, J. R. (2008c). Single-molecule spectroscopic study of enhanced intrinsic phycoerythrin fluorescence on silver nanostructured surfaces. *Anal. Chem.* 80 (18), 6942–6948. doi:10.1021/ac800760z

Ray, K., Chowdhury, M. H., Szmacinski, H., and Lakowicz, J. R. (2008a). Metal-enhanced intrinsic fluorescence of proteins on silver nanostructured surfaces toward label-free detection. *J. Phys. Chem. C* 112 (46), 17957–17963. doi:10.1021/jp807025n

Ray, K., Chowdhury, M. H., Zhang, J., Fu, Y., Szmacinski, H., Nowaczyk, K., et al. (2009a). "Plasmon-controlled fluorescence towards high-sensitivity optical sensing," in *Optical sensor systems in biotechnology*. Editor G. Rao (Berlin, Heidelberg: Springer Berlin Heidelberg), 1–28.

Ray, K., and Lakowicz, J. R. (2013). Metal-enhanced fluorescence lifetime imaging and spectroscopy on a modified sers substrate. *J. Phys. Chem. C* 117 (30), 15790–15797. doi:10.1021/jp404590j

Ray, K., Szmacinski, H., and Lakowicz, J. R. (2009b). Enhanced fluorescence of proteins and label-free bioassays using aluminum nanostructures. *Anal. Chem.* 81 (15), 6049–6054. doi:10.1021/ac900263k

Ray, K., Zhang, J., and Lakowicz, J. R. (2008b). Fluorescence lifetime correlation spectroscopic study of fluorophore-labeled silver nanoparticles. *Anal. Chem.* 80 (19), 7313–7318. doi:10.1021/ac8009356

Reinhard, B. M., Sheikholeslami, S., Mastroianni, A., Alivisatos, A. P., and Liphardt, J. (2007). Use of plasmon coupling to reveal the dynamics of DNA bending and cleavage by single ecorv restriction enzymes. *Proc. Natl. Acad. Sci. U. S. A.* 104 (8), 2667–2672. Epub 20070216. doi:10.1073/pnas.0607826104

Rippa, M., Marchesano, V., Vestri, A., Sagnelli, D., Fusco, G., Zyss, J., et al. (2024). Fractal plasmonic molecule for multi-sensing: sers platform for sars-Cov-2 detection. *ACS Appl. Nano Mater.* 7 (7), 6958–6968. doi:10.1021/acsanm.3c06006

Rivera, N., and Kaminer, I. (2020). Light-matter interactions with photonic quasiparticles. *Nat. Rev. Phys.* 2, 538–561. doi:10.1038/s42254-020-0224-2

Roccapriore, K. M., Cho, S.-H., Lupini, A. R., Milliron, D. J., and Kalinin, S. V. (2022). Sculpting the plasmonic responses of nanoparticles by directed electron beam irradiation. *Small* 18 (1), 2105099. doi:10.1002/smll.202105099

Rothemund, P. W. K. (2006). Folding DNA to create nanoscale shapes and patterns. *Nature* 440 (7082), 297–302. doi:10.1038/nature04586

Roy, P., Claude, J.-B., Tiwari, S., Barulin, A., and Wenger, J. (2023). Ultraviolet nanophotonics enables autofluorescence correlation spectroscopy on label-free proteins with a single tryptophan. *Nano Lett.* 23 (2), 497–504. doi:10.1021/acs.nanolett.2c03797

Ruan, Q., Shao, L., Shu, Y., Wang, J., and Wu, H. (2014). Growth of monodisperse gold nanospheres with diameters from 20 Nm to 220 Nm and their core/satellite nanostructures. *Adv. Opt. Mater.* 2 (1), 65–73. doi:10.1002/adom.201300359

Scarabelli, L., and Liz-Marzán, L. M. (2021). An extended protocol for the synthesis of monodisperse gold nanotriangles. *ACS Nano* 15 (12), 18600–18607. doi:10.1021/acsnano.1c10538

Schmid, T., Opilik, L., Blum, C., and Zenobi, R. (2013). Nanoscale chemical imaging using tip-enhanced Raman spectroscopy: a critical review. *Angew. Chem. Int. Ed.* 52 (23), 5940–5954. doi:10.1002/anie.201203849

Schreiber, R., Do, J., Roller, E.-M., Zhang, T., Schüller, V. J., Nickels, P. C., et al. (2014). Hierarchical assembly of metal nanoparticles, quantum dots and organic dyes using DNA origami scaffolds. *Nat. Nanotechnol.* 9 (1), 74–78. doi:10.1038/nnano.2013.253

Semeniak, D., Cruz, D. F., Chilkoti, A., and Mikkelsen, M. H. (2023). Plasmonic fluorescence enhancement in diagnostics for clinical tests at point-of-care: a review of recent technologies. *Adv. Mater.* 35 (34), 2107986. doi:10.1002/adma.202107986

Seok, J. Y., Lee, J., and Yang, M. (2018). Self-generated nanoporous silver framework for high-performance iron oxide pseudocapacitor anodes. *ACS Appl. Mater. Interfaces* 10 (20), 17223–17231. doi:10.1021/acsami.8b03725

Sim, J.-H., Lee, S. H., Yang, J.-Y., Lee, W.-C., Mun, C., Lee, S., et al. (2022). Plasmonic hotspot engineering of Ag-coated polymer substrates with high reproducibility and photothermal stability. *Sensors Actuators B Chem.* 354, 131110. doi:10.1016/j.snb.2021.131110

Spitzberg, J. D., Zrehen, A., van Kooten, X. F., and Meller, A. (2019). Plasmonic-nanopore biosensors for superior single-molecule detection. *Adv. Mater* 31 (23), e1900422. Epub 20190403. doi:10.1002/adma.201900422

Sun, Y., Yin, Y., Mayers, B. T., Herricks, T., and Xia, Y. (2002). Uniform silver nanowires synthesis by reducing Agno3 with ethylene glycol in the presence of seeds and poly(vinyl pyrrolidone). *Chem. Mater.* 14 (11), 4736–4745. doi:10.1021/cm020587b

Szmacinski, H., Ray, K., and Lakowicz, J. R. (2009). Effect of plasmonic nanostructures and nanofilms on fluorescence resonance energy transfer. *J. Biophot.* 2 (4), 243–252. doi:10.1002/jbio.200910003

Tang, L., Li, T., Luo, Y., Feng, S., Cai, Z., Zhang, H., et al. (2020). Vertical chemical vapor deposition growth of highly uniform 2d transition metal dichalcogenides. *ACS Nano* 14 (4), 4646–4653. Epub 20200417. doi:10.1021/acsnano.0c00296

Tawa, K., and Knoll, W. (2004). Mismatching base-pair dependence of the kinetics of DNA-DNA hybridization studied by surface plasmon fluorescence spectroscopy. *Nucleic Acids Res.* 32 (8), 2372–2377. Epub 20040428. doi:10.1093/nar/gkh572

Tian, S., Neumann, O., McClain, M. J., Yang, X., Zhou, L., Zhang, C., et al. (2017). Aluminum nanocrystals: a sustainable substrate for quantitative sers-based DNA detection. *Nano Lett.* 17 (8), 5071–5077. doi:10.1021/acs.nanolett.7b02338

Toma, K., Vala, M., Adam, P., Homola, J., Knoll, W., and Dostalek, J. (2013). Compact surface plasmon-enhanced fluorescence biochip. *Opt. Express* 21 (8), 10121–10132. doi:10.1364/OE.21.010121

Vareiro, M. M., Liu, J., Knoll, W., Zak, K., Williams, D., and Jenkins, A. T. (2005). Surface plasmon fluorescence measurements of human chorionic gonadotrophin: role of antibody orientation in obtaining enhanced sensitivity and limit of detection. *Anal. Chem.* 77 (8), 2426–2431. doi:10.1021/ac0482460

Vestler, D., Shishkin, I., Gurvitz, E. A., Nasir, M. E., Ben-Moshe, A., Slobozhanyuk, A. P., et al. (2018). Circular dichroism enhancement in plasmonic nanorod metamaterials. *Opt. Express* 26, 17841. doi:10.1364/oe.26.017841

Vietz, C., Kaminska, I., Sanz, P. M., Tinnefeld, P., and Acuna, G. P. (2017). Broadband fluorescence enhancement with self-assembled silver nanoparticle optical antennas. *ACS Nano* 11 (5), 4969–4975. doi:10.1021/acsnano.7b01621

Wang, H., Chen, L., Shen, X., Zhu, L., He, J., and Chen, H. (2012). Unconventional chain-growth mode in the assembly of colloidal gold nanoparticles. *Angew. Chem. Int. Ed. Engl.* 51 (32), 8021–8025. Epub 20120718. doi:10.1002/anie.201203088

Wang, H.-M., Huang, X.-Q., Wang, A.-J., Luo, X., Liu, W.-D., Yuan, P.-X., et al. (2020a). Construction of efficient "on-off-on" fluorescence aptasensor for ultrasensitive detection of prostate specific antigen via covalent energy transfer between G-C3n4 quantum dots and palladium triangular plates. *Anal. Chim. Acta* 1104, 53–59. doi:10.1016/j.aca.2020.01.009

Wang, P., Huh, J.-H., Park, H., Yang, D., Zhang, Y., Zhang, Y., et al. (2020b). DNA origami guided self-assembly of plasmonic polymers with robust long-range plasmonic resonance. *Nano Lett.* 20 (12), 8926–8932. doi:10.1021/acs.nanolett.0c04055

Wang, Y., Su, Q., Chen, C. H., Yu, M. L., Han, G. J., Wang, G. Q., et al. (2010). Low temperature growth of vanadium pentoxide nanomaterials by chemical vapour deposition using vo(acac)2 as precursor. *J. Phys. D Appl. Phys.* 43 (18), 185102. doi:10.1088/0022-3727/43/18/185102

Wei, Q., Acuna, G., Kim, S., Vietz, C., Tseng, D., Chae, J., et al. (2017). Plasmonics enhanced smartphone fluorescence microscopy. *Sci. Rep.* 7 (1), 2124. doi:10.1038/s41598-017-02395-8

Wurtz, G. A., Pollard, R., Hendren, W., Wiederrecht, G. P., Gosztola, D. J., Podolskiy, V. A., et al. (2011). Designed ultrafast optical nonlinearity in a plasmonic nanorod metamaterial enhanced by nonlocality. *Nat. Nanotechnol.* 6, 107–111. doi:10.1038/nnano.2010.278

Xu, W., Wang, L., Zhang, R., Sun, X., Huang, L., Su, H., et al. (2020). Diagnosis and prognosis of myocardial infarction on a plasmonic chip. *Nat. Commun.* 11 (1), 1654. Epub 20200403. doi:10.1038/s41467-020-15487-3

Yang, X., Su, D., Yu, X., Zeng, P., Liang, H., Zhang, G., et al. (2023). Hot spot engineering in hierarchical plasmonic nanostructures. *Small* 19 (22), 2205659. doi:10.1002/smll.202205659

Yeltik, A., Guzelturk, B., Hernandez-Martinez, P. L., Govorov, A. O., and Demir, H. V. (2013). Phonon-assisted exciton transfer into silicon using nanoemitters: the role of Phonons and temperature effects in förster resonance energy transfer. *ACS Nano* 7 (12), 10492–10501. doi:10.1021/nn404627p

Yoshida, A., Uchida, N., and Kometani, N. (2009). Synthesis and spectroscopic studies of composite gold nanorods with a double-shell structure composed of spacer and cyanine dye J-aggregate layers. *Langmuir* 25 (19), 11802–11807. doi:10.1021/la901431r

You, P.-Y., Li, F.-C., Liu, M.-H., and Chan, Y.-H. (2019). Colorimetric and fluorescent dual-mode immunoassay based on plasmon-enhanced fluorescence of polymer dots for detection of psa in whole blood. *ACS Appl. Mater. Interfaces* 11 (10), 9841–9849. doi:10.1021/acsami.9b00204

Yuan, H., Khatua, S., Zijlstra, P., Yorulmaz, M., and Orrit, M. (2013). Thousand-Fold enhancement of single-molecule fluorescence near a single gold nanorod. *Angew. Chem. Int. Ed.* 52 (4), 1217–1221. doi:10.1002/anie.201208125

Zhang, B., Kumar, R. B., Dai, H., and Feldman, B. J. (2014). A plasmonic chip for biomarker discovery and diagnosis of type 1 diabetes. *Nat. Med.* 20 (8), 948–953. doi:10.1038/nm.3619

Zhang, L., Lu, X., Sun, J., Wang, C., and Dong, P. (2024). Insights into the plasmonic "hot spots" and efficient hot electron injection induced by Ag nanoparticles in a covalent organic framework for photocatalytic H2 evolution. *J. Mater. Chem. A* 12 (9), 5392–5405. doi:10.1039/D3TA06724F

Zhang, L., Wang, L., He, S., Zhu, C., Gong, Z., Zhang, Y., et al. (2023). High-performance organic electrochemical transistor based on photo-annealed plasmonic gold nanoparticle-doped pedot:pss. *ACS Appl. Mater Interfaces* 15 (2), 3224–3234. Epub 20230109. doi:10.1021/acsami.2c19867

Zhang, T., Gao, N., Li, S., Lang, M. J., and Xu, Q.-H. (2015). Single-particle spectroscopic study on fluorescence enhancement by plasmon coupled gold nanorod dimers assembled on DNA origami. *J. Phys. Chem. Lett.* 6 (11), 2043–2049. doi:10.1021/acs.jpclett.5b00747

Zhao, F., Zeng, J., Parvez Arnob, M. M., Sun, P., Qi, J., Motwani, P., et al. (2014). Monolithic npg nanoparticles with large surface area, tunable plasmonics, and high-density internal hot-spots. *Nanoscale* 6 (14), 8199–8207. doi:10.1039/C4NR01645A

Zheng, J., Cheng, X., Zhang, H., Bai, X., Ai, R., Shao, L., et al. (2021). Gold nanorods: the most versatile plasmonic nanoparticles. *Chem. Rev.* 121 (21), 13342–13453. doi:10.1021/acs.chemrev.1c00422

Zheng, P., Liang, L., Arora, S., Ray, K., Semancik, S., and Barman, I. (2023). Pyramidal hyperbolic metasurfaces enhance spontaneous emission of nitrogen-vacancy centers in nanodiamond. *Adv. Opt. Mater.* 11 (6), 2202548. doi:10.1002/adom.202202548

frontiers | Frontiers in Chemistry

TYPE Original Research
PUBLISHED 20 August 2024
DOI 10.3389/fchem.2024.1460224

OPEN ACCESS

EDITED BY
Guangjiu Zhao,
Tianjin University, China

REVIEWED BY
Jun Chen,
Chinese Academy of Sciences (CAS), China
Somnath Bhowmick,
The Cyprus Institute, Cyprus

*CORRESPONDENCE
Wensheng Bian,
bian@iccas.ac.cn

RECEIVED 05 July 2024
ACCEPTED 05 August 2024
PUBLISHED 20 August 2024

CITATION
Li D, Fayyaz F and Bian W (2024) A theoretical study on excited-state dynamical properties and laser cooling of zinc monohydride including spin-orbit couplings.
Front. Chem. 12:1460224.
doi: 10.3389/fchem.2024.1460224

A theoretical study on excited-state dynamical properties and laser cooling of zinc monohydride including spin-orbit couplings

Donghui Li[1], Faiza Fayyaz[1,2] and Wensheng Bian[1,2]*

[1]Beijing National Laboratory for Molecular Sciences, Institute of Chemistry, Chinese Academy of Sciences, Beijing, China, [2]School of Chemical Sciences, University of Chinese Academy of Sciences, Beijing, China

By means of highly accurate *ab initio* and dynamical calculations, we identify a suitable laser cooling candidate that contains a transition metal element, namely zinc monohydride (ZnH). The internally contracted multireference configuration interaction method is employed to compute the five lowest-lying Λ-S states of ZnH with the spin-orbit coupling effects included, and very good agreement is obtained between our calculated and experimental spectroscopic data. Our findings show that the position of crossing point of the $A^2\Pi$ and $B^2\Sigma^+$ states of ZnH is above the $v' = 2$ vibrational level of the $A^2\Pi$ state indicating that the crossings with higher electronic states will have no effect on laser cooling. Hence, we construct a feasible laser-cooling scheme for ZnH using five lasers based on the $A^2\Pi_{1/2} \rightarrow X^2\Sigma^+_{1/2}$ transition, which features a large vibrational branching ratio R_{00} (0.8458), a large number of scattered photons (9.8×10^3) and an extremely short radiative lifetime (64 ns). The present work demonstrates the importance of electronic state crossings and spin-orbit couplings in the study of molecular laser cooling.

KEYWORDS

electronic state crossing, vibrational branching ratio, ultracold molecule, *ab initio*, spin-orbit coupling

1 Introduction

In recent years, it has attracted great research interests to establish more promising laser cooling candidates owing to their importance for a lot of potential applications such as precision measurements, quantum information storage and quantum computers (Hudson et al., 2011; Yan et al., 2013; Baron et al., 2014). Around a decade ago, the SrF molecules were successfully cooled to the micro-kelvin level using the direct laser cooling method (Shuman et al., 2010), and after that much research in molecular laser cooling has been initiated. However, so far only a few kinds of diatomic molecules have been experimentally cooled to the ultracold regime. Therefore, it is of considerable interests in searching for more promising candidates for laser cooling, and theoretical calculations could play an important role (Wells and Lane, 2011; Fu et al., 2017; Cao et al., 2019; Moussa et al., 2021; Xia et al., 2021). There are three criteria for laser cooling candidates that are generally recognized (Di Rosa, 2004): a highly diagonal Franck-Condon factor (FCF) matrix, a very short radiative lifetime, and no interference from intermediate states. In addition, Bian (Li

et al., 2020) recently proposed the fourth criterion for molecular laser cooling, that is, no electronic-state crossing, or the crossing point between the two electronic states is high enough in energy relative to the ground vibrational level. Therefore, when searching for molecular candidates, all electronic states that are close to those selected for the cooling scheme should be computed and checked in advance.

Research on the spectroscopic investigation of ZnH has been ongoing since 1923, when Hulthen observed and analysed the $A^2\Pi \rightarrow X^2\Sigma^+$ transition of ZnH for the first time (Hulthen, 1923). Forty years later, there has been extensive progress in the determination of electronic states of ZnH such as $C^2\Sigma^+ \rightarrow X^2\Sigma^+$ transition was observed and analysed by M.A. Khan (Khan, 1962) in 1962. Balfour and co-workers (Balfour et al., 1986) investigated $B^2\Sigma^+ \rightarrow X^2\Sigma^+$ transition using high resolution photographic spectroscopy and reported the approximate FCFs for this transition in 1986. Moreover, ZnH remained a subject of FTIR and rotational spectroscopy. Hence, Shayesteh et al. (Shayesteh et al., 2006) measured the high resolution infrared emission spectra of ZnH in 2006 and Bucchino et al. (Bucchino and Ziurys, 2013) recorded pure rotational spectra, including the $N = 0 \rightarrow 1$ and $N = 1 \rightarrow 2$ (here N represents the rotational energy levels) transitions, for the ground state of ZnH in 2013. Bucchino and co-workers also determined the fine structure and hyperfine constants, including the Fermi contact, dipolar, and electric quadrupole parameters of Zn nuclei. Subsequently, Abbasi et al. (Abbasi and Shayesteh, 2017) detected the high-resolution emission spectra of the $A^2\Pi \rightarrow X^2\Sigma^+$ and $B^2\Sigma^+ \rightarrow X^2\Sigma^+$ transitions for ZnH using a Fourier transform spectrometer in 2017. They obtained the Dunham coefficients, empirical band constants, and determined the purely electronic matrix elements.

Apart from experiments, ZnH has been of great interest to theoretical and computational scientists. Such as, in 1967, the spin-orbit coupling (SOC) constant of the $A^2\Pi$ state was computed for ZnH by means of the self-consistent field molecular orbital (SCF MO) theory (Ishiguro and Kobori, 1967). In 1994, Jamorski applied an averaged relativistic effective Hamiltonian method to get the spectroscopic constants of four Λ-S states and corresponding Ω states of ZnH (Jamorski et al., 1994). On the other hand, in 2009, Hayashi and co-workers (Hayashi et al., 2009) did *ab initio* study for the low-lying electronic states of ZnH and ZnH^+. They used highly accurate multireference configuration interaction (MRCI) method with the Davidson correction (+Q) and calculated the spectroscopic constants for the bound states. Likewise, in 2017 Zhao et al. (2017) applied internally contracted MRCI+Q (icMRCI + Q) method and obtained the PECs of the seven lowest-lying Λ-S states and corresponding Ω states of ZnH. Moreover, they estimated radiative lifetimes, calculated FCFs for many transitions as well as reported the spectroscopic constants of five bound Λ-S and corresponding Ω states.

So far, as far as we know, there have not been any theoretical investigations reported on laser cooling of ZnH. In this work, by means of highly accurate *ab initio* and dynamical calculations including the SOC effects, we identify a suitable molecular candidate for laser cooling, which can fulfil the known criteria of molecular laser cooling including the fourth one proposed in our recent work. The paper is organized as follows. Section 2 briefly describes the theoretical methods and computational details. In Section 3, we discuss our calculated results, underscoring the importance of electronic state crossings and SOCs on laser cooling, and construct a feasible laser cooling scheme for ZnH. The conclusions are presented in Section 4.

2 Methods and computational details

In this paper, all the *ab initio* calculations of ZnH are carried out in the C_{2v} point group with the MOLPRO 2015.1 program package (Werner et al., 2015). The potential energies of the five Λ-S states of ZnH are computed with the complete active space self-consistent field (CASSCF) (Werner and Knowles, 1985) method. The seven-state averaged CASSCF calculations are performed for the orbital optimization, using the HF orbitals as the starting guess. Then, these CASSCF energies are taken as the reference to compute the energies of each electronic state by the icMRCI + Q method. (Langhoff and Davidson, 1974). The electrons in the 3s and 3p orbitals of the Zn atom are not included in the active space, so the core correlation on Zn is not considered in this work. It is well-known that the selection of a reasonable active space plays a crucial role in the CASSCF and MRCI + Q calculations (Liu et al., 2009; Yu and Bian, 2011; Yu and Bian, 2012). The active space of ZnH is denoted as CAS (3e, 6o) including the Zn 4s4p5s and H 1s orbitals. The outer virtual orbitals are added to give a better description on the dissociation behavior, particularly for excited electronic states (Shen et al., 2017). As for basis sets, we use the aug-cc-pwCV5Z-DK basis sets for Zn and H (Dunning and Peterson, 2000; van Mourik et al., 2000). Moreover, the SOC effects are considered by means of the state interaction approach with the Breit-Pauli Hamiltonian (H_{BP}) in the SOC calculations (Berning et al., 2000), indicating that the SO eigenstates are acquired by diagonalizing $\hat{H}_{el} + \hat{H}_{SO}$ in the basis of eigenfunctions of $\hat{H}_{el}$. Additionally, the $\hat{H}_{SO}$ and $\hat{H}_{el}$ are derived from the icMRCI + Q computations.

The Einstein spontaneous emission coefficient ($A_{v'v}$) from the higher-energy state (v', J') to the lower-energy state (v, J) can be determined with the expression (Herzberg, 1950):

$$A_{v'v} = 3.1361891 \times 10^{-7} \frac{S(J',J)}{2J'+1} \Delta E_{v',v}^{\ 3} \left| \langle \Psi_{v',J'} | M(r) | \Psi_{v,J} \rangle \right|^2 \quad (1)$$

Whereas $A_{v'v}$ is expressed in units of s^{-1}, $S(J', J)$ is represented in the Hönl-London rotational intensity factor, $\Delta E_{v',v}$ is the energy difference in cm^{-1} unit, $\Psi_{v,J}$ and $\Psi_{v',J'}$ are the unit normalized radial wave functions, and $M(r)$ is the transition dipole function in Debye unit, v and J are vibrational and rotational levels of the lower-energy state, respectively, and v' and J' are vibrational and rotational levels of the higher-energy state, respectively.

The $R_{v'v}$ can be determined by the following expression:

$$R_{v'v} = A_{v'v} \Big/ \sum_{v} A_{v'v} \quad (2)$$

For a given vibrational level v' of an excited state, the radiative lifetime ($\tau_{v'}$) can be evaluated with the following expression:

$$T_{Doppler} = h/(4k_B \pi \tau) \quad (3)$$

The Doppler temperature ($T_{Doppler}$) which is the minimum temperature with the Doppler method for the translational

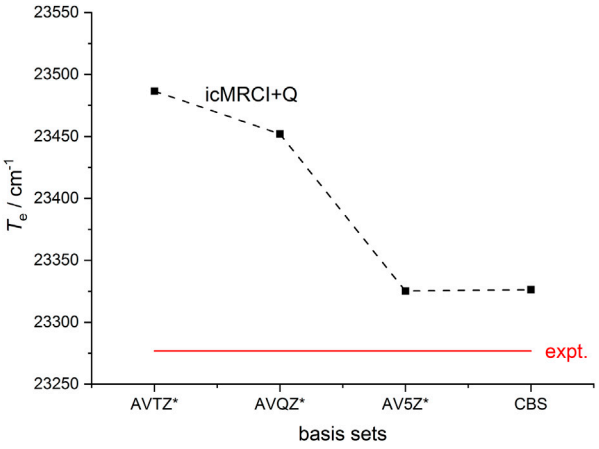

FIGURE 1
The convergence pattern of the adiabatic relative electronic energy relative to the ground state (T_e) of the $A^2\Pi$ state for ZnH toward the estimated complete basis set (CBS) limit using the icMRCI(3e, 6o) + Q method with the AVnZ* (n = T, Q, 5) basis sets. AVnZ* represents aug-cc-pwCVTZ-DK, aug-cc-pwCVQZ-DK and aug-cc-pwCV5Z-DK respectively. The corresponding experimental value (Huber and Herzberg, 1979) is also shown.

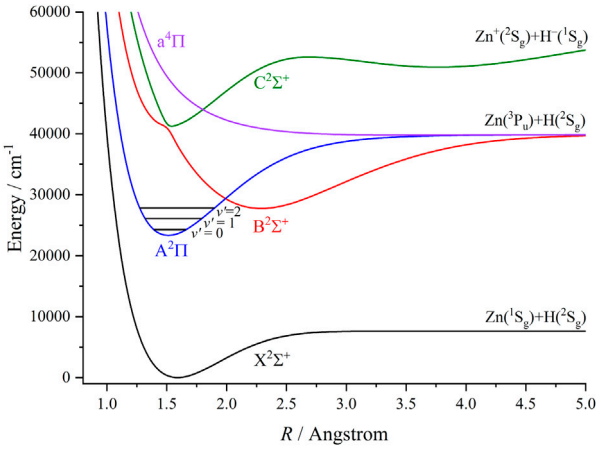

FIGURE 2
Potential energy curves of ZnH as a function of the interatomic distance (R) for the five lowest-lying Λ-S states at the icMRCI + Q level.

cooling, can be determined with the following expression: (Fu et al., 2017):

$$T_{recoil} = h^2 / (mk_B\lambda^2) \quad (4)$$

where h and k_B are Planck′s and Boltzmann′s constants, respectively, and τ is the radiative lifetime of the excited state.

The recoil temperature ($T_{Doppler}$) can be determined with the following expression: (Li et al., 2019):

$$\tau_{v'} = 1 / \sum_{v} A_{v'v} \quad (5)$$

where m is the relative molecular mass and λ is the laser wavelength λ_{00}.

For the bound Λ-S and Ω states of ZnH, We use the LEVEL 8.0 program (Le Roy, 2017) to determine the $A_{v'v}$, FCFs, and the spectroscopic constants including the equilibrium bond length (R_e), adiabatic relative electronic energy referred to the ground state (T_e), the harmonic and anharmonic vibrational frequencies (ω_e and $\omega_e\chi_e$), dissociation energy (D_e) and the rotational constant (B_e).

3 Results and discussion

3.1 PECs and molecular spectroscopic constants

The icMRCI + Q calculations are carried out to check the convergence of the computed results with distinct basis sets (the aug-cc-pwCVTZ-DK, aug-cc-pwCVQZ-DK and aug-cc-pwCV5Z-DK basis sets are denoted as AVTZ, AVQZ and AV5Z, respectively), and the calculated T_e results of the $A^2\Pi$ state are shown in Figure 1. Here the complete basis set (CBS) energy is evaluated by a three-point extrapolation scheme. (Peterson et al., 1994; Koput and Peterson, 2002; Peterson and Dunning, 2002). The plotted curve in Figure 1 indicates that the result obtained by the AV5Z (aug-cc-pwCV5Z-DK) basis sets is very close to the CBS result, and in very good agreement with the experimental value. (Huber and Herzberg, 1979). We conclude that the aug-cc-pwCV5Z-DK basis set is large enough and thus is used for further calculations in this work. Figure 2 depicts the PECs of the five lowest-lying Λ-S electronic states of ZnH, derived from the icMRCI + Q calculations. As can be seen, the ground state $X^2\Sigma^+$ converges towards the lowest neutral atomic Zn (^1S_g) + H (^2S_g) limit, while the $A^2\Pi$, $B^2\Sigma^+$ and $a^4\Pi$ states correlate with the Zn (^3P_u) + H (^2S_g) limit. Additionally, the $C^2\Sigma^+$ state corresponds to the $Zn^+(^2S_g)$ + $H^-(^1S_g)$ limit. In this work the $A^2\Pi$ state is used to establish laser cooling cycles for ZnH, and thus we did not consider much higher excited states (e.g., the $1^4\Sigma^+$ state), which will not influence our discussion. As the values of spectroscopic constants for the low-lying bound states of ZnH are already determined experimentally and reported in literature, we compared our computed results with these data that could verify the accuracy and reliability of our calculations. Table 1 provides a comparison of our computed and already available spectroscopic constants values of the three bound Λ-S states of ZnH. For the first excited state $A^2\Pi$, the experimentally determined value (Huber and Herzberg, 1979) is 23276.9 cm^{-1} whereas our computed value is 23325.25 cm^{-1}, using larger basis set. In contrast, the previously computed value (Zhao et al., 2017) at smaller basis sets (aug-cc-pwCVTZ-DK) is 23469 cm^{-1}, deviated from experimental value by approximately 190 cm^{-1}. Furthermore, our computed spectroscopic constants, i.e., R_e, ω_e, $\omega_e\chi_e$ and B_e values of the $A^2\Pi$ state and R_e, ω_e, $\omega_e\chi_e$, D_e and B_e values of the ground state $X^2\Sigma^+$ are very close to the experimental values (Huber and Herzberg, 1979). Moreover, our computed R_e, ω_e, $\omega_e\chi_e$ and B_e values of the $B^2\Sigma^+$ state are highly consistent to the measurements (Huber and Herzberg, 1979). Over all, it can be seen that our results align very well with the experimental data (Huber and Herzberg, 1979), though the deviation in the T_e value for the $B^2\Sigma^+$ between our calculated data and the experimental result is slightly larger than

TABLE 1 Spectroscopic constants of the three Λ-S states for ZnH.

State	Method	T_e (cm^{-1})	R_e (Å)	ω_e (cm^{-1})	$\omega_e\chi_e$ (cm^{-1})	D_e (eV)	B_e (cm^{-1})
$X^2\Sigma^+$	This work	0	1.592	1603.27	53.57	0.9420	6.7054
	Expt.[a]	0	1.5949	1607.6	55.14	0.91	6.6794
	Calc.[b]	0	1.5926	1600	51.11		6.7026
$A^2\Pi$	This work	23325.25	1.512	1907.25	41.14	2.0488	7.4279
	Expt.[a]	23276.9	1.5119	1910.2	40.8		7.4332
	Calc.[b]	23469	1.514	1903	40.57	2.02	7.4129
$B^2\Sigma^+$	This work	27740.86	2.290	1018.27	16.43	1.4308	3.2450
	Expt.[a]	27587.7	2.273	1020.7	16.5	1.40	3.288
	Calc.[b]	27584.15	2.293	1006	16.62	1.42	3.2323

[a]Reference (Huber and Herzberg, 1979).
[b]Reference (Zhao et al., 2017).

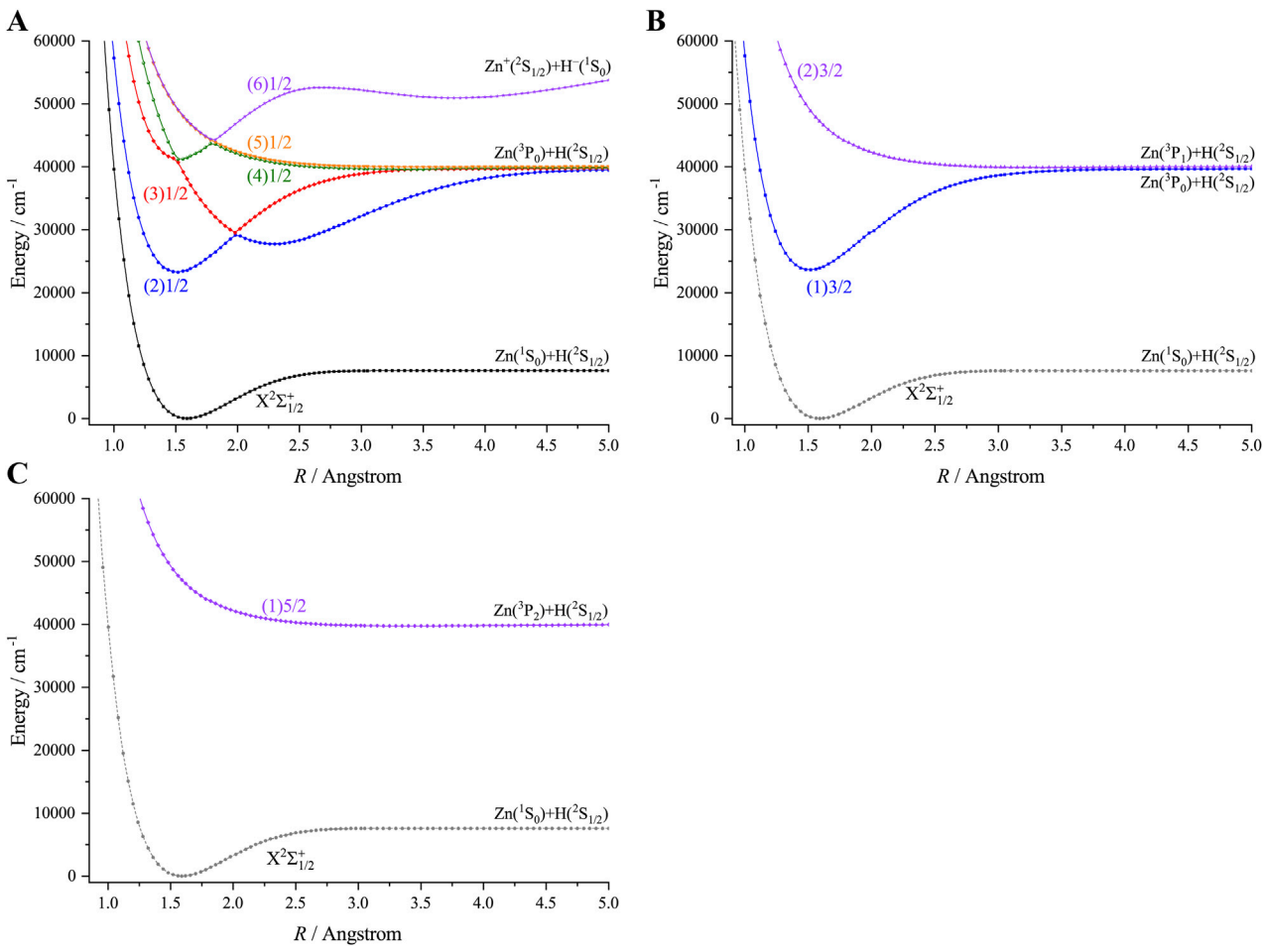

FIGURE 3
Potential energy curves of ZnH as a function of the interatomic distance (R) for **(A)** Ω = 1/2, **(B)** Ω = 3/2 and **(C)** Ω = 5/2 at the icMRCI + Q level.

that from the previous calculations (Zhao et al., 2017). It is worth noting that accurate determination of the T_e value for the $A^2\Pi$ state plays a pivotal role in obtaining the laser wavelengths for laser-driven cycling. In this regard, our calculated T_e values match well with corresponding experimental results, raising the confidence to further investigate laser cooling of ZnH.

TABLE 2 Spectroscopic constants of the 4 Ω states for ZnH.

State	Method	T_e (cm^{-1})	R_e (Å)	ω_e (cm^{-1})	$\omega_e\chi_e$ (cm^{-1})	D_e (eV)	B_e (cm^{-1})
$X^2\Sigma^+_{1/2}$	This work	0	1.592	1602.24	53.68	0.9422	6.7065
	Expt.[a]	0	1.5949	1607.6	55.14	0.91	6.6794
	Calc.[b]	0	1.5926	1600	51.05		6.7030
$A^2\Pi_{1/2}$	This work	23280.05	1.512	1909.69	41.27	2.0425	7.4317
	Expt.[a]	23276.9	1.5119	1910.2	40.8		7.4332
	Calc.[b]	23390.07	1.5135	1911	44.1	1.94	7.4179
$A^2\Pi_{3/2}$	This work	23611.89	1.512	1909.55	41.02	1.9917	7.4271
	Calc.[b]	23632.03	1.5141	1902	40.5	1.97	7.4096
$B^2\Sigma^+_{1/2}$	This work	27739.10	2.290	1018.35	16.47	1.4219	3.2447
	Expt.[a]	27587.7	2.273	1020.7	16.5	1.40	3.288
	Calc.[b]	27584.15					

[a]Reference (Huber and Herzberg, 1979).
[b]Reference (Zhao et al., 2017).

Inclusion of the SOC effects has resulted in the splitting of five Λ-S states ($X^2\Sigma^+$, $A^2\Pi$, $B^2\Sigma^+$, $C^2\Sigma^+$ and $a^4\Pi$) of ZnH into 9 Ω states, of which 6 states have Ω = 1/2 ($X^2\Sigma^+_{1/2}$, $A^2\Pi_{1/2}$, $B^2\Sigma^+_{1/2}$, $C^2\Sigma^+_{1/2}$, $a^4\Pi_{1/2}$ and (2) $a^4\Pi_{1/2}$), two states have Ω = 3/2 ($A^2\Pi_{3/2}$ and $a^4\Pi_{3/2}$), and one state has Ω = 5/2 ($a^4\Pi_{5/2}$). The PECs of the 9 Ω states of ZnH are depicted in Figure 3. The spectroscopic constants of the 4 Ω states of ZnH, namely, $X^2\Sigma^+_{1/2}$, $A^2\Pi_{1/2}$, $A^2\Pi_{3/2}$ and $B^2\Sigma^+_{1/2}$, are presented in Table 2. As can be seen, the spectroscopic constants of the 2 Ω states $X^2\Sigma^+_{1/2}$ and $B^2\Sigma^+_{1/2}$ are very close to those of Λ-S states of ZnH. In addition, our calculated SO splitting value of the $A^2\Pi$ state (331.84 cm^{-1}) is in very good agreement with the experimental value (Huber and Herzberg, 1979) (342.66 cm^{-1}) and outperforms the previous theoretical result (Zhao et al., 2017) (241.96 cm^{-1}). It is evident that SO splitting value of the $A^2\Pi$ state is relatively large and indicates that the SOC effects should be considered while studying the excited states of ZnH. Hence, SOC effects are important for laser cooling of ZnH.

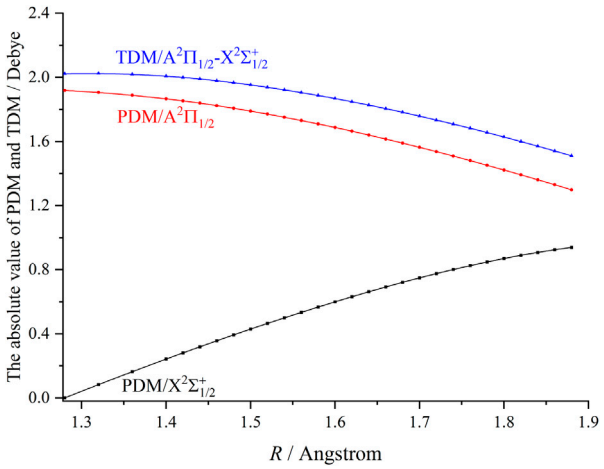

FIGURE 4
The computed permanent dipole moments (PDMs) and transition dipole moments (TDMs) for the $X^2\Sigma^+_{1/2}$ and $A^2\Pi_{1/2}$ states of ZnH at the icMRCI + Q level.

3.2 The effects of the electronic state crossings and spin-orbit couplings

From Figure 2, we can see that the $A^2\Pi$ and $B^2\Sigma^+$ states of ZnH have a crossing point, which can lead to nonradiative transition (Wu et al., 2019), and result in predissociation. It is evident that, for polyatomic molecules, this type of electronic state crossings will become potential energy surface intersections (Liu et al., 2003; Zhao et al., 2006). We can see that the location of crossing point between the $A^2\Pi$ and $B^2\Sigma^+$ states of ZnH is above the $v' = 2$ vibrational level of the $A^2\Pi$ state (1540 cm^{-1}) indicating that the crossings with higher electronic states will not affect laser cooling. With the inclusion of the SOC effects, the $A^2\Pi$ state will split into two states ($A^2\Pi_{1/2}$ and $A^2\Pi_{3/2}$), and the potential energy of the $A^2\Pi_{1/2}$ state is a little lower than that of $A^2\Pi_{3/2}$. Thus we will use the $A^2\Pi_{1/2} \rightarrow X^2\Sigma^+_{1/2}$ transition to construct a laser cooling scheme for ZnH. Consequently, hereafter, a feasible laser cooling scheme for ZnH is constructed on the basis of the $A^2\Pi_{1/2} \rightarrow X^2\Sigma^+_{1/2}$ transition, which meets the known criteria including the fourth one proposed in our recent work (Li et al., 2020).

3.3 Laser cooling scheme proposed for ZnH using specific spin-orbit states

Given the significance of the SOC effects as demonstrated above, we construct a laser cooling scheme for ZnH based on the $A^2\Pi_{1/2} \rightarrow X^2\Sigma^+_{1/2}$ transition, which is free from interference by any intermediate state. In this scheme, ZnH molecules are initially excited from the $X^2\Sigma^+_{1/2}$ ($v = 0$) state to the $A^2\Pi_{1/2}$ ($v' = 0$) state, then they decay back to the $X^2\Sigma^+_{1/2}$ state. This will generate ultracold ZnH molecules when the cooling cycles are consistently repeated.

10.3389/fchem.2024.1460224

TABLE 3 Calculated Einstein A coefficients $A_{\nu'\nu}$ and vibrational branching ratio $R_{\nu'\nu}$ of the $A^2\Pi_{1/2}$ (ν') → $X^2\Sigma^+_{1/2}$ (ν) transition for ZnH.

	$\nu' = 0$		$\nu' = 1$		$\nu' = 2$	
	$A_{\nu'\nu}$	$R_{\nu'\nu}$	$A_{\nu'\nu}$	$R_{\nu'\nu}$	$A_{\nu'\nu}$	$R_{\nu'\nu}$
$\nu = 0$	1.32×10^7	0.8458	2.35×10^6	1.55×10^{-2}	8.23×10^4	5.80×10^{-3}
$\nu = 1$	2.11×10^6	1.35×10^{-1}	8.19×10^6	0.5419	4.16×10^6	2.93×10^{-1}
$\nu = 2$	2.59×10^5	1.66×10^{-2}	3.58×10^6	2.37×10^{-1}	3.89×10^6	2.74×10^{-1}
$\nu = 3$	3.28×10^4	2.10×10^{-3}	7.95×10^5	5.26×10^{-2}	4.03×10^6	2.84×10^{-1}

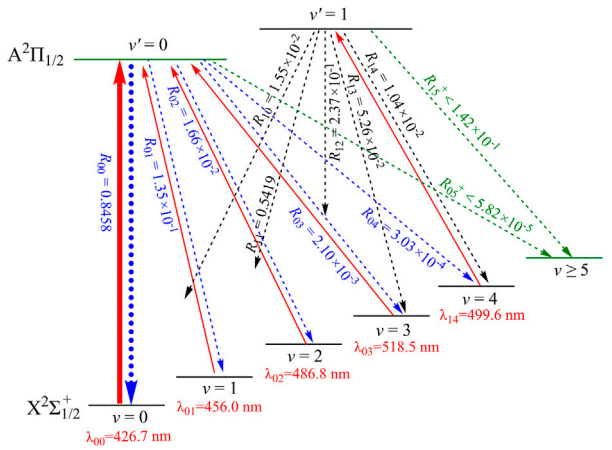

FIGURE 5
Constructed five-laser cooling scheme for ZnH using the $A^2\Pi_{1/2}$ (ν') → $X^2\Sigma^+_{1/2}$ (ν) transitions. Solid arrows indicate laser-driven transitions at certain wavelengths $\lambda_{\nu'\nu}$. Dashed arrows indicate spontaneous decays from the $A^2\Pi_{1/2}$ (ν' = 0, 1) states with the calculated vibrational branching ratios.

Figure 4 presents the permanent dipole moments (PDMs) and transition dipole moments (TDMs) for the $A^2\Pi_{1/2} \rightarrow X^2\Sigma^+_{1/2}$ transition of ZnH at the icMRCI + Q level. As can be seen, the TDMs of ZnH gradually decrease with the increasing bond length, reaching 1.88 debye at R_e. In addition, our computed FCF ($f_{\nu'\nu}$) value of the $A^2\Pi_{1/2}$ ($\nu' = 0$) → $X^2\Sigma^+_{1/2}$ ($\nu = 0$) transition (or the f_{00} value) for ZnH is 0.8367. This relatively large f_{00} value indicates that the spontaneous decays to ν = 1–4 vibrational levels of the $X^2\Sigma^+_{1/2}$ state are highly suppressed. Based on the $A^2\Pi_{1/2} \rightarrow X^2\Sigma^+_{1/2}$ transition, we use the ν' = 0, 1 levels of the $A^2\Pi_{1/2}$ state of ZnH with five lasers to establish laser cooling scheme. Furthermore, we have computed and tabulated the Einstein A coefficients ($A_{\nu'\nu}$, Equation 1) and vibrational branching ratios ($R_{\nu'\nu}$, Equation 2) values of the $A^2\Pi_{1/2} \rightarrow X^2\Sigma^+_{1/2}$ transition (see Table 3), since the relative strengths of photon loss channels are directly linked to the $R_{\nu'\nu}$ rather than the $f_{\nu'\nu}$ in laser cooling process. A very large A_{00} value of 1.32×10^7 s^{-1} and very minimal scattering probabilities into off-diagonal bands provide favourable conditions for rapid and efficient laser cooling cycles.

In addition, the evaluated Doppler and recoil temperatures ($T_{Doppler}$ and T_{recoil} can be evaluated with the Equations 3 and 4, respectively) for the $A^2\Pi_{1/2}$ ($\nu' = 0$) → $X^2\Sigma^+_{1/2}$ ($\nu = 0$) transition of ZnH are 59.73 μK and 1.59 μK, respectively. The computed radiative lifetime ($\tau_{\nu'}$, Equation 5) for the main cooling transition of ZnH is 64 ns, which is extremely short and ensures a rapid laser cooling process.

Our constructed five-laser cooling scheme for the production of ultracold ZnH is depicted in Figure 5. As illustrated, the laser wavelength for the main cycling will drive the $X^2\Sigma^+_{1/2}$ (ν = 0, J = 1) → $A^2\Pi_{1/2}$ (ν' = 0, J' = 0) transition of ZnH at the wavelength λ_{00} of 426.7 nm (here J means the rotational quantum number). According to the angular momentum and parity selection rules, the $A^2\Pi_{1/2}$ (ν' = 0, J' = 0) state can only decay back to the initial $X^2\Sigma^+_{1/2}$ (ν = 0, J = 1) state, thereby eliminating rotational branching. Additionally, to minimize vibrational branching losses, another 4 repump lasers are employed to recover the molecules that have decayed to the $X^2\Sigma^+_{1/2}$ (ν = 1, 2, 3, 4) states of ZnH. Consequently, quasi-closed cooling cycles could be achieved using the constructed cooling scheme as presented in Figure 5. Furthermore, the calculated R_{00} value of ZnH is 0.8458, indicating that the $A^2\Pi_{1/2}$ ($\nu' = 0$) → $X^2\Sigma^+_{1/2}$ ($\nu = 0$) transition of ZnH has the largest possibility, whereas the vibrational branching loss should be solved in laser cooling cycle process. Thus the off-diagonal $R_{\nu'\nu}$ of ZnH are also computed. In addition, we use $R_{05^+} + R_{04} \times R_{15^+}$ (here 5^+ means $\nu \geq$ 5 levels) to access the possibilities of the undesirable decay paths for ZnH. The negligible value of 1.01×10^{-4} indicates that following the present cooling scheme, ZnH on average, can scatter at least 9.8×10^3 photons, which are sufficient for cooling ZnH to ultracold temperatures, in principle (Shuman et al., 2010). In our constructed five-laser cooling scheme for ZnH, the $X^2\Sigma^+_{1/2}$ (ν = 0) → $A^2\Pi_{1/2}$ (ν' = 0) transition is the main pump. While the $X^2\Sigma^+_{1/2}$ (ν = 1, 2, 3) → $A^2\Pi_{1/2}$ (ν' = 0) and $X^2\Sigma^+_{1/2}$ (ν = 4) → $A^2\Pi_{1/2}$ (ν' = 1) transitions are the secondary vibrational repumps. In the constructed laser-driven cycling for ZnH, all the calculated laser wavelengths fall in the visible range, making them readily accessible.

4 Conclusions

In this work, the five lowest-lying Λ-S states of ZnH are investigated by means of highly accurate *ab initio* and dynamical calculations including the SOC effects. Our computational results agree very well with experimental spectroscopic data. In addition, we study direct laser cooling of ZnH, and reveal the effects of electronic state crossings and SOC. Our calculations indicate that ZnH is a suitable candidate for laser cooling, which can fulfil the known criteria including the fourth one proposed in our recent work. The position of crossing point between the $A^2\Pi$ and $B^2\Sigma^+$ states of ZnH is higher than the $\nu' = 2$ vibrational level of the $A^2\Pi$ state indicating that the crossings with higher electronic states will not affect the laser cooling. Hence, we construct a practical laser-

cooling scheme for ZnH based on the $A^2\Pi_{1/2} \rightarrow X^2\Sigma^+_{1/2}$ transition. Our calculated excitation energy to the $A^2\Pi$ state of ZnH is 23325.25 cm^{-1}, which closely matches with the experimental value of 23276.9 cm^{-1} [38]. This enables us to determine laser wavelengths in laser-cooling cycles accurately. The Doppler and recoil temperatures for the main transition of ZnH are 59.73 μK and 1.59 μK, respectively. The vibrational branching ratios ($R_{v'v}$) for the $A^2\Pi_{1/2}$ ($v' = 0$) $\rightarrow X^2\Sigma^+_{1/2}$ transition of ZnH are shown to be diagonally distributed with R_{00} being 0.8458. The radiative lifetime for the $A^2\Pi_{1/2}$ ($v' = 0$) $\rightarrow X^2\Sigma^+_{1/2}$ ($v = 0$) transition of ZnH is extremely short (64 ns). The present constructed scheme is able to scatter 9.8×10^3 photons for ZnH, which are sufficient for cooling ZnH to ultracold temperatures. It is expected that this theoretical study will encourage for the experimental laser cooling of ZnH to ultracold temperatures.

Data availability statement

The original contributions presented in the study are included in the article/supplementary material, further inquiries can be directed to the corresponding author.

Author contributions

DL: Conceptualization, Data curation, Formal analysis, Investigation, Writing–original draft, Writing–review and editing. FF: Writing–original draft, Validation, Writing–review and editing. WB: Conceptualization, Formal analysis, Funding acquisition, Investigation, Resources, Supervision, Validation, Writing–review and editing.

Funding

The author(s) declare that financial support was received for the research, authorship, and/or publication of this article. This work was supported by the National Natural Science Foundation of China (Nos. 22320102004, 21773251) and the Junior Fellow Program of Beijing National Laboratory for Molecular Science (No. 2022BMS20096).

Conflict of interest

The authors declare that the research was conducted in the absence of any commercial or financial relationships that could be construed as a potential conflict of interest.

Publisher's note

All claims expressed in this article are solely those of the authors and do not necessarily represent those of their affiliated organizations, or those of the publisher, the editors and the reviewers. Any product that may be evaluated in this article, or claim that may be made by its manufacturer, is not guaranteed or endorsed by the publisher.

References

Abbasi, M., and Shayesteh, A. (2017). Fourier transform emission spectra and deperturbation analysis of the $A^2\Pi \rightarrow X^2\Sigma^+$ and $B^2\Sigma^+ \rightarrow X^2\Sigma^+$ electronic transitions of ZnH. *J. Mol. Spectrosc.* 340, 21–28. doi:10.1016/j.jms.2017.07.012

Balfour, W. J., Chandrasekhar, K. S., and Lindgren, B. (1986). The $B^2\Sigma^+$ state of zinc deuteride. *J. Mol. Spectrosc.* 119, 126–136. doi:10.1016/0022-2852(86)90207-9

Baron, J., Campbell, W. C., DeMille, D., Doyle, J. M., Gabrielse, G., Gurevich, Y. V., et al. (2014). Order of magnitude smaller limit on the electric dipole moment of the electron. *Science* 343, 269–272. doi:10.1126/science.1248213

Berning, A., Schweizer, M., Werner, H.-J., Knowles, P. J., and Palmieri, P. (2000). Spin-orbit matrix elements for internally contracted multireference configuration interaction wavefunctions. *Mol. Phys.* 98, 1823–1833. doi:10.1080/00268970009483386

Bucchino, M. P., and Ziurys, L. M. (2013). Terahertz spectroscopy of ^{25}MgH ($X^2\Sigma^+$) and ^{67}ZnH ($X^2\Sigma^+$): bonding in simple metal hydrides. *J. Phys. Chem. A* 117, 9732–9737. doi:10.1021/jp3123743

Cao, J., Li, F., Xia, W., and Bian, W. (2019). van der Waals interactions in bimolecular reactions. *Chin. J. Chem. Phys.* 32, 157–166. doi:10.1063/1674-0068/cjcp1901007

Di Rosa, M. D. (2004). Laser-cooling molecules: concept, candidates, and supporting hyperfine-resolved measurements of rotational lines in the A-X (0,0) band of CaH. *Eur. Phys. J. D* 31, 395–402. doi:10.1140/epjd/e2004-00167-2

Dunning, T. H., and Peterson, K. A. (2000). Approximating the basis set dependence of coupled cluster calculations: evaluation of perturbation theory approximations for stable molecules. *J. Chem. Phys.* 113, 7799–7808. doi:10.1063/1.1316041

Fu, M., Ma, H., Cao, J., and Bian, W. (2017). Laser cooling of CaBr molecules and production of ultracold Br atoms: a theoretical study including spin-orbit coupling. *J. Chem. Phys.* 146, 134309. doi:10.1063/1.4979566

Hayashi, S., Leonard, C., and Chambaud, G. (2009). *Ab initio* study of HZnF. *J. Phys. Chem. A* 113, 14615–14624. doi:10.1021/jp9043607

Herzberg, G. (1950). *Spectra of diatomic molecules*. second ed. New York: Van Nostrand Reinhold.

Huber, K. P., and Herzberg, G. (1979). *Molecular spectra and molecular structure IV: constants of diatomic molecules*. New York: NY: Van Nostrand Reinhold.

Hudson, J. J., Kara, D. M., Smallman, I. J., Sauer, B. E., Tarbutt, M. R., and Hinds, E. A. (2011). Improved measurement of the shape of the electron. *Nature* 473, 493–496. doi:10.1038/nature10104

Hulthen, E. (1923). Dissertation: University of Lund.

Ishiguro, E., and Kobori, M. (1967). Spin orbit coupling constants in simple diatomic molecules. *J. Phys. Soc. Jpn.* 22, 263–270. doi:10.1143/jpsj.22.263

Jamorski, C., Dargelos, A., Teichteil, C., and Daudey, J. P. (1994). Theoretical determination of spectral lines for the Zn atom and the ZnH molecule. *J. Chem. Phys.* 100, 917–925. doi:10.1063/1.466574

Khan, M. A. (1962). New band systems of ZnH and ZnD in the far ultra-violet region. *Proc. Phys. Soc. Lond.* 80, 599–607. doi:10.1088/0370-1328/80/3/303

Koput, J., and Peterson, K. A. (2002). *Ab initio* potential energy surface and vibrational-rotational energy levels of $X^2\Sigma^+$ CaOH. *J. Phys. Chem. A* 106, 9595–9599. doi:10.1021/jp026283u

Langhoff, S. R., and Davidson, E. R. (1974). Configuration interaction calculations on the nitrogen molecule. *Int. J. Quantum Chem.* 8, 61–72. doi:10.1002/qua.560080106

Le Roy, R. J. (2017). LEVEL: a computer program for solving the radial Schrödinger equation for bound and quasibound levels. *J. Qual. Spectrosc. Radiat. Transfer* 186, 167–178.

Li, D., Fu, M., Ma, H., Bian, W., Du, Z., and Chen, C. (2020). A theoretical study on laser cooling feasibility of group IVA hydrides XH (X = Si, Ge, Sn, and Pb): the role of electronic state crossing. *Front. Chem.* 8, 20. doi:10.3389/fchem.2020.00020

Li, R., Yuan, X., Liang, G., Wu, Y., Wang, J., and Yan, B. (2019). Laser cooling of the SiO^+ molecular ion: a theoretical contribution. *Chem. Phys.* 525, 110412. doi:10.1016/j.chemphys.2019.110412

Liu, C., Zhang, D., and Bian, W. (2003). Theoretical investigation of the reaction of Co^+ with OCS. *J. Phys. Chem. A* 107, 8618–8622. doi:10.1021/jp034693s

Liu, K., Yu, L., and Bian, W. (2009). Extensive theoretical study on various low-lying electronic states of silicon monochloride cation including spin-orbit coupling. *J. Phys. Chem. A* 113, 1678–1685. doi:10.1021/jp809618y

Moussa, A., El-Kork, N., and Korek, M. (2021). Laser cooling and electronic structure studies of CaK and its ions $CaK^{\pm}$. *New J. Phys.* 23, 013017. doi:10.1088/1367-2630/abd50d

Peterson, K. A., and Dunning, T. H. (2002). Accurate correlation consistent basis sets for molecular core-valence correlation effects: the second row atoms Al-Ar, and the first row atoms B-Ne revisited. *J. Chem. Phys.* 117, 10548–10560. doi:10.1063/1.1520138

Peterson, K. A., Woon, D. E., and Dunning, T. H., Jr. (1994). Benchmark calculations with correlated molecular wave functions. IV. The classical barrier height of the H + H_2 → H_2 + H reaction. *J. Chem. Phys.* 100, 7410–7415. doi:10.1063/1.466884

Shayesteh, A., Le Roy, R. J., Varberg, T. D., and Bernath, P. F. (2006). Multi-isotopologue analyses of new vibration-rotation and pure rotation spectra of ZnH and CdH. *J. Mol. Spectrosc.* 237, 87–96. doi:10.1016/j.jms.2006.03.004

Shen, Z., Ma, H., Zhang, C., Fu, M., Wu, Y., Bian, W., et al. (2017). Dynamical importance of van der Waals saddle and excited potential surface in C(^1D) + D_2 complex-forming reaction. *Nat. Commun.* 8, 14094. doi:10.1038/ncomms14094

Shuman, E. S., Barry, J. F., and DeMille, D. (2010). Laser cooling of a diatomic molecule. *Nature* 467, 820–823. doi:10.1038/nature09443

van Mourik, T., Dunning, T. H., and Peterson, K. A. (2000). *Ab initio* characterization of the HCO^x (x = -1, 0, +1) species: structures, vibrational frequencies, CH bond dissociation energies, and HCO ionization potential and electron affinity. *J. Phys. Chem. A* 104, 2287–2293. doi:10.1021/jp9925583

Wells, N., and Lane, I. C. (2011). Electronic states and spin-forbidden cooling transitions of AlH and AlF. *Phys. Chem. Chem. Phys.* 13, 19018–19025. doi:10.1039/c1cp21313j

Werner, H.-J., and Knowles, P. J. (1985). A second order multiconfiguration SCF procedure with optimum convergence. *J. Chem. Phys.* 82, 5053–5063. doi:10.1063/1.448627

Werner, H.-J., Knowles, P. J., Lindh, R., Manby, F. R., Schütz, M., Celani, P., et al. (2015). Molpro, Version 2015.1, A package of *ab initio* programs. Available at: http://www.molpro.net.

Wu, Y., Cao, J., Ma, H., Zhang, C., Bian, W., Nunez-Reyes, D., et al. (2019). Conical intersection-regulated intermediates in bimolecular reactions: insights from C(^1D) + HD dynamics. *Sci. Adv.* 5, eaaw0446. doi:10.1126/sciadv.aaw0446

Xia, W., Ma, H., and Bian, W. (2021). Production of ultracold CaCCH and SrCCH molecules by direct laser cooling: a theoretical study based on accurate *ab initio* calculations. *J. Chem. Phys.* 155, 204304. doi:10.1063/5.0072013

Yan, B., Moses, S. A., Gadway, B., Covey, J. P., Hazzard, K. R. A., Rey, A. M., et al. (2013). Observation of dipolar spin-exchange interactions with lattice-confined polar molecules. *Nature* 501, 521–525. doi:10.1038/nature12483

Yu, L., and Bian, W. (2011). Extensive theoretical study on electronically excited states and predissociation mechanisms of sulfur monoxide including spin-orbit coupling. *J. Comput. Chem.* 32, 1577–1588. doi:10.1002/jcc.21737

Yu, L., and Bian, W. (2012). Electronically excited-state properties and predissociation mechanisms of phosphorus monofluoride: a theoretical study including spin-orbit coupling. *J. Chem. Phys.* 137, 014313. doi:10.1063/1.4731635

Zhao, H., Bian, W., and Liu, K. (2006). A theoretical study of the reaction of O(^{3}P) with isobutene. *J. Phys. Chem. A* 110, 7858–7866. doi:10.1021/jp060583k

Zhao, S., Liang, G., Li, R., Li, Q., Zhang, Z., and Yan, B. (2017). Theoretical study on the electronic structure and transition properties of excited state of ZnH molecule. *Acta Phys. Sin.* 66, 063103. doi:10.7498/aps.66.063103

frontiers | Frontiers in Chemistry

TYPE Original Research
PUBLISHED 23 September 2024
DOI 10.3389/fchem.2024.1474820

OPEN ACCESS

EDITED BY
Xianglei Kong,
Nankai University, China

REVIEWED BY
Andreas Türler,
University of Bern, Switzerland
Christian Tantardini,
UiT The Arctic University of Norway, Norway
Susanta Lahiri,
Saha Institute of Nuclear Physics (SINP), India

*CORRESPONDENCE
A. Yakushev,
a.yakushev@gsi.de

RECEIVED 02 August 2024
ACCEPTED 06 September 2024
PUBLISHED 23 September 2024

CITATION
Yakushev A, Khuyagbaatar J, Düllmann CE, Block M, Cantemir RA, Cox DM, Dietzel D, Giacoppo F, Hrabar Y, Iliaš M, Jäger E, Krier J, Krupp D, Kurz N, Lens L, Löchner S, Mokry C, Mošať P, Pershina V, Raeder S, Rudolph D, Runke J, Sarmiento LG, Schausten B, Scherer U, Thörle-Pospiech P, Trautmann N, Wegrzecki M and Wieczorek P (2024) Manifestation of relativistic effects in the chemical properties of nihonium and moscovium revealed by gas chromatography studies.
Front. Chem. 12:1474820.
doi: 10.3389/fchem.2024.1474820

Manifestation of relativistic effects in the chemical properties of nihonium and moscovium revealed by gas chromatography studies

A. Yakushev[1,2]*, J. Khuyagbaatar[1,2], Ch. E. Düllmann[1,2,3], M. Block[1,2,3], R. A. Cantemir[1], D. M. Cox[4], D. Dietzel[1,3], F. Giacoppo[1,2], Y. Hrabar[4], M. Iliaš[1,2], E. Jäger[1], J. Krier[1], D. Krupp[5], N. Kurz[1], L. Lens[5], S. Löchner[1], Ch. Mokry[2,3], P. Mošať[1], V. Pershina[1], S. Raeder[1], D. Rudolph[4], J. Runke[1,3], L. G. Sarmiento[4], B. Schausten[1], U. Scherer[5], P. Thörle-Pospiech[2,3], N. Trautmann[3], M. Wegrzecki[6] and P. Wieczorek[1]

[1]GSI Helmholtzzentrum für Schwerionenforschung, Darmstadt, Germany, [2]Helmholtz-Institut Mainz, Mainz, Germany, [3]Department of Chemistry, Johannes Gutenberg-Universität Mainz, Mainz, Germany, [4]Department of Physics, Lund University, Lund, Sweden, [5]Hochschule Mannheim, Mannheim, Germany, [6]Łukasiewicz - Instytut Mikroelektroniki i Fotoniki, Warsaw, Poland

Chemical reactivity of the superheavy elements nihonium (Nh, element 113) and moscovium (Mc, element 115) has been studied by the gas-solid chromatography method using a new combined chromatography and detection setup. The Mc isotope, ^{288}Mc, was produced in the nuclear fusion reaction of ^{48}Ca ions with ^{243}Am targets at the GSI Helmholtzzentrum Darmstadt, Germany. After isolating ^{288}Mc ions in the gas-filled separator TASCA, adsorption of ^{288}Mc and its decay product ^{284}Nh on silicon oxide and gold surfaces was investigated. As a result of this work, the values of the adsorption enthalpy of Nh and Mc on the silicon oxide surface were determined for the first time, $-\Delta H_{ads}^{SiO_2}(\mathrm{Mc}) = 54^{+11}_{-5}$ kJ/mol and $-\Delta H_{ads}^{SiO_2}(\mathrm{Nh}) = 58^{+8}_{-3}$ kJ/mol (68% c.i.). The obtained $-\Delta H_{ads}$ values are in good agreement with results of advanced relativistic calculations. Both elements, Nh and Mc, were shown to interact more weakly with the silicon oxide surface than their lighter homologues Tl and Bi, respectively. However, Nh and Mc turned out to be more reactive than the neighbouring closed-shell and quasi-closed-shell elements copernicium (Cn, element 112) and flerovium (Fl, element 114), respectively. The established trend is explained by the influence of strong relativistic effects on the valence atomic orbitals of these elements.

KEYWORDS

superheavy element chemistry, element 113–nihonium, element 115–moscovium, gas phase chromatography, recoil separators

1 Introduction

1.1 Relativistic effects and periodicity trends in the superheavy element chemistry

Significant progress in the synthesis of the heaviest man-made chemical elements was achieved in the last decades resulting in the completion of the 7th row in the Periodic Table of the Elements (PTE) (Oganessian and Utyonkov, 2015). Due to decreasing nuclear fusion- and survival probabilities with increasing atomic number Z, the production rates of the superheavy elements (SHE) decrease rapidly, reaching a level of a single atom per month for oganesson (Og, element 118) (Oganessian and Utyonkov, 2015). The commonly used technique for SHE isolation is the kinematic separation in a recoil separator. The time between the production of a nuclear fusion reaction product in the target and its implantation as a recoil ion in the detection system is about 1 microsecond, allowing studies of nuclear decay properties of very short-lived isotopes. Experimental methods for chemical studies of SHE are more demanding and time-consuming, and therefore less efficient, especially for short-lived SHE isotopes. This makes studies of chemical properties more challenging (Türler and Pershina, 2013). Among the chemical techniques applied for SHE, a fast and efficient chemical separation can be achieved by gas-solid chromatography studies of volatile species (Türler and Pershina, 2013; Türler et al., 2015).

Chemical properties of yet unstudied SHE can be extrapolated based on the general law of periodicity, which connects the electronic structure of the elements with their position in the PTE. However, with increasing nuclear charge of the SHE, the influence of increasingly important relativistic effects on chemical properties has to be taken into account (Schwerdtfeger et al., 2020; Pyper, 2020; Pershina, 2019; Pershina, 2015). Apparently, the strong contraction of the s and $p_{1/2}$ atomic orbitals (AO) and a large spin-orbit (SO) splitting of the electron shells with the orbital angular momentum quantum number $l \geq 1$, can lead to properties different from those of their lighter homologues. Thus, reliable predictions of chemical properties of SHE become of extreme importance for the heaviest members of groups 12–18 (Schwerdtfeger et al., 2020; Pershina, 2019; Smits et al., 2024). Since the reactivity of atoms is generally connected to the energy level of their valence AO, relativistic calculations of the AO energy levels and of the first ionization potentials (IP) allow assessing the validity of trends within the groups of the PTE (Eliav et al., 2015; Borschevsky et al., 2015; Dzuba and Flambaum, 2016; Trombach et al., 2019). A strong relativistic stabilization of the spherical atomic orbitals with closed-shell $7s^2$ and quasi closed-shell $7p_{1/2}^2$ electronic configurations, together with the large spin-orbit splitting within the 7p shell were shown to result in low AO energies and large IP values for Cn and Fl, respectively (Schwerdtfeger et al., 2020; Pershina, 2015; Eliav et al., 2015). Accordingly, these elements were predicted to be the least reactive members of groups 12 and 14 (Pitzer, 1975; Schwerdtfeger and Seth, 2002). These predictions were recently confirmed experimentally (Eichler et al., 2007; Eichler et al., 2010; Yakushev et al., 2014; Yakushev and Eichler, 2016; Yakushev et al., 2022).

The neighbouring odd-Z elements nihonium (Nh, element 113) and moscovium (Mc, element 115) are presently in the focus of theoretical studies. Since Nh and Mc possess one unpaired electron in the $7p_{1/2}$ or $7p_{3/2}$ subshells, respectively, higher AO energies and lower IP values than for Cn and Fl are predicted for Nh and Mc. This implies that the reactivity of Nh and Mc is higher compared with that of their closed-shell neighbours Cn and Fl. Therefore, chemical reactivity, i.e., the tendency to form chemical bonds, is predicted to be higher for Nh and Mc than for Cn and Fl (Schwerdtfeger et al., 2020; Pershina, 2015; Trombach et al., 2019). However, experimental data on the reactivity of Nh and Mc are required to validate the predicted local minimum at Fl. Indeed, Nh and Mc are expected to form chemical compounds, e.g., hydroxides, which should adsorb more strongly on surfaces than pure atoms (Pershina et al., 2009; Pershina and Iliaš, 2019). Recently, motivated by experimental developments (Yakushev et al., 2021), the interaction of Nh and Mc with Au and quartz surfaces was studied on the basis of periodic relativistic density functional theory (DFT) calculations (Pershina, 2016; Pershina et al., 2021). As a result, equal values of the adsorption energy/enthalpy ($E_{ads} = -\Delta H_{ads}$) on quartz, of 58 kJ/mol, were predicted for elemental Nh and Mc (Pershina et al., 2021). Significantly (by about 100 kJ/mol) higher E_{ads} values were predicted for the adsorption of these elements on the Au (111) surface in several theoretical works (Trombach et al., 2019; Pershina, 2018; Rusakov et al., 2013; Fox-Beyer and van Wüllen, 2012). The obtained E_{ads} values for Nh and Mc turned out to be significantly (by about 50–100 kJ/mol) lower than those of their lighter homologues, Tl and Bi, respectively, on both types of the surfaces, quartz and Au. This is due to the strong relativistic stabilization of the $7p_{1/2}$ AO with respect to the $6p_{1/2}$ AO (Pershina, 2018; Pershina, 2016; Pershina et al., 2021). Thus, all the available predictions agree that both Nh and Mc should be more reactive than Cn and Fl and should easily adsorb at room temperature on Au, and also adsorb on less reactive quartz surfaces (Ilias and Pershina, 2022).

1.2 Experimental challenges and methods

The gas chromatography method has proven being efficient for chemical studies of SHE compared to methods applied for chemical studies in the liquid phase (Türler and Pershina, 2013; Türler et al., 2015). However, the overall efficiency of this method is drastically dependent on the volatility and chemical reactivity of the species under study. In chemistry experiments with the lighter SHE rutherfordium (Rf, element 104) to bohrium (Bh, element 107), the chemical separation was achieved by the combination of the gas-jet transport with gas-solid chromatography (Türler and Pershina, 2013; Türler et al., 2015). A rather low overall efficiency of this multi-step technique was compensated by the relatively high production rates (Türler and Pershina, 2013). A significantly higher overall efficiency was achieved in the chemical study of hassium (Hs, element 108), which was separated in the form of the volatile compound HsO_4 (Düllmann et al., 2002). This technique is based on the combination of gas-solid isothermal chromatography and thermochromatography with a detection system, i.e., by registration of the nuclear decay of a species adsorbed inside the chromatography column itself. The method was developed further during the past two decades, all along to the chemistry studies of the rather inert Cn and Fl (Eichler et al., 2007; Eichler et al., 2010; Yakushev et al., 2014; Yakushev and Eichler, 2016; Yakushev et al., 2022). The necessity of the spatial separation of the single volatile superheavy atoms from other volatile species that contain radionuclides with similar nuclear

decay properties as the nuclide under study and that are created in vastly larger amounts in the form of unwanted side products of the nuclear reactions was recognised (Düllmann et al., 2005). This includes especially Rn isotopes and their daughters. This separation is nowadays routinely achieved by employing physical preseparation in an electromagnetic recoil separator (Yakushev et al., 2014; Yakushev et al., 2022; Wittwer et al., 2010).

Several offline and online studies of the adsorption of Tl species on quartz and gold surfaces were performed, in which a stronger interaction of Tl with Au than with quartz was found (Serov et al., 2013; Steinegger et al., 2016; Lens et al., 2018). In thermochromatography studies under dry and oxygen-free conditions, as well as in the presence of hydrogen, the deposition of Tl on gold was observed at a temperature of about 900°C and was assigned to elemental Tl (Serov et al., 2013). However, independent of the chemical composition in the gas phase, the deposition of Tl on quartz at a temperature of about 300°C was ascribed to be due to TlOH formation caused by a high reactivity of Tl towards hydroxyl groups expected to be present on the quartz surface (Serov et al., 2013). Whereas initial experimental studies with homologues are usually performed in chromatography columns made of bulk materials like quartz (fused silica) or Au metal foils, SHE experiments are often conducted in channels made of silicon radiation detectors with thin hetero-layers covering the detector surfaces. Thin silicon oxide (SiO_2) or Au layers on silicon detectors are produced by oxidation or metal vapour deposition, respectively, and have poorly defined structures. These thin layers serve as reactive solid surface in the gas-solid chromatography process and are usually complex and differ from those used in most theoretical calculations on the adsorption of SHE.

For Cn and Fl, the focus of the chemical studies was on the interaction with Au surfaces (Eichler et al., 2007; Eichler et al., 2010; Yakushev et al., 2014; Yakushev and Eichler, 2016; Yakushev et al., 2022; Wittwer et al., 2010). In these experiments the adsorption enthalpy, $-\Delta H_{ads}^{Au}$, could be measured in a range of approximately 65–35 kJ/mol. Despite the limited number of observed Cn and Fl atoms, both elements were conclusively shown to exhibit high volatility and a rather low reactivity towards Au, characterizing them as volatile metals. In one specific experiment, a SiO_2-covered detector array was installed in front of the Au-covered ones. Neither Fl nor its decay product Cn adsorbed on this SiO_2 surface at room temperature (Yakushev et al., 2022). The low reactivity of Fl, which was confirmed experimentally in several experiments (Eichler et al., 2010; Yakushev et al., 2014; Yakushev and Eichler, 2016; Yakushev et al., 2022), is ascribed to the strong relativistic stabilization of the closed $7p_{1/2}$ subshell (Schwerdtfeger et al., 2020; Pyper, 2020; Pershina, 2019). In contrast to rather inert Cn and Fl, which can be transported as gaseous species to a chromatography and detection setup (Eichler et al., 2010; Yakushev et al., 2014; Yakushev and Eichler, 2016; Yakushev et al., 2022), Nh and Mc might not. This makes experimental studies of these expectedly more reactive elements even more challenging (Yakushev et al., 2021). In fact, the transport of the presumably less volatile Nh to a detection setup was found to be inefficient (likely due to adsorption losses) through a tube made from a material as inert as polytetrafluoroethylene (PTFE) (Yakushev et al., 2021).

The longest-lived known Mc and Nh isotopes can be produced directly or as decay products in nuclear fusion reactions of ^{48}Ca with ^{243}Am and ^{249}Bk targets, leading to the production of Mc and tennessine (Ts, element 117) isotopes, respectively (Oganessian and Utyonkov, 2015). The experimentally easiest access to Mc and Nh is via the nuclear fusion reaction ^{243}Am (^{48}Ca, 3n) ^{288}Mc, which has a high cross section of approximately 10–20 pb (Oganessian et al., 2013; Rudolph et al., 2013; Gates et al., 2015; Oganessian et al., 2022; Oganessian et al., 2022b), similar to that for ^{288}Fl produced in the reaction ^{244}Pu (^{48}Ca, 4n) ^{288}Fl (Düllmann et al., 2010; Såmark-Roth et al., 2023), which was successfully used in chemical studies (Eichler et al., 2010; Yakushev et al., 2014; Yakushev and Eichler, 2016; Yakushev et al., 2022). The decay properties of the members of the ^{288}Mc decay chain are rather well established based on more than two hundred observed decay chains (Oganessian et al., 2013; Rudolph et al., 2013; Gates et al., 2015; Oganessian et al., 2022; Oganessian et al., 2022b). The second member of the ^{288}Mc decay chain, ^{284}Nh, has a half-life of $T_{1/2} = 0.90^{+0.07}_{-0.06}$ s (Oganessian et al., 2022b), similar to those of the isotopes $^{287\text{-}289}$Fl, which were in the focus of recent chemical studies (Yakushev et al., 2021; Eichler, 2013; Dmitriev et al., 2014; Aksenov et al., 2017). However, its directly produced shorter-lived precursor, ^{288}Mc ($T_{1/2} = 193^{+15}_{-13}$ ms) (Oganessian et al., 2022b), was out of reach due to the short lifetime that elapses before the Mc atoms reach the combined chromatography and detection system. The observation of several decay chains originating from ^{284}Nh was claimed in early studies without physical pre-separation (Türler et al., 2015; Eichler, 2013; Dmitriev et al., 2014). The quality of the nuclear decay data in those works was limited by a rather high background in the α-particle spectra (Türler et al., 2015; Eichler, 2013; Dmitriev et al., 2014), which hampered the safe identification of decay chains (Türler et al., 2015; Yakushev et al., 2021). Two recent experiments employing preseparation were conducted behind the Dubna Gas-Filled Recoil Separator (DGFRS) (Akseneov et al., 2017), and behind the TransActinide Separator and Chemistry Apparatus (TASCA) (Yakushev et al., 2021). The low-background conditions led to a much higher sensitivity. However, no conclusive information on the chemical properties of Nh could be derived due to non-observation of ^{284}Nh events in these experiments (Yakushev et al., 2021; Aksenov et al., 2017). The non-observation of Nh atoms in the experiments with preseparation was explained by losses due to the irreversible adsorption of Nh atoms on surfaces they encountered prior to reaching the detection setup, indicating a rather high chemical reactivity of the Nh atoms (Yakushev et al., 2021; Aksenov et al., 2017). Thus, no conclusive and confirmed results on the chemical properties of Nh were obtained in the previous studies. This called for further developments of the experimental setup. Gas chromatography studies of reactive species came within reach by employing the newly developed miniCOMPACT detector array (Yakushev et al., 2021), as demonstrated in adsorption studies of the lighter homologue of Mc, ^{211}Bi[1] and short-lived radioisotopes of the very reactive Fr (Götz et al., 2021). This improved detection system is promising for studies of Nh and is proven to be fast enough to observe a relevant fraction of all produced ^{288}Mc.

1 Dietzel, D., Yakushev, A., Düllmann, Ch. E., Khuyagbaatar, J., Krier, J., Jäger, E., et al. (2024). Off-line single-atom gas chromatographic adsorption studies of ^{211}Bi on SiO_2 surfaces in the novel miniCOMPACT setup. *Submitt. Radiochim. Acta*. [under revision].

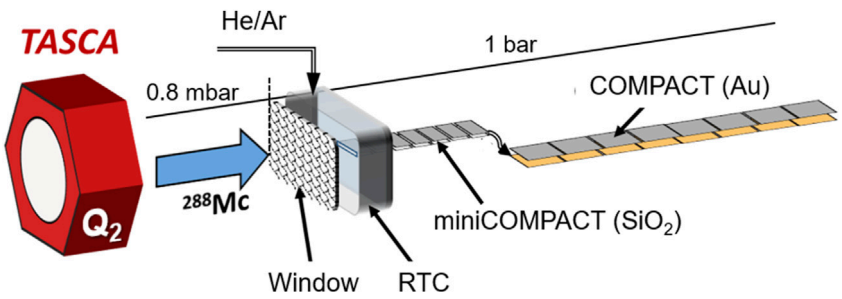

FIGURE 1
Experimental setup behind the second quadrupole (Q_2) at the end of the TASCA separator. Recoiling ^{288}Mc produced in the nuclear reaction were separated with TASCA and entered the Recoil Transfer Chamber (RTC) behind TASCA through a Mylar window. They were thermalized inside the RTC, the inner surface of which was covered with a Teflon™ layer and flushed out with a He/Ar gas mixture to the gas chromatography setup. The first gas chromatography and detection channel, miniCOMPACT, is connected directly to the RTC exit and covered with a SiO_2 layer. The second detector array COMPACT has an Au layer on the detector surface. Both detector arrays were operated at room temperature.

2 Materials and methods

2.1 Experimental setup

The nuclear reaction ^{243}Am (^{48}Ca, 3n)^{288}Mc, utilized for the discovery of element 115, Mc (Oganessian and Utyonkov, 2015), and for the detailed studies of the decay properties of the long α-decay chain starting from the isotope ^{288}Mc (Oganessian et al., 2013; Rudolph et al., 2013; Gates et al., 2015; Oganessian et al., 2022; Oganessian et al., 2022b), was also used for the present chemical studies of Mc and Nh. The gas-filled recoil separator TASCA (Semchenkov et al., 2008) was used to separate products of the fusion-evaporation reaction from the intense primary beam and from the unwanted products of multi-nucleon transfer reactions. The chemical reactivity of Mc and Nh was investigated applying the gas-solid chromatography method in the isothermal regime at room temperature (20°C) (Türler and Pershina, 2013; Türler et al., 2015) via adsorption studies on two surface types, SiO_2 and Au. The gas chromatography setup behind TASCA, as shown in Figure 1, was similar to that described in the first experiment on Nh chemistry at TASCA (Yakushev et al., 2021), except for the connecting tube between the Recoil Transfer Chamber (RTC) and the first detector array. The distance from the RTC gas volume to the first detector element was reduced to about 1 mm.

A pulsed (5 ms beam-on, 15 ms beam-off) $^{48}Ca^{10+}$ ion beam was provided by the UNIversal Linear ACcelerator (UNILAC) at GSI Darmstadt with a typical beam intensity of 5 10^{12} s^{-1}. The target wheel contained four $^{243}Am_2O_3$ targets and rotated with a speed of 2000 revolutions per second, synchronized with beam pulses (Jäger et al., 2014). The ^{243}Am targets with an average thickness of 0.83(1) mg/cm^2 were electro-deposited on 2.2(1) μm Ti foils (Runke et al., 2014). The beam energy in the middle of the ^{243}Am targets was 243.0(2) MeV. In total, 1.2(1) 10^{19} ^{48}Ca ions impinged on the targets during two experimental runs of 15 and 26 days duration, respectively. The evaporation residues were guided through the magnetic recoil separator TASCA with one dipole (D) and two quadrupole (Q) magnets in DQ_1Q_2 configuration, operated in the High-Transmission Mode (Semchenkov et al., 2008). TASCA was filled with He at a pressure of p_{He} = 0.8 mbar and was set to a magnetic rigidity of $B{\cdot}\rho$ = 2.21 Tm (Rudolph et al., 2013; Khuyagbaatar et al., 2012) to center ^{288}Mc recoils in the TASCA focal plane. The nominal transmission efficiency in TASCA to focus the recoiling ^{288}Mc ions into the RTC window area is about 40% (Yakushev et al., 2021). Products recoiling from the target and separated in TASCA according to their magnetic rigidities were thermalized in the RTC in a 1:1 gas mixture of He and Ar at 1 bar, similarly to the first Nh study at TASCA (Yakushev et al., 2021). Due to a large number of collisions with gas atoms, the isolated ions lose their kinetic energy, and their charge state is decreased accordingly to +1 or +2. The thermalized ions can be neutralized in gas by recombination or collisions with gas impurities or with any surface. The gas was circulated in a closed loop by a membrane pump at a flow rate of 2.9 L/min. The rare gases, He (99.9999%) and Ar (99.999%), were purified further by passing cartridges MC50-902FV and MC400-902FV (SAES™). These cartridges had internal particle filters, which efficiently remove aerosol particles with sizes down to 3 nm diameter and reduced the water and oxygen content to a level of about 1 ppm. The most critical impurity, water, was monitored by the dew point transmitter Pura (Michell Instruments). The isolated nuclear reaction products were flushed into the gas chromatography and detection setup. Two different detector channels were used, namely, a miniCOMPACT detector (Yakushev et al., 2021; Götz et al., 2021), followed by a COMPACT detector, used in the previous Fl chemistry studies at TASCA (Yakushev et al., 2014; Yakushev et al., 2022). The miniCOMPACT detector array was directly connected to the RTC via an exit slit with a cross section of (10.0 × 0.5) mm^2, fitting to the cross section of the miniCOMPACT channel, and allowing for an effective transport and detection of less-volatile species. As Nh and Mc should interact more strongly with gold than with quartz (Pershina et al., 2021), the silicon photodiodes of the miniCOMPACT detector array were covered with a 30–50 nm-thick SiO_2 layer. The photodiodes of the COMPACT detector array were covered with a 30 to 50 nm-thick Au layer. A 30-cm long capillary made of PTFE with an inner diameter of 2 mm connected the Au-covered COMPACT detector array to the miniCOMPACT array. Both detectors consisted of two panels, each divided into 32 detector elements. The opposite detector panels (top and bottom) were mounted with the active detector surfaces facing each other, and thus, forming a narrow gas channel with a distance between the opposite panels of 0.6 mm or 0.8 mm for the COMPACT array and the miniCOMPACT array, respectively. Each detector panel of the miniCOMPACT and COMPACT detectors consists of 32 Positive-Intrinsic-Negative (PIN) diodes mounted in a row (Wegrzecki et al., 2013). They registered α particles and fission

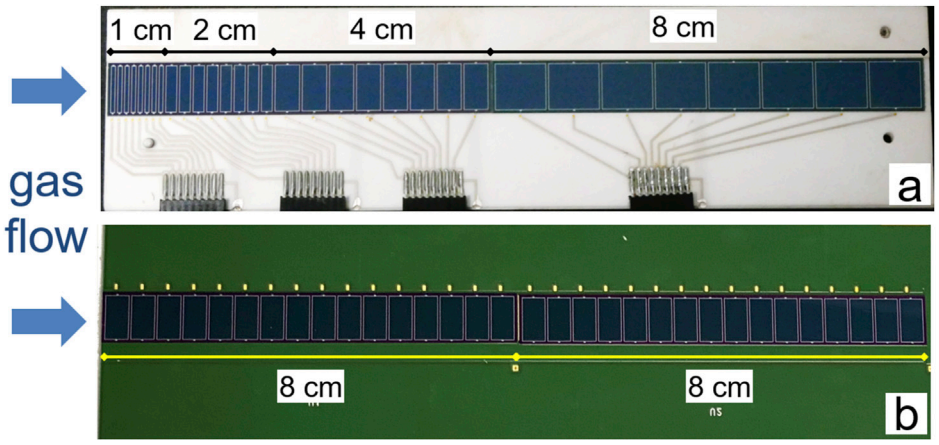

FIGURE 2
The open miniCOMPACT detector arrays. Only one of two detector panels forming the narrow channel is shown, as used in the first **(A)** and second experimental run **(B)**. The direction of the gas flow through the detector channel is indicated with arrows.

fragments emitted by nuclear decays occurring inside the detector channel. Two different segmentation geometries of the miniCOMPACT detector arrays were used in the first and the second run. In the first run, a 15-cm long miniCOMPACT array had differently-sized detector elements mounted on a ceramic printed circuit board (PCB) as shown in Figure 2A. Each detector panel consisted of two silicon chips, which were 7 cm and 8 cm long. The first 7-cm long silicon chip was divided into three eight-element groups. They were 1, 2, and 4 cm long. The following 8-cm long chip had eight equal detector elements. In the second run, a 16-cm long miniCOMPACT detector array was used. The panels of the second detector consisted of two equal, 8-cm long silicon chips, each divided into sixteen detector elements, and were mounted on a multilayer FR4 PCB (flame retarding printed circuit board) as shown in Figure 2B.

2.2 Method of calculation

Theoretical calculations accompany our experimental study. We have calculated electronic energies of gas-phase reactions that single metal atoms (M, where M = Bi and Mc) and singly-charged metal ions (M+) could undergo in the recoil chamber. The aim was to investigate a potential reactivity of Bi and Mc species towards water and oxygen, which are present as gas impurities at the trace level.

Our considered systems are SHE, which can only be treated appropriately when relativistic effects are explicitly taken into account in the calculations. A well-proven method for such work is the Density Functional Theory (DFT) approach (Hohenberg and Kohn, 1964). The theory underlying is the DFT is the self-consistent Kohn–Sham approach (Kohn and Sham, 1965). Kohn-Sham DFT is a first-principles computational method to predict accurately chemical properties and to analyse them in simple chemical terms. Specifically, the Kohn-Sham approach in general delivers correct electron densities and related properties, as well as the total energy, but implies a one-electron representation of the many-electron systems. Although the precise exchange-correlation (XC) functional is unknown, by using appropriate XC functionals, binding energies may typically be determined with a precision of a few kJ/mol (Te Velde et al., 2001). DFT keeps at all levels of approximation the appealing one-electron molecular orbital (MO) view on chemical reactions and properties. The computed orbitals are suitable for typical MO-theoretical analyses and interpretations. The Kohn-Sham method also effectively incorporates all correlation effects. The calculations of electronic structures of the molecules of interest were performed using the Density Functional Theory approach implemented in the AMS ADF software (SCM, 2024). The AMS electronic structure approach uses the zeroth order regular approximation (ZORA) two-component Hamiltonian incorporating both scalar relativistic (SR) and SO relativistic effects. Although the regular approximation is not gauge invariant at any order, the scaled ZORA energy is exactly gauge invariant for hydrogen ions. The scaled ZORA approach, as it was used in our ADF calculations, is nearly gauge-invariant for many-electron systems, as explained in detail in Ref. (Van Lenthe et al., 1994). Briefly, the scaled ZORA equation differs from the original ZORA equation by the denominator to introduce a scaling of the ZORA energy. The calculated scaled-ZORA total energies prove to be very close to the fully relativistic energies for atoms. For all-electron calculations, the original ZORA total energy cannot be used as it suffers from gauge invariance problems that are particularly serious for deep-core states. The scaled ZORA total energy solved this problem, delivering results within “chemical” accuracy. The same holds for two-component calculations with the SO ZORA Hamiltonian. The spin-polarized non-collinear approach, also called as Kramers unrestricted approach, was applied. The basis sets are a combination of numerical AOs and Slater-type orbitals (STOs). The used basis sets are of the Triple Zeta plus Double Polarization (TZ2P) size. These basis sets are well saturated and describe the polarization of the electron density of an atom in molecules. Since correlation effects are also very important for SHE systems and can contribute up to the 50% of the binding energy, those are taken into account by using XC functionals. We utilized the BP86 (Becke, 1988) exchange-correlation functional. The geometry optimizations of studied molecules were carried out with the SO ZORA Hamiltonian, ensuring that both SR and SO relativistic effects were reflected in the optimized molecular structures.

10.3389/fchem.2024.1474820

TABLE 1 Energies of α particles ($E_α$) and SF (E_{SF}) fragments[a] and time intervals (Δt) of the observed decay chain members and fission events without α-decaying precursors. The total time difference for decay chain members following missing ones are given in parentheses.

Chain number	^{288}Mc $E_α$, MeV	^{284}Nh $E_α$, MeV $Δt_1$, s	^{280}Rg $E_α$, MeV $Δt_2$, s	^{276}Mt $E_α$, MeV $Δt_3$, s	^{272}Bh $E_α$, MeV $Δt_4$, s	^{268}Db $E_{α/SF}$, MeV $Δt_5$, h	^{264}Lr E_{SF}, MeV $Δt_6$, h
1	**10.33**[b] –	**9.84**[c] 0.646	missing	**9.51** (22.86)	missing	**85 + n.d.**[d] (40.6)	
2	**10.22** –	missing	**9.32** (1.48)	missing	**8.98** (2.06)	**7.83** 9.5	**74 + 70** 4.7
3	missing	**9.25** –	**9.71** 3.33	9.76 0.515	**9.05** 7.43	**>64+>66**[e] 13.8	
4	missing	**9.79** –	9.70 9.22	**8.95** 0.289	**8.97** 3.27	**7.69** 24.2	98 + 110 6.4
5	missing	**9.88** –	**9.64** 3.69	9.51 0.938	**8.95** 50.13	93 + 116 43.4	
6	missing	**9.57** –	**9.69** 3.19	**9.56** 0.813	**8.91** 8.94	**112 + n.d**[d] 64.8	
7	missing	**9.47** –	**9.70** 0.813	**0.76**[f] 0.125	missing	**7.77** (14.3)	**117 + 66** 13.3
8	missing	**9.85** –	**9.04** 3.05	**9.59** 0.105	**9.04** 34.84	**7.82** 7.8	**49 + n.d** 12.9
9	missing	**9.86** –	9.53 0.253	**9.27** 0.125	**8.82** 8.39	**91 + 93**[g] 19.1	
10	**10.38** –	**9.44** 0.318	9.84 19.38	**9.47** 2.05	missing	n.d.[h]	
11	missing	**9.98** –	**9.72** 8.41	**9.45** 0.285	missing	n.d.[h]	
12	10.02 –	**9.84** 1.69	**9.72** 0.293	missing	**9.05** (3.93)	**116 + 86**[g] 37	
13	missing	9.92 –	**9.78** 1.93	**9.54** 0.084	8.07 5.76	**111 + 83**[g] 81.2	
14	missing	9.96 –	missing	**9.62** (92.68)	8.58 13.46	**83 + 89**[g] 30.1	
15	missing	**9.60** –	**9.68** 0.937	**9.44** 1.12	**9.06** 5.18	70 + 75[i] 8.9	
16	missing	**9.65** –	**9.61** 6.74	**9.24** 0.034	**8.84** 6.42	**87 + 103**[i] 43.7	
17	missing	**9.63** –	**9.58** 16.91	**9.37** 0.432	missing	**11 + 28**[i] 21.9	
18	missing	**9.75**	missing	**9.63** (0.551)	**9.08** 5.44	77 + n.d.[i,j] 31.8	

Fission events without α-decaying precursors				
SF 1	SF 2	SF 3	SF 4	SF 5
105 + n.d	104 + 113	91 + 70	99 + 93	99 + 22

[a]The SF fragment energy values were not corrected for the pulse height defect.
[b]The energy values of decay chain members, where decay occurred during the beam-off periods, are given in bold.
[c]The decays from decay chain members starting with ^{284}Nh occurred 4 mm downstream to the decay from ^{288}Mc.
[d]One SF fragment was not detected (n.d.) due to the not working opposite detector strip.
[e]This event occurred in the second Au-covered COMPACT detector. The full SF fragment energy could not be detected due to a high amplification gain of the preamps.
[f]A small energy signal was detected. This can be explained by α particle hitting mainly the inactive area of the detector.
[g]No candidates for α decay of ^{268}Db.
[h]SF events were not detected due to a technical problem with the data acquisition system lasted for several hours.
[i]Several candidates for the α decay were found. No unambiguous conclusion on α decay of ^{268}Db could be made.
[j]All signals were registered on the same detector side pointing at the deposition on the inactive surface of the opposite detector side.

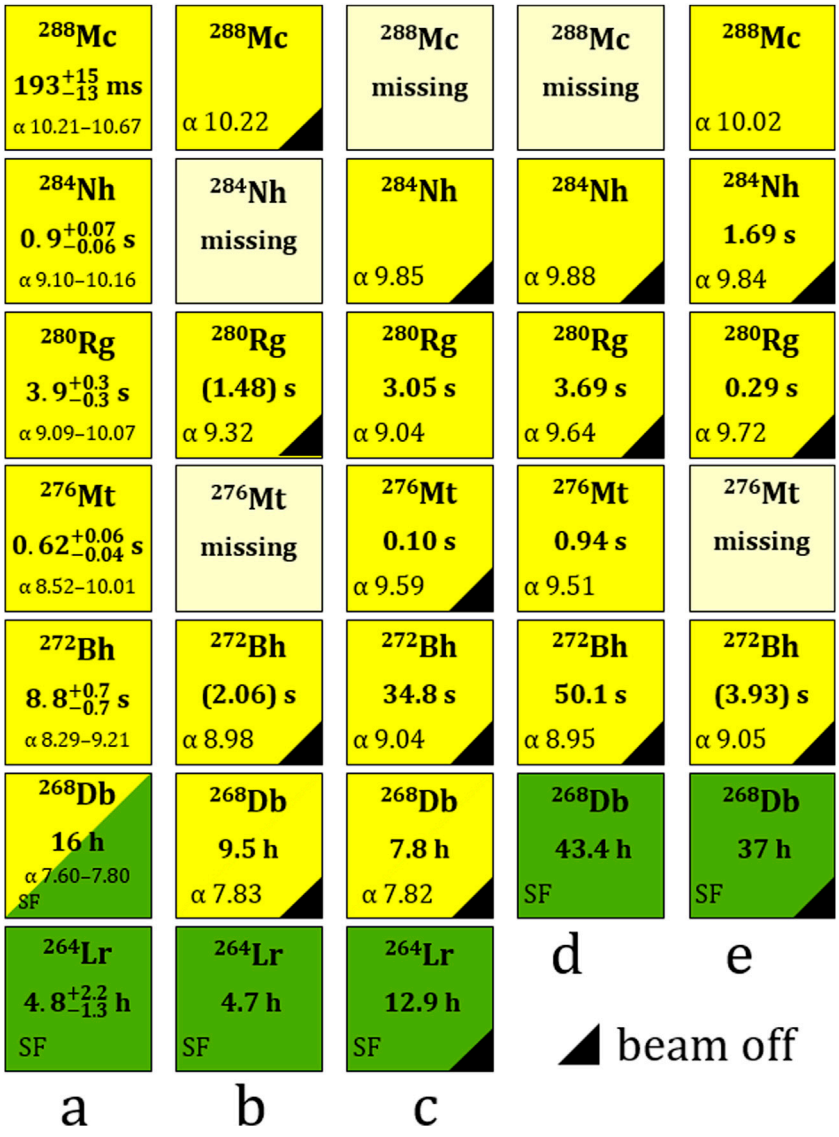

FIGURE 3
The decay properties of the ^{288}Mc-decay chain members. **(A)** The presently known decay properties along the long decay chain from ^{288}Mc are shown for comparison (Oganessian et al., 2022). **(B–E)** Four representative decay chains (#2, #8, #5, #12 in Table 1) out of eighteen observed in our experiments are shown. Color coding: α decay (yellow) and spontaneous fission (green). Half-lives **(A)** and correlation times **(B–E)** are indicated for decay chain members. The total time difference for decay chain members following missing ones are given in parentheses. The α-particle energies are given in mega electron volts (MeV). The black triangles represent the decays observed during beam-off periods.

3 Results

3.1 Observation of decay chains from ^{288}Mc and ^{284}Nh

A search for position- and time-correlated nuclear decay chains was performed, to identify multiple genetically-linked members of the well-known long ^{288}Mc decay chain, decaying by emission of α-particles within the energy interval (8.0–10.5) MeV and within a 200-s time interval. This search resulted in the finding of eighteen decay chains, seven in the first run and eleven in the second run. The decay chains were assigned to ^{288}Mc or to ^{284}Nh in accordance with their known decay properties (Oganessian et al., 2022; Oganessian et al., 2022b; Forsberg et al., 2016; Rudolph, 2022). As usual for such an experiment, where an atom is adsorbed on a detector surface inside a gas chromatography channel, α particles or fission fragments have to penetrate several inactive layers. They deposit a fraction of their kinetic energy in a SiO_2 or Au layer on top of the detector surface, and then in an inactive silicon layer on top of the diode. In addition, if the particles cross the detector channel, they experience further energy loss in the gas. These energy losses depend strongly on the angle to the surface, at which the particle is emitted. Thus, the energy distributions of registered α particles and spontaneous fission (SF) fragments have usually tailing towards low energies in contrast to the orresponding energy distributions registered in physics experiments, where the ions are implanted into

a silicon detector. The energy calibration of the detectors was performed using a ^{227}Ac source emanating ^{219}Rn, and was linearly extrapolated up to the fission fragment energies. Independently, the search for high-energy events with an energy of $E_{SF} > 20$ MeV was performed on a time scale of hours to days, to identify candidates for long-lived decay chain members terminating the decay chains by SF. In total, twenty-one candidate SF events were identified in the two runs. Sixteen SF events, twelve with two fragments and four with one fragment, occurred at the same detector positions, where chains with multiple α-decaying members were also detected, several hours before the SF events. These position-correlated SF events were assigned to the SF decay of ^{268}Db or ^{264}Lr (Oganessian et al., 2022). For two out of the eighteen registered decay chains, no terminating SF events were found, presumably due to a several-hour long problem with the data acquisition system in the period following the detection of these two chains. The decay parameters, energies and time intervals of the members of all observed decay chains are listed in Table 1. Figure 3 shows four representative examples (b–e) of observed chains, along with the reference decay chain (a).

Based on the decay properties along the long ^{288}Mc decay chain (Figure 3A), four out of eighteen chains were attributed to originate from ^{288}Mc (*cf.* Table 1). The missing observation of ^{288}Mc in the other fourteen chains is attributed to the decay losses of the short-lived nucleus ^{288}Mc ($T_{1/2} = 193^{+15}_{-13}$ ms) during the transport of the ^{288}Mc atoms into the detector channel. The observed ratio of the number of detected decay chains starting with ^{288}Mc decay to that of chains starting with ^{284}Nh ($T_{1/2} = 0.90^{+0.07}_{-0.06}$ s) allows a rough estimate of the mean flush-out time from the RTC window into miniCOMPACT of about 0.4 s. The transport time corresponds to approximately two half-lives for ^{288}Mc, but it was short enough for the efficient transport of ^{284}Nh. Within the observed decay chains, eleven α particles from the decay chain members ^{284}Nh, ^{280}Rg, ^{276}Mt, ^{270}Bh, were missing, in agreement with the mean detection efficiency for a single α particle emitted inside the miniCOMPACT detector channel of about 80%. The search for the α decay of the long-lived ^{268}Db was performed within the energy interval (7.7–8.0) MeV and within the time interval between the last member of the α-decay chain occurring during the time interval of 200 s and the concluding SF event. Several candidates for α decay of ^{268}Db were found (Table 1). However, this search was hindered in some cases by a non-zero background in this energy range, especially from non-volatile byproducts within the first centimeters of the miniCOMPACT detector. The measured time intervals between neighbouring members of all registered decay chains show a very good agreement with the known half-lives, deduced from the observation of about two hundred chains in physics experiments (Oganessian et al., 2013; Rudolph et al., 2013; Gates et al., 2015; Oganessian et al., 2022b). The experimental distributions of correlation times for the decay chain members ^{284}Nh, ^{280}Rg, ^{276}Mt, ^{272}Bh and ^{268}Db are shown in Figure 4, in comparison with lifetime probability curves calculated for the recently published most precise half-lives (Oganessian et al., 2022; Oganessian et al., 2022b).

Five SF events, which were observed without position and time correlation to any α-decaying precursors within the energy range (9.0–10.5) MeV and a time interval of 1000 s. They could not be assigned to any registered long decay chain from ^{288}Mc or

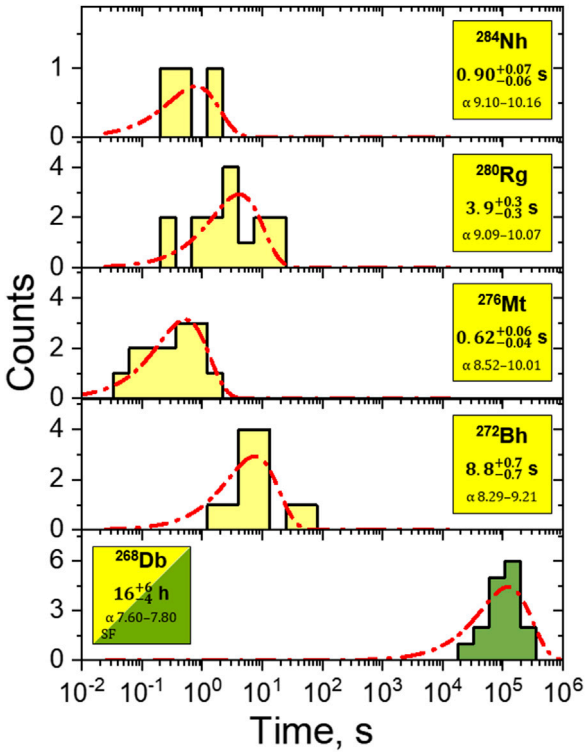

FIGURE 4
The lifetime distributions of the observed decay chain members ^{284}Nh, ^{280}Rg, ^{276}Mt, ^{272}Bh, and ^{268}Db. The experimental lifetime distributions are shown for ^{284}Nh, ^{280}Rg, ^{276}Mt, ^{272}Bh, and ^{268}Db (bars), in comparison with the lifetime probability curves (dash-dotted lines) calculated for the recently published half-lives of these isotopes (Oganessian et al., 2022; Oganessian et al., 2022b). Yellow denotes α-decay, green denotes spontaneous fission.

^{284}Nh. Two such SF events were registered in the first centimeter of the miniCOMPACT array, and three at the 4th, 6th and 10th centimeter. In four cases, both fission fragments were detected. These SF-only events were considered as real ones and could be attributed to SF branches in early chain members (Oganessian et al., 2022; Forsberg et al., 2016; Rudolph, 2022). A detailed analysis on decay scenario aspects along the decay chain from ^{288}Mc will be published elsewhere[2]. Even though the spatial distribution of these SF events in the detector channel resembles the distribution of decay chains from ^{284}Nh, the ambiguity in the assignment of these SF-only events did not allow including them for the evaluation of the chemical behaviour.

A comparison of the number of events registered in the present experiment to the number of decay chains from the Mc decay spectroscopy experiment at TASCA (Rudolph et al., 2013) normalized to the number of produced ^{288}Mc nuclei reveals that roughly 40% of the reaction products guided to the TASCA focal plane were extracted into the gas chromatography channel. The losses were primarily caused by adsorption of non-volatile species on the RTC surface before reaching the detection setup. In addition,

2 Khuyagbaatar, J., Yakushev, A., Düllmann, Ch. E., and Mošať, P. (2024).

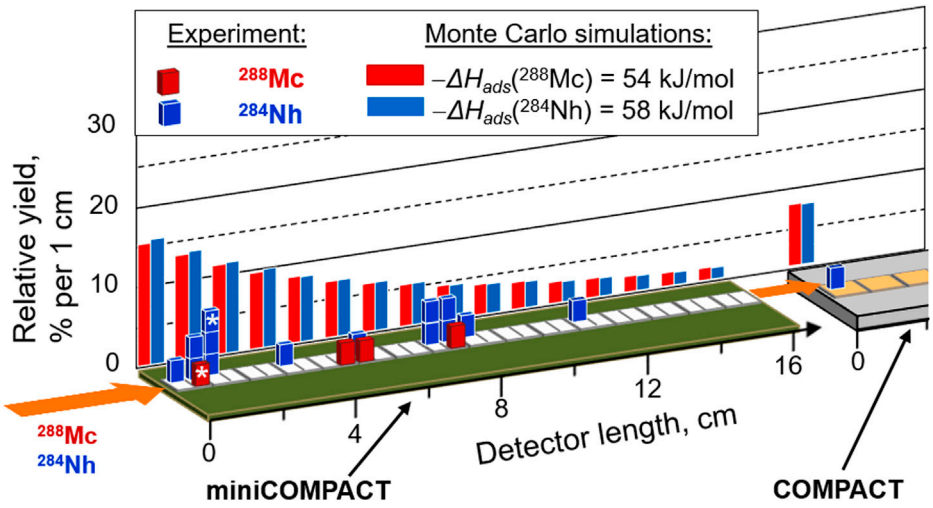

FIGURE 5
Event distribution in the detection setup. The positions of all observed decay chains in the detection setup assigned to ^{288}Mc (red bars) and ^{284}Nh (blue bars) are shown together with results of Monte Carlo simulations for the most probable values of the adsorption enthalpy on SiO_2, $-\Delta H_{ads}$ (Mc) = 54 kJ/mol and $-\Delta H_{ads}$ (Nh) = 58 kJ/mol, for Mc and Nh, respectively. According to simulations, a fraction of about 8% of both, Mc and Nh atoms, entering the miniCOMPACT pass through. This fraction is indicated as deposition in the first centimeter of COMPACT. In one decay chain, the observed decays from ^{288}Mc and ^{284}Nh were distributed over two detectors; their positions are marked with an asterisk.

decay losses also significantly contributed to the overall losses of the short-lived ^{288}Mc.

3.2 Distribution of Mc and Nh in the detection setup

All observed decay chains originating from ^{288}Mc or ^{284}Nh were found in the miniCOMPACT detector, except for one decay chain from ^{284}Nh, which was registered in the first centimeter of the Au-covered COMPACT. Thus, while all four Mc atoms adsorbed on the SiO_2 surface, one of the 14 Nh atoms passed the miniCOMPACT detector and a 30-cm long connecting tube made of PTFE between miniCOMPACT and COMPACT, but adsorbed on the very first Au-covered detector. This observation may suggest a stronger interaction with the Au surface compared to interaction with SiO_2 and PTFE surfaces, in line with the predictions (Pershina et al., 2021). This encourages future studies with higher statistics. The positions of the observed decay chains starting with ^{288}Mc and starting with ^{284}Nh in the detector channel are presented in Figure 5. All four events originating from ^{288}Mc and about 85% of the ^{284}Nh events were registered in the first half of the SiO_2-covered miniCOMPACT detector.

4 Discussion

Atoms without retention on the surface would pass miniCOMPACT within about 20 ms. Thus, almost all Nh and Mc nuclei would pass the miniCOMPACT detector array without decay. Clearly, the observation of the decay of Nh and Mc nuclei in the miniCOMPACT detector array demonstrated retention due to adsorption of Nh and Mc on SiO_2 at room temperature. A key question is in which chemical form Mc and Nh deposited on the SiO_2 detector surface. Despite the short lifetime of Mc and Nh, the possibility to form compounds through rare interactions with gas impurities cannot be excluded. The main gas impurities, O_2 and H_2O,

TABLE 2 Calculated values of the energy of reaction for selected chemical reactions of metal M (M = Bi, Mc) with oxygen and water. The initial metallic species are neutral atoms (M) or monovalent cations (M(+)). The initial oxygen and water are molecular O_2 and H_2O.

Chemical reaction	Energy of reaction, eV			
	M = Tl	M = Bi	M = Nh	M = Mc
$M(+) + O_2 = MO(+) + O$	5.928	2.666	5.705	5.697
$M(+) + H_2O = MO(+) + H_2$	5.431	2.168	5.207	5.200
$M(+) + H_2O = M(OH) + H (+)$	9.448	8.613	9.547	10.200
$M + O_2 = MO(+) + O (-)$	10.977	8.928	11.765	10.320
$M + H_2O = M(OH) + H$	2.065	2.444	5.073	2.393

were kept at a ppm level at most, similarly to the previous experiments at TASCA (Yakushev et al., 2014; Yakushev et al., 2022). To form compounds (oxides or hydroxides) in reactions with traces of O_2 and H_2O, Mc ions or atoms should be able to break rather strong chemical bonds in the O_2 and H_2O molecules after their thermalization in the gas. Energies of selected reactions of the M atoms and M+ ions with the O_2 and H_2O molecules, where M is a superheavy element Mc or Nh, or their nearest homologues Bi or Tl, were calculated with the ADF BAND code and are presented in Table 2. All values are positive, ranging from 2.07 to 11.77 eV. Because of the rather high positive values of the heat of reaction, these interactions are not energetically favored at room temperature for Mc and Nh and neither for their homologues Bi and Tl. Thus, the thermodynamical analysis of possible reactions with trace gas impurities clearly suggests that Mc and Nh should stay in the elemental form before they adsorb on the SiO_2 surface. In order to obtain more quantitative information on the interaction strength between Mc and Nh atoms and the SiO_2 surface, the Monte Carlo simulation method was applied to obtain numerical information on the interaction strength between SHE species and a surface. This approach is based on the model of mobile adsorption (Zvara, 1985) and allows to simulate individual histories of a large number of single atoms (e.g., 10^6) migrating through the chromatography column, using actual experimental parameters including the dimension of the column, the gas composition and flow rate, the radionuclide's half-life etc. Single Mc or Nh atoms moving with the carrier gas along the detector arrays experience many collisions with the surface. In each surface collision, the adsorbed atom is immobilized at the surface for a time τa, which depends on the (experimentally known) oscillation period τ_0, the activation energy needed for its desorption from the surface (E_{des}), which is a free parameter, and on the temperature, according to the Frenkel's equation (Frenkel, 1948) (Equation 1).

$$\tau_a = \tau_0 \cdot exp\left(\left(\frac{E_{des}}{RT}\right)\right) \quad (1)$$

Supposed that the energy needed for the desorption is equal to the negative adsorption enthalpy, $E_{des} = -\Delta H_{ads}^{SiO_2}$, such simulations were performed for the adsorption of Mc and Nh atoms on SiO_2 resulting in simulated distributions of Mc and Nh for different $-\Delta H_{ads}^{SiO_2}$ values. The statistically analysed agreement between the experimental distributions of ^{288}Mc and ^{284}Nh in miniCOMPACT and the simulated ones enabled deducing the adsorption enthalpy values of Mc and Nh atoms on the SiO_2 surface, ($-\Delta H_{ads}^{SiO_2}$), to $54\,^{+11}_{-5}$ kJ/mol for Mc and $58\,^{+8}_{-3}$ kJ/mol for Nh. The distribution of Mc and Nh atoms in miniCOMPACT for their most probable $-\Delta H_{ads}^{SiO_2}$ values are depicted in Figure 3. The lower and upper limits for these values were determined for a confidence interval (c.i.) of 68% by statistical analysis employing a method of c.i. calculation for experiments with small event numbers (Brüchle, 2003). The obtained $-\Delta H_{ads}$ values for Mc and Nh on the SiO_2 surface agree with the theoretically predicted E_{ads} values for elemental Nh and Mc on quartz (Pershina et al., 2021), supporting the assignment of Mc and Nh deposition in elemental form.

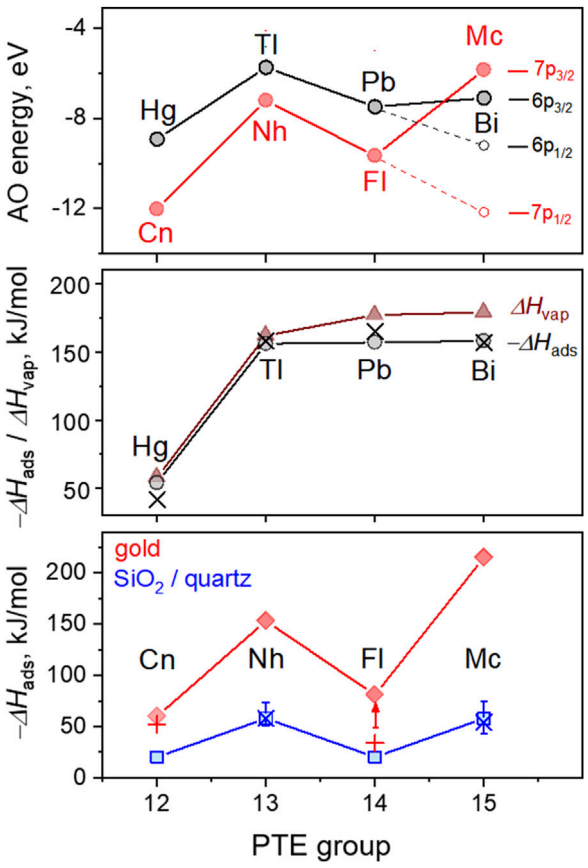

FIGURE 6
Calculated energies of the highest occupied atomic orbitals for elements of the groups 12–15 of the 6th and 7th period; adsorption enthalpies ($-\Delta H_{ads}$) on quartz (theoretical values of 6p and 7p elements and experimental values of 6p elements); $-\Delta H_{ads}$ values on the SiO_2 (experimental values of 7p elements) and Au surfaces (theoretical and experimental values of 7p elements); and vaporization enthalpies (ΔH_{vap}). Upper panel: calculated Dirac-Fock energies of the highest occupied AO (in eV) are shown with red symbols for Cn to Mc and with black ones for their homologues, Hg to Bi (Desclaux, 1973). The black and red arrows show the values of the spin-orbit splitting for the 6p and 7p shells, respectively. Middle panel: The calculated and experimental values of $-\Delta H_{ads}$ on quartz for SHE homologues, Hg to Bi, are shown as grey circles and black crosses, respectively (Pershina, 2018; Trombach et al., 2019; Serov et al., 2013; Steinegger et al., 2016; Düllmann et al., 2022; Kraus, 2021). The experimental values of ΔH_{vap} are shown as brown solid triangles (Zhang et al., 2011). Lower panel: calculated values of $-\Delta H_{ads}$ on quartz and Au for Cn to Mc are shown with blue square and red diamond symbols, respectively (Pershina, 2018; Pershina et al., 2021; Trombach et al., 2019; Düllmann et al., 2022). Experimental $-\Delta H_{ads}$ on Au for Cn and Fl are shown as red crosses and an arrow in the case of a limit (Eichler et al., 2010; Yakushev et al., 2014; Yakushev et al., 2022). Experimental values from this work, $-\Delta H_{ads}^{SiO_2}$ (Mc) = $54\,^{+11}_{-5}$ kJ/mol and $-\Delta H_{ads}^{SiO_2}$ (Nh) = $58\,^{+8}_{-3}$ kJ/mol, are shown by blue crosses with error bars. All panels: the lines connecting the data points are shown to guide the eye. All $-\Delta H_{ads}$ values are given in kJ/mol.

Theoretical and experimental thermodynamic values for the reactivity and volatility of the superheavy elements in groups 12–15 and their nearest lighter homologues are summarized in Figure 6. For the heaviest members of the groups 12–15 of the PTE, trends in AO energies of the highest occupied orbitals show an irregular course with minima for groups 12 and 14. The spread is

significantly more pronounced for SHE compared with their lighter homologues due to the strong spin-orbit splitting in the 7p shell and stabilisation of the 7s and $7p_{1/2}$ (sub) shells in Cn and Fl, respectively (Figure 6, upper panel). This trend also determines the chemical behaviour, e.g., the adsorption strength of these elements on the gold and quartz surfaces. The calculated and experimental values of $-\Delta H_{ads}$ on quartz for elements of the 6th row are shown in Figure 6 (middle panel) in comparison with their heat of vaporization (ΔH_{vap}) values.

The trend in $-\Delta H_{ads}$ values for the 6p elements is indicative of a strong increase in the interaction strength with the surface from Hg to Tl that remains almost unchanged for Tl, Pb, and Bi (Pershina, 2018; Trombach et al., 2019; Düllmann et al., 2022). The theoretical $-\Delta H_{ads}$ values show a good agreement with the experimental ones (Serov et al., 2013; Steinegger et al., 2016; Kraus, 2021). The experimental $-\Delta H_{ads}$ value for Bi was obtained in recent off-line gas chromatography studies with Po and At isotopes at the U-120 M cyclotron in Řež, Czech Republic, and will be published elsewhere. The ΔH_{vap} values for these elements follow a similar trend (Zhang et al., 2011). For the heaviest members of groups 12–15, the calculated and experimental $-\Delta H_{ads}$ values on quartz and Au are shown in Figure 6 (lower panel). The predicted $-\Delta H_{ads}$ values for adsorption of Nh and Mc on quartz are significantly lower than those of their lighter homologues, Tl and Bi, respectively. Moreover, the trend of the $-\Delta H_{ads}$ values of the superheavy elements Cn to Mc has also an irregular course, similar to that of the energies of their highest occupied AOs. This difference in the trends between the 6p and 7p elements is attributed to the larger spin-orbital effects on the 7p AO (Figure 6, upper panel) and the relativistic stabilization of the $7p_{1/2}$ orbital, and is in line with the reduced chemical reactivity in Fl (Schwerdtfeger et al., 2020; Pershina, 2015; Eliav et al., 2015).

5 Conclusion

Eighteen decay chains originating from ^{288}Mc and its decay products were identified upon adsorption on silicon oxide and gold surfaces (Table 1). The decay properties of the registered chain members are in excellent agreement with those obtained in earlier physics studies. Taking into account experimental conditions and results of state-of-the-art theoretical predictions, we conclude that Nh and Mc were deposited on the silicon oxide surface in the elemental state. The thermodynamic quantities for Nh and Mc, namely, $-\Delta H_{ads}^{SiO_2}(\mathrm{Mc}) = 54^{+11}_{-5}$ kJ/mol and $-\Delta H_{ads}^{SiO_2}(\mathrm{Nh}) = 58^{+8}_{-3}$ kJ/mol (68% c.i.), were deduced by using Monte Carlo simulations. Our experimental observations indicate a stronger chemical interaction of Nh and Mc compared to their neighbours Cn and Fl, in accordance with theoretical predictions. The obtained values are significantly (about 100 kJ/mol) lower than those of their lighter homologues, Tl (Serov et al., 2013; Steinegger et al., 2016) and Bi. Thus, the lowest chemical reactivity in groups 13 and 15 is observed for the 7p elements Nh and Mc. This is due to strong relativistic effects, i.e., the large energy splitting in the 7p shell and the stabilization of the $7p_{1/2}^2$ subshell has been confirmed experimentally. This work opens the door to future chemical research with even heavier elements, Lv and Ts, to shed light on the evolution of relativistic effects as the $7p_{3/2}$ subshell is being filled. However, a fast and efficient extraction from a gas-filled chamber to a chemistry setup is required for future SHE experiments beyond Mc to minimize the transport time of very short-lived products to a chemistry apparatus down to a few milliseconds. Recent numerical and experimental results show promise for such chemistry experiments, if a chemistry setup is coupled to a buffer gas cell, in which ions are carried to a chemistry device by electrical fields (Varentsov and Yakushev, 2019; Götz et al., 2021).

Data availability statement

The raw data supporting the conclusions of this article will be made available by the authors, without undue reservation.

Author contributions

AY: Conceptualization, Data curation, Formal Analysis, Investigation, Methodology, Project administration, Validation, Writing–original draft, Writing–review and editing. JKh: Data curation, Formal Analysis, Investigation, Software, Validation, Writing–review and editing. CD: Conceptualization, Funding acquisition, Methodology, Project administration, Resources, Supervision, Validation, Writing–review and editing. MB: Formal Analysis, Investigation, Validation, Writing–review and editing. RC: Data curation, Methodology, Resources, Software, Writing–review and editing. DC: Data curation, Formal Analysis, Investigation, Writing–review and editing. DD: Data curation, Formal Analysis, Investigation, Validation, Writing–review and editing. FG: Data curation, Investigation, Validation, Writing–review and editing. YH: Data curation, Formal Analysis, Writing–review and editing. MI: Methodology, Software, Validation, Writing–review and editing. EJ: Data curation, Resources, Software, Writing–review and editing. JKr: Data curation, Methodology, Resources, Writing–review and editing. DK: Data curation, Formal Analysis, Methodology, Writing–review and editing. NK: Data curation, Formal Analysis, Methodology, Resources, Software, Validation, Writing–review and editing. LL: Methodology, Writing–review and editing, Conceptualization, Data curation, Formal Analysis, Investigation. SL: Data curation, Formal Analysis, Resources, Software, Writing–review and editing. CM: Data curation, Methodology, Writing–review and editing. PM: Data curation, Formal Analysis, Investigation, Methodology, Software, Validation, Writing–review and editing. VP: Conceptualization, Formal Analysis, Investigation, Software, Validation, Writing–review and editing. SR: Data curation, Formal Analysis, Validation, Writing–review and editing. DR: Data curation, Formal Analysis, Investigation, Validation, Writing–review and editing. JR: Data curation, Methodology, Resources, Writing–review and editing. LS: Data curation, Formal Analysis, Methodology, Software, Validation, Writing–review and editing. BS: Data curation, Resources, Writing–review and editing. US: Data curation, Formal Analysis, Methodology, Validation, Writing–review and editing. PT-P: Data curation, Resources, Writing–review and editing. NT: Investigation,

Methodology, Validation, Writing–review and editing. MW: Conceptualization, Methodology, Resources, Writing–review and editing. PW: Data curation, Formal Analysis, Methodology, Resources, Software, Writing–review and editing.

Funding

The author(s) declare that financial support was received for the research, authorship, and/or publication of this article. This work has been financially supported by the German BMBF (project 05P21UMFN2), the Swedish Research Council (Vetenskapsrådet, VR 2016-3969), and the Knut and Alice Wallenberg Foundation (KAW 2015.0021). The publication is funded by the Open Access Publishing Fund of GSI Helmholtzzentrum für Schwerionenforschung.

Acknowledgments

The results presented here are based on the experiments U308 and U327, which were performed at the beam line X8/TASCA at the GSI Helmholtzzentrum für Schwerionenforschung GmbH, Darmstadt (Germany) in the frame of FAIR Phase-0. The authors would like to thank the GSI staff of the ECR ion source group and the accelerator UNILAC for providing stable and intense ion beams, as well as the GSI department of experiment electronics, and the detector and target laboratories of GSI. The ^{243}Am target material was provided by the U.S. DOE through ORNL.

Conflict of interest

The authors declare that the research was conducted in the absence of any commercial or financial relationships that could be construed as a potential conflict of interest.

Publisher's note

References

Aksenov, N. V., Steinegger, P., Abdullin, F.Sh., Albin, Yu. V., Bozhikov, G. A., Chepigin, V. I., et al. (2017). On the volatility of nihonium (Nh, Z = 113). *Eur. Phys. J.* A 53, 158. doi:10.1140/epja/i2017-12348-8

Becke, A. D. (1988). Density-functional exchange-energy approximation with correct asymptotic behavior. *Phys. Rev. A* 38, 3098–3100. doi:10.1103/physreva.38.3098

Borschevsky, A., Pašteka, L. F., Pershina, V., Eliav, E., and Kaldor, U. (2015). Ionization potentials and electron affinities of the superheavy elements 115–117 and their sixth-row homologues Bi, Po, and at. *Phys. Rev. A* 91, 020501. (R). doi:10.1103/physreva.91.020501

Brüchle, W. (2003). Confidence intervals for experiments with background and small numbers of events. *Radiochim. Acta* 91, 71–80. doi:10.1524/ract.91.2.71.19989

Desclaux, J. P. (1973). Relativistic Dirac-Fock expectation values for atoms with Z = 1 to Z = 120. *Data Nucl. Data Tables* 12, 311–406. doi:10.1016/0092-640x(73)90020-x

Dmitriev, S. N., Aksenov, N. V., Albin, Yu. V., Bozhikov, G. A., Chelnokov, M. L., Chepigin, V. I., et al. (2014). Pioneering experiments on the chemical properties of element 113. *Mendeleev Commun.* 24, 253–256. doi:10.1016/j.mencom.2014.09.001

Düllmann, Ch. E., Block, M., Heßberger, F. P., Khuyagbaatar, J., Kindler, B., Kratz, J. V., et al. (2022). Five decades of GSI superheavy element discoveries and chemical investigation. *Radiochim. Acta* 110 (6-9), 417–439. doi:10.1515/ract-2022-0015

Düllmann, Ch. E., Brüchle, W., Dressler, R., Eberhardt, K., Eichler, B., Eichler, R., et al. (2002). Chemical investigation of hassium (element 108). *Nature* 418, 859–862. doi:10.1038/nature00980

Düllmann, Ch. E., Folden, C. M., Gregorich, K. E., Hoffman, D. C., Leitner, D., Pang, G. K., et al. (2005). Heavy-ion-induced production and physical preseparation of short-lived isotopes for chemistry experiments. *Nucl. Instrum. Meth. A* 551, 528–539. doi:10.1016/j.nima.2005.05.077

Düllmann, Ch. E., Schädel, M., Yakushev, A., Türler, A., Eberhardt, K., Kratz, J. V., et al. (2010). Production and decay of element 114: high cross sections and the new nucleus ^{277}Hs. *Phys. Rev. Lett.* 104, 252701. doi:10.1103/physrevlett.104.252701

Dzuba, V. A., and Flambaum, V. V. (2016). Electron structure of superheavy elements uut, Fl and uup (Z=113 to 115). *Hyperfine Interact.* 237, 160. doi:10.1007/s10751-016-1365-7

Eichler, R. (2013). First foot prints of chemistry on the shore of the Island of Superheavy Elements. *J. Phys. Conf. Ser.* 420, 012003. doi:10.1088/1742-6596/420/1/012003

Eichler, R., Aksenov, N. V., Albin, Yu. V., Belozerov, A. V., Bozhikov, G. A., Chepigin, V. I., et al. (2010). Indication for a volatile element 114. *Radiochim. Acta* 98, 133–139. doi:10.1524/ract.2010.1705

Eichler, R., Aksenov, N. V., Belozerov, A. V., Bozhikov, G. A., Chepigin, V. I., Dmitriev, S. N., et al. (2007). Chemical characterization of element 112. *Nature* 447, 72–75. doi:10.1038/nature05761

Eliav, E., Fritzsche, S., and Kaldor, U. (2015). Electronic structure theory of the superheavy elements. *Nucl. Phys. A* 944, 518–550. doi:10.1016/j.nuclphysa.2015.06.017

Forsberg, U., Rudolph, D., Andersson, L.-L., Di Nitto, A., Düllmann, Ch. E., Fahlander, C., et al. (2016). Recoil-α-fission and recoil-α–α-fission events observed in the reaction ^{48}Ca + ^{243}Am. *Nucl. Phys. A* 953, 117–138. doi:10.1016/j.nuclphysa.2016.04.025

Fox-Beyer, B. S., and van Wüllen, C. (2012). Theoretical modelling of the adsorption of thallium and element 113 atoms on gold using two-component density functional methods with effective core potentials. *Chem. Phys.* 395, 95–103. doi:10.1016/j.chemphys.2011.04.029

Frenkel, Ya. I. (1948). *Statistical physics*. Moscow-Leningrad: Izd. Akad. Nauk SSSR. [book in Russian].

Gates, J. M., Gregorich, K. E., Gothe, O. R., Uribe, E. C., Pang, G. K., Bleuel, D. L., et al. (2015). Decay spectroscopy of element 115 daughters: ^{280}Rg → ^{276}Mt and ^{276}Mt → ^{272}Bh. *Phys. Rev. C* 92, 021301. (R). doi:10.1103/physrevc.92.021301

Götz, S., Raeder, S., Block, M., Düllmann, Ch. E., Folden III, C. M., Glennon, K. J., et al. (2021). Rapid extraction of short-lived isotopes from a buffer gas cell for use in gas-phase chemistry experiments, Part II: on-line studies with short-lived accelerator-produced radionuclides. *B* 507, 27–35. doi:10.1016/j.nimb.2021.09.004

Hohenberg, P., and Kohn, W. (1964). Inhomogeneous electron gas. *Phys. Rev. B* 136, 864–B871. doi:10.1103/physrev.136.b864

Ilias, M., and Pershina, V. (2022). Reactivity of group 13 elements Tl and element 113, Nh, and of their hydroxides with respect to various quartz surfaces from periodic relativistic DFT calculations. *Inorg. Chem.* 61 (40), 15910–15920. doi:10.1021/acs.inorgchem.2c02103

Jäger, E., Brand, H., Düllmann, Ch.E., Khuyagbaatar, J., Krier, J., Schädel, M., et al. (2014). High intensity target wheel at TASCA: target wheel control system and target monitoring. *J. Radioanal. Nucl. Chem.* 299, 1073–1079. doi:10.1007/s10967-013-2645-1

Khuyagbaatar, J., Ackermann, D., Andersson, L.-L., Ballof, J., Brüchle, W., Düllmann, Ch. E., et al. (2012). Study of the average charge states of ^{188}Pb and ^{252,254}No ions at the gas-filled separator TASCA. *Nucl. Instr. Meth. A* 689, 40–46. doi:10.1016/j.nima.2012.06.007

Kohn, W., and Sham, L. J. (1965). Self-consistent equations including exchange and correlation effects. *Phys. Rev. A* 140, 1133–A1138. doi:10.1103/physrev.140.a1133

Kraus, B. (2021). *Optimization of vacuum adsorption chromatography for superheavy element experiments [Doctoral dissertation]*. Switzerland: University of Bern.

Lens, L., Yakushev, A., Düllmann, Ch. E., Asai, M., Ballof, J., Block, M., et al. (2018). Online chemical adsorption studies of Hg, Tl, and Pb on SiO_2 and Au surfaces in preparation for chemical investigations on Cn, Nh, and Fl at TASCA. *Radiochim. Acta* 106, 949–962. doi:10.1515/ract-2017-2914

Oganessian, Yu Ts., Abdullin, F.Sh., Dmitriev, S. N., Gostic, J. M., Hamilton, J. H., Henderson, R. A., et al. (2013). Investigation of the ^{243}Am + ^{48}Ca reaction products previously observed in the experiments on elements 113, 115, and 117. *Phys. Rev. C* 87, 014302. doi:10.1103/physrevc.87.014302

Oganessian, Yu. Ts., and Utyonkov, V. K. (2015). Superheavy nuclei from ^{48}Ca-induced reactions. *Nucl. Phys. A* 944, 62–98. doi:10.1016/j.nuclphysa.2015.07.003

Oganessian, Yu. Ts., Utyonkov, V. K., Kovrizhnykh, N. D., Abdullin, F.Sh., Dmitriev, S. N., Dzhioev, A. A., et al. (2022). New isotope ^{286}Mc produced in the ^{243}Am + ^{48}Ca reaction. *Phys. Rev. C* 106, 064306. doi:10.1103/physrevc.106.064306

Oganessian, Yu. Ts., Utyonkov, V. K., Kovrizhnykh, N. D., Abdullin, F.Sh., Dmitriev, S. N., Ibadullayev, D., et al. (2022). First experiment at the Super Heavy Element Factory: high cross section of ^{288}Mc in the ^{243}Am + ^{48}Ca reaction and identification of the new isotope ^{264}Lr. *Phys. Rev. C* 106, L031301. doi:10.1103/PhysRevC.106.L031301

Pershina, V. (2015). Electronic structure and properties of superheavy elements. *Nucl. Phys. A* 944, 578–613. doi:10.1016/j.nuclphysa.2015.04.007

Pershina, V. (2016). A theoretical study on the adsorption behavior of element 113 and its homologue Tl on a quartz surface: relativistic periodic DFT calculations. *J. Phys. Chem. C* 120 (36), 20232–20238. doi:10.1021/acs.jpcc.6b07834

Pershina, V. (2018). Reactivity of superheavy elements Cn, Nh, and Fl and their lighter homologues Hg, Tl, and Pb, respectively, with a gold surface from periodic DFT calculations. *Inorg. Chem.* 57 (7), 3948–3955. doi:10.1021/acs.inorgchem.8b00101

Pershina, V. (2019). Relativity in the electronic structure of the heaviest elements and its influence on periodicities in properties. *Radiochim. Acta* 107, 833–863. doi:10.1515/ract-2018-3098

Pershina, V., Anton, J., and Jacob, T. (2009). Electronic structures and properties of M-Au and MOH, where M = Tl and element 113. *Chem. Phys. Lett.* 480, 157–160. doi:10.1016/j.cplett.2009.08.069

Pershina, V., and Iliaš, M. (2019). Properties and reactivity of hydroxides of group 13 elements in, Tl, and Nh from molecular and periodic DFT calculations. *Inorg. Chem.* 58, 9866–9873. doi:10.1021/acs.inorgchem.9b00949

Pershina, V., Ilias, M., and Yakushev, A. (2021). Reactivity of the superheavy element 115, Mc, and its lighter homologue, Bi, with respect to gold and hydroxylated quartz surfaces from periodic relativistic DFT calculations: a comparison with element 113. *Nh. Inorg. Chem.* 60 (13), 9848–9856.

Pitzer, K. S. (1975). Are elements 112, 114, and 118 relatively inert gases? *J. Chem. Phys.* 63, 1032–1033. doi:10.1063/1.431398

Pyper, N. C. (2020). Relativity and the periodic table. *Phil. Trans. R. Soc. A* 378, 20190305. doi:10.1098/rsta.2019.0305

Rudolph, D. (2022). Results and plans for nuclear spectroscopy of superheavy nuclei: the Lund perspective. *Eur. Phys. J.* A 58, 242. doi:10.1140/epja/s10050-022-00868-7

Rudolph, D., Forsberg, U., Golubev, P., Sarmiento, L. G., Yakushev, A., Andersson, L.-L., et al. (2013). Spectroscopy of element 115 decay chains. *Phys. Rev. Lett.* 111, 112502. doi:10.1103/physrevlett.111.112502

Runke, J., Düllmann, Ch. E., Eberhardt, K., Ellison, P. A., Gregorich, K. E., Hofmann, S., et al. (2014). Preparation of actinide targets for the synthesis of the heaviest elements. *J. Radioanal. Nucl. Chem.* 299, 1081–1084. doi:10.1007/s10967-013-2616-6

Rusakov, A. A., Demidov, Y. A., and Zaitsevskii, A. (2013). Estimating the adsorption energy of element 113 on a gold surface. *Centr. Eur. J. Phys.* 11, 1537–1540. doi:10.2478/s11534-013-0311-4

Såmark-Roth, A., Cox, D. M., Rudolph, D., Sarmiento, L. G., Albertsson, M., Carlsson, B. G., et al. (2023). Spectroscopy along flerovium decay chains. III. details on experiment, analysis, ^{282}Cn, and spontaneous fission branches. *Phys. Rev. C* 107, 024301. doi:10.1103/PhysRevC.107.024301

Schwerdtfeger, P., and Seth, M. (2002). Relativistic quantum chemistry of the superheavy elements. Closed-shell element 114 as a case study. *J. Nucl. Radiochem. Sci.* 3 (1), 133–136. doi:10.14494/jnrs2000.3.133

Schwerdtfeger, P., Smits, O. R., and Pyykkö, P. (2020). The periodic table and the physics that drives it. *Nat. Rev. Chem.* 4, 359–380. doi:10.1038/s41570-020-0195-y

SCM (2024). *Amsterdam modelling suite AMS ADF 2024.1, SCM, theoretical chemistry*. Amsterdam, Netherlands: Vrije Universiteit. Available at: http://www.scm.com.

Semchenkov, A., Brüchle, W., Jäger, E., Schimpf, E., Schädel, M., Mühle, C., et al. (2008). The TransActinide separator and chemistry apparatus (TASCA) at GSI – optimization of ion-optical structures and magnet designs. *Nucl. Instrum. Methods B* 266, 4153–4161. doi:10.1016/j.nimb.2008.05.132

Serov, A., Eichler, R., Dressler, R., Piguet, D., Türler, A., Vögele, A., et al. (2013). Adsorption interaction of carrier-free thallium species with gold and quartz surfaces. *Radiochim. Acta* 101, 421–426. doi:10.1524/ract.2013.2045

Steinegger, P., Asai, M., Dressler, R., Eichler, R., Kaneya, Y., Mitsukai, A., et al. (2016). Vacuum chromatography of Tl on SiO_2 at the single-atom level. *J. Phys. Chem. C* 120, 7122–7132. doi:10.1021/acs.jpcc.5b12033

Smits, O. R., Düllmann, Ch. E., Indelicato, P., Nazarewicz, W., and Schwerdtfeger, P. (2024). The quest for superheavy elements and the limit of the periodic table. *Nat. Rev. Phys.* 6, 86–98. doi:10.1038/s42254-023-00668-y

Te Velde, G., Bickelhaupt, F. M., Baerends, E. J., Fonseca Guerra, C., Van Gisbergen, S. J. A., Snijders, J. G., et al. (2001). Chemistry with ADF. *J. Comput. Chem.* 22 (9), 931–967. doi:10.1002/jcc.1056

Trombach, L., Ehlert, S., Grimme, S., Schwerdtfeger, P., and Mewes, J.-M. (2019). Exploring the chemical nature of super-heavy main-group elements by means of efficient plane-wave density-functional theory. *Phys. Chem. Chem. Phys.* 21 (33), 18048–18058. doi:10.1039/c9cp02455g

Türler, A., Eichler, R., and Yakushev, A. (2015). Chemical studies of elements with Z ≥ 104 in gas phase. *Nucl. Phys. A* 944, 640–689. doi:10.1016/j.nuclphysa.2015.09.012

Türler, A., and Pershina, V. (2013). Advances in the production and chemistry of the heaviest elements. *Chem. Rev.* 113 (2), 1237–1312. doi:10.1021/cr3002438

Van Lenthe, E., Baerends, E. J., and Snijders, J. G. (1994). Relativistic total energy using regular approximations. *J. Chem. Phys.* 101, 9783–9792. doi:10.1063/1.467943

Varentsov, V., and Yakushev, A. (2019). Concept of a new universal high-density gas stopping cell setup for study of gas-phase chemistry and nuclear properties of super heavy elements (UniCell). *Nucl. Instrum. Methods A* 940, 206–214. doi:10.1016/j.nima.2019.06.032

Węgrzecki, M., Bar, J., Budzyński, T., Cież, M., Grabiec, P., Kozłowski, R., et al. (2013). "Design and properties of silicon charged-particle detectors developed at the Institute of electron technology (ITE)," in Proc. SPIE 8902, Electron Technology Conference 2013, China, 25 July 2013. doi:10.1117/12.2031041

Wittwer, D., Abdullin, F.Sh., Aksenov, N. V., Albin, Yu. V., Bozhikov, G. A., Dmitriev, S. N., et al. (2010). Gas phase chemical studies of superheavy elements using the Dubna gas-filled recoil separator - stopping range determination. *Nucl. Instr. Meth. B* 268, 28–35. doi:10.1016/j.nimb.2009.09.062

Yakushev, A., and Eichler, R. (2016). Gas-phase chemistry of element 114, flerovium. *EPJ Web Conf.* 131, 07003. doi:10.1051/epjconf/201613107003

Yakushev, A., Gates, J. M., Türler, A., Schädel, M., Düllmann, Ch. E., Ackermann, D., et al. (2014). Superheavy element Flerovium (element 114) is a volatile metal. *Inorg. Chem.* 53, 1624–1629. doi:10.1021/ic4026766

Yakushev, A., Lens, L., Düllmann, Ch. E., Block, M., Brand, H., Dasgupta, M., et al. (2021). First study on nihonium (Nh, element 113) chemistry at TASCA. *Front. Chem.* 9, 753738. doi:10.3389/fchem.2021.753738

Yakushev, A., Lens, L., Düllmann, Ch. E., Khuyagbaatar, J., Jäger, E., Krier, J., et al. (2022). On the adsorption and reactivity of element 114, flerovium. *Front. Chem.* 10, 976635. doi:10.3389/fchem.2022.976635

Zhang, Y., Evans, J. R. G., and Yang, S. (2011). Corrected values for boiling points and enthalpies of vaporization of elements in handbooks. *J. Chem. Eng. Data* 56, 328–337. doi:10.1021/je1011086

Zvára, I. (1985). Simulation of thermochromatographic processes by the Monte Carlo method. *Radiochim. Acta* 38, 95–102. doi:10.1524/ract.1985.38.2.95

Frontiers in Chemistry

Explores all fields of chemical science across the periodic table

Advances our understanding of how atoms, ions, and molecules come together and come apart. It explores the role of chemistry in our everyday lives - from electronic devices to health and wellbeing.

Discover the latest Research Topics

See more →

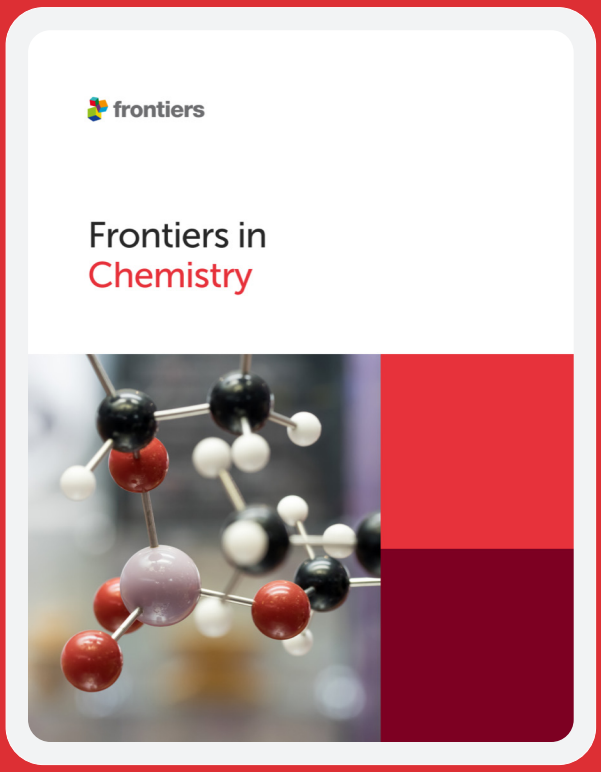

Frontiers

Avenue du Tribunal-Fédéral 34
1005 Lausanne, Switzerland
frontiersin.org

Contact us

+41 (0)21 510 17 00
frontiersin.org/about/contact